

INFORMATION TO USERS

This manuscript has been reproduced from the microfilm master. UMI films the text directly from the original or copy submitted. Thus, some thesis and dissertation copies are in typewriter face, while others may be from any type of computer printer.

The quality of this reproduction is dependent upon the quality of the copy submitted. Broken or indistinct print, colored or poor quality illustrations and photographs, print bleedthrough, substandard margins, and improper alignment can adversely affect reproduction.

In the unlikely event that the author did not send UMI a complete manuscript and there are missing pages, these will be noted. Also, if unauthorized copyright material had to be removed, a note will indicate the deletion.

Oversize materials (e.g., maps, drawings, charts) are reproduced by sectioning the original, beginning at the upper left-hand corner and continuing from left to right in equal sections with small overlaps.

Photographs included in the original manuscript have been reproduced xerographically in this copy. Higher quality 6" x 9" black and white photographic prints are available for any photographs or illustrations appearing in this copy for an additional charge. Contact UMI directly to order.

Bell & Howell Information and Learning
300 North Zeeb Road, Ann Arbor, MI 48106-1346 USA
800-521-0600



IMPROVED SIGNAL PROCESSING APPROACHES TO LANDMINE DETECTION

by

Ping Gao

Department of Electrical and Computer Engineering
Duke University

Date: November 3, 2000

Approved:

Leslie Collins
Dr. Leslie M. Collins, Supervisor

Lawrence Carin
Dr. Lawrence Carin

Jeffrey Krolik
Dr. Jeffrey Krolik

Loren W. Nolte
Dr. Loren W. Nolte

David Higdon
Dr. David Higdon

Dissertation submitted in partial fulfillment of the
requirements for the degree of Doctor of Philosophy
in the Department of Electrical and Computer Engineering
in the Graduate School of
Duke University

2000

UMI Number: 3003927

Copyright 2000 by
Gao, Ping

All rights reserved.

UMI®

UMI Microform 3003927

Copyright 2001 by Bell & Howell Information and Learning Company.
All rights reserved. This microform edition is protected against
unauthorized copying under Title 17, United States Code.

Bell & Howell Information and Learning Company
300 North Zeeb Road
P.O. Box 1346
Ann Arbor, MI 48106-1346

Copyright © 2000 by Ping Gao
All rights reserved

ABSTRACT

(Engineering—Electrical and Computer)

IMPROVED SIGNAL PROCESSING APPROACHES TO LANDMINE DETECTION

by

Ping Gao

Department of Electrical and Computer Engineering
Duke University

Date: November 3, 2000

Approved:

Leslie Collins
Dr. Leslie M. Collins, Supervisor

Dr. Lawrence Carin
Dr. Lawrence Carin

Jeffrey Krolik
Dr. Jeffrey Krolik

Loren W. Nolte
Dr. Loren W. Nolte

David Higdon
Dr. David Higdon

An abstract of a dissertation submitted in partial fulfillment
of the requirements for the degree of Doctor of Philosophy
in the Department of Electrical and Computer Engineering
in the Graduate School of
Duke University

2000

Abstract

The fundamental goals of landmine detection are to achieve a high probability of detection (P_d) and a low probability of false alarm (P_{fa}). Conventional approaches, which either perform a threshold test directly on the sensor output that is a scalar value or calculate the energy present in the signal and then perform a threshold test (energy detector), usually fulfill the first goal at the cost of a high P_{fa} .

Electromagnetic induction (EMI) is a well established technology for landmine detection. Traditional EMI systems are pulsed systems, often referred to as time-domain EMI. The design of most such sensors allows it to only measure the late-time induced response. Alternatively, EMI sensors can be operated in the frequency-domain, which mitigates the late-time problem.

The goal of this work is to develop better algorithms to achieve a high P_d and a low P_{fa} using either time-domain or frequency-domain EMI data. We incorporate the underlying physics of the system into a Bayesian detection theoretic framework using a forward model, and also incorporate spatial information as well as environmental uncertainties, such as unknown depth and orientation of the underground object, *etc.*, into the algorithm development to generate the optimal and various sub-optimal detectors for this problem. The optimal processor requires integration over uncertain parameters, thus, is mathematically complex and its numerical solution is computationally expensive. In order to implement a detector in real-time, sub-optimal solutions are also investigated.

Theoretical performance bounds for these detectors are derived. It is shown theoretically that the one dimensional likelihood ratio test and the one dimensional

generalized likelihood ratio test are equivalent under some reasonable assumptions for both the single-channel and multi-channel EMI data at a single survey location.

Additionally, the advantages and disadvantages of time-domain and frequency-domain EMI sensors are reviewed. Both theoretical studies and simulations are used to investigate the sensitivity of the performance of a Bayesian classifier to various parameters associated with time-domain and frequency-domain operations. Experimental data from four metallic objects from both a time-domain and a frequency-domain instrument is used to compare performance both across sensors and across classification algorithms.

Acknowledgements

I am greatly indebted to my advisor, Dr. Leslie M. Collins, for her support, guidance, ideas and inspiration throughout the course of this dissertation. The pressure I received made me a very productive four years at Duke. I would also like to thank Drs Lawrence Carin, Jeffrey Krolik, Loren Nolte, David Higdon, and Brani Vidakovic for their willingness to join my committee.

In particular, I would like to thank Dr. Lawrence Carin, Dr. Stacy Tantum, Dr. Yan Zhang, Dr. Thomas Altshuler, Ms. Vivian George, Dr. Regina Dugan, Dr. Erol Gelenbe, Mr. Taskin Kocak, and Ms. Sining Chen for the valuable discussions and suggestions regarding this work. My thanks to Dr. Dean Keiswetter and Dr. I.J. Won for their assistance with the GEM-3. I also thank Mr. Richard Weaver for supplying the landmines and for his support through the Joint UXO Coordinate Office (JUXOCO), and John Moulton and John Cary at EOIR, Ms. Yingyi Tan and Mr. Divid Ferguson, and the personnel at Range 71A, Fort A. P. Hill, VA. for their support of data collection throughout the hot summer of 1998.

I have greatly enjoyed the experience of sharing office with David Ferguson, Granger Hickman, Lisa Gresham, Sandy Throckmorton, Stacy Tantum, Jennifer Rasimas, and Jammie Shorey. I would like to thank them for their help from time to time, as well as for the many discussions which have helped improve my understanding of the subject.

I would like to thank my family for their love, support, encouragement, and confidence in my ability. You taught me to believe in myself and to set my goals high. I could always count on you to help me put the challenges I faced into perspective

and I know that you will always be there for me.

Haochuan, what I have achieved would not have been possible without you. Your constant love, support, encouragement and understanding help me through the tough time. Kenny, my son, I love you. Your smile melts my heart, gives me the greatest joy of life.

Ping

Support for this work was provided by the Army Research Office (ARO) under grant DAAH04-96-1-0448 (Demining MURI), the Joint UXO Coordination Office (JUX-OCO) via a grant (DAAG55-98-1-0340) administered through the ARO. Experimental data were collected in Ft. A. P. Hill, VA. and Geophex Ltd.

Contents

Abstract	iv
Acknowledgements	vi
List of Figures	xiv
List of Tables	xxiii
1 Introduction	1
2 Background	10
2.1 Brief Description of Land Mines	10
2.2 Electromagnetic Induction Systems	11
2.2.1 Time-Domain EMI Sensor	13
2.2.1.1 Geonics EM61 Sensor	14
2.2.1.2 Geonics EM61-3D Sensor	15
2.2.1.3 AN/PSS-12 Sensor	15
2.2.2 Frequency-Domain EMI System	17
2.2.2.1 The GEM-3	17
2.2.2.2 Model for Wideband Frequency-Domain EMI Responses	19
2.2.3 DARPA Background Clutter Data Collection	25
2.3 LRT and GLRT	27
2.3.1 Likelihood Ratio Test	28
2.3.2 Receiver Operating Characteristics	29

2.3.3	Detectability Index	29
2.3.4	Detection of A Known Signal	31
2.3.5	Composite Signal with Uncertain Parameters Problem	32
2.3.6	GLRT	33
2.4	Monte Carlo Integration	34
3	Analyses of Time-Domain EMI Data	36
3.1	Introduction	36
3.2	Theoretical Performance Analyses of TD EMI Data	37
3.2.1	Fixed Parameter Case	38
3.2.1.1	Single Time Sample of TD EMI Data	38
3.2.1.2	LRT (Matched Filter) on Multi-Channel TD EMI Data	39
3.2.1.3	Integral/Summed-Data Detector on Multi-Channel TD EMI Data	40
3.2.1.4	Energy Detector on Multi-Channel TD EMI Data . .	41
3.2.2	Random Parameter Case	42
3.2.2.1	GLRT/Matched Filter	44
3.2.2.2	Integral/Summed-Data Detector	45
3.2.2.3	Energy Detector	46
3.2.2.4	Single Time Sample of TD EMI Data	46
3.2.3	Equivalence of the GLRT and the LRT for TD EMI Data . .	47
3.2.3.1	Equivalence of the GLRT and the LRT for Single Channel EMI Data	47
3.2.3.2	Equivalence of the GLRT and the LRT for Multi- Channel EMI Data	52
3.2.4	Requirements of Noise Variance for Different Detectors to Achieve a Certain Performance	59

3.2.5	Simulations	61
3.3	One-Dimensional Results on <i>DARPA</i> data	68
3.3.1	One-Dimensional Processor for Single Channel EMI Sensor Data	68
3.3.1.1	One-Dimensional LRT	68
3.3.1.2	Other Processors	70
3.3.1.3	Results	70
3.3.2	One-Dimensional Processor for Multi-Channel EMI Sensor Data	73
3.3.2.1	One-Dimensional LRT	73
3.3.2.2	One-Dimensional GLRT	75
3.3.2.3	Other Processors	76
3.3.2.4	Results	77
3.4	Two-Dimensional GLRT	78
3.4.1	Detector Design - 2-Dimensional Likelihood Ratio Test	79
3.4.1.1	Processing Stage 1	86
3.4.1.2	Processing Stage 2	89
3.4.1.3	Cascade of the Two Generalized Likelihood Ratios to Make a Decision	90
3.4.2	Results	91
3.4.3	Summary	98
4	Analyses of Frequency-Domain EMI Data	101
4.1	Broadband FD EMI Signatures and Detection of Low-Metal Landmines	101
4.1.1	Introduction	101
4.1.2	Experiment 1: Investigating the Statistical Properties and the Effects of Soil on Measured GEM-3 Signatures	103
4.1.2.1	Goals	103

4.1.2.2	Mine Descriptions	104
4.1.2.3	Sensor	104
4.1.2.4	Data Collection - General Protocol	106
4.1.2.5	General Approach and Notation	108
4.1.2.6	Characterization of the Noise Process	111
4.1.2.7	Calculation of the Average Background Corrected Mine Signatures	117
4.1.2.8	Detectability Analysis	121
4.1.2.9	Discriminability Analysis	126
4.1.2.10	Summary of Results	127
4.1.3	Experiment 2: JUXOCO Calibration Lanes	128
4.1.3.1	Data Collection	129
4.1.3.2	Background Correction	134
4.1.3.3	Analysis of the Effects of Spatial and Environmental Parameters on Mine Signatures	137
4.1.3.4	Discussion of Results	140
4.1.4	Experiment 3: Main Test Grid at JUXOCO	140
4.1.4.1	Experiment Description	140
4.1.4.2	Algorithm Development and Performance Evaluation	141
4.1.5	Discussions	144
4.2	Classification of Landmine-Like Metal Targets Using Wideband Frequency-Domain EMI	146
4.2.1	Introduction	146
4.2.2	Forward Model-Based Bayesian Classifier Formulation	147
4.2.3	Simulated and Experimental Data and Results of FPP and OP	152

4.2.3.1	Simulated Data	153
4.2.3.2	Simulation Results	154
4.2.3.3	Measured Data	157
4.2.3.4	Experimental Results	161
4.2.3.5	Summary	162
4.2.4	Sub-Optimal Processor	164
4.2.4.1	Processor Design	164
4.2.4.2	Results	165
4.2.4.3	Discussion	166
5	A Comparison of the Classification Performance of Metallic Objects Using TD and FD EMI Data	169
5.1	Introduction	169
5.2	Theory - Classification of Two Objects in the TD and the FD	172
5.2.1	Time-Domain Derivations	173
5.2.2	Frequency-Domain Derivations	176
5.2.2.1	i.i.d. FD noise	176
5.2.2.2	FD Noise Equivalent to i.i.d. TD noise	179
5.3	Simulation Results for Classification Performance of Two Objects . .	181
5.3.1	Comparison of TD simulations and their theoretical predictions	181
5.3.2	Comparison of FD simulations and their theoretical predictions	183
5.4	Classification of Four Objects	185
5.4.1	Simulation study	186
5.4.1.1	Fixed Amplitude	187
5.4.1.2	Uncertain Amplitude	191

5.4.2	Experimental Study	195
5.5	Summary	198
6	Conclusion	204
A	Deciding the upper frequency of the signal	209
B	Defining the final sample time for the TD signal	210
	Bibliography	211
	Biography	219

List of Figures

1.1	Flow chart of mine detection.	3
2.1	Model of the GEM-3 receive coil. The circle surrounded the shaded area indicates the path of the induced current and thus the line contour for integration; and shaded area indicates surface area for integration. Entire wire diameter is noted.	18
2.2	Equivalent electric and magnetic surface currents for modeling electromagnetic interaction with a highly conducting and/or permeable body of revolution (BOR).	21
2.3	Comparison of measurements and theoretical predictions for the thin brass disk when the distance from the target to the sensor is 20 cm.	25
2.4	Typical site layout from <i>DARPA Background Clutter Data Collection Experiment</i>	27
3.1	d^2 as a function of sample time t_s , when parameters are fixed and known values. $\alpha_1 = 2.1$, $\alpha_0 = 2.5$, and $\sigma = 0.14$.	40
3.2	The integration area for Equation (3.43), α_1 and α_0 are integration variables. The square is divided into upper and lower triangular portion.	57
3.3	ROC of simulations of various detection algorithms for a multi-channel TD EMI sensor at a fixed decay rate for both target and clutter. The decay rate of the target is $\alpha_1 = 2.1$, the decay rate for clutter is $\alpha_0 = 2.5$, and the initial magnitude is 220 for both target and clutter. Gradient: matched filter, delta: energy detector; square: integral detector; cross: threshold test on single time sample.	62

3.4 ROC of simulation of various detection algorithms for multi-channel TD EMI sensor data with uncertain decay rate for both target and clutter. Distribution of the decay rate α_1 is $\mathcal{N}(2.1, 0.2^2)$, and for α_0 is $\mathcal{N}(2.5, 0.2^2)$, the initial magnitude is 220 for both target and clutter. Circle: the LRT; gradient: matched filter, delta: energy detector; square: integral detector; cross: threshold test on single time sample.	63
3.5 ROC of simulation of various detection algorithms for multi-channel TD EMI sensor data with uncertain decay rate and uncertain initial magnitude of target and clutter. Distribution of the decay rate α_1 is $\mathcal{N}(2.1, 0.2^2)$, and for α_0 is $\mathcal{N}(2.5, 0.2^2)$, the distribution of the initial magnitude for target, A_1 , is $\mathcal{N}(220, 20^2)$, for clutter A_0 is distributed as $\mathcal{N}(210, 40^2)$. Circle: LRT; gradient: matched filter; delta: energy detector; square: integral detector.	65
3.6 Comparison of ROC of the theoretical d'^2 value and simulations of various detectors for the fixed decay rate case. 1) (upper left) the threshold test for single time sample TD EMI sensor data. 2) (upper right) the integral detector, 3) (lower left) the energy detector, and 4) (lower right) the matched filter for multi-channel TD EMI sensor data. Delta: simulation; square: theoretical d' .	66
3.7 Comparison of ROC of the theoretical d'^2 value and simulation of various detectors for the random decay rate case. 1) (upper left) the threshold test for single time sample TD EMI sensor data, 2) (upper right) the integral detector, 3) (lower left) the energy detector, and 4) (lower right) the GLRT/matched filter for multi-channel TD EMI sensor data. Delta: simulation; square: theoretical d' .	67
3.8 ROC for various processors at the theoretically calculated noise variance required achieving (0.1,0.7) performance for fixed decay rates. The left plot, (a), shows the entire scale; the right plot, (b), shows an enlarged version of (a).	68
3.9 ROC for various processors at the theoretically calculated noise variance required achieving (0.1,0.7) performance for random decay rates. The left plot, (a), shows the entire scale; the right plot, (b), shows an enlarged version of (a).	69
3.10 The histogram of the received data from EM61 sensor @ A.P. Hill FP20 (Z1 coil) site	71

3.11	The histogram of the received data from EM61 sensor @ Fort Carson Turkey Creek (Z2 coil, after removing drift) site	72
3.12	ROCs of 1-D Results for EM61 @ A.P. Hill FP20 site (LR is calculated using parametric estimated pdf's)	73
3.13	ROCs of 1-D Results for EM61 @ A.P. Hill FP22 site (LR is calculated using parametric estimated pdf's)	74
3.14	ROCs of 1-D Results for EM61 @ Fort Carson Turkey Creek site (LR is calculated using parametric estimated pdf's)	75
3.15	ROCs of 1-D Results for EM61 @ Seabee site (LR is calculated using parametric estimated pdf's)	76
3.16	ROCs of 1-D Results for Turkey Creek and Seabee sites (LR is calculated using kernel estimation of pdf's)	77
3.17	A typical plot of the EM61-3D sensor output for target and clutter .	78
3.18	Comparison of the performance of 1-D GLRT and other processors for EM61-3D data @ Fort A.P. Hill FP20 and FP22 sites	79
3.19	Comparison of the performance of 1-D GLRT and other processors for EM61-3D data @ Fort Carson Seabee and Turkey Creek sites	80
3.20	Schematic of data placement and data available for a testing location	80
3.21	Theoretical prediction of EM61 response from a metal object with an aspect ratio of 0.5 at a depth of 0.5m	81
3.22	Typical spatial response patterns of both mine/UXO and clutter/noise from single channel EMI sensor data	84
3.23	Typical spatial patterns of both mine/UXO and clutter/noise based on the 1-D GLR of multi-channel EMI sensor data	85
3.24	The neighborhood locations used when calculating generalized likelihood ratio 1 and 2	87

3.25 (Top) Probability density functions for the ratio of two Gaussian rv's. and a Gaussian approximation for a target present (H_1) case. (Bottom) Error between two pdf's shown in the top figure.	92
3.26 (Top) Probability density functions for the ratio of two Gaussian rv's. and a Gaussian approximation for a target not present (H_0) case. (Bottom) Error between two pdf's shown in the top figure.	93
3.27 A comparison of performance of the first stage processing using syn- thetic data based on the exact pdf of d and the Gaussian approximation.	94
3.28 ROC of different detectors based on EM61 data at Fort A.P. Hill FP20 and FP22 sites. The left one is corresponding to Ft. A. P. Hill FP20 site, the right one is corresponding to FP22 site. Solid line = 2-D GLRT detector performance; dashed line = performance of standard threshold detector on the received data from EM61 sensor.	94
3.29 ROC of different detectors based on EM61 data at Fort Carson Seabee and Turkey Creek sites. The left one is corresponding to Ft. Carson Seabee site, the right one is corresponding to Turkey Creek site. Solid line = 2-D GLRT detector performance; dashed line = performance of standard threshold detector on the received data from EM61 sensor.	95
3.30 ROC of different detectors based on EM61-3D data at Fort A.P. Hill FP20 and FP22 sites. The left one is corresponding to Ft. A.P. Hill FP20 site, the right one is corresponding to FP22 site. Solid line = 2-D GLRT detector performance; dashed line = 1-D GLRT performance; dashed-dotted line = integral detector performance; dash-dot-dot line = energy detector performance.	96
3.31 ROC of different detectors based on EM61-3D data at Fort Carson Turkey Creek and Seabee sites. The left one is corresponding to Ft. Carson Seabee site, the right one is corresponding to Turkey Creek site. Solid line = 2-D GLRT detector performance; dashed line = 1-D GLRT performance; dashed-dotted line = integral detector per- formance; dash-dot-dot line = energy detector performance.	97
4.1 Grayscale-coded histograms of the in-phase data obtained at 2,370 Hz during the free space background measurements. The change in both the mean and standard deviation of each data set indicates that the sensor response "drifts", or is not stable over time.	112

4.2	Variation of mean of in-phase and quadrature background scan for the seven measured samples in free-space. Line type order (beginning with backg1 and ending with backg7) = solid, dash, dash-dot, triangle, square, circle, diamond.	113
4.3	Variation of mean of in-phase and quadrature background scan for the seven measured samples in soil. Line type order (beginning with backg1 and ending with backg7) = solid, dash, dash-dot, triangle, square, circle, diamond.	114
4.4	Standard deviation of the seven scans as a function of frequency in free-space (in-phase and quadrature). Line type order (beginning with backg1 and ending with backg7) = solid, dash, dash-dot, triangle, square, circle, diamond.	115
4.5	Standard deviation of the seven scans as a function of frequency in soil (in-phase and quadrature). Line type order (beginning with backg1 and ending with backg7) = solid, dash, dash-dot, triangle, square, circle, diamond.	116
4.6	Comparison of background corrected signatures in air and soil. Solid = in-phase component, dashed = quadrature component, lines without symbols measured in soil, lines with circles measured in free-space. . .	119
4.7	Comparison of background corrected signatures in air and soil. Soil signatures are corrected by initial background measurements. Solid = in-phase component, dashed = quadrature component, lines without symbols measured in soil, lines with circles measured in free-space. . .	120
4.8	The ROC curves of the matched filter and energy detector for VS2.2 and M14 in free space.	125
4.9	Schematic illustration of the implementation of the matched filter bank.	127
4.10	Layout of the test site at 71A, Ft. A. P. Hill, VA.	129
4.11	Examples of clutter frequency domain EMI responses, data measured on 7/7/99 in the calibration area	131
4.12	Example of spatial data collection and the associated numbering scheme	132

4.13 Variation in in-phase and quadrature signals measured on 7/7/98 in the calibration area.	133
4.14 Background correction example at the first, fifth, and tenth spatial position. “Previous” background approach is coincident with true solution for the first spatial position, “Following” background approach is coincident with true solution for the final spatial position.	136
4.15 Change in the signature for a VS50 mine as a function of soil moisture.	138
4.16 Change in the signature for a VS50 mine as a function of spatial position	139
4.17 Performance of the baseline algorithm and three GLRT-based algorithms.	143
4.18 Comparison of the processor which ignores target/sensor orientation uncertainty (“fixed position” processor) and the optimal processor under uncertain height, fixed horizontal position conditions.	155
4.19 Comparison of the “fixed position” processor and optimal processor performance under the uncertain horizontal position, but fixed height condition.	156
4.20 Comparison of the “fixed position” processor and optimal processor performance when both height and horizontal position are uncertain.	157
4.21 Wideband frequency-domain response of a Valmara in free space and buried 1 inch below the surface of the ground in North Carolina clay soil. The units “ppm” reflect the sensor output multiplied by 10^6	158
4.22 Wideband frequency-domain response of a VS50 in free space and buried 1 inch below the surface of the ground in North Carolina clay soil. The units “ppm” reflect the sensor output multiplied by 10^6	159
4.23 Comparison of the “fixed position” processor and optimal processor performance under the condition of both height and horizontal position unknown for measured data.	162
4.24 The wideband EMI signature of the thick brass disk while the height of the sensor (left) and the distance from the sensor to the target in a horizontal plane (right) change.	165

5.1	Comparison of the theoretical prediction (o) and simulation (x and *) of classification performance as a function of initial sample time using linear (left) and logarithmic (right) sample schemes for TD data. The final sample time T_2 is 0.0138s, the noise standard deviation (STD) is 0.8, and the sampling period is 3.142e-4s	183
5.2	Comparison of theoretical prediction (o) and simulation (x and *) classification performance as a function of final sample time using linear sample scheme for TD data. The initial sample time T_s is 1e-5s, the noise standard deviation (STD) is 0.8.	184
5.3	Comparison of theoretical prediction (o) and simulation (x and *) of classification performance as a function of noise variance using linear (left) and logarithmic (right) sample schemes for TD data. The initial sample time T_s is 7e-4s and the final sample time T_2 is 6e-3s.	185
5.4	Comparison of theoretical prediction of classification performance (o) and simulation (x and *) as a function of number of sample frequencies using linear (left) and logarithmic (right) sample schemes for FD data. The noise standard deviation is 4e-4 for linear sampling case and 4e-3 for logarithmic sampling and the upper sample frequency is 16 kHz.	186
5.5	Comparison of theoretical prediction of classification performance (o) and simulation (x and *) as a function of noise variance using linear (left) and logarithmic (right) sample schemes for FD i.i.d. noise. The number of sample frequency is 200.	187
5.6	The TD responses of the 4 objects used in this study	189
5.7	The FD responses of the 4 objects used in this study (left - real part and right - imaginary part).	190
5.8	Classification performance of the 4 objects as a function of the initial sample time using TD linear (left) and logarithmic (right) samples for TD data. The noise standard deviation is 0.4, the final sample time is 6.06e-4s, and the sample period is 2.38e-6s.	191
5.9	Classification performance of the 4 objects as a function of the final sample time using TD linear samples. The initial sample T_s is 1e-5s and the noise standard deviation is 0.4.	192

5.10 Classification performance of the 4 objects as a function of the noise variance $\sigma_{n_t}^2$ using TD linear (left) and logarithmic (right) samples. The initial sample time T_s is 1e-5s and the final sample time T_2 is 3e-4s.	193
5.11 Classification performance as a function of number of frequencies used for linear (left) and logarithmic (right) samples with i.i.d. FD noise. The noise standard deviation is 5e-5 and the upper frequency is 21 kHz.	194
5.12 Classification performance as a function of noise variance $\sigma_{n_f}^2$ for linear (left) and logarithmic (right) samples with i.i.d. FD noise. The number of sample frequency is 100 and the upper frequency is 21 kHz.	195
5.13 Classification performance of FPP as a function of the initial sample time for the TD data with uncertain amplitude. Left – linearly sampled data; right – logarithmically sampled data.	196
5.14 Classification performance of FPP as a function of ending sample time for the TD data with uncertain amplitude.	197
5.15 Classification performance of FPP as a function of noise variance for the TD data with uncertain amplitude. Left – linearly sampled data; right – logarithmically sampled data.	198
5.16 Classification performance of the FPP (left) and the OP (right) as a function of the initial sample time for TD data with uncertain amplitude case. The covariance matrices of the amplitude A_1 and A_2 are listed in Table 5.1. The final sample time is 6.06e-4s, and the noise standard deviation is 0.4.	199
5.17 Classification performance of the FPP (left) and the OP (right) as a function of the final sample time for linear samples for uncertain amplitude case. The initial sample time is 1e-5s, the noise standard deviation is 0.4, and the sample period is 2.38e-6s.	201
5.18 Classification performance of the FPP (left) and the OP (right) as a function of the noise variance $\sigma_{n_t}^2$ for TD linear samples for the uncertain amplitude case. The initial sample time is 1e-5s, the final sample time is 3e-4s, and the sample period is 1.0e-6s.	202

5.19 Classification performance of the FPP (left) and the OP (right) as a function of the number of frequencies used for linear samples for FD i.i.d. noise, the uncertain amplitude case. The noise standard deviation σ_{n_f} is 5e-5 and the bandwidth is 21 kHz.	202
5.20 Classification performance of FPP (left) and OP (right) as a function of the noise standard deviation (STD) σ_{n_f} for linear samples for FD i.i.d. noise, the uncertain amplitude case. The number of sample frequency is 100 and the bandwidth is 21 kHz.	203

List of Tables

2.1	Soil and moisture variation represented in the <i>DARPA</i> experiment	26
3.1	The noise variance σ^2 required to achieve $P_d=0.7$ and $P_{fa}=0.1$ for fixed and random decay rates.	60
3.2	The theoretical values of d'^2 for various processors and known/random parameter cases.	64
3.3	Threshold values used for the first step process, β_1 , for all four test sites and two types of sensors, EM61 and EM61-3D sensor	98
3.4	P_{fa} value when $P_d = 0.95$ for EM61 sensor	98
3.5	P_{fa} value when $P_d = 0.95$ for EM61-3D sensor	98
4.1	Mines tested in the first experiment. AP = Anti-personnel mine, AT = Anti-tank mine. M = High metal content, LM = Low metal content	105
4.2	The distance from the top of the mine to the bottom of the sensor head in the first experiment when target is both in free space and buried conditions.	107
4.3	Discrimination performance of matched filter classifier for signatures estimated in free-space and applied in free-space (Air-Air), signatures estimated in soil and applied in soil (Soil-Soil), and signatures estimated in free-space and applied in soil (Air-Soil).	126
4.4	Ratio between the false alarm probability of the various algorithms and the false alarm probability of the baseline algorithm at the particular probabilities of detection.	144
4.5	The probability of correct classification of the optimal classifier when targets are at a fixed known position as the noise variance is increased from σ_n^2 to $2^9\sigma_n^2$	151

4.6	The variance of the background noise and the ratio of the mean of the response and its standard derivation as a function of frequency for the magnitude and phase components, respectively.	160
4.7	The performance of the various processors before and after normalization using simulated data when (1) target position is known and fixed, (2) $h \sim \mathcal{N}(20\text{cm}, 1.53^2\text{cm}^2)$ and x, y is fixed, (3) horizontal position is uniformly distributed in a 20 cm by 20 cm square and height is fixed, and (4) both height and horizontal position are random, following the distributions mentioned above. 'No Norm.' means processing occurred without normalization, 'Norm.' means processing followed normalization. 'OP' means optimal classifier, and 'FPP' indicates fixed position processor.	167
4.8	The performance of the sub-optimal and optimal processors before and after normalization evaluated on measured data. 'FPP' represents the fixed-position or sub-optimal processor, 'No Norm.' means processing occurred without normalization, 'OP' represents the optimal processor, and 'Norm.' means processing followed normalization	168
5.1	The mean vectors and covariance matrices of the Gaussian amplitude (A_1 and A_2) obtained from experimental data.	200
5.2	Correct classification probability of the FPP and the OP using the PSS-12 and the GEM-3 measured data.	200

Chapter 1

Introduction

According to several sources (including the United Nations, the U.S. State Department, the Red Cross, and various humanitarian demining agencies), it is estimated that there are over 100 million landmines buried across 70 countries, with an estimated 2 million more laid per year [1, 2]. It is also reported that landmines kill or maim at least 26,000 people annually. Most victims, more than 80%, are innocent civilians, many of which are children. Once laid, mines can continue to maim or kill for many decades after any hostilities have ended. For this reason the antipersonnel mine has been referred to as “a weapon of mass destruction in slow motion” [1].

In addition to political efforts geared towards banning the production and usage of antipersonnel land mines and preventing their further emplacement, researchers are seeking efficient and cost-effective means of detecting and neutralizing the innumerable land mines already laid underground worldwide, since mine detection is currently time consuming, hazardous, and frequently unreliable [3]. Currently, fewer than 100,000 landmines are cleared each year [2]. The United Nations estimates that it will take \$33 billion and 1,100 years to clear all the mines in contaminated areas across the world at the current rate of clearance and this prediction assumes that no additional mines are emplaced [2]. Thus, landmine detection is a research area that has received more and more attention due to its importance and the urgent need for solutions.

In general, the entire process of mine detection can be summarized by a flow chart as illustrated in Figure 1.1. The detection of a land mine excludes any physical contact with the mine. As a result, an electric field, a magnetic field, and/or an electromagnetic wave are generally used to probe for the mines. Mine detection systems that are in use or have been proposed for use are based on electromagnetic induction (EMI), which is essentially a metal detector, ground penetrating radar (GPR), magnetometer, and infrared imager etc. Acoustic sensors are also being considered.

The electric, magnetic, or electromagnetic responses from the location of interest are converted to an electronic signal. Signal processing is then applied to the electronic signal for noise reduction, signal enhancement, and feature extraction. The processed signal or extracted features help to differentiate between mines and soil and between mines and clutter.

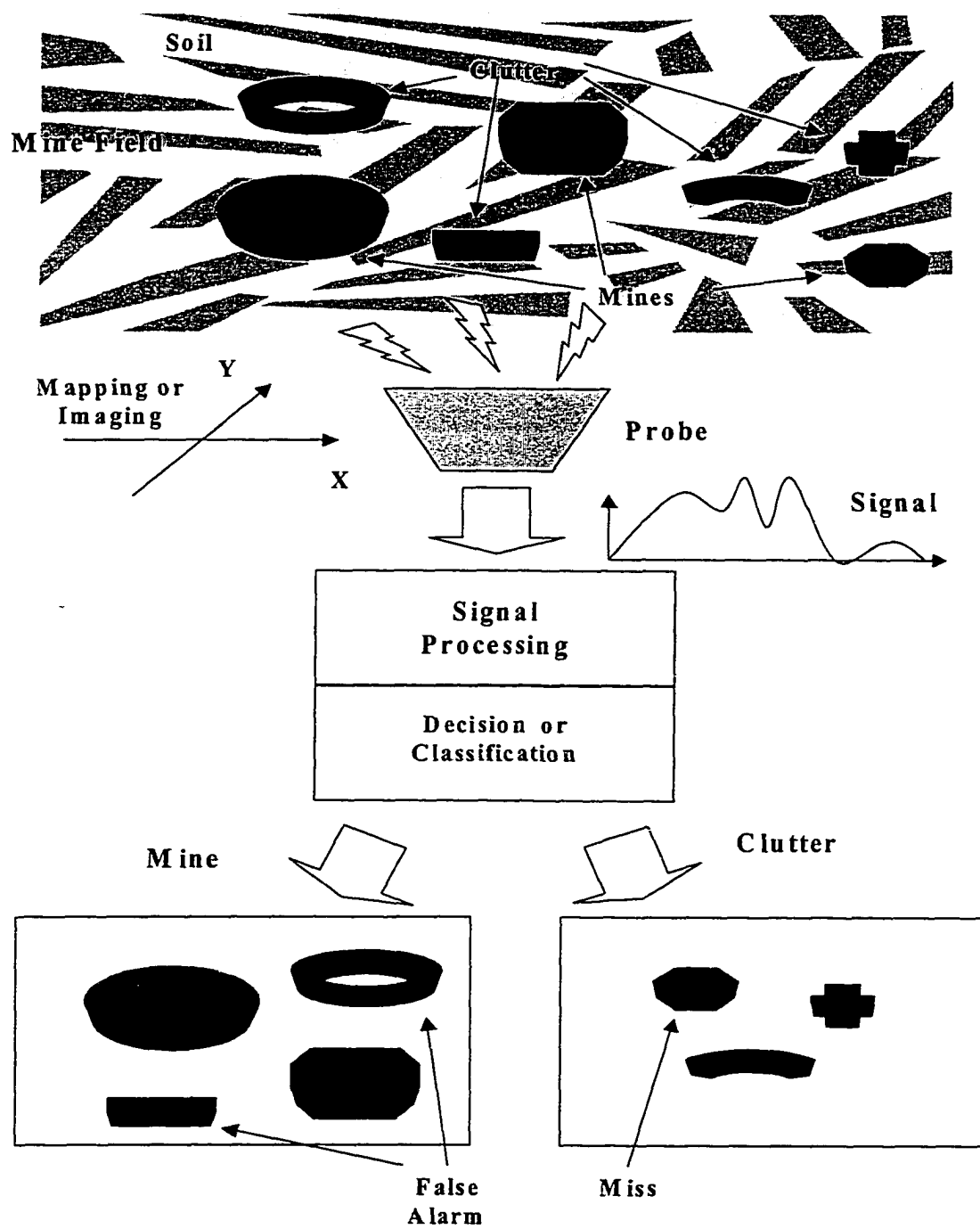


Figure 1.1: Flow chart of mine detection.

Since most mines have at least some metal content, the EMI sensor (basically a metal detector) is the most commonly-used mine detection system. The underlying principle of an EMI sensor is that a time-varying current is passed through a coil, producing a time-varying magnetic field. The time-varying magnetic field generates an eddy current inside a conducting (mostly metal) object, which returns an inductive magnetic field from the conductive object. In addition, given that the mine contains parts that are magnetic permeable, the target will also return an inductive magnetic field. The returned induced magnetic field (through either or both of the physical processes discussed above) can be further sensed by a coil and converted to an electric signal.

The most traditional EMI sensor is a pulsed system with only one output. The sensor records the late-time induced field from the ground and underground objects and either samples it or integrates it to a single value. Such sensors are called integrated, or single-channel, time-domain EMI sensors. The standard approach of signal processing and decision making using data from such a single-channel EMI sensor is to perform a threshold test on the data obtained at each surveyed location. The extension of the threshold approach for multi-channel EMI data, where multiple time samples are available, is to perform a threshold test on either the energy present in the received signal, or on the integral (sum) of the sampled values obtained at each surveyed location.

For any detection system, the goal is to achieve a high probability of detection (P_d) while at the same time maintaining a low probability of false alarm (P_{fa}). This is of particular importance for the landmine detection problem since a perfect P_d is necessary for safety concerns and P_{fa} is directly proportional to the time and costs

required to clear the contaminated areas. However, it is most often the case that the mine detection systems achieve a high P_d at the cost of a high P_{fa} . Although the EMI sensor is effective for metal detection up to the microgram level, the false alarm rate for an EMI system on a battlefield is often extremely high. Usually in an area that was once a battlefield, it is very hard to differentiate a mine from the debris of weapons and shells; and the average ratio of real mines to the suspect objects is 1/100. This results in a very slow speed of remediation.

To improve mine detection systems (*i.e.* to achieve a high detection rate and a low false alarm rate) is an important research issue as well as a challenging task. Various methods have been investigated to improve mine detection performance. Just as the mine detection process can be divided into three steps (physical sensing, signal processing, and decision making), mine detection research efforts also try to focus on each or all of the three segments of the mine detection process.

Many researchers have tried to improve mine detection by utilizing more and more complex physical sensors each of which is sensitive to a different phenomenology. In recent years, largely due to the progress of focal plane array (FPA) infrared imagers, electromagnetic radiation in the infrared region has been demonstrated for mine detection [4, 5, 6, 7, 8]. Ground penetrating radar has also been utilized, and provides complex response signals for depth profiling of the ground [9, 10, 11, 12].

More complex EMI sensors have been studied that are able to provide a more complete measured response, thus providing more information to enhance the differentiation between mines and clutter. Multi-channel EMI systems have been built and it has been suggested that these allow mine detection performance which is less

dependent on the relative orientation of the object and the EMI sensor [13, 14]. In addition, multi-channel EMI sensors provide information about the geometry and orientation of the target, which can be further utilized by signal processing algorithms [15, 16].

Frequency-domain EMI sensors have also been investigated and compared to the traditional time-domain EMI sensor. A broadband frequency-domain EMI sensor is able to provide a spectrum of the object of interest (for frequencies up to a mega Hertz) for target detection and identification [17, 18, 19].

Besides the efforts to improve the physical sensing mechanism of the EMI mine detector, it is also possible to improve the over-all performance of the EMI sensor by incorporating a more sophisticated signal processing algorithm that is based on the physical nature of the EMI response. On the other hand, the more complicated signals obtained from the more sophisticated EMI systems may also require more complex signal processing methods. Thus, it is necessary to understand the phenomenology of the EMI response. In references [14, 20, 13, 21, 22, 23, 24], EMI modeling has been performed theoretically and compared to experimental data. The EMI physics can be completely described by Maxwell's equations. However, due to mathematical complexity, analytical solutions can only be obtained for some simple object geometries.

In recent years, detection theory and statistics has begun to be utilized to improve mine detection and classification performance. There have been several studies on landmine and minefield detection using statistical approaches. In [25, 26, 27, 28, 29, 30, 31, 32], the statistical characterization and modeling of mine fields have been

addressed. In [5, 7, 33, 34], better utilization of multispectral sensor data for the mine detection problem is discussed. In [35, 36, 37], the authors have considered discrimination of landmines from clutter by extracting decay rates from time-domain EMI signals.

The goal of this work is to develop better algorithms, which can achieve a high P_d and a low P_{fa} . We integrate the underlying physics of the system and Bayesian detection theory as well as forward model and other environmental factors into the algorithm development to generate the optimal and various sub-optimal detectors for this problem. Since the response of a sensor to a target is dependent on many factors such as distance, orientation, *etc.*, the optimal processor integrates over these uncertain factors. This integration is mathematically complex and its numerical solution is usually computationally expensive. In order to process data and make decisions in real-time, sub-optimal solutions are also investigated. Such processors can take on a very important role, since they are simpler to compute, take less time, thus, can be implemented in real-time. However, the optimal performance also provides a performance bound, and allows us to assess the degree of performance degradation that occurs with the sub-optimal processing.

Based on measured landmine and clutter field data collected with EMI sensors, it is clear that the statistics of the sensor response obtained from a local area surrounding the test position are a function of whether a landmine is present or not. Therefore, we formulated a detector that utilizes the responses from the location under test and its vicinity. Theoretical analyses have been performed to show that the one dimensional likelihood ratio test (LRT) and the one dimensional generalized likelihood ratio test (GLRT) provide the same performance under some reasonable

assumptions. In order to obtain the detector performance bounds, theoretical derivations and simulations are also investigated for time-domain and frequency-domain EMI data.

The remainder of this manuscript is organized as follows.

In Chapter 2, various background material regarding this work are introduced. First, the time-domain and frequency-domain EMI systems from which the data of this work were collected are briefly described. Next, Bayesian detection theory is reviewed. Then, a numerical method to evaluate complicated integrals, the Monte Carlo method, is reviewed.

Chapter 3 investigates time-domain EMI data. It begins with the theoretical analyses of the performance of various detectors using time-domain EMI data. Theoretical derivations of the equivalence of the one dimensional LRT and the one dimensional GLRT for single-channel and multi-channel TD EMI data are provided. Performance of those detectors are also evaluated using experimental data gathered in conjunction with the *DARPA Background Clutter Data Collection Experiment* [38]. The detector that incorporates the spatial information contained in the data and the underlying physics of the sensor, the 2D-GLRT, is developed and performance results from experimental data are presented.

Chapter 4 investigates frequency-domain EMI data. First, the efforts of a series of experiments to obtain frequency-domain (FD) EMI data, using the GEM-3 [17], a prototype FD EMI data, for the low-metal mine detection problem are described, and the algorithm development is summarized next. Second, classification of metallic

objects is investigated. This is of interest because for landmine and UXO detection problems it is important to discriminate targets from discrete clutter objects in order to reduce the false alarm rate. A forward model-based Bayesian classifier is formulated. The uncertainties associated with the depth and position of the underground objects are incorporated into the classifier design. To reduce computational complexity, a sub-optimal processor is also investigated for the particular set of objects used in this study.

Chapter 5 presents a comparison of time-domain and frequency-domain EMI processing. The example of a TD EMI sensor is the AN/PSS-12 [39] and the example of a FD EMI sensor is the GEM-3 [40]. Both theoretical studies and simulations are used to investigate the sensitivity of the performance of a Bayesian classifier to various parameters associated with TD and FD system operation, including sampling rate, initial and final sample time, and signal to noise ratio, etc. Theoretical performance bounds are derived as a function of those parameters for the two object classification case, then verified by simulations. Next, the four-object classification problem is considered, the simulation results are provided, and then the experimental data from the PSS-12 and the GEM-3 are used to evaluate the classification performance for the four objects.

Finally, the conclusions are discussed in Chapter 6.

Chapter 2

Background

This chapter seeks to describe the background for this work, *e.g.* a description of various land mines, and systems from which data analyzed in this work were collected, *etc.*

2.1 Brief Description of Land Mines

Land mines are a form of ordnance, which are usually placed on or just under the ground in an armed state. They are designed to explode when a triggering stimulus is present, such as pressure from a foot, vehicular traffic or the magnetic or electromagnetic signature of a vehicle passing nearby [41]. Land mines are usually symmetric in cross-section with a circular or rectangular shape and are generally placed with the largest dimension parallel to the ground surface.

Generally, landmines can be divided into two categories: anti-personnel mines and anti-tank mines. An anti-personnel (AP) mine can be defined as a device designed to be triggered by a small amount of pressure, *e.g.* 40 lbs. Therefore, it only maims or kills the person who triggers it. Generally, AP mines are rather small in diameter, only around or less than 10 cm, and thus are often more difficult to detect. In contrast, anti-tank (AT) mines are bigger and explode when compressed by objects weighing hundreds of kilograms. They are specifically designed to blow up tanks and other vehicles.

In recent years, mine technologies have evolved significantly. The development of plastic mines, as well as those containing a minimum amount of metal, called low-metal mines, has made these weapons much cheaper, more durable, more reliable, and even harder to detect and dismantle [1]. The manufacture of mines is quite simple, thus, the associated production costs are very low. Prices of a land mine usually range from \$3 to \$15. As a result, in past years more countries have manufactured and sold mines to make profits. Approximately 50 nations have produced and exported AP mines, and at least 350 models are currently available, not only to official armies, but essentially to all fighting groups and armed factions worldwide [1]. Since there are so many types of mines used or in use, and they are of different shapes, diameters, materials, structure, etc., it makes landmine detection an extremely difficult problem to which there is no omnipotent solution.

2.2 Electromagnetic Induction Systems

Mine detection systems that are in use or are proposed for use are electromagnetic induction (EMI), ground penetrating radar (GPR), magnetometer, infrared imager, etc. Among these landmine detection systems, EMI systems are the most widely employed to locate mines for both military and humanitarian demining. Therefore, in this work EMI data is chosen as the major type of data to process.

The discovery of electromagnetic induction by Michael Faraday and Joseph Henry is one of the most important scientific events of the 19th century. Maxwell combined these basic laws and formulated theoretical concepts of electromagnetics, primarily through experiments by many scientists, into a consistent set of vector equations,

the acclaimed *Maxwell's equations* [42]. Based upon Maxwell's Equations, the EMI method is one of the most commonly employed technologies among many techniques in use or being proposed for use as land mine and unexploded ordnance (UXO) detectors.

The EMI sensor is essentially a metal detector, which normally operates at low frequencies (<1MHz), at which conductivity- and permeability-dependent skin depth of the materials varies significantly [14, 22, 21, 13, 19]. In addition, the displacement current component of the response to the near field loop-induced fields is weak enough to be neglected [20]. Therefore, most such systems are insensitive to dielectric discontinuities and primarily sense changes in conductivity and permeability. Traditional EMI systems are of primary use for the detection of mines with substantial metal content, or for UXO, which generally contains significant metal. Traditional EMI systems are of little or no use for purely dielectric targets although recent work has shown that EMI systems operating at higher frequencies may be able to detect voids in conducting soil [43, 44]. Nevertheless, most mines have at least some metal content, and EMI systems are currently the most widely used fieldable sensors for detecting such targets.

Traditionally, an EMI sensor is operated in the time-domain (TD), i.e. the transmitting coil sends out a pulse. It has been shown [14, 13, 20] that the response, r , of the pulsed EMI system from a general conducting, permeable target can be modeled as a superposition of weighted, resonant responses:

$$r(t) = \sum_{n=1}^N A_n e^{-j\omega_n t} \quad (2.1)$$

where ω_n is the n^{th} natural resonant frequency of the object and A_n is the initial

magnitude of the response corresponding to that frequency. In practice, the real part of ω_n is very small and thus can be ignored [20]. Thus, the late time field, which is the field recorded by EMI sensors, is dominated by the lowest mode. Therefore, in some cases the response can be approximately modeled as a single exponential damping:

$$r = Ae^{-\alpha t} \quad (2.2)$$

where A is the initial magnitude and α is the lowest natural resonant frequency. The initial magnitude, A , depends strongly on the excitation level, the depth and the orientation of the underground objects. The resonant frequency, α , is a function of conductivity and permeability, etc. Both theoretical and experimental data demonstrate that α is unique to each metal type [14, 13, 20]; thus can be used to detect land mines.

Equivalently, Equation (2.1) can also be represented in the frequency-domain (FD). Note that the response in the time-domain is only of positive time index. Thus, approximately the response in the frequency-domain can be modeled as

$$R(\omega) = \sum_{n=1}^N \frac{A_n}{\omega + j\omega_n} \quad (2.3)$$

2.2.1 Time-Domain EMI Sensor

There are two kinds of time-domain EMI sensors: single channel, or integrated time-domain, and multi-channel time-domain EMI systems. The single channel sensor, which is the conventional EMI sensor, performs an operation (sample, integrate or sum) on the time-domain response over a predetermined time range to obtain a scalar value at each surveyed location. In contrast, the multi-channel sensor provides a waveform of the response at multiple sampling times. If the multi-channel data is

incorporated into a detector correctly, better performance can be achieved than that obtained with the standard time-domain EMI data [26].

2.2.1.1 Geonics EM61 Sensor

The Geonics EM61 is an example of single channel time-domain EMI sensors. It is configured with two 0.5 m square coils. One coil (Z1) is placed approximately 0.4 m above the other coil (Z2), which is 0.3 m above ground. The lower coil, *i.e.* Z2, is used both for transmitting and receiving the electromagnetic field. The upper coil, Z1, is used to receive the induction field only. The system operates at a center frequency of 75 Hz. The sensor records one sample per 0.2 m. The EM61 integrates the time-domain induced response within the time interval from 0.18 ms to 0.87 ms after each transmit pulse to obtain a single value at each surveyed location [38]. Thus, its response can be expressed as:

$$r = \sum_{i=0}^M A e^{-\alpha(t_0+i\Delta t)} \quad (2.4)$$

where t_0 is the initial time for the integration, and the integration ends at $t_0 + M\Delta t$.

Data obtained from the Z2 coil in the *DARPA* experiment (described later in Sec. 2.2.3) had a significant pseudo-periodical drift and DC changes, which may have been caused by a weak battery and the heat of a 10 Amp current employed when transmitting pulses. When utilizing the data set collected by the Z2 coil of the Geonics EM61 sensor, the drift was removed first.

2.2.1.2 Geonics EM61-3D Sensor

The second time-domain sensor considered in this work is a prototype multi-channel sensor, the Geonics EM61-3D, which is a three component time-domain pulsed EMI system. The system consists of a 1 m square transmitter coil and three orthogonal 0.5 m receiver coils positioned approximately 0.3 m above the ground. The system operates at a base frequency of 7.5 Hz, and it samples the induced response at 20 geometrically spaced time gates from 320 μ s to 30 ms following the incident pulse, with the sampling rate of 3 samples (60 time gates) per second [38]. Thus, the received signal from the Geonics EM61-3D sensor, r , can be expressed as:

$$r(t) = Ae^{-\alpha t} \quad (2.5)$$

where t_i , the element of t , is the sampling time, and $i = 1, 2, \dots, N$, and $N = 20$.

2.2.1.3 AN/PSS-12 Sensor

The AN/PSS-12 is manufactured by Schiebel Corporation of Austria. It is the U.S. Army's currently fielded hand-held metal detector. It is a pulsed induction system. The AN/PSS-12 consists of two concentric coils, a transmitting (outer) coil and a receiving (inner) coil. A linearly increasing current is driven into the transmitting coil and after a few tens of microseconds this current is rapidly turned off. The magnetic field radiated by this linearly increasing current induces eddy currents to flow in any nearby metallic objects in accordance with Faraday's Law of Induction. These induced eddy currents in turn radiate a scattered magnetic field which induces a voltage in the receive coil. The output of the receiving coil (voltage as a function of time) decays exponentially.

The AN/PSS-12 generates an audio tone whose frequency is roughly proportional to the amount of change in the received waveform due to the metallic object relative to a fixed background signal. In the field operation, the operator decides whether a target present based on this audio signal. For identification/discrimination purposes, it is important to capture as much of the decaying exponential waveform associated with the object as possible, because different decays can generate an audio tone with the same frequency. It presents instrumentation challenges to capture a high fidelity representation of the response. In early time, the voltage at the output of the receive coil can approach 100 volts. Without a proper protection a voltage of this amplitude can destroy sensitive data acquisition circuits. Later in time, when the object response may dominate, voltage levels can be very low - on the order of microvolts, which requires large amplification, especially when digital-to-analog converters (DAC) with limited resolution are employed.

In order to measure the response as a function of time, a modification of the AN/PSS-12 was performed by colleagues at Auburn University. A National Instruments DAQ Card-5102 (PCMCIA) was used in conjunction with a laptop computer as the data collection device. The 5102 provides two channels of analogue inputs, a trigger input, and two digital trigger inputs/outputs. Channel one of the 5102, with the proper attenuation, was used to capture the early part of the response directly at the output of the receiving coil. Data collected is stored in the memory of the laptop computer for subsequent analysis. The control software of the 5012 is LabVIEW.

2.2.2 Frequency-Domain EMI System

When operating the EMI sensor in the frequency-domain, a much higher signal-to-noise ratio (SNR) can be achieved. The frequency-domain EMI sensor transmits an excitation that only contains a particular set of frequencies. Thus, the response from the earth plus the underground objects only contains these frequencies but with a different magnitude and phase (assuming a linear system). Therefore, the receiving coil is subject only to the additive noise at the frequencies of interest, not within the whole frequency band, as is the case for time-domain systems. Since the frequency-domain EMI signature differs significantly across targets [19], which provides the underlying physical mechanisms for discriminating, identifying, or classifying targets, it provides a promising approach for landmine detection.

2.2.2.1 The GEM-3

In this work, data from a prototype wideband frequency-domain EMI sensor, the GEM-3, developed by Geophex Ltd., was analyzed for detection and classification purposes. The GEM-3 uses a pair of concentric, circular coils to transmit a continuous, wideband, digital electromagnetic waveform [17, 40]. The resulting field induces a secondary current in the earth as well as in any buried objects. The set of two transmitter coils has been designed so that they create a zone of magnetic cavity at the center of the two coils. A third receiving coil is placed within the magnetic cavity so that it senses only the weak secondary field returned from the earth and buried objects.

The receiving coil can be modeled as shown in Figure 2.1. Faraday's Law gives

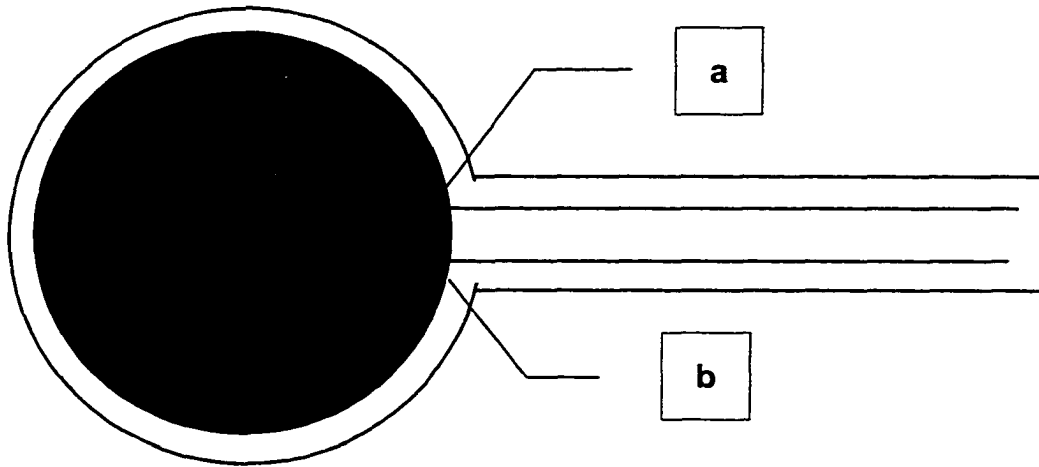


Figure 2.1: Model of the GEM-3 receive coil. The circle surrounded the shaded area indicates the path of the induced current and thus the line contour for integration; and shaded area indicates surface area for integration. Entire wire diameter is noted.

the equation governing response induced in the receiving coil:

$$emf = \oint_c E \cdot dl = -\frac{d}{dt} \iint_s B \cdot \hat{n} ds = -\frac{d\Phi}{dt} \quad (2.6)$$

where emf is the electromotive force, E is the electric field intensity, l is the path length through the wire, B is the magnetic flux density, \hat{n} is the unit vector perpendicular to ds , ds is the differential surface element on the surface S circumscribed by the coil, and Φ is the magnetic flux. Since the electric field, E , is zero inside the wire, the above equation can be rewritten as

$$V_b - V_a = \frac{d}{dt} \iint_s B \cdot \hat{n} ds = \frac{d\Phi}{dt} \quad (2.7)$$

For the time-harmonic electromagnetic fields, Equation (2.7) can be written in

the form of

$$V_b - V_a = j\omega\Phi(\omega) \quad (2.8)$$

Thus, the measured frequency-domain voltage across the loop is proportional to the magnetic flux and, correspondingly, to the magnetic flux density.

In practice, the version of the GEM-3 used in this work measures the current through a resistor in series with the receiving loop. Measuring the current is equivalent to measuring the voltage across the loop. This current is 90 degrees out of phase with the voltage, and therefore the magnetic flux density. The in-phase and quadrature components at each frequency of interest are obtained by convolving the received time-series with a sine time-series (for in-phase) and cosine time-series (for quadrature) at the frequency of interest. The data obtained from the convolution are converted into units called parts-per-million (ppm) defined as

$$ppm = \frac{\text{measured_data}}{\text{calibration_data}} \cdot 10^6 \quad (2.9)$$

The calibration data at each frequency had previously been obtained (and programmed into the GEM-3) by suspending the sensor in air [17, 40] and measuring the sensor output. This normalization attempts to remove the system impulse response from the measured data. The ppm data are logged by the sensor for each frequency as in-phase and quadrature components. The phase relationships and frequency dependence are not corrected at this point.

2.2.2.2 Model for Wideband Frequency-Domain EMI Responses

In order to model the signature of targets of interest, a method of moment (MoM) analysis is used to predict the theoretical response from the target [19, 45], which was developed by Dr. Lawrence Carin and Dr. Norbert Geng. The calculation provides

the theoretical induced voltage (magnitude and phase, or in-phase and quadrature components) for each target and frequency considered.

The fields induced by a highly (but not perfectly) conducting and/or permeable target in free space, due to EMI excitation at kilohertz frequencies, are the quantities of interest. The problem is solved via a frequency-domain boundary-integral equation formulation. Moreover, to make such an analysis tractable, it is specialized to a particular class of targets: those that can be modeled as a body of revolution, or BOR [46] (*i.e.*, targets possessing rotational symmetry). Although here only consider near-field effects for metallic and ferrous targets, the general formulation is very similar to those used previously for far-zone scattering from low-loss dielectric targets [47, 48]. In particular, the problem is formulated in terms of the tangential electric E and magnetic H fields on the target surface, or, equivalently, in terms of electric and magnetic surface currents, $\mathbf{J} = \mathbf{n} \times \mathbf{H}$ and $\mathbf{K} = \mathbf{E} \times \mathbf{n}$, respectively, where \mathbf{n} is the outward unit normal. If \mathbf{E}_1 and \mathbf{H}_1 represent respectively the electric and magnetic fields inside the target, and \mathbf{E}_2 and \mathbf{H}_2 represent the “scattered” fields outside the target, boundary conditions at the interface yield the relationships (enforced at the boundary)

$$\begin{aligned}\mathbf{n} \times [\mathcal{L}_1^{EJ}(-\mathbf{J}) + \mathcal{L}_1^{EK}(-\mathbf{K})] &= \mathbf{n} \times [\mathcal{L}_2^{EJ}(-\mathbf{J}) + \mathcal{L}_2^{EK}(-\mathbf{K})] + \mathbf{n} \times \mathbf{E}^i \\ \mathbf{n} \times [\mathcal{L}_1^{HJ}(-\mathbf{J}) + \mathcal{L}_1^{HK}(-\mathbf{K})] &= \mathbf{n} \times [\mathcal{L}_2^{HJ}(-\mathbf{J}) + \mathcal{L}_2^{HK}(-\mathbf{K})] + \mathbf{n} \times \mathbf{H}^i\end{aligned}\quad (2.10)$$

where \mathbf{E}^i and \mathbf{H}^i represent the incident fields. The operators \mathbf{n} involve well-known manipulations of the homogeneous-media Green’s function [48, 49, 50], or medium parameters inside ($n=1$) and outside ($n=2$) the body. The problem therefore reduces to solving for \mathbf{J} and \mathbf{K} , for particular incident fields \mathbf{E}^i and \mathbf{H}^i . In the Method of Moments (MoM) solution for BORs [46, 48, 47, 49, 50, 51], $\mathbf{J}, \mathbf{K}, \mathcal{L}_n, \mathbf{E}^i$ and \mathbf{H}^i are expanded in a Fourier series in the azimuthal variable ϕ , and, for each Fourier

component, \mathbf{J} and \mathbf{K} are expanded in terms of one-dimensional basis functions along the BOR generating arc (see Figure 2.2). Geng and Carin used subsectional basis functions and testing functions, as in [49, 50, 51]. The interested reader is referred to [49, 50, 51] for details concerning implementation of the general algorithm, while here we focus on issues of particular relevance to the EMI problem.

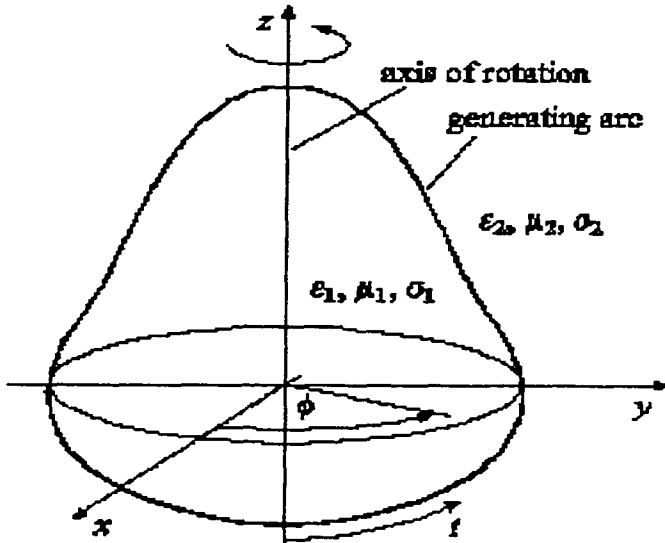


Figure 2.2: Equivalent electric and magnetic surface currents for modeling electromagnetic interaction with a highly conducting and/or permeable body of revolution (BOR).

First the requirements concerning the subsectional-basis-function discretization of \mathbf{J} and \mathbf{K} are considered. For scattering from low-loss targets, it is well known that approximately ten basis functions are required per wavelength [48]. In such problems, this rule is applied to the smallest wavelength of interest in the problem, generally corresponding to the medium inside the target. For the highly conducting targets of interest here, the wavenumber inside the target approximately satisfies $k_1 = (1 - j)/\delta$, where δ is the skin depth. To sample the Green's-function phase $\exp(-jk_1 R)$ sufficiently, it is required that $\Delta t/\delta \ll 2\pi$ and $\Delta t/\delta \ll 1$ (for the real

and imaginary parts of k_1 , respectively), where Δt is the basis-function width; these constraints are usually sufficient to satisfy the outer-region sampling requirements (k_2 generally representing the *free-space* wavenumber). Extensive numerical experiments indicate that accurate results are obtained if $\Delta t < \delta/3$.

As discussed above, for EMI applications generally current-loop excitation is of interest, as distinguished from the plane-wave fields considered for radar problems. While the fields due to a current loop are well known [42, 52], how such are placed into the BOR framework, as well as appropriate approximations for the EMI problem are discussed. In particular, the incident fields are derived from the vector potential [42, 52]

$$A_\phi(\rho, z) \approx \frac{\mu_0 I a}{4\pi} \int_0^{2\pi} \frac{d\phi' \cos \phi'}{\sqrt{\rho^2 + a^2 + z^2 - 2a\rho \cos \phi'}} \quad (2.11)$$

where the origin of the local cylindrical coordinate system (ρ, ϕ, z) is situated at the loop center, with axis parallel to z , and I and a are the loop current and radius, respectively. The expression in Equation (2.11) invokes a quasi-static approximation, since, at the wavelengths of interest (in air and soil), the electrical distance between the sensor and target is infinitesimal. Similar approximations can be used (but have not been here) with regard to the Green's-function components in the air region (\mathcal{L}_2 in Equation (2.10)), while the very high conductivity and/or permeability inside the target necessitate a rigorous analysis (*i.e.*, a rigorous formulation of \mathcal{L}_1). The incident electric and magnetic fields are readily computed as

$$H_\rho^i(\rho, z) = -\frac{1}{\mu} \frac{\partial A_\phi}{\partial z}, \quad H_z^i(\rho, z) = -\frac{1}{\mu \rho} \frac{\partial(\rho A_\phi)}{\partial \rho}, \quad E_\phi^i(\rho, z) \approx -j\omega A_\phi \quad (2.12)$$

and these fields are finally expressed in terms of complete elliptical integrals. If the loop axis and the BOR axis are aligned, the fields in Equation (2.12) can be applied

directly to the BOR MoM solution, and only the lowest order Fourier-series mode is excited (reflecting azimuthal symmetry). If the axes are not aligned, a Fourier-series representation of the incident tangential fields on the BOR surface is generally required (with the BOR problem solved separately using the incident fields from each such mode [46, 47, 48, 49]). While the Fourier components for plane-wave incidence can be expressed in closed form [46], Geng and Carin have not found such a simple representation for the loop-induced fields. Therefore, in the general case, they numerically determine the Fourier coefficients. For example,

$$\tilde{H}_{mi}(t) = \frac{1}{2\pi} \int_0^{2\pi} H_t^i(t, \phi) \exp(-jm\phi) d\phi \quad (2.13)$$

where H_t^i represents the incident magnetic field along the generating arc (Figure 2.2), and (t, ϕ) represents the local BOR coordinate system. Thus, while the space-domain fields for the loop can be expressed in closed form, the requisite Fourier components are evaluated numerically. However, the incident fields are generally slowly varying in ϕ and integrals of the type in Equation (2.13) do not present a significant numerical challenge.

Before proceeding to a comparison of theoretical and measured results, Geng and Carin noted that the EMI fields induced by a conducting and/or ferrous target are generally measured in the near zone. Therefore, when calculating the induced fields, they cannot invoke the simplifying far-zone approximation generally used for radar-scattering problems [42, 46, 48]. They therefore calculate the EMI “scattered” fields via a rigorous convolution of the calculated currents \mathbf{J} and \mathbf{K} with the free-space Green’s function (e.g., with \mathcal{L}_2), performing integrals similar to those used in calculating the components of the MoM impedance matrix. Additionally, it is noted that an actual EMI sensor does not measure the induced fields, but rather the electromo-

tive force induced on a sensing current loop. To calculate such, a method that uses appropriate magnetic field components, integrated over the aperture of the sensing loop, to generate a theoretical induced voltage for each target and frequency considered, is applied.

The simulation outputs from the model can be used to calibrate the frequency-domain EMI sensor. Let $c(\omega)$ represent the calibration constant for frequency ω , the K by 1 vector M represent a set of measurements obtained at several (K) positions, and the K by 1 vector B represent model outputs for the same target and positions. We have the relation that $Bc(\omega) = M$, and a least-squares method is used to obtain the calibration constants as a function of frequency.

Using data collected from a prototype wideband frequency-domain EMI sensor, the GEM-3, the effectiveness of a numeric model is tested. Figure 2.3 shows the comparison of the theoretical model predictions and the measurements. A description of the object used and how the data was collected can be found in Sec. 4.2.3.3. It is

noted that the model predicts the GEM-3 response well [19].

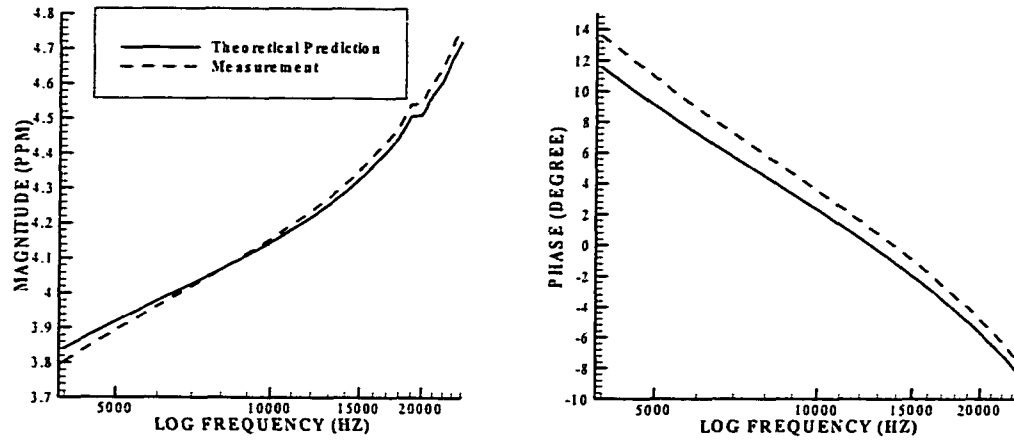


Figure 2.3: Comparison of measurements and theoretical predictions for the thin brass disk when the distance from the target to the sensor is 20 cm.

2.2.3 DARPA Background Clutter Data Collection

The time-domain EMI data analyzed first was collected during the *Defense Advanced Research Projects Agency (DARPA) Background Clutter Data Collection Experiment* [38]. The original objective of the *Backgrounds Clutter Data Collection Experiment* [38] was to collect data to aid in the understanding of the effects of clutter on system performance. During the course of the experiment, four types of sensors which are ground penetrating radar (GPR), electromagnetic induction (EMI), magnetometer, and infrared (IR) camera were used to collect data at four sites across two U.S. locations: Fort Carson, Colorado and Fort A. P. Hill, Virginia. These locations represented three soil types as illustrated in Table 2.1, along with substantial variability

in man-made contamination (anthropic clutter). Three of the four sites have a small amount of anthropic clutter, while at one of the sites (Fort A. P. Hill, FP20) the amount of such was substantial. In addition to the indigenous anthropic clutter, a few synthetic calibration targets, UXO items and land mines were emplaced on each site.

	Moist	Dry
Sand	Fort A.P. Hill	Fort Carson
Clay	Fort Leonard Wood	Fort Carson

Table 2.1: Soil and moisture variation represented in the *DARPA* experiment

Each of these sites was laid out in a rectangular grid. A typical layout for a test site is illustrated in Figure 2.4. The site measured 125 m by 100 m and consisted of three areas: a center square, side bars, and a calibration area. The center square, measuring 100 m by 100 m, was primarily intended for clutter characterization, although 5 groups of registration targets (15 total) were emplaced there to aid calibration and location registration. Replicas of the calibration targets, along with synthetic UXO items and land mines were emplaced in blue, red, yellow, and orange side bars on the site. A complete description of the targets and their deployment can be found in [38]. The blue bar contained UXO and demagnetized spheres. The red bar consisted of copies of the registration targets, other targets for calibration, and system-stressing targets. The yellow side bar contained mines, infrared calibration sources, and dielectric targets. Finally the orange side bar consisted of a combination of these, and other targets. The total area of the blue, yellow and orange bars was 1300 square meters. The calibration area consisted of a 30 m by 15 m portion of the blue, red and yellow side bars. The locations and descriptions of the targets in the calibration area (14 of which could be detected by EMI systems) and the center

square (10 of which could be detected by EMI systems) were released to the public, the remaining locations (blue, yellow and orange side bars) were not disclosed. In this work, data from the blue, yellow and orange bars which are outside of the calibration area are not processed when evaluating performance of the various detection schemes because these data will cause invalid false alarms.

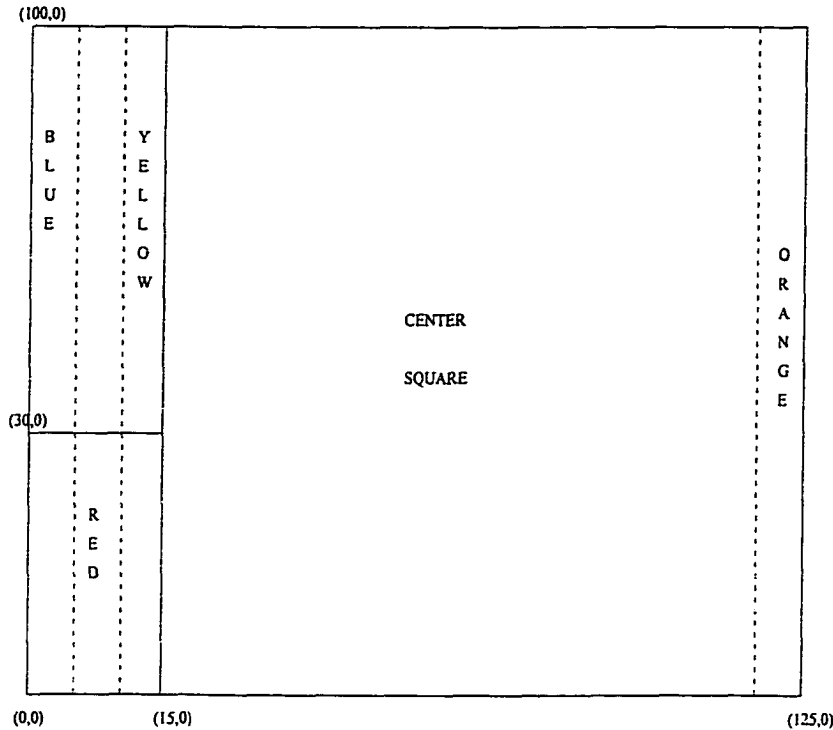


Figure 2.4: Typical site layout from *DARPA Background Clutter Data Collection Experiment*

2.3 LRT and GLRT

In this section, the Bayesian approach to the detection problem is discussed. By using detection theory, the optimal detector can be formulated. The generalized likelihood ratio test, which is a sub-optimal detector that avoids computational expensiveness,

is also discussed in this section.

2.3.1 Likelihood Ratio Test

For the land mine detection problem, only two decisions must be made: target or clutter present. Therefore, it is a binary decision problem. The likelihood ratio test can provide an optimal detector under a wide variety of criteria [53]. In order to define the likelihood ratio, two hypotheses are made: H_1 is the hypothesis that a target is present, and H_0 is the hypothesis that a target is not present, *i.e.* only clutter is present. The likelihood ratio is defined as:

$$\lambda(x) = \frac{p(x|H_1)}{p(x|H_0)} \quad (2.14)$$

where $p(x|H_1)$ is the conditional probability density function (pdf) of the data x given H_1 , $p(x|H_0)$ is the conditional pdf given H_0 , and both density functions are assumed to be known exactly.

The value of the likelihood ratio represents the possibility of a set of data being the result of the presence of a target. The larger $\lambda(x)$, the higher the possibility of target being present at x . Hence, this likelihood ratio is compared with a threshold, δ , to decide whether the target is present or not:

- If $\lambda \geq \delta$, the decision is H_1 , *i.e.* a target is present.
- If $\lambda < \delta$, the decision is H_0 , *i.e.* a target is not present.

The two most often used criteria for choosing the threshold δ are: Neyman-Pearson criterion and Bayes criterion [54, 55]. Neyman-Pearson criterion is used to maximize P_d for a given fixed P_{fa} . Bayes criterion is used to minimize the average risk, which

is optimal in the sense that no other strategies can yield a smaller average risk.

2.3.2 Receiver Operating Characteristics

A complete description of the performance of a processor is the *receiver operating characteristic* (ROC), which is a plot of the probability of detection versus the probability of false alarm for various values of the threshold [55]. Each point of the ROC curve, (P_{fa}, F_d) , corresponds to a value of the threshold δ . The slope of the tangent to the ROC at a particular point is equal to the value of the threshold δ , *i.e.*

$$\delta = \frac{dF_d}{dP_{fa}} \quad (2.15)$$

When the threshold δ decreases from ∞ to 0, the slope of the tangent to the ROC monotonically decreases from the origin $(0, 0)$ to the upper terminus $(1, 1)$.

The ROC of the worst possible receiver is the line defined by $P_d = P_{fa}$, which is called the *chance diagonal*. No ROC can be lower than the chance diagonal, because if a receiver produces an ROC which is lower than the chance diagonal, then its ROC can always be transformed to a curve higher than the chance diagonal by reversing the decision rule, *i.e.* choosing H_1 whenever the “bad” receiver chose H_0 , and vice versa.

2.3.3 Detectability Index

At times, it is impossible or impractical to generate complete ROC curves. For this reason, a measure of discriminability, d' , has been defined which does not require an ROC curve to be computed [56]. Whereas the method of generating ROC curves using

the optimal detector places no restrictions on the shape of the underlying response distributions, calculation of d' assumes that those distributions are Gaussian. When the data under H_1 and H_0 are Gaussian random variables (rv's), the performance of the detector is completely characterized by the quantity d'^2 [55, 56]. For the special one-dimensional case where the signal parameters are known exactly, the theoretical value of d' can be calculated as

$$d' = \frac{\mu_1 - \mu_0}{\sigma}, \quad (2.16)$$

where μ_1 and μ_0 are the means of the density functions of the signal plus noise and noise alone cases, respectively, and the standard deviation, σ , of both density functions is equal.

If l is the output of a processor, which is a function of received signal r from the sensor, and $E(\cdot)$ and $Var(\cdot)$ represent the mean and variance, d' is defined as the distance between the means of the two hypotheses when the variance is normalized to one,

$$d'^2 \equiv \frac{[E(l|H_1) - E(l|H_0)]^2}{[Var(l|H_1) + Var(l|H_0)]/2} \quad (2.17)$$

In the multi-dimensional case, when the received signal is a sampled function of time or frequency, etc., and the signal, s , (H_1 : signal plus noise; H_0 : noise alone) is known exactly, then

$$(d')^2 = (\Delta m)^T Q (\Delta m), \quad (2.18)$$

where $\Delta m = s$ and Q is a diagonal matrix for which $Q_{i,i} = [\sigma^2(t_i)]^{-1}$. If the variance at each sample is the same, Equation (2.18) reduces to

$$(d')^2 = \frac{s^T s}{\sigma^2}, \quad (2.19)$$

which is also one definition of the signal-to-noise ratio. When the statistics of the process are known to be deterministic, but are not known in advance, the statistics of the two density functions can be estimated across realizations and Equation (2.18) can be used to calculate d' where $\Delta\mathbf{m} = \tilde{\mathbf{s}}$ and $Q_{i,i} = [\hat{\sigma}^2(t_i)]^{-1}$, where $\tilde{\mathbf{s}}$ is the estimated time-varying signal and $\hat{\sigma}^2$ is the estimated variance [55]. In this case, Equation (2.18) becomes

$$(d')^2 = \frac{\tilde{\mathbf{s}}^T \tilde{\mathbf{s}}}{\hat{\sigma}^2}. \quad (2.20)$$

This method of calculating d'' requires only that the statistics of the signal be known.

2.3.4 Detection of A Known Signal

If the distribution of the signal under H_1 and H_0 are known exactly, the likelihood ratio test can be formulated as in Equation (2.14).

When $p(x|H_1)$ and $p(x|H_0)$ are univariate Gaussian distribution with identical variance, but different means, *i.e.* $x|H_1 \sim \mathcal{N}(a, \sigma^2)$, $x|H_0 \sim \mathcal{N}(b, \sigma^2)$, the likelihood ratio is formed as:

$$\lambda(x) = \frac{\frac{1}{\sqrt{2\pi}\sigma} \exp\left[-\frac{(x-a)^2}{2\sigma^2}\right]}{\frac{1}{\sqrt{2\pi}\sigma} \exp\left[-\frac{(x-b)^2}{2\sigma^2}\right]} \quad (2.21)$$

This expression assumes that σ is also known. By taking the logarithm, which is a monotonically increasing function of λ , the log-likelihood ratio is:

$$\Lambda(x) = \frac{-(x-a)^2 + (x-b)^2}{2\sigma^2} = \frac{2x(a+b) + b^2 - a^2}{2\sigma^2}. \quad (2.22)$$

The constant terms can be incorporated into threshold, therefore the LRT can be

simplified to:

$$\Lambda(x) = x \underset{H_0}{\overset{H_1}{\gtrless}} \delta, \quad (2.23)$$

which is obviously a threshold test. Thus, for this case the optimal detector reduces to a simple threshold detector, which is easy to implement. However, if the assumption made, which is that all the parameters are known exactly, is not satisfied, the threshold test is not necessarily, and is often not, the optimal detector.

2.3.5 Composite Signal with Uncertain Parameters Problem

The formulation of the likelihood ratio for the composite signal problem is discussed. Assume \mathbf{x} is a composite signal consisting of n elements, x_1, x_2, \dots, x_n , and $p(\mathbf{x}|H_1)$ and $p(\mathbf{x}|H_0)$ are the conditional pdf's of \mathbf{x} given H_1 and H_0 .

If the x_i 's are independent and identically distributed (i.i.d.) Gaussian variates with a common variance under H_1 and H_0 , i.e. $x_i|H_1 \sim \mathcal{N}(m_{1i}, \sigma^2)$, and $x_i|H_0 \sim \mathcal{N}(m_{0i}, \sigma^2)$, where $i = 1, 2, \dots, n$, m_{1i} and m_{0i} are the known means of the i^{th} element corresponding to H_1 and H_0 , respectively, and σ^2 is the common variance for both the H_1 and H_0 hypotheses. Then, the likelihood ratio is defined for this case as:

$$\lambda(\mathbf{x}) = \frac{\prod_{i=1}^n \frac{1}{\sqrt{2\pi}\sigma} \exp\left(-\frac{(x_i - m_{1i})^2}{2\sigma^2}\right)}{\prod_{i=1}^n \frac{1}{\sqrt{2\pi}\sigma} \exp\left(-\frac{(x_i - m_{0i})^2}{2\sigma^2}\right)} \quad (2.24)$$

By taking the logarithm and incorporating the constant terms into the threshold, the log-likelihood ratio can be simplified to:

$$\lambda(\mathbf{x}) = \sum_{i=1}^n x_i(m_{1i} - m_{0i}) \quad (2.25)$$

Therefore, in this case the optimal detector is a matched filter for the signal $\mathbf{s} = (\mathbf{m}_1 - \mathbf{m}_0)$, and the impulse response of the matched filter is:

$$h(i) = \begin{cases} s_{n-i} = m_{1(n-i)} - m_{0(n-i)} & \text{for } 1 \leq i \leq n \\ 0 & \text{otherwise} \end{cases} \quad (2.26)$$

The case discussed above is the simplest case. When $p(\mathbf{x}|H_1)$ and $p(\mathbf{x}|H_0)$ are the conditional pdf's of \mathbf{x} given H_1 and H_0 with uncertain parameters α and β , respectively, then from Bayesian detection theory, the likelihood ratio of composite signal with unknown parameters are in the form of [55]:

$$\lambda(\mathbf{x}) = \frac{\int_{\text{all}\alpha} p(\mathbf{x}|\alpha, H_1)p(\alpha|H_1)d\alpha}{\int_{\text{all}\beta} p(\mathbf{x}|\beta, H_0)p(\beta|H_0)d\beta} \quad (2.27)$$

This is also called the Bayes factor in statistics. Therefore, the likelihood ratio is the ratio of two integrals, for which it is often difficult to find the analytical solution and is computationally difficult to evaluate. The most often used numerical method to evaluate this type of integral is the Monte Carlo method, which is discussed in Sec. 2.4.

2.3.6 GLRT

A generalized likelihood ratio test (GLRT) provides an approximation to the likelihood ratio test, and avoids the evaluation of the complicated integrals shown in Equation (2.27). The GLRT is defined as:

$$\lambda(X) = \frac{p(X|\alpha, H_1)|_{\hat{\alpha}}}{p(X|\beta, H_0)|_{\hat{\beta}}} \quad (2.28)$$

where $p(X|\alpha, H_1)|_{\hat{\alpha}}$ and $p(X|\beta, H_0)|_{\hat{\beta}}$ are conditional pdf's of X given (α, H_1) and (β, H_0) evaluated at the values of $\hat{\alpha}$ and $\hat{\beta}$, respectively. The values of $\hat{\alpha}$ and $\hat{\beta}$ are

estimates of the parameters α and β . The estimates of the parameters are usually obtained from maximum likelihood estimator (MLE). Alternative ways of estimating α and β are maximum a posteriori (MAP) estimate and minimum mean square error (MMSE) estimate, etc.

2.4 Monte Carlo Integration

The Monte Carlo method is a numerical method for evaluating integrals which relies upon random numbers [57]. The value of the integration $J = \int_a^b f(x)dx$ is the area under the curve $f(x)$, which also can be expressed as the product of the length of the interval and the average value of function, $\overline{f(x)}$.

$$\int_a^b f(x)dx = (b - a)\overline{f(x)} \quad (2.29)$$

The average of $f(x)$, $\overline{f(x)}$, is equal to:

$$\overline{f(x)} = \lim_{N \rightarrow \infty} \frac{1}{N} \sum_{i=1}^N f(x_i) \quad (2.30)$$

where the x_i 's are uniformly distributed in the interval of $[a, b]$. If N , the number of points included when computing $\overline{f(x)}$, is large enough, $\overline{f(x)}_N$ tends to the real average value. Therefore, the Monte Carlo estimate of the integral is:

$$\hat{J} \approx (b - a) \frac{1}{N} \sum_{i=1}^N f(x_i) \quad (2.31)$$

When using Monte Carlo method to compute the integration required by the likelihood ratio, we consider:

$$J(\mathbf{y}) = \int f(\mathbf{y}|\mathbf{x})g(\mathbf{x})d\mathbf{x} = E_g[f(\mathbf{y}|\mathbf{x})] < +\infty \quad (2.32)$$

where \mathbf{y} and \mathbf{x} can be vectors, and $g(\mathbf{x})$ is a density function. In this case, the Monte Carlo method approximates Equation (2.32) as [58]:

$$\hat{J}(\mathbf{y}) = \frac{1}{N} \sum_{i=1}^N f(\mathbf{y}|\mathbf{x}_i) \quad (2.33)$$

where $\mathbf{x}_1, \mathbf{x}_2, \dots, \mathbf{x}_N$ are i.i.d. random samples derived from the density of $g(\mathbf{x})$. There is a large literature on the Monte Carlo evaluation of Bayes Factors. Care has to be taken since the problem can be unstable.

Chapter 3

Analyses of Time-Domain EMI Data

In the chapter, the time-domain (TD) electromagnetic induction (EMI) signal processing work is described.

3.1 Introduction

A brief description of TD EMI sensors is presented in Chapter Two. In this chapter, the TD EMI signal processing work is described. First, the theoretical derivation of the performance of a variety of detectors using TD single channel and/or multi-channel EMI data is presented, based on the EMI exponential decay model and the assumption that the sensor response is subject to additive white Gaussian noise. Theoretical performance predictions derived using simplified assumptions are compared with simulation results using synthetic data. The characteristics of the target and clutter (decay rates) are considered to be both fixed and uncertain, the latter case is more common in practice. Then, equivalence of the GLRT and the LRT for single channel and multi-channel TD EMI data is shown in Sec. 3.2.3. Also, the required noise variance to achieve a particular performance level using the different detectors is investigated in Sec. 3.2.4. Following the theoretical analyses, the performance of the same set of detectors applied to the *DARPA* data utilizing only one-dimensional information (data at a single test location) is shown in Sec. 3.3. Next, the 2-D GLRT, a detector that incorporates spatial information into the detector design, is described and results for the *DARPA* data are provided in Sec. 3.4.

3.2 Theoretical Performance Analyses of TD EMI Data

The TD EMI model shown in Equation (2.4) and Equation (2.5) is used for the single channel and multi-channel TD EMI data. Here, we have normalized the initial value, A , and have thus concentrated on the information conveyed by the resonant frequency α . Note that since the actual sensor output is subject to noise, only approximate normalization for real data is possible. Because the signal-to-noise ratio during the early time response is high (since the response is essentially an exponential decay), the estimate of A is reasonably accurate.

In this section, theoretical analyses of the performance for the LRT, the GLRT, the integral/sum detector (a threshold test on the integral/sum of the entire TD EMI signal at the location under test), and the energy detector (a threshold test on the energy of the TD EMI signal present at the location under test) and the single-point detector (a threshold test on a single time sample of the TD EMI response at the location under test) are investigated. Additionally, when a single time sample of the time-domain EMI response is considered, the sample time that can provide the best performance using this type of data is derived. These results are then verified by simulation in Sec. 3.2.5.

It is assumed that the sensor is subject to i.i.d. Gaussian noise at each time sample. Therefore, the conditional density of $r(r_1, r_2, \dots, r_N)$ is jointly Gaussian. As stated in Sec. 2.3.3, for the Gaussian noise problem, the performance of the detector is completely characterized by the quantity d'^2 [55, 56], where d' is defined as

Equation (2.17). Hence, based on the assumptions stated previously, the d'^2 value of each detector is derived under a variety of assumptions regarding the amount of information which is known.

3.2.1 Fixed Parameter Case

As described previously, the output from the EMI sensor depends on whether or not a mine is present at the location under test. It is a function of the noise variance, σ^2 , and the decay rate, α_1 for H_1 , and α_0 for H_0 . There are also other factors, such as temperature, humidity, environmental noise, *etc.*, which affect the response. In this study, these additional parameters are not considered. If the parameters, α_1 , α_0 , and σ^2 , are known values, or can be estimated (either by MLE, MMSE, *etc.*) the d'^2 corresponding to single time sample data, the LRT, an integral, and an energy detector on multi-channel time-domain EMI data can be calculated as follows.

3.2.1.1 Single Time Sample of TD EMI Data

If a time-domain EMI sensor samples the induced response at a single time point, the performance of this sensor depends on the sample time used by the sensor. Thus, in order to achieve the best performance under the physical constraints imposed by the sensor, the time at which a sample is taken after the incident pulse vanishes becomes a key issue.

It is assumed that the sensor is subject to additive i.i.d. Gaussian noise, *i.e.* $\mathcal{N}(0, \sigma^2)$. From detection theory, we know that the optimal detector operating on

this type of data is simply a threshold test. Therefore,

$$d'^2 = \frac{(e^{-\alpha_1 t_s} - e^{-\alpha_0 t_s})^2}{\sigma^2} \quad (3.1)$$

where t_s is the operating sample time of the sensor. Figure 3.1 plots d'^2 as a function of sample time t_s . To determine the sample time that maximizes d' , the derivative of d' with respect to t_s is taken, and set to zero. The sample time maximizing d' is

$$t_{\max} = \frac{\ln \alpha_0 - \ln \alpha_1}{\alpha_0 - \alpha_1} \quad (3.2)$$

where $\ln(-)$ is natural logarithm. Note that the best sample time is a function of the decay rates of target and clutter, so it is object dependent.

3.2.1.2 LRT (Matched Filter) on Multi-Channel TD EMI Data

The LRT is defined as $\lambda(r) \equiv \frac{p(r|H_1)}{p(r|H_0)}$ [53, 55, 56], where r is the sensor output, H_1 is the target present hypothesis, and H_0 is the no-target hypothesis. If the decay rates for targets and clutter, α_1 and α_0 , are known constants, from the definition of the likelihood ratio (LR), the LRT reduces to a matched filter: $y = \sum_i r_i (e^{-\alpha_1 t_i} - e^{-\alpha_0 t_i})$. This is a signal known exactly (SKE) case, and the LR is distributed as a Gaussian random variable (rv), i.e. under H_1 , $y \sim \mathcal{N}(\mu_1, \sigma_1^2)$, and under H_0 , $y \sim \mathcal{N}(\mu_0, \sigma_0^2)$, where $\mu_1 = \sum_i (e^{-\alpha_1 t_i} - e^{-\alpha_0 t_i}) e^{-\alpha_1 t_i}$, $\sigma_1^2 = \sum_i (e^{-\alpha_1 t_i} - e^{-\alpha_0 t_i})^2 \sigma^2$, $\mu_0 = \sum_i (e^{-\alpha_1 t_i} - e^{-\alpha_0 t_i}) e^{-\alpha_0 t_i}$, and $\sigma_0^2 = \sigma^2$. Thus,

$$d'^2 = \frac{(\mu_1 - \mu_0)^2}{\sigma_0^2} = \frac{\sum_i (e^{-\alpha_1 t_i} - e^{-\alpha_0 t_i})^2}{\sigma^2} \quad (3.3)$$

As expected, d' is proportional to the energy of the difference signal and inversely proportional to the noise variance.

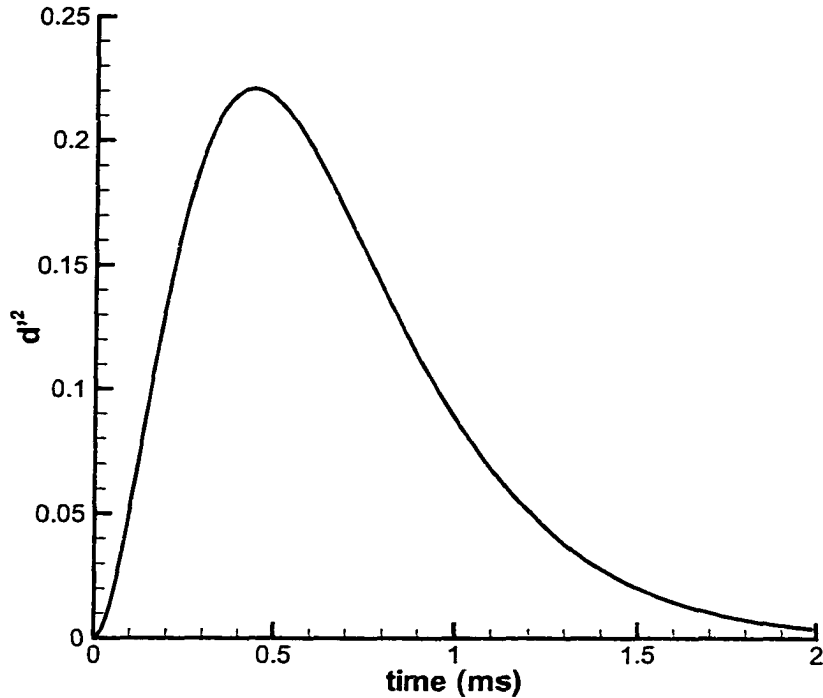


Figure 3.1: d'^2 as a function of sample time t_s when parameters are fixed and known values. $\alpha_1 = 2.1$, $\alpha_0 = 2.5$, and $\sigma = 0.14$.

3.2.1.3 Integral/Summed-Data Detector on Multi-Channel TD EMI Data

An integral detector, also called summed-data detector, integrates (sums) the sampled time sequence, then compares the sum to a threshold to make a decision as to whether a mine is present or not. The output of an integral detector is $x = \sum_i r_i$, thus under H_1 , $x \sim \mathcal{N}(\sum_i e^{-\alpha_1 t_i}, N\sigma^2)$, and under H_0 , $x \sim \mathcal{N}(\sum_i e^{-\alpha_0 t_i}, N\sigma^2)$. Hence,

$$d'^2 = \frac{[\sum_i (e^{-\alpha_1 t_i} - e^{-\alpha_0 t_i})]^2}{N\sigma^2} \quad (3.4)$$

Since the output from a single channel TD EMI sensor is essentially the output of an integral detector on multi-channel TD EMI data (if the sample times are set according to single channel sensor parameters), no separate analysis on single channel

data is provided.

3.2.1.4 Energy Detector on Multi-Channel TD EMI Data

The energy detector compares the energy ($E = \sum_i r_i^2$) present in the signal to a threshold to make a decision. Based on the assumptions made before, under H_1 ,

$$E = \sum_i (e^{-\alpha_1 t_i} + n_i)^2 = \sum_i e^{-2\alpha_1 t_i} + 2 \sum_i e^{-\alpha_1 t_i} n_i + \sum_i n_i^2 \quad (3.5)$$

The first term of the right-hand side of Equation (3.5) is a constant, the second term is a Gaussian distributed random variable with mean of zero and variance of $4\sigma^2 \sum_i e^{-2\alpha_1 t_i}$, and the third term is distributed as $\sigma^2 \chi_N^2$ [54], where χ_N^2 is a chi-square distribution with N degrees of freedom. Based on the Central Limit Theorem, the third term can be approximated by a Gaussian random variable with a mean of $N\sigma^2$ and a variance of $2N\sigma^4$. The correlation between the second and the third terms of Equation (3.5) is:

$$\begin{aligned} E[\sum_i (e^{-\alpha_1 t_i} n_i)(\sum_i n_i^2)] &= E[(\sum_i e^{-\alpha_1 t_i} n_i)(n_1^2 + n_2^2 + \dots + n_N^2)] \\ &= \sum_i E[(e^{-\alpha_1 t_i} n_i)(n_1^2 + n_2^2 + \dots + n_N^2)] \end{aligned} \quad (3.6)$$

Since n_i and n_j are independent, if $i \neq j$, $E[n_i n_j^2] = E[n_i] E[n_j^2] = 0$, and $E[n_i^3] = 0$ (since the mean of the odd power of a zero-mean Gaussian random variable is zero), then

$$E[\sum_i e^{-\alpha_1 t_i} n_i] E[(\sum_i n_i^2)] = (\sum_i e^{-\alpha_1 t_i} E[n_i]) E[\sum_i n_i^2] = 0 \quad (3.7)$$

So,

$$E[(\sum_i e^{-\alpha_1 t_i} n_i)(\sum_i n_i^2)] = 0 \quad (3.8)$$

The correlation between the second and the third terms of Equation (3.5) is zero, implying they are independent since they are (approximately) Gaussian distributed

[59]. Thus, the energy under H_1 can be approximated by a Gaussian distribution with a mean of $\sum e^{-2\alpha_1 t_i} + N\sigma^2$ and variance $4\sigma^2 \sum e^{-2\alpha_1 t_i} + 2N\sigma^4$. Similarly, under H_0 the energy also follows a Gaussian distribution with a mean of $\sum e^{-2\alpha_0 t_i} + N\sigma^2$ and variance $4\sigma^2 \sum e^{-2\alpha_0 t_i} + 2N\sigma^4$. Therefore,

$$d'^2 = \frac{(\mu_1 - \mu_0)^2}{(\sigma_1^2 + \sigma_0^2)/2} = \frac{\left[\sum_i (e^{-2\alpha_1 t_i} - e^{-2\alpha_0 t_i}) \right]^2}{2\sigma^2 [\sum_i e^{-2\alpha_1 t_i} + e^{-2\alpha_0 t_i}] + 2N\sigma^4} \quad (3.9)$$

3.2.2 Random Parameter Case

In practice, the decay rates of both targets and clutter are not known constants, but vary within some ranges. Without compromising generality and for simplicity of further calculation, a reasonable assumption on the distribution of α_1 and α_0 is Gaussian. Furthermore, α_1 and α_0 are independent of additive sensor noise, since they are intrinsic properties of the objects being considered. Practically, the decay rate cannot be negative, thus, the distributions of α_1 and α_0 can be considered as truncated Gaussian distributions:

$$p(\alpha_1) = \left(\Phi\left(\frac{\alpha_1^u - \mu_{\alpha_1}}{\sigma_{\alpha_1}}\right) - \Phi\left(\frac{\alpha_1^l - \mu_{\alpha_1}}{\sigma_{\alpha_1}}\right) \right)^{-1} \frac{1}{\sqrt{2\pi\sigma_{\alpha_1}^2}} e^{-(\alpha_1 - \mu_{\alpha_1})^2/2\sigma_{\alpha_1}^2}$$

and

$$p(\alpha_0) = \left(\Phi\left(\frac{\alpha_0^u - \mu_{\alpha_0}}{\sigma_{\alpha_0}}\right) - \Phi\left(\frac{\alpha_0^l - \mu_{\alpha_0}}{\sigma_{\alpha_0}}\right) \right)^{-1} \frac{1}{\sqrt{2\pi\sigma_{\alpha_0}^2}} e^{-(\alpha_0 - \mu_{\alpha_0})^2/2\sigma_{\alpha_0}^2},$$

where $\Phi(x) = \frac{1}{\sqrt{2\pi}} \int_{-\infty}^x e^{-t^2/2} dt$, $\mu_{\alpha_1}, \sigma_{\alpha_1}^2, \mu_{\alpha_0}, \sigma_{\alpha_0}^2$ are the mean and the variance of α_1 and α_0 , respectively, and α_1^u, α_1^l and α_0^u, α_0^l are the left and right truncated points of α_1 and α_0 , respectively. $\alpha_1^l = \alpha_0^l = 0$ and $\alpha_1^u \leq \alpha_0^u$ based on the underlying physics illustrated in Sec. 2.2. The limits of α_1^u, α_0^u are infinity. Based on the field data collected in the DARPA experiment [38], $\Phi\left(\frac{\alpha_1^u - \mu_{\alpha_1}}{\sigma_{\alpha_1}}\right) - \Phi\left(\frac{\alpha_1^l - \mu_{\alpha_1}}{\sigma_{\alpha_1}}\right)$ and $\Phi\left(\frac{\alpha_0^u - \mu_{\alpha_0}}{\sigma_{\alpha_0}}\right) - \Phi\left(\frac{\alpha_0^l - \mu_{\alpha_0}}{\sigma_{\alpha_0}}\right)$

are very close to 1.

The likelihood ratio test with uncertain parameters is defined as [53, 55, 56]:

$$\lambda(r) = \frac{\int p(r|H_1, \theta_1)p(\theta_1|H_1)d\theta_1}{\int p(r|H_0, \theta_0)p(\theta_0|H_0)d\theta_0} \begin{matrix} H_1 \\ > \\ H_0 \end{matrix} < \gamma \quad (3.10)$$

where r is the measured, or available, data (which can be a scalar or a vector), H_1 and H_0 are the hypotheses of target present and target not present, respectively, $p(r|H_1, \theta_1)$ and $p(r|H_0, \theta_0)$ are the pdf's describing the statistical nature of the response, r , given hypotheses (H_1 or H_0) and parameters (θ_1 or θ_0). θ_1 and θ_0 are unknown parameter sets associated with each hypothesis which follow the distributions $p(\theta_1|H_1)$ and $p(\theta_0|H_0)$. In this problem, θ_1 or θ_0 correspond to the decay rate under the two hypotheses, respectively. When the likelihood ratio is greater than a threshold, γ , H_1 is chosen, *i.e.* the target is present; otherwise, H_0 is chosen, *i.e.* no target is present at the test location.

For a more general distribution of α_1 and α_0 , no quantity such as d'^2 can easily be derived to characterize the performance. However, a ROC can be obtained through simulation using synthetic data. The noise variance, σ^2 , is not consider to be a random parameter.

3.2.2.1 GLRT/Matched Filter

The GLRT simplifies the calculation of likelihood ratio. Instead of integrating over the θ_1 and θ_0 parameters as shown in Equation (3.10), it is defined as [56]:

$$\Omega(r) \equiv \frac{p(r|H_1, \hat{\theta}_1)}{p(r|H_0, \hat{\theta}_0)} \begin{matrix} > \\ < \end{matrix} \gamma \quad (3.11)$$

where r is defined as before, and $\hat{\theta}_1$ and $\hat{\theta}_0$ are the maximum likelihood estimates (MLE) of the parameters θ_1 and θ_0 . Based on the assumptions made before, the generalized likelihood ratio is:

$$\Omega(r) = \frac{(2\pi\sigma^2)^{-N/2} e^{-\frac{1}{2\sigma^2} \sum_i (r_i - e^{-\hat{\mu}_{\alpha_1} t_i})^2}}{(2\pi\sigma^2)^{-N/2} e^{-\frac{1}{2\sigma^2} \sum_i (r_i - e^{-\hat{\mu}_{\alpha_0} t_i})^2}} = e^{-\frac{1}{2\sigma^2} \sum_i [2r_i(e^{-\hat{\mu}_{\alpha_0} t_i} - e^{-\hat{\mu}_{\alpha_1} t_i}) + e^{-2\hat{\mu}_{\alpha_1} t_i} + e^{-2\hat{\mu}_{\alpha_0} t_i}]} \quad (3.12)$$

where $\hat{\mu}_{\alpha_1}$ and $\hat{\mu}_{\alpha_0}$ are estimates of μ_{α_1} and μ_{α_0} . ML estimates were used in this study. By taking the logarithm and incorporating the constant into the threshold, the log-GLR is

$$y = \sum_i r_i(e^{-\hat{\mu}_{\alpha_1} t_i} - e^{-\hat{\mu}_{\alpha_0} t_i}) \quad (3.13)$$

This is essentially a matched filter, which is matched to the difference between the target response and the clutter response at the estimated decay rates. Thus,

$$\begin{aligned} y|H_1 &= \sum_i (e^{-\alpha_1 t_i} + n_i)(e^{-\hat{\mu}_{\alpha_1} t_i} - e^{-\hat{\mu}_{\alpha_0} t_i}) \\ &= \sum_i e^{-\alpha_1 t_i}(e^{-\hat{\mu}_{\alpha_1} t_i} - e^{-\hat{\mu}_{\alpha_0} t_i}) + \sum_i n_i(e^{-\hat{\mu}_{\alpha_1} t_i} - e^{-\hat{\mu}_{\alpha_0} t_i}) \end{aligned} \quad (3.14)$$

When the variance of α_1 is relatively small compared to the variance of the noise (this often is the case as has been verified experimentally [26]), $e^{-\alpha_1 t_i}$ can be approximated by a straight line through the mean value of α_1 with a slope of the derivative

of $e^{-\alpha_1 t_i}$ at $\alpha_1 = \mu_{\alpha_1}$, i.e.

$$e^{-\alpha_1 t_i} \approx -t_i e^{-\hat{\mu}_{\alpha_1} t_i} \alpha_1 + e^{-\hat{\mu}_{\alpha_1} t_i} + t_i e^{-\hat{\mu}_{\alpha_1} t_i} \hat{\mu}_{\alpha_1} \quad (3.15)$$

Thus, by substituting Equation (3.15) into (3.14), y is seen to be a linear combination of Gaussian distributed random variables (rv's). Therefore, $y \sim \mathcal{N}(\mu_{1y}, \text{var}(y_1))$, where

$$\begin{aligned} \mu_{1y} &= \sum_i e^{-\hat{\mu}_{\alpha_1} t_i} (e^{-\hat{\mu}_{\alpha_1} t_i} - e^{-\hat{\mu}_{\alpha_0} t_i}) \\ \text{var}(y_1) &= \sum_i [(e^{-\hat{\mu}_{\alpha_1} t_i} - e^{-\hat{\mu}_{\alpha_0} t_i}) t_i e^{-\hat{\mu}_{\alpha_1} t_i}]^2 \sigma_{\alpha_1}^2 + \sum_i (e^{-\hat{\mu}_{\alpha_1} t_i} - e^{-\hat{\mu}_{\alpha_0} t_i})^2 \sigma^2 \end{aligned} \quad (3.16)$$

Similarly, $y|H_0 \sim \mathcal{N}((\mu_{0y}, \text{var}(y_0)))$, where

$$\begin{aligned} \mu_{0y} &= \sum_i e^{-\hat{\mu}_{\alpha_0} t_i} (e^{-\hat{\mu}_{\alpha_1} t_i} - e^{-\hat{\mu}_{\alpha_0} t_i}) \\ \text{var}(y_0) &= \sum_i [(e^{-\hat{\mu}_{\alpha_1} t_i} - e^{-\hat{\mu}_{\alpha_0} t_i}) t_i e^{-\hat{\mu}_{\alpha_0} t_i}]^2 \sigma_{\alpha_0}^2 + \sum_i (e^{-\hat{\mu}_{\alpha_1} t_i} - e^{-\hat{\mu}_{\alpha_0} t_i})^2 \sigma^2 \end{aligned} \quad (3.17)$$

Therefore,

$$\begin{aligned} d'^2 &= \frac{(\mu_1 - \mu_0)^2}{(\sigma_1^2 + \sigma_0^2)/2} \\ &= \frac{[\sum_i (e^{-\hat{\mu}_{\alpha_1} t_i} - e^{-\hat{\mu}_{\alpha_0} t_i})^2]^2}{\frac{1}{2} \left(\sum_i t_i^2 (e^{-\hat{\mu}_{\alpha_1} t_i} - e^{-\hat{\mu}_{\alpha_0} t_i})^2 (e^{-2\hat{\mu}_{\alpha_1} t_i} \sigma_{\alpha_1}^2 - e^{-2\hat{\mu}_{\alpha_0} t_i} \sigma_{\alpha_0}^2) \right) + \sum_i (e^{-\hat{\mu}_{\alpha_1} t_i} - e^{-\hat{\mu}_{\alpha_0} t_i})^2 \sigma^2} \end{aligned} \quad (3.18)$$

It is shown in Sec. 3.2.3 that the LRT reduces to the GLRT for EMI data with Gaussian noise. Therefore, no additional analysis is required to determine the performance of the LRT.

3.2.2.2 Integral/Summed-Data Detector

Letting $x = \sum_i r_i$ correspond to an integral detector output, and using the approximation expressed in Equation (3.15), then under H_1 , $x = \sum_i (e^{-\alpha_1 t_i} + n_i)$, so

$$x|H_1 \sim \mathcal{N}(\sum_i e^{-\hat{\mu}_{\alpha_1} t_i}, (\sum_i t_i e^{-\hat{\mu}_{\alpha_1} t_i})^2 \sigma_{\alpha_1}^2 + N\sigma^2) \quad (3.19)$$

Similarly,

$$x|H_0 \sim \mathcal{N}(\sum e^{-\hat{\mu}_{\alpha_0} t_i}, (\sum t_i e^{-\hat{\mu}_{\alpha_0} t_i})^2 \sigma_{\alpha_0}^2 + N\sigma^2) \quad (3.20)$$

Hence,

$$d'^2 = \frac{\left(\sum_i (e^{-\hat{\mu}_{\alpha_1} t_i} - e^{-\hat{\mu}_{\alpha_0} t_i}) \right)^2}{\frac{1}{2} \left[(\sum_i t_i e^{-\hat{\mu}_{\alpha_1} t_i})^2 \sigma_{\alpha_1}^2 + (\sum_i t_i e^{-\hat{\mu}_{\alpha_0} t_i})^2 \sigma_{\alpha_0}^2 \right] + N\sigma^2} \quad (3.21)$$

3.2.2.3 Energy Detector

The output of an energy detector on EMI data is either $x = \sum_i (e^{-\alpha_1 t_i} + n_i)^2$ under H_1 , or $\sum_i (e^{-\alpha_0 t_i} + n_i)^2$ under H_0 . Since both α_1 and α_0 are random variables, the distribution of the energy cannot be accurately approximated by a Gaussian random variable. Therefore, it is not valid to calculate d' since the definition of d' is based on Gaussian distributed data. Even though d' is not applicable, we can explain the fact that an energy detector exhibits better performance than an integral detector (see Figures 3.3, 3.4 and 3.5). Since the noise is i.i.d. at each sample time, the noise variance at each sample of the sensor is the same. For lower-level signals, corresponding to later samples, the signal-to-noise-ratio (SNR) is lower than that for higher-level signals. Because the operation of calculating the energy puts more weight on higher values and less weight on lower signals (when the value of the signal is greater than 0), lower SNR time samples contribute less, and consequently, the noise affects the results of the energy detector less than the integral detector, which assigns equal weights to each time sample.

3.2.2.4 Single Time Sample of TD EMI Data

If the decay rate of target or clutter is not known constant, d' is more complicated. Borrowing the result of Sec. 3.2.3, the LRT and GLRT is equivalent for TD EMI

data under some specific assumptions. Hence, using the approximation in Equation (3.15), it can be shown that

$$d'^2 = \frac{(e^{-\hat{\mu}_{\alpha_1} t_s} - e^{-\hat{\mu}_{\alpha_0} t_s})^2}{\sigma^2 + \frac{t_s^2}{2} [e^{-2\hat{\mu}_{\alpha_1} t_s} \sigma_{\alpha_1}^2 + e^{-2\hat{\mu}_{\alpha_0} t_s} \sigma_{\alpha_0}^2]} \quad (3.22)$$

Again, t_s is the sample time.

It is difficult to obtain an analytical expression of the sample time that maximizes d' , since it involves transcendental function, however, the maximum can be evaluated numerically. If $\sigma_{\alpha_1}^2 \ll 1$, $\sigma_{\alpha_0}^2 \ll 1$, then $d'^2 \approx \frac{(e^{-\hat{\mu}_{\alpha_1} t_s} - e^{-\hat{\mu}_{\alpha_0} t_s})^2}{\sigma^2}$, so $t_{\max} \approx \frac{\ln \hat{\mu}_{\alpha_0} - \ln \hat{\mu}_{\alpha_1}}{\hat{\mu}_{\alpha_0} - \hat{\mu}_{\alpha_1}}$, where t_{\max} is the sample time that maximizes d' .

3.2.3 Equivalence of the GLRT and the LRT for TD EMI Data

In many applications, the GLRT is often used instead of the LRT to reduce computational complexity at the cost of sacrificing performance. It is not in general an optimal processor [56]. In the following analyses, we show that under some reasonable assumptions made for the statistics governing the land mine detection problem using TD EMI sensor data, the GLRT and the LRT provide the same performance.

3.2.3.1 Equivalence of the GLRT and the LRT for Single Channel EMI Data

In this problem, the GLRT always provides the same performance as that of the LRT with as long as the statistics of the decay rates of targets and clutter follow certain

assumptions.

Under the ideal conditions, in which the target and clutter are completely homogeneous, $s_1(t) = A_1 \exp(-\alpha_1 t)$ under H_1 , which indicates the target signal, $s_0(t) = A_0 \exp(-\alpha_0 t)$ under H_0 , which represents clutter, or background, e.g. soil. If we assume that the sensor is subject to additive i.i.d. Gaussian noise n with zero mean and known variance σ^2 , and all the parameters, A_1, A_0, α_1 , and α_0 , are known exactly, then the received signal from a single channel sensor, r , under H_1 is:

$$r = \sum_{i=0}^{N-1} [A_1 e^{-\alpha_1(t_0+i\Delta t)} + n(i)] \quad (3.23)$$

and under H_0 the received signal, r , is:

$$r = \sum_{i=0}^{N-1} [A_0 e^{-\alpha_0(t_0+i\Delta t)} + n(i)] \quad (3.24)$$

Therefore, r under H_1 and H_0 are Gaussian distributed with mean of

$$M_1 = A_1 \sum_{i=0}^{N-1} e^{-\alpha_1(t_0+i\Delta t)}$$

and

$$M_0 = A_0 \sum_{i=0}^{N-1} e^{-\alpha_0(t_0+i\Delta t)}$$

and variance $N\sigma^2$. Under the assumption that targets have slower decay rates than that of clutter, i.e. $M_1 > M_0$, the threshold detector is optimal as shown in Sec. 2.2.

However, when the parameters A_1, A_0, α_1 , and α_0 are not known exactly, or known to vary spatially, then $p(r|H_1)$ and $p(r|H_0)$ are functions of these random parameters.

Since targets and clutter are rarely homogeneous, which was confirmed upon inspection of the EM61 data from *DARPA* study, the one dimensional likelihood ratio test performed at the received signal r becomes [55]:

$$\lambda(r) = \frac{\int p(r|H_1, \alpha_1)p(\alpha_1)d\alpha_1}{\int p(r|H_0, \alpha_0)p(\alpha_0)d\alpha_0} \quad (3.25)$$

where $p(\alpha_1)$ and $p(\alpha_0)$ are the *priori* pdf's of α_1 and α_0 , respectively, and we have normalized the initial magnitude so that $A_1 = A_0 = 1$. For additive i.i.d. Gaussian noise, the likelihood ratio can be expressed as:

$$\lambda(r) = \frac{\int_{\alpha_1^l}^{\alpha_1^u} \frac{1}{\sqrt{2\pi N\sigma^2}} e^{-\frac{(r - \sum e^{-\alpha_1(t_0+i\Delta t)})^2}{2N\sigma^2}} p(\alpha_1)d\alpha_1}{\int_{\alpha_0^l}^{\alpha_0^u} \frac{1}{\sqrt{2\pi N\sigma^2}} e^{-\frac{(r - \sum e^{-\alpha_0(t_0+i\Delta t)})^2}{2N\sigma^2}} p(\alpha_0)d\alpha_0} \quad (3.26)$$

where the limits of the integrals, $\alpha_1^l, \alpha_1^u, \alpha_0^l$ and α_0^u are determined from the appropriate density functions.

Although this integral can be calculated via Monte Carlo integration [58], we prove that this likelihood ratio is a monotonic function of r , and therefore that the LRT and the threshold test are essentially the same under the assumptions, *i.e.* the detector reduces to a threshold test.

Proposition: Assume the single TD EMI sensor response is modeled as: $r = \sum_{i=0}^{N-1} e^{-\alpha_k(t_0+i\Delta t)}$ where $k = 1$ or 0 , representing H_1 and H_0 , respectively, t_0 is the starting sample time, $t_0 + (N - 1)\Delta t$ is the ending sample time, $\alpha_0^l, \alpha_0^u, \alpha_1^l$, and α_1^u are the lower and upper integration limits, and $\alpha_0^l \geq \alpha_1^l \geq 0$ and $\alpha_0^u \geq \alpha_1^u > \alpha_0^l$

based on the underlying physics illustrated in Sec. 2.2. Also, assume the sensor is subject to additive i.i.d. Gaussian noise. Then, the LRT in Equation (3.26) reduces to a threshold test.

Proof: In order to prove this relationship, we differentiate $\lambda(r)$ with respect to the received signal, r . If the derivative of $\lambda(r)$ with respect to r is always greater than or equal to zero, $\lambda(r)$ is a monotonically non-decreasing function of r . Writing $\lambda(r)$ as $\lambda(r) = \frac{f(r)}{g(r)}$, so

$$\lambda'_r = \left(\frac{f(r)}{g(r)}\right)' = \frac{f'(r)g(r) - f(r)g'(r)}{g^2(r)} = \frac{h(r)}{g^2(r)}$$

Now we need to demonstrate:

$$h(r) = \left(\frac{d}{dr}f(r)\right)g(r) - f(r)\left(\frac{d}{dr}g(r)\right) > 0 \quad (3.27)$$

Taking the appropriate derivatives, and for simplicity in notation letting $s(\alpha_1) = \sum_{i=0}^{N-1} e^{-\alpha_1(t_0+i\Delta t)}$ and $s(\alpha_0) = \sum_{i=0}^{N-1} e^{-\alpha_0(t_0+i\Delta t)}$.

$$\begin{aligned} h(r) &= \int_{\alpha_1^l}^{\alpha_1^u} -\frac{2(r - s(\alpha_1))}{2N\sigma^2} e^{-\frac{(r-s(\alpha_1))^2}{2N\sigma^2}} p(\alpha_1) d\alpha_1 \int_{\alpha_0^l}^{\alpha_0^u} e^{-\frac{(r-s(\alpha_0))^2}{2N\sigma^2}} p(\alpha_0) d\alpha_0 \\ &\quad - \int_{\alpha_0^l}^{\alpha_0^u} -\frac{2(r - s(\alpha_0))}{2N\sigma^2} e^{-\frac{(r-s(\alpha_0))^2}{2N\sigma^2}} p(\alpha_0) d\alpha_0 \int_{\alpha_1^l}^{\alpha_1^u} e^{-\frac{(r-s(\alpha_1))^2}{2N\sigma^2}} p(\alpha_1) d\alpha_1 \\ &= -\frac{1}{N\sigma^2} \int_{\alpha_1^l}^{\alpha_1^u} (r - s(\alpha_1)) e^{-\frac{(r-s(\alpha_1))^2}{2N\sigma^2}} p(\alpha_1) d\alpha_1 \int_{\alpha_0^l}^{\alpha_0^u} e^{-\frac{(r-s(\alpha_0))^2}{2N\sigma^2}} p(\alpha_0) d\alpha_0 \\ &\quad + \frac{1}{N\sigma^2} \int_{\alpha_0^l}^{\alpha_0^u} (r - s(\alpha_0)) e^{-\frac{(r-s(\alpha_0))^2}{2N\sigma^2}} p(\alpha_0) d\alpha_0 \int_{\alpha_1^l}^{\alpha_1^u} e^{-\frac{(r-s(\alpha_1))^2}{2N\sigma^2}} p(\alpha_1) d\alpha_1 \quad (3.28) \end{aligned}$$

Simplifying and combining two single integrals into a double integral,

$$\begin{aligned}
h(r) &= \frac{1}{N\sigma^2} \int_{\alpha_0^l}^{\alpha_0^u} \int_{\alpha_1^l}^{\alpha_1^u} [(r - s(\alpha_0)) - (r - s(\alpha_1))] e^{-\frac{(r-s(\alpha_1))^2}{2N\sigma^2}} p(\alpha_1) e^{-\frac{(r-s(\alpha_0))^2}{2N\sigma^2}} p(\alpha_0) d\alpha_1 d\alpha_0 \\
&= \frac{1}{N\sigma^2} \int_{\alpha_0^l}^{\alpha_0^u} \int_{\alpha_1^l}^{\alpha_1^u} (s(\alpha_1) - s(\alpha_0)) e^{-\frac{(r-s(\alpha_1))^2}{2N\sigma^2}} p(\alpha_1) e^{-\frac{(r-s(\alpha_0))^2}{2N\sigma^2}} p(\alpha_0) d\alpha_1 d\alpha_0
\end{aligned} \quad (3.29)$$

Because pdf's are always greater than or equal to zero, if the first term of Equation (3.29), $(s(\alpha_1) - s(\alpha_0))$, is greater than zero, $h(r)$ is always greater than or equal to zero. So if $\alpha_1 < \alpha_0$, $(s(\alpha_1) - s(\alpha_0)) > 0$, then $h(r) > 0$. If α_1 is not always less than α_0 , but mean of α_1 is less than mean of α_0 which is the case for a single channel EMI sensor data, then the double integral can be divided into four areas of integrals as:

$$\int_{\alpha_0^l}^{\alpha_1^u} \left[\int_{\alpha_1^l}^{\alpha_0^l} d\alpha_1 + \int_{\alpha_0^l}^{\alpha_1^u} d\alpha_1 \right] d\alpha_0 + \int_{\alpha_1^u}^{\alpha_0^u} \left[\int_{\alpha_0^l}^{\alpha_0^l} d\alpha_1 + \int_{\alpha_0^l}^{\alpha_1^u} d\alpha_1 \right] d\alpha_0 \quad (3.30)$$

where $0 < \alpha_1^l \leq \alpha_0^l < \alpha_1^u \leq \alpha_0^u$. In the first, third, and fourth integrals of Equation (3.30), $\alpha_1 \leq \alpha_0$, so these three terms contribute only non-negative values to $h(r)$. In the second integral of Equation (3.30), both α_1 and α_0 are being integrated over the same region, so that simplification of this integral results zero, since from Equation (3.28) it can be easily found that the integral is zero if the integration regions of α_1 and α_0 are same. Thus, $h(r) \geq 0$ for these reasonable assumptions on the parameters involved. Therefore, $\lambda'_r \geq 0$, $\lambda(r)$ is a monotonic function of r .

This analysis has shown that, for single channel integrated time-domain EMI sensors such as the EM61 operating under the assumption of additive i.i.d. Gaussian noise, the mean magnitude of response of a target is larger than that of clutter, and the mean decay rate of target signatures is slower than that of clutter

$(\alpha_1^l \leq \alpha_0^l < \alpha_1^u \leq \alpha_0^u)$, the optimal processor for the detection of targets in the single location is simply a threshold detector when $A_1 = A_0 = 1$, and σ^2 is known.

3.2.3.2 Equivalence of the GLRT and the LRT for Multi-Channel EMI Data

In the following analyses, it is shown that under some reasonable assumptions made for the statistics governing the land mine detection problem using multi-channel EMI sensor data, the GLRT and the LRT provide the same performance. In this problem, the GLRT (shown in Sec. 3.2.2.1 that it is essentially a matched filter, $z = \sum_{i=1}^N [r_i(e^{-\hat{\mu}_{\alpha_1} t_i} - e^{-\hat{\mu}_{\alpha_0} t_i})]$) always provides the same performance as that of the LRT with as long as the statistics of the decay rates of targets and clutter follow certain assumptions.

Proposition: Assume the multi-channel EMI sensor response is modeled as $r = e^{-\alpha_n t}$, where $n = 1$ or 0 , representing H_1 and H_0 , respectively, t is a N by 1 vector of the sampling times, α_1 and α_0 are truncated Gaussian distributed random variables with means μ_{α_1} and μ_{α_0} , and variances $\sigma_{\alpha_1}^2$ and $\sigma_{\alpha_0}^2$, and left truncated points of α_1^l, α_0^l and right truncated points of α_1^u, α_0^u , respectively. Furthermore, it is assumed that $\alpha_0^l \geq \alpha_1^l \geq 0$ and $\alpha_0^l < \alpha_1^u \leq \alpha_0^u$ based on the underlying physics illustrated in Sec. 2.2. The limits of α_1^u, α_0^u are infinity. The means and variances of α_1 and α_0 satisfy $\mu_{\alpha_1} < \mu_{\alpha_0}, \frac{\mu_{\alpha_0}}{\mu_{\alpha_1}} \geq \frac{\sigma_{\alpha_0}^2}{\sigma_{\alpha_1}^2} \geq 1$. Also, assume the sensor is subject to i.i.d. Gaussian noise at each sample time. The GLRT on r is in the form of $z = \sum_{i=1}^N r_i(e^{-\hat{\mu}_{\alpha_1} t_i} - e^{-\hat{\mu}_{\alpha_0} t_i})$, and the LRT is of the form shown in Equation (3.10).

Then, the GLRT and LRT are equivalent, thus, provide the same performance.

Proof: If it can be shown that $d\lambda/dz \geq 0$, which means the LR, λ , is a non-decreasing function of the output of a matched filter, z , thus, a monotonic function of z , the LRT and the GLRT are equivalent. Because λ is not an explicit function of z , the chain rule is utilized to prove this relationship,

$$\frac{d\lambda}{dz} = \sum_{i=1}^N \frac{\partial \lambda}{\partial r_i} \frac{1}{\partial z / \partial r_i} \quad (3.31)$$

where r_i is the received signal from the sensor at the i^{th} sample time at one location and N is the number of times at which the sensor samples the response. Under H_1 the output of multi-channel time-domain EMI sensor is $r_i = e^{-\alpha_1 t_i} + n_i$ ($i = 1, 2, , N$) and under H_0 the sensor output is $r_i = e^{-\alpha_0 t_i} + n_i$, where r_i represents the output from the sensor at the sample time t_i , n_i is i.i.d. Gaussian noise with zero mean and variance of σ^2 . Since the noise terms are i.i.d., the covariance matrix for \mathbf{n} is the identity matrix scaled by σ^2 .

The likelihood ratio is then

$$\begin{aligned} \lambda &= \frac{\int_{-\infty}^{\infty} p(\mathbf{r}|H_1, \alpha_1) p(\alpha_1|H_1) d\alpha_1}{\int_{-\infty}^{\infty} p(\mathbf{r}|H_0, \alpha_0) p(\alpha_0|H_0) d\alpha_0} \\ &= \frac{\int_{\alpha_1^L}^{\alpha_1^U} (2\pi\sigma^2)^{-N/2} e^{-\frac{1}{2\sigma^2} \sum_{i=1}^N [(r_i - e^{-\alpha_1 t_i})^2]} \left(\Phi\left(\frac{\alpha_1^U - \mu_{\alpha_1}}{\sigma_{\alpha_1}}\right) - \Phi\left(\frac{\alpha_1^L - \mu_{\alpha_1}}{\sigma_{\alpha_1}}\right) \right)^{-1} (2\pi\sigma_{\alpha_1}^2)^{-1/2} e^{-\frac{1}{2\sigma_{\alpha_1}^2} (\alpha_1 - \mu_{\alpha_1})^2} d\alpha_1}{\int_{\alpha_0^L}^{\alpha_0^U} (2\pi\sigma^2)^{-N/2} e^{-\frac{1}{2\sigma^2} \sum_{i=1}^N [(r_i - e^{-\alpha_0 t_i})^2]} \left(\Phi\left(\frac{\alpha_0^U - \mu_{\alpha_0}}{\sigma_{\alpha_0}}\right) - \Phi\left(\frac{\alpha_0^L - \mu_{\alpha_0}}{\sigma_{\alpha_0}}\right) \right)^{-1} (2\pi\sigma_{\alpha_0}^2)^{-1/2} e^{-\frac{1}{2\sigma_{\alpha_0}^2} (\alpha_0 - \mu_{\alpha_0})^2} d\alpha_0} \\ &= \frac{\int_{\alpha_1^L}^{\alpha_1^U} F(\mathbf{r}, \alpha_1) d\alpha_1}{\int_{\alpha_0^L}^{\alpha_0^U} G(\mathbf{r}, \alpha_0) d\alpha_0} \end{aligned} \quad (3.32)$$

where

$$F(\mathbf{r}, \alpha_1) = K_1 e^{-\sum_{i=1}^N (r_i - e^{-\alpha_1 t_i})^2 / 2\sigma^2} e^{-(\alpha_1 - \mu_{\alpha_1})^2 / 2\sigma_{\alpha_1}^2} \quad (3.33)$$

and

$$G(\mathbf{r}, \alpha_0) = K_0 e^{-\sum_{i=1}^N (r_i - e^{-\alpha_0 t_i})^2 / 2\sigma^2} e^{-(\alpha_0 - \mu_{\alpha_0})^2 / 2\sigma_{\alpha_0}^2} \quad (3.34)$$

where

$$K_1^{-1} = \left(\Phi\left(\frac{\alpha_1^u - \mu_{\alpha_1}}{\sigma_{\alpha_1}}\right) - \Phi\left(\frac{\alpha_1^l - \mu_{\alpha_1}}{\sigma_{\alpha_1}}\right) \right) (2\pi)^{(N+1)/2} \sigma^N \sigma_{\alpha_1} \quad (3.35)$$

and

$$K_0^{-1} = \left(\Phi\left(\frac{\alpha_0^u - \mu_{\alpha_0}}{\sigma_{\alpha_0}}\right) - \Phi\left(\frac{\alpha_0^l - \mu_{\alpha_0}}{\sigma_{\alpha_0}}\right) \right) (2\pi)^{(N+1)/2} \sigma^N \sigma_{\alpha_0} \quad (3.36)$$

thus, $K_0 > 0$ and $K_1 > 0$. Taking the partial derivative of λ with respect to r_i :

$$\begin{aligned} \frac{\partial}{\partial r_i} \left(\int_{\alpha_1^l}^{\alpha_1^u} F(\mathbf{r}, \alpha_1) d\alpha_1 \right)'_{r_i} &= \int_{\alpha_0^l}^{\alpha_0^u} G(\mathbf{r}, \alpha_0) d\alpha_0 - \int_{\alpha_1^l}^{\alpha_1^u} F(\mathbf{r}, \alpha_1) d\alpha_1 \left(\frac{\int_{\alpha_0^l}^{\alpha_0^u} G(\mathbf{r}, \alpha_0) d\alpha_0}{\int_{\alpha_0^l}^{\alpha_0^u} G(\mathbf{r}, \alpha_0) d\alpha_0} \right)'_{r_i} \\ &= \left[\int_{\alpha_0^l}^{\alpha_0^u} G(\mathbf{r}, \alpha_0) d\alpha_0 \right] \end{aligned} \quad (3.37)$$

where the $(\cdot)'$ notation denotes a derivative with respect to r_i . We now write $\partial \lambda / \partial r_i = h(r_i) / w(\mathbf{r})$. Since the denominator, $w(\mathbf{r})$, is always positive, if $h(r_i)$ is non-negative, $\partial \lambda / \partial r_i$ is non-negative as well. Based on a theorem presented in [59], the derivative of the integral is equal to the integral of the derivative if the integrand is differentiable with respect to r_i , i.e.

$$\left(\int_{\alpha_1^l}^{\alpha_1^u} F(\mathbf{r}, \alpha_1) d\alpha_1 \right)'_{r_i} = \int_{\alpha_1^l}^{\alpha_1^u} (F(\mathbf{r}, \alpha_1))'_{r_i} d\alpha_1 \quad (3.38)$$

Therefore, the numerator is:

$$\begin{aligned}
 h(r_i) &= \int_{\alpha_0^l}^{\alpha_0^u} \frac{\partial F(\mathbf{r}, \alpha_1)}{\partial r_i} d\alpha_1 \int_{\alpha_0^l}^{\alpha_0^u} G(\mathbf{r}, \alpha_0) d\alpha_0 - \int_{\alpha_0^l}^{\alpha_0^u} \frac{\partial G(\mathbf{r}, \alpha_0)}{\partial r_i} d\alpha_0 \int_{\alpha_1^l}^{\alpha_1^u} F(\mathbf{r}, \alpha_1) d\alpha_1 \\
 &= \int_{\alpha_0^l}^{\alpha_0^u} \int_{\alpha_1^l}^{\alpha_1^u} \left(\frac{\partial F(\mathbf{r}, \alpha_1)}{\partial r_i} G(\mathbf{r}, \alpha_0) - \frac{\partial G(\mathbf{r}, \alpha_0)}{\partial r_i} F(\mathbf{r}, \alpha_1) \right) d\alpha_1 d\alpha_0
 \end{aligned} \tag{3.39}$$

Taking the derivative of $F(\mathbf{r}, \alpha_1)$ with respect to r_i ,

$$\frac{\partial F(\mathbf{r}, \alpha_1)}{\partial r_i} = K_1 \sigma^2 (e^{-\alpha_1 t_i} - r_i) e^{-\frac{1}{2\sigma^2} \left[\sum_{j=1}^N (r_j - e^{-\alpha_1 t_j})^2 \right]} e^{-\frac{(\alpha_1 - \mu_{\alpha_1})^2}{2\sigma_{\alpha_1}^2}} \tag{3.40}$$

Similarly,

$$\frac{\partial G(\mathbf{r}, \alpha_0)}{\partial r_i} = K_0 \sigma^2 (e^{-\alpha_0 t_i} - r_i) e^{-\frac{1}{2\sigma^2} \left[\sum_{j=1}^N (r_j - e^{-\alpha_0 t_j})^2 \right]} e^{-\frac{(\alpha_0 - \mu_{\alpha_0})^2}{2\sigma_{\alpha_0}^2}} \tag{3.41}$$

After combining constants, $h(r_i)$ can be expressed as:

$$\begin{aligned}
 h(r_i) &= K_0 K_1 \sigma^2 \int_{\alpha_0^l}^{\alpha_0^u} \int_{\alpha_1^l}^{\alpha_1^u} e^{-\frac{1}{2\sigma^2} \left[\sum_{j=1}^N (r_j - e^{-\alpha_1 t_j})^2 \right]} e^{-\frac{1}{2\sigma^2} \left[\sum_{j=1}^N (r_j - e^{-\alpha_0 t_j})^2 \right]} e^{-\frac{(\alpha_1 - \mu_{\alpha_1})^2}{2\sigma_{\alpha_1}^2}} e^{-\frac{(\alpha_0 - \mu_{\alpha_0})^2}{2\sigma_{\alpha_0}^2}} \\
 &\quad \times (e^{-\alpha_1 t_i} - e^{-\alpha_0 t_i}) d\alpha_1 d\alpha_0
 \end{aligned} \tag{3.42}$$

Because exponential functions are always positive, the first four terms of the integrand of the integral in Equation (3.42) are always positive; the constant term associated with the integral is also positive. Obviously, if the decay rate of the target, α_1 , is always slower than that of clutter, α_0 , the fifth term in Equation (3.42), $(e^{-\alpha_1 t_i} - e^{-\alpha_0 t_i})$, is also positive, so $h(r_i) \geq 0$. Although in practice α_1 is not always smaller than α_0 , we have assumed the relationships of $\mu_{\alpha_1} < \mu_{\alpha_0}$, $\alpha_1^l \leq \alpha_0^l < \alpha_1^u \leq \alpha_0^u$. The integration area can be divided into four sub-areas, and each sub-area can be

integrated separately. Let $K = K_0 K_1 \sigma^2$, thus, $K > 0$.

$$h(r_i) = K \int_{\alpha_0^l}^{\alpha_1^u} \left\{ \int_{\alpha_1^l}^{\alpha_0^l} (\cdot) d\alpha_1 + \int_{\alpha_0^l}^{\alpha_1^u} (\cdot) d\alpha_1 \right\} d\alpha_0 + K \int_{\alpha_1^u}^{\alpha_0^u} \left\{ \int_{\alpha_1^l}^{\alpha_0^l} (\cdot) d\alpha_1 + \int_{\alpha_0^l}^{\alpha_1^u} (\cdot) d\alpha_1 \right\} d\alpha_0 \quad (3.43)$$

It is easily shown that for the first, third, and fourth integrals in Equation (3.43), the integration is over an area in which α_1 is always less than α_0 , thus, integration in these three sub-areas contributes positive or nonnegative value to $h(r_i)$. In the second integral in Equation (3.43), α_1 and α_0 are integrated over an identical region. Use $h_2(r_i)$ to represent the second integral in Equation (3.43) after neglecting the positive constant K . The integration area can be further divided into upper triangular and lower triangular portions (Figure 3.2 illustrates how the integration areas are divided.) Therefore, $h_2(r_i)$ can be written as

$$\begin{aligned} h_2(r_i) &= \int_{\alpha_0^l}^{\alpha_1^u} \int_{\alpha_0^l}^{\alpha_0} (e^{-\alpha_1 t_i} - e^{-\alpha_0 t_i}) e^{-\frac{1}{2\sigma^2} \left[\sum_{j=1}^N (r_j - e^{-\alpha_1 t_j})^2 \right]} e^{-\frac{1}{2\sigma^2} \left[\sum_{j=1}^N (r_j - e^{-\alpha_0 t_j})^2 \right]} \\ &\quad \times e^{-\frac{(\alpha_1 - \mu_{\alpha_1})^2}{2\sigma_{\alpha_1}^2}} e^{-\frac{(\alpha_0 - \mu_{\alpha_0})^2}{2\sigma_{\alpha_0}^2}} d\alpha_1 d\alpha_0 \\ &+ \int_{\alpha_0^l}^{\alpha_1^u} \int_{\alpha_1^l}^{\alpha_1} (e^{-\alpha_1 t_i} - e^{-\alpha_0 t_i}) e^{-\frac{1}{2\sigma^2} \left[\sum_{j=1}^N (r_j - e^{-\alpha_1 t_j})^2 \right]} e^{-\frac{1}{2\sigma^2} \left[\sum_{j=1}^N (r_j - e^{-\alpha_0 t_j})^2 \right]} \\ &\quad \times e^{-\frac{(\alpha_1 - \mu_{\alpha_1})^2}{2\sigma_{\alpha_1}^2}} e^{-\frac{(\alpha_0 - \mu_{\alpha_0})^2}{2\sigma_{\alpha_0}^2}} d\alpha_0 d\alpha_1. \end{aligned} \quad (3.44)$$

Then, keeping the first integral in Equation (3.44) the same, and exchanging variables α_1 and α_0 via a change of variables in the second integral in Equation (3.44), and changing the integration limits correspondingly, $h_2(r_i)$ becomes

$$h_2(r_i) = \int_{\alpha_0^l}^{\alpha_1^u} \int_{\alpha_0^l}^{\alpha_0} (e^{-\alpha_1 t_i} - e^{-\alpha_0 t_i}) e^{-\frac{1}{2\sigma^2} \left[\sum_{j=1}^N (r_j - e^{-\alpha_1 t_j})^2 \right]} e^{-\frac{1}{2\sigma^2} \left[\sum_{j=1}^N (r_j - e^{-\alpha_0 t_j})^2 \right]} \times$$

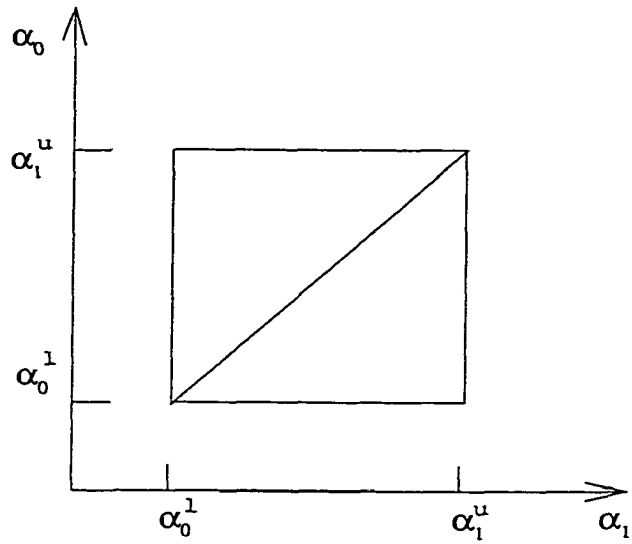


Figure 3.2: The integration area for Equation (3.43), α_1 and α_0 are integration variables. The square is divided into upper and lower triangular portion.

$$\begin{aligned}
 & e^{-\frac{(\alpha_1 - \mu_{\alpha_1})^2}{2\sigma_{\alpha_1}^2}} e^{-\frac{(\alpha_0 - \mu_{\alpha_0})^2}{2\sigma_{\alpha_0}^2}} d\alpha_1 d\alpha_0 \\
 & + \int_{\alpha_0^l}^{\alpha_0^u} \int_{\alpha_1^l}^{\alpha_0} (e^{-\alpha_0 t_i} - e^{-\alpha_1 t_i}) e^{-\frac{1}{2\sigma^2} \left[\sum_{j=1}^N (r_j - e^{-\alpha_1 t_j})^2 \right]} e^{-\frac{1}{2\sigma^2} \left[\sum_{j=1}^N (r_j - e^{-\alpha_0 t_j})^2 \right]} \times \\
 & \quad e^{-\frac{(\alpha_0 - \mu_{\alpha_1})^2}{2\sigma_{\alpha_1}^2}} e^{-\frac{(\alpha_1 - \mu_{\alpha_0})^2}{2\sigma_{\alpha_0}^2}} d\alpha_1 d\alpha_0 \\
 & = \int_{\alpha_0^l}^{\alpha_0^u} \int_{\alpha_1^l}^{\alpha_0} (e^{-\alpha_1 t_i} - e^{-\alpha_0 t_i}) e^{-\frac{1}{2\sigma^2} \left[\sum_{j=1}^N (r_j - e^{-\alpha_1 t_j})^2 \right]} e^{-\frac{1}{2\sigma^2} \left[\sum_{j=1}^N (r_j - e^{-\alpha_0 t_j})^2 \right]} \times \\
 & \quad [e^{-\frac{(\alpha_1 - \mu_{\alpha_1})^2}{2\sigma_{\alpha_1}^2}} e^{-\frac{(\alpha_0 - \mu_{\alpha_0})^2}{2\sigma_{\alpha_0}^2}} - e^{-\frac{(\alpha_0 - \mu_{\alpha_1})^2}{2\sigma_{\alpha_1}^2}} e^{-\frac{(\alpha_1 - \mu_{\alpha_0})^2}{2\sigma_{\alpha_0}^2}}] d\alpha_1 d\alpha_0 \quad (3.45)
 \end{aligned}$$

In Equation (3.45), the integration is in the upper triangular portion where $\alpha_1 < \alpha_0$, so $e^{-\alpha_1 t_i} - e^{\alpha_0 t_i} > 0$. The second and third term of the integrand of Equation (3.45) are exponential functions, therefore, they are always positive, and the fourth

term, represented by $v(\alpha_1, \alpha_0)$, can be simplified to

$$\begin{aligned}
v(\alpha_1, \alpha_0) &= e^{-\frac{\mu_{\alpha_1}^2}{\sigma_{\alpha_1}^2} - \frac{\mu_{\alpha_0}^2}{\sigma_{\alpha_0}^2}} \cdot [e^{-\frac{\alpha_1^2 - 2\mu_{\alpha_1}\alpha_1}{2\sigma_{\alpha_1}^2} - \frac{\alpha_0^2 - 2\mu_{\alpha_0}\alpha_0}{2\sigma_{\alpha_0}^2}} - e^{-\frac{\alpha_0^2 - 2\mu_{\alpha_1}\alpha_0}{2\sigma_{\alpha_1}^2} - \frac{\alpha_1^2 - 2\mu_{\alpha_0}\alpha_1}{2\sigma_{\alpha_0}^2}}] \\
&= e^{-\frac{\mu_{\alpha_1}^2}{\sigma_{\alpha_1}^2} - \frac{\mu_{\alpha_0}^2}{\sigma_{\alpha_0}^2}} \\
&\quad [e^{-\frac{\alpha_1^2\sigma_{\alpha_0}^2 + \alpha_0^2\sigma_{\alpha_1}^2}{2\sigma_{\alpha_1}^2\sigma_{\alpha_0}^2}} e^{\frac{\mu_{\alpha_0}\alpha_0\sigma_{\alpha_1}^2 + \mu_{\alpha_1}\alpha_1\sigma_{\alpha_0}^2}{\sigma_{\alpha_1}^2\sigma_{\alpha_0}^2}} - e^{-\frac{\alpha_1^2\sigma_{\alpha_0}^2 + \alpha_0^2\sigma_{\alpha_1}^2}{2\sigma_{\alpha_1}^2\sigma_{\alpha_0}^2}} e^{\frac{\mu_{\alpha_1}\alpha_0\sigma_{\alpha_0}^2 + \mu_{\alpha_0}\alpha_1\sigma_{\alpha_1}^2}{\sigma_{\alpha_1}^2\sigma_{\alpha_0}^2}}]
\end{aligned} \tag{3.46}$$

It is assumed that $\frac{\mu_{\alpha_0}}{\mu_{\alpha_1}} \geq \frac{\sigma_{\alpha_0}^2}{\sigma_{\alpha_1}^2} \geq 1$, then $\mu_{\alpha_0}\sigma_{\alpha_1}^2 \geq \mu_{\alpha_1}\sigma_{\alpha_0}^2$. Multiplying a positive value on each side of the inequality ($\alpha_1 \leq \alpha_0$ in the upper triangular integration area for $v(\alpha_1, \alpha_0)$), $(\alpha_0 - \alpha_1)\mu_{\alpha_0}\sigma_{\alpha_1}^2 \geq (\alpha_0 - \alpha_1)\mu_{\alpha_1}\sigma_{\alpha_0}^2$. This is equivalent to $\mu_{\alpha_0}\alpha_0\sigma_{\alpha_1}^2 + \mu_{\alpha_1}\alpha_1\sigma_{\alpha_0}^2 \geq \mu_{\alpha_1}\alpha_0\sigma_{\alpha_0}^2 + \mu_{\alpha_0}\alpha_1\sigma_{\alpha_1}^2$. Thus, $e^{\frac{\mu_{\alpha_0}\alpha_0\sigma_{\alpha_1}^2 + \mu_{\alpha_1}\alpha_1\sigma_{\alpha_0}^2}{\sigma_{\alpha_1}^2\sigma_{\alpha_0}^2}} \geq e^{\frac{\mu_{\alpha_1}\alpha_0\sigma_{\alpha_0}^2 + \mu_{\alpha_0}\alpha_1\sigma_{\alpha_1}^2}{\sigma_{\alpha_1}^2\sigma_{\alpha_0}^2}} > 0$. Also because $\alpha_1 \leq \alpha_0$ and $\sigma_{\alpha_1}^2 \leq \sigma_{\alpha_0}^2$, then, $\alpha_1^2(\sigma_{\alpha_0}^2 - \sigma_{\alpha_1}^2) \leq \alpha_0^2(\sigma_{\alpha_0}^2 - \sigma_{\alpha_1}^2)$. This yields $\alpha_1^2\sigma_{\alpha_0}^2 + \alpha_0^2\sigma_{\alpha_1}^2 \leq \alpha_0^2\sigma_{\alpha_0}^2 + \alpha_1^2\sigma_{\alpha_1}^2$, then $e^{-\frac{\alpha_1^2\sigma_{\alpha_0}^2 + \alpha_0^2\sigma_{\alpha_1}^2}{2\sigma_{\alpha_0}^2\sigma_{\alpha_1}^2}} \geq e^{-\frac{\alpha_0^2\sigma_{\alpha_0}^2 + \alpha_1^2\sigma_{\alpha_1}^2}{2\sigma_{\alpha_0}^2\sigma_{\alpha_1}^2}} > 0$. Therefore, $v(\alpha_1, \alpha_0) \geq 0$. Then, $h_2(r_i) \geq 0$. So far, it has been shown rigorously that all the terms in Equation (3.43) are positive or nonnegative under the assumptions made above, thus, $h(r_i) \geq 0$. More generally, when $\alpha_1^l = \alpha_0^l = 0, \alpha_1^u = \alpha_0^u = +\infty$, $h(r_i) = h_2(r_i) \geq 0$. At this point, we have proven $\partial\lambda/\partial r_i \geq 0$. Next, consider $\partial z/\partial r_i$.

$$\frac{\partial z}{\partial r_i} = e^{-\hat{\mu}_{\alpha_1}t_i} - e^{-\hat{\mu}_{\alpha_0}t_i} > 0 \tag{3.47}$$

Given Equation (3.31), $\partial\lambda/\partial r_i \geq 0$ and $\partial z/\partial r_i \geq 0$, then $d\lambda/dz$ is non-negative as well. Therefore, this makes the relationship stated in Proposition proved, *i.e.* the LRT and the GLRT/matched filter are essentially the same for this problem and provide the same performance.

3.2.4 Requirements of Noise Variance for Different Detectors to Achieve a Certain Performance

It is of interest to determine what noise level is required to achieve a particular P_d and P_{fa} for different signal processing techniques using the appropriate sensor data. With this motivation, we investigated the required noise variance for each detector in order to achieve a pre-determined performance using multi-channel EMI sensor. P_d and P_{fa} are defined as [53, 55]:

$$\begin{aligned} P_d &\equiv \int_{\gamma}^{\infty} f(x|H_1)dx \\ P_{fa} &\equiv \int_{\gamma}^{\infty} f(x|H_0)dx \end{aligned} \quad (3.48)$$

If the outputs of the detectors follow a Gaussian distribution, it is possible to theoretically calculate the value of noise variance required for known parameters t, α_1 and α_0 . For the matched filter in the known parameter case, x is Gaussian distributed as derived above (Sec. 3.2.1.2). The distribution of x under H_1 is: $x|H_1 \sim \mathcal{N}(\mu_1, \sigma_1^2)$, where $\mu_1 = \sum_i (e^{-\alpha_1 t_i} - e^{-\alpha_0 t_i}) e^{-\alpha_1 t_i}$ and $\sigma_1^2 = \sum_i (e^{-\alpha_1 t_i} - e^{-\alpha_0 t_i})^2 \sigma^2$, and under H_0 $x|H_0 \sim \mathcal{N}(\mu_0, \sigma_0^2)$ where $\mu_0 = \sum_i (e^{-\alpha_1 t_i} - e^{-\alpha_0 t_i}) e^{-\alpha_0 t_i}$, $\sigma_0^2 = \sum_i (e^{-\alpha_1 t_i} - e^{-\alpha_0 t_i})^2 \sigma^2$, so [54]

$$P_d = \int_{\gamma}^{\infty} \frac{1}{\sqrt{2\pi\sigma_1^2}} e^{-\frac{(x-\mu_1)^2}{2\sigma_1^2}} dx \quad (3.49)$$

Upon letting $y = \frac{x-\mu_1}{\sigma_1}$,

$$P_d = \int_{\frac{\gamma-\mu_1}{\sigma_1}}^{\infty} \frac{1}{\sqrt{2\pi}} e^{-\frac{y^2}{2}} dy = cerf\left(\frac{\gamma-\mu_1}{\sigma_1}\right) \quad (3.50)$$

where $cerf(.)$ is the complementary error function defined by: $cerf(x) = \int_x^{\infty} \frac{1}{\sqrt{2\pi}} e^{-\frac{z^2}{2}} dz$. Similarly,

$$P_{fa} = cerf\left(\frac{\gamma-\mu_0}{\sigma_0}\right). \quad (3.51)$$

The value of noise variance required to achieve a particular P_d and P_{fa} can be obtained by table look-up [54]. For the other detectors, Equation (3.50) and (3.51) are still applicable as long as the detector outputs are Gaussian distributed. Corresponding to each detector, appropriate μ_1, σ_1^2, μ_0 , and σ_0^2 values are substituted into Equation (3.50) and (3.51).

For the random parameter case, no explicit expression for P_d and P_{fa} could be derived, thus no calculation of the theoretical noise variance was made. However, the variance can be estimated through simulation. Table 3.1 lists the noise variance required to achieve $P_{fa} = 0.1$ and $P_d = 0.7$ for both fixed and random parameter case.

	Fixed Parameter	Random Parameter
Matched Filter	17.5	8.6
Energy Detector	16.3	7.3
Integral Detector	10.8	4.9
Threshold Test on Single Time Sample	7.9	3.7

Table 3.1: The noise variance σ^2 required to achieve $P_d=0.7$ and $P_{fa}=0.1$ for fixed and random decay rates.

The values in Table 3.1 were obtained by using signal $A_1 e^{-\alpha_1 t}$ for H_1 and $A_0 e^{-\alpha_0 t}$ for H_0 . Here t is a 20 by 1 vector of [.3525, .4275, .525, .6475, .8025, 1.003, 1.258, 1.583, 1.998, 2.525, 3.198, 4.055, 5.148, 6.543, 8.323, 10.59, 13.49, 17.19, 21.90, 27.92] measured in ms and $A_1 = A_0 = 220$ (equivalent to using $A_1 = A_0 = 1$). In the fixed parameter case, $\alpha_1 = 2.1$ and $\alpha_0 = 2.5$. These values are chosen based on the DARPA experiment data [38]. In the random environment case, $\alpha_1 \sim \mathcal{N}(2.1, 0.2^2)$ and $\alpha_0 \sim \mathcal{N}(2.5, 0.2^2)$. These values and distributions were chosen based on the statistics of real data. From Table 3.1, it can be concluded that to achieve a particular level of performance for either the fixed or random parameter case, the matched

filter can always withstand the highest noise level among the four algorithms investigated. Additionally, an energy detector can achieve the same performance as an integral detector under a higher noise level, or lower SNR. In addition, as expected if the environment is known exactly, the algorithms can afford lower SNR. In practice, however, the environment is always uncertain.

3.2.5 Simulations

Simulations for TD EMI sensor data using different detection strategies were implemented. The synthetic data was obtained by adding Gaussian white noise to an exponentially damped signal. In the parameter-known case, the decay rate of the target, α_1 , is 2.1, and that of clutter, α_0 , is chosen to be 2.5. Those values were chosen by inspecting histograms of the decay rate from target and clutter obtained from *DARPA* data, and they are the empirical MLE. For the random parameter case, the distributions of the decay rate and noise variance were also estimated from the *DARPA* experiment data.

The various signal processing approaches have been implemented on synthetic data. Figure 3.3 and Figure 3.4 show the ROCs for the integral, energy and matched filter detectors and the threshold detector of single time sample data (at the sample time that maximizes the performance) for both fixed parameter and random parameter (α_1 and α_0 uncertain) cases, respectively. As expected, the performance of the LRT/GLRT is better than that of energy detector, which in turn is better than the integral detector, and the performance of threshold detector using single time sample data is the worst among all the detectors considered, since the remaining detectors use multiple time samples of EMI data as their inputs. Additionally,

Simulation of fixed decay rate for target and clutter

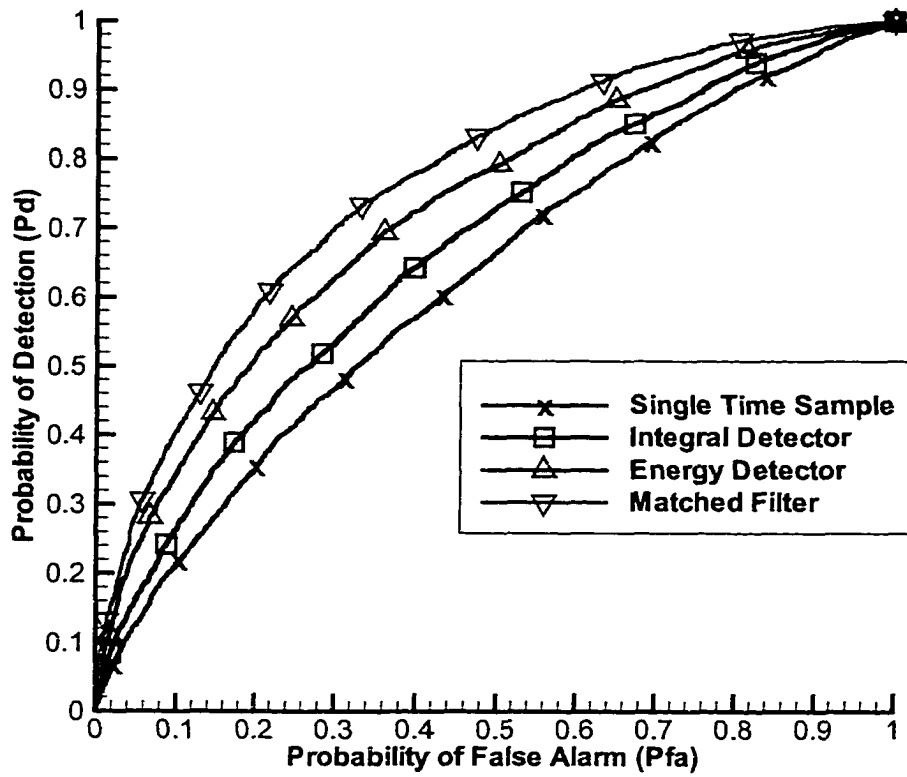


Figure 3.3: ROC of simulations of various detection algorithms for a multi-channel TD EMI sensor at a fixed decay rate for both target and clutter. The decay rate of the target is $\alpha_1 = 2.1$, the decay rate for clutter is $\alpha_0 = 2.5$, and the initial magnitude is 220 for both target and clutter. Gradient: matched filter, delta: energy detector; square: integral detector; cross: threshold test on single time sample.

Figure 3.4 shows the performance of the LRT when parameters are uncertain, in which Monte Carlo integration was used to compute the integrals in Equation (3.10).

$f(r|H_i) = \sum_{k=1}^M f(r|H_i, \alpha_{ik})/M$ was used to evaluate the integral in the numerator and denominator of Equation (3.10), where i is 1 or 0, α_{ik} is chosen from Gaussian distributions with means and variances stated above. 1000 iterations were used when calculating the integral ($M = 1000$).

Simulation of uncertain decay rate for target and clutter

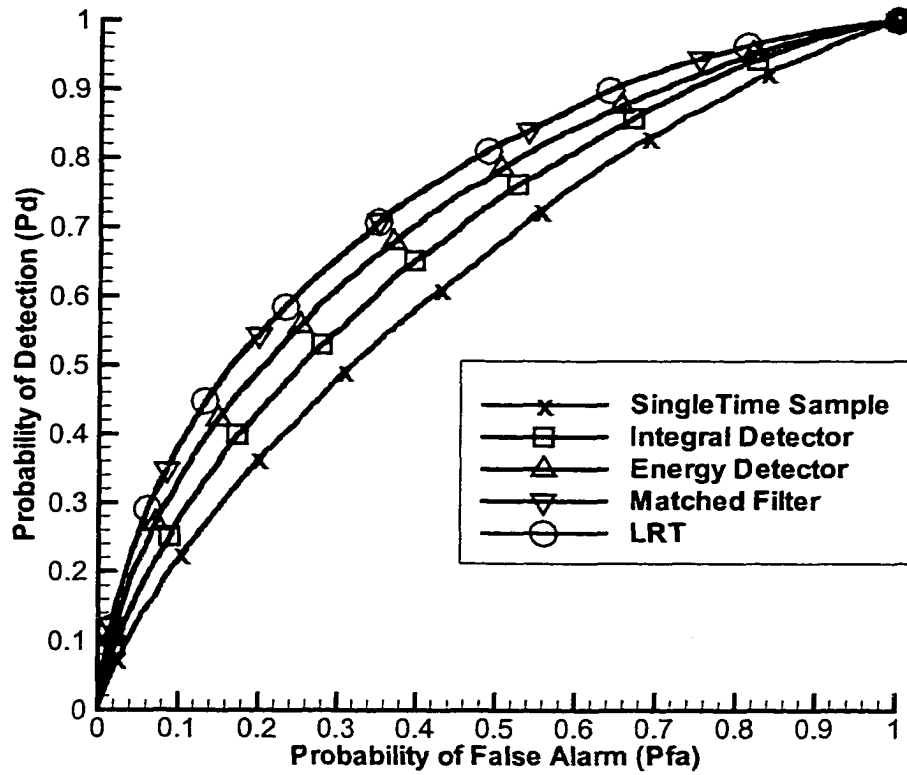


Figure 3.4: ROC of simulation of various detection algorithms for multi-channel TD EMI sensor data with uncertain decay rate for both target and clutter. Distribution of the decay rate α_1 is $\mathcal{N}(2.1, 0.2^2)$, and for α_0 is $\mathcal{N}(2.5, 0.2^2)$, the initial magnitude is 220 for both target and clutter. Circle: the LRT; gradient: matched filter, delta: energy detector; square: integral detector; cross: threshold test on single time sample.

It is clear that for the random parameter case, the ROC for the LRT is equivalent to that of the matched filter (GLRT), which agrees the theoretical derivation, presented in Sec. 3.2.3. Furthermore, a simulation obtained when both the decay rate as well as the initial amplitude are random is shown in Figure 3.5. Again, the LRT and the GLRT exhibit the same performance.

Next, the theoretical calculation of d'^2 and simulation results for the processors

were compared. Table 3.2 lists the d^2 values for each of the detection schemes under both fixed and random parameter cases. Figures 3.6 and 3.7 compare the ROCs generated for the Gaussian detection problem with the calculated d^2 values and simulation results. ROCs for the theoretical values match the simulation results consistently in all cases. Note that when the variances of the decay rates of target and clutter are small, the uncertainty has almost no effect on the performance.

Again, Table 3.1 lists the theoretical noise variance required to achieve $P_{fa} = 0.1$ and $P_d = 0.7$ for the fixed parameter case and the estimated noise variance required to achieve the same performance for the random parameter case. These estimated values were determined by adjusting the noise variance during the simulations. Figure 3.8 shows that the ROC curves for the various algorithms at the theoretical required noise variances for the fixed parameter case. It can be seen that the ROC curves approximately cross the point (0.1, 0.7), indicating the simulations verify the theoretical calculations. Figure 3.9 shows similar ROC curves for random decay rates with the simulated noise at the level listed in Table 3.1.

	Fixed Parameter	Random Parameter
Matched Filter	1.12	0.87
Energy Detector	0.73	≈ 0.72
Integral Detector	0.42	0.38
Threshold Test on Single Time Sample	0.22	≈ 0.22

Table 3.2: The theoretical values of d^2 for various processors and known/random parameter cases.

Simulation of uncertain initial magnitude & decay rate

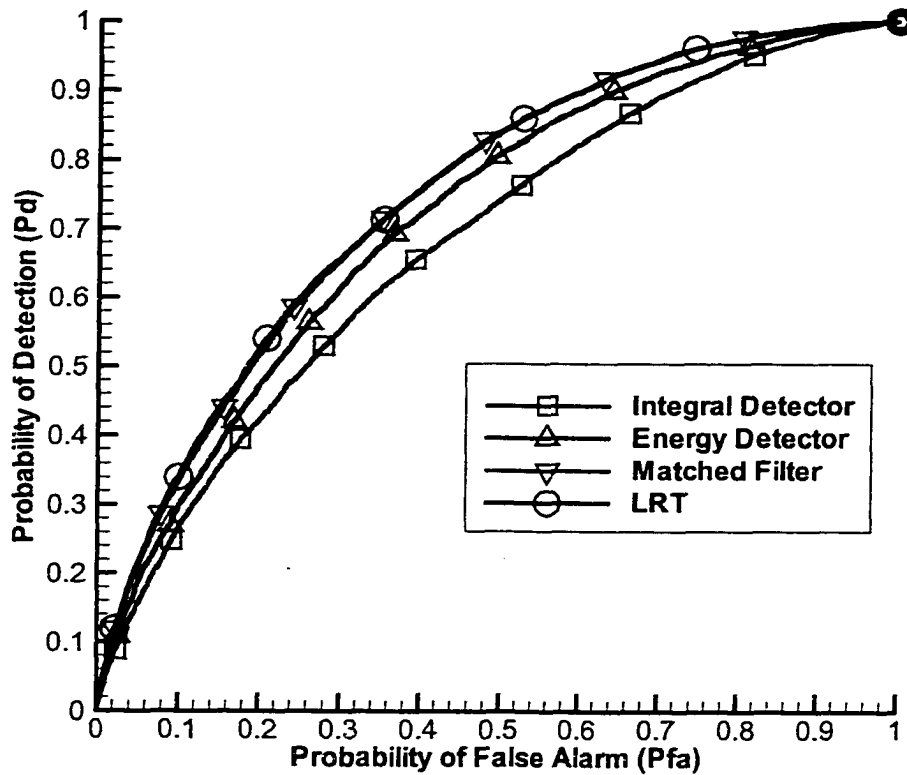


Figure 3.5: ROC of simulation of various detection algorithms for multi-channel TD EMI sensor data with uncertain decay rate and uncertain initial magnitude of target and clutter. Distribution of the decay rate α_1 is $\mathcal{N}(2.1, 0.2^2)$, and for α_0 is $\mathcal{N}(2.5, 0.2^2)$, the distribution of the initial magnitude for target, A_1 , is $\mathcal{N}(220, 20^2)$, for clutter A_0 is distributed as $\mathcal{N}(210, 40^2)$. Circle: LRT; gradient: matched filter; delta: energy detector; square: integral detector.

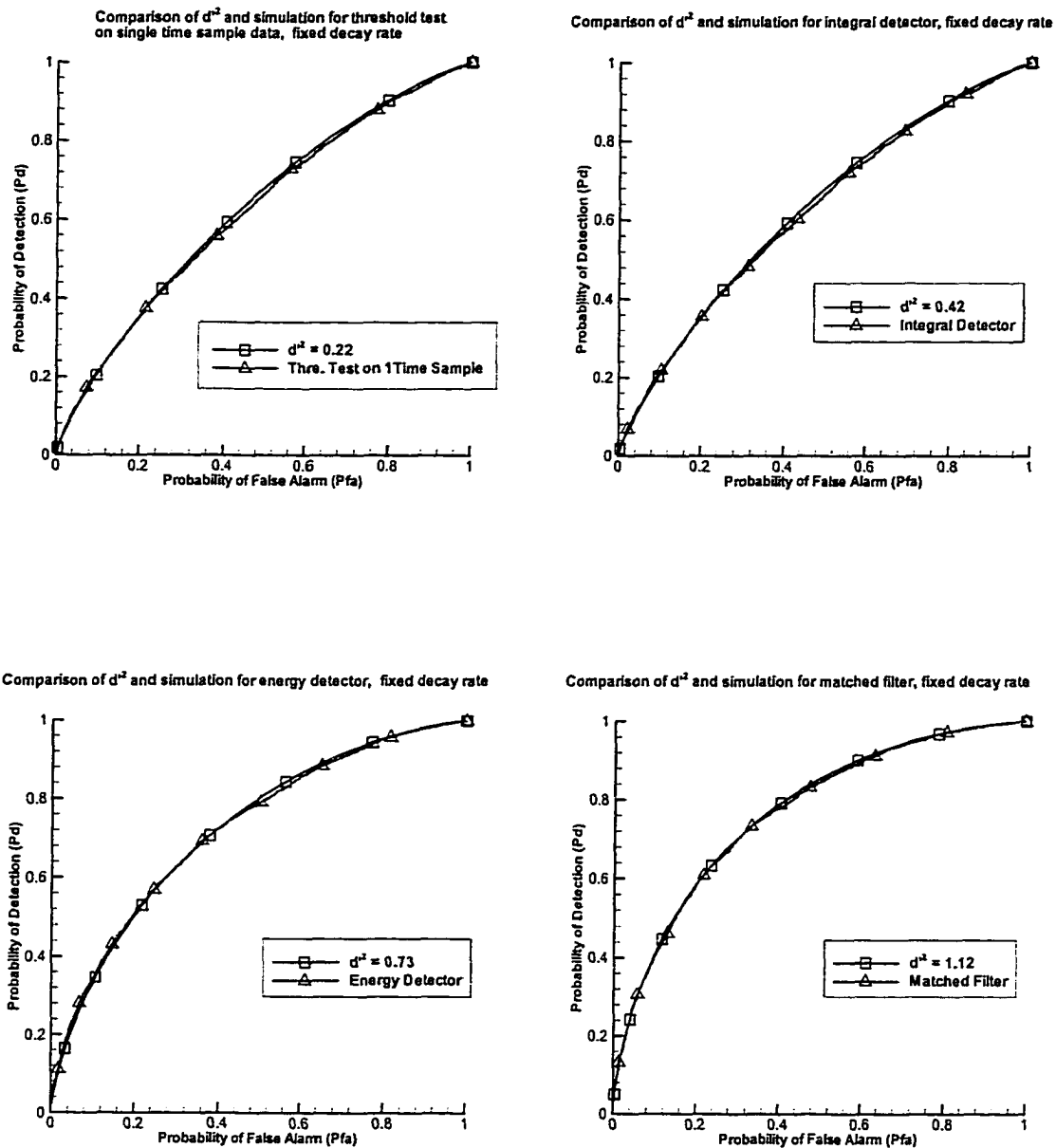


Figure 3.6: Comparison of ROC of the theoretical d'^2 value and simulations of various detectors for the fixed decay rate case. 1) (upper left) the threshold test for single time sample TD EMI sensor data. 2) (upper right) the integral detector, 3) (lower left) the energy detector, and 4) (lower right) the matched filter for multi-channel TD EMI sensor data. Delta: simulation; square: theoretical d' .

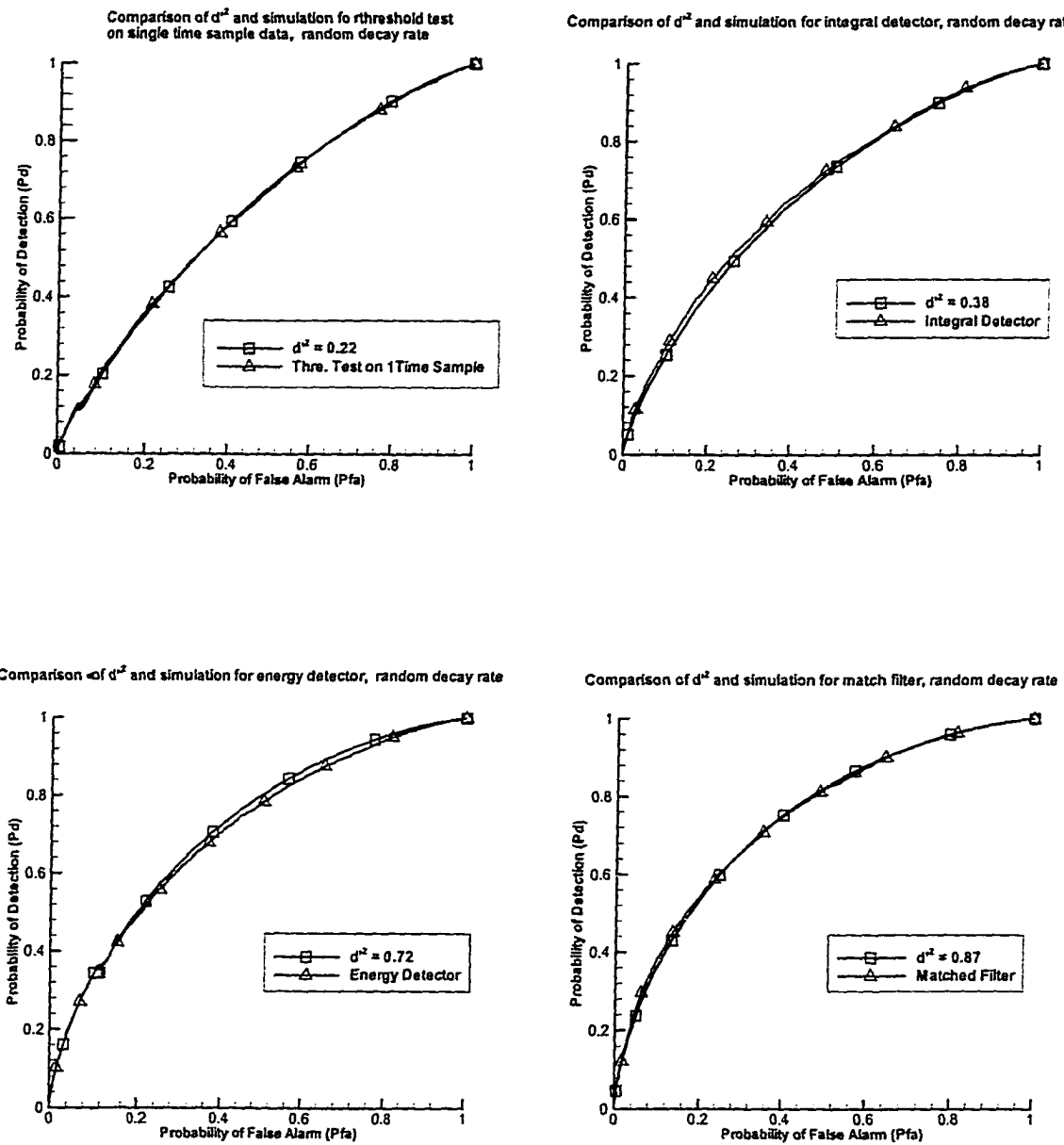


Figure 3.7: Comparison of ROC of the theoretical d'^2 value and simulation of various detectors for the random decay rate case. 1) (upper left) the threshold test for single time sample TD EMI sensor data, 2) (upper right) the integral detector, 3) (lower left) the energy detector, and 4) (lower right) the GLRT/matched filter for multi-channel TD EMI sensor data. Delta: simulation; square: theoretical d' .

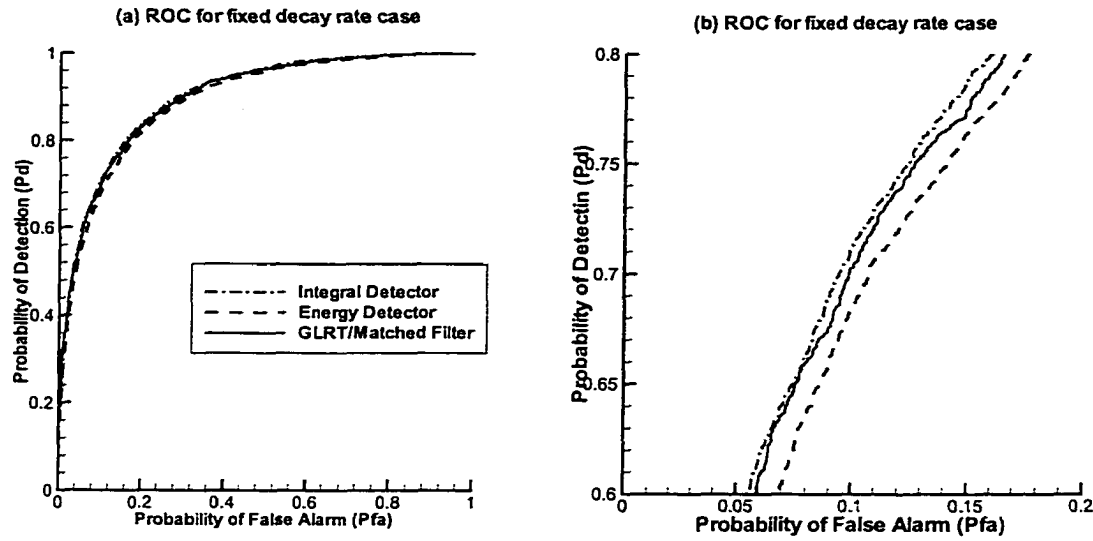


Figure 3.8: ROC for various processors at the theoretically calculated noise variance required achieving (0.1,0.7) performance for fixed decay rates. The left plot, (a), shows the entire scale; the right plot, (b), shows an enlarged version of (a).

3.3 One-Dimensional Results on *DARPA* data

3.3.1 One-Dimensional Processor for Single Channel EMI Sensor Data

3.3.1.1 One-Dimensional LRT

The detector is formulated in terms of binary hypothesis test, with hypothesis H_1 denoting the alternative target-present, and H_0 denoting the null, or no-target-present, hypothesis. The one dimensional LRT performed on the received data, r , is defined as:

$$\lambda(r) = \frac{p(r|H_1)}{p(r|H_0)} \stackrel{H_1}{>} \stackrel{H_0}{\leq} \delta \quad (3.52)$$

where $p(r|H_1)$ and $p(r|H_0)$ are the pdf's of the received data under H_1 and H_0 , respectively, and assumed that all parameters of the pdf's are known.

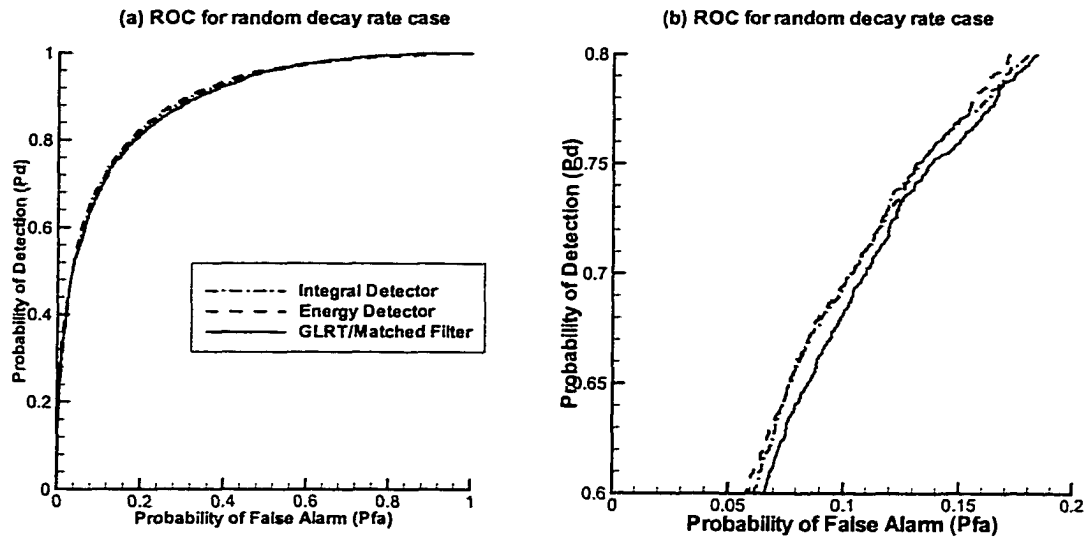


Figure 3.9: ROC for various processors at the theoretically calculated noise variance required achieving (0.1,0.7) performance for random decay rates. The left plot, (a), shows the entire scale; the right plot, (b), shows an enlarged version of (a).

In order to perform this likelihood ratio test, it is necessary to obtain valid estimations of the pdf's. The response is modeled as $s_1(t) = A_1 \exp(-\alpha_1 t)$ under H_1 , which indicates the target signal, and $s_0(t) = A_0 \exp(-\alpha_0 t)$ under H_0 , which represents clutter, or background, *e.g.* soil. Also, it is assumed that the sensor is subject to additive Gaussian white noise n with zero mean and known variance σ^2 . When all the parameters, A_1, A_0, α_1 , and α_0 are known exactly, the threshold detector is optimal as shown in Sec. 2.2.

However, when the parameters, A_1, A_0, α_1 , and α_0 , are uncertain $p(r|H_1)$ and $p(r|H_0)$ are functions of random parameters. Since targets and clutter are rarely homogeneous, which was confirmed upon inspection of the EM61 data from *DARPA* study, the one dimensional likelihood ratio test performed at the received signal r becomes Equation (3.25) [55]. For additive Gaussian white noise, the likelihood ratio can be expressed as Equation (3.26).

In Sec. 3.2.3.1 it is prove that this likelihood ratio is a monotonic function of r , and therefore that the LRT and the threshold test are essentially the same under the assumptions, *i.e.* the detector reduces to a threshold test.

3.3.1.2 Other Processors

For single channel EMI sensor, because the 1-D LRT reduces to threshold test under the assumption defined previously, there is no need to build the 1-D LRT or 1-D GLRT separately. The energy detector, which is always the most often chosen *ad hoc* detector, gives the same performance as the threshold test. The reason is that the responses of a single channel TD EMI system are only one data point at each location and always positive (except ferromagnetic material), however, for positive value the square operation is a monotonic function of the input.

3.3.1.3 Results

As defined in Equation (3.52), the 1-D LRT can be performed on the received data if $p(r|H_1)$ and $p(r|H_0)$ are available. The histogram of the received data are shown in Figures 3.10 and 3.11. Obviously, the values of targets are more likely to be large, which matches with the theoretical assumption made in Sec. 3.2.

By inspecting the histogram, it is found that the distribution of the received data can be modeled by various density functions. For example, for Fort A.P. Hill FP20 site the distribution of the clutter data, *i.e.* $p(r|H_0)$, can be modeled as a Gamma distribution (considering the positive values) and that of the targets, *i.e.* $p(r|H_1)$,

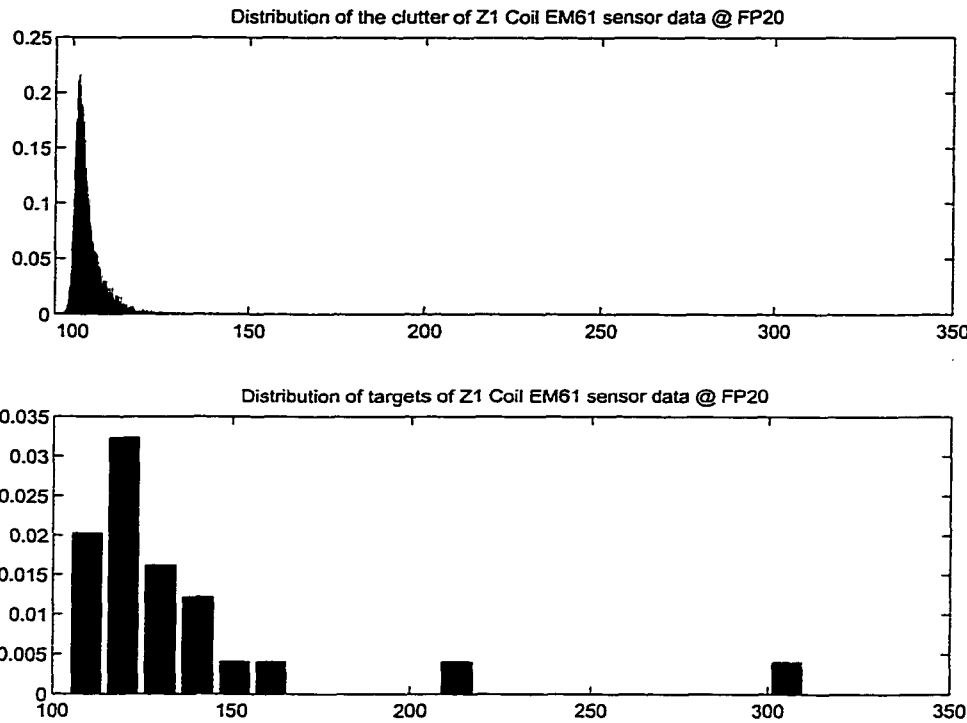


Figure 3.10: The histogram of the received data from EM61 sensor @ A.P. Hill FP20 (Z1 coil) site

can be modeled as a truncated Gaussian, or simply the noninformative uniform distribution. For the other sites, clutter distribution can be modeled as Laplacian and uniform for target. A uniform distribution is often chosen in order to avoid training to the exact target distribution from each site.

Figures 3.12, 3.13, 3.14, and 3.15 present the performance of the 1-D LRT that is obtained using the estimated density functions, $p(r|H_1)$ and $p(r|H_0)$, to calculate the likelihood ratio for four different surveyed sites. From these plots, it is shown that the 1-D LRT provides a similar performance to that of the threshold test. Because the number of target is far less than that of clutter, the ROC curve is not smooth.

It is theoretically proven that for the single channel EMI sensor data if assuming

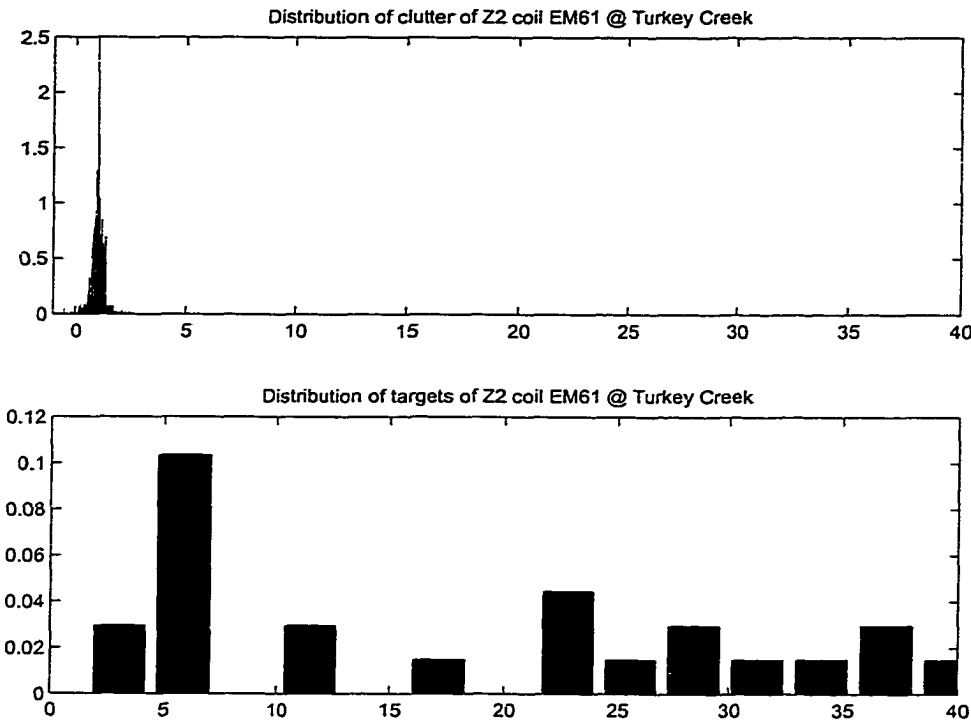


Figure 3.11: The histogram of the received data from EM61 sensor @ Fort Carson Turkey Creek (Z2 coil, after removing drift) site

the sensor is subject to additive i.i.d. Gaussian noise, the one dimensional optimal detector reduces to threshold test. This result is also verified by simulating this scenario. The likelihood ratio is computed by using Equation (3.52). The integrations were evaluated by two dimensional numerical integration method and by the Monte Carlo numerical method. If the number of the iteration times is large enough, then the performances of the 1-D LRT and the threshold test are the same.

Figure 3.16 shows the ROC curves of the 1-D LRT in which $p(r|H_1)$ and $p(r|H_0)$ were estimated by kernel estimation [60, 61]. For some sites, this method can achieve a better performance due to a closer fit to the target density function. However, as shown in Sec. 3.2, the optimal detector in this case is essentially a threshold test, so no further substantial improvement is expected.

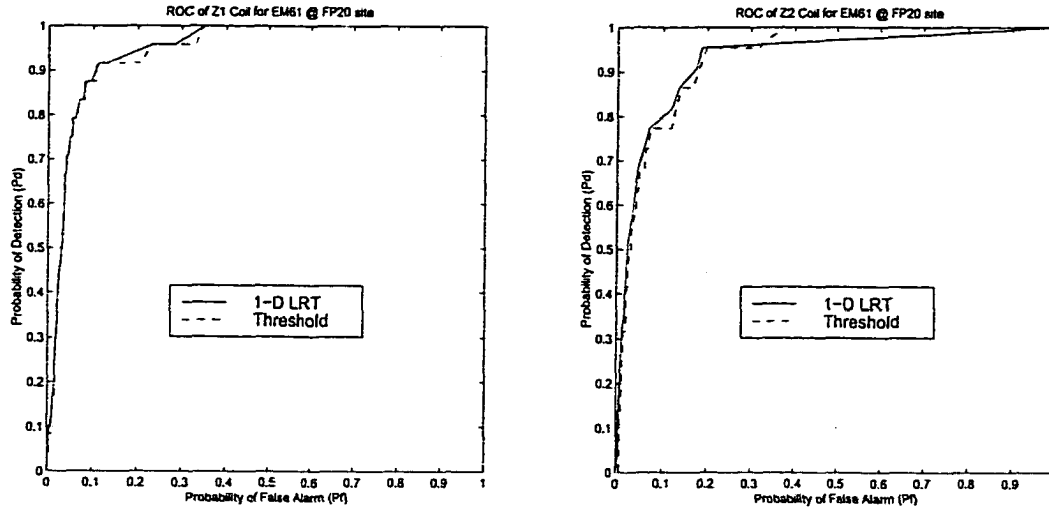


Figure 3.12: ROCs of 1-D Results for EM61 @ A.P. Hill FP20 site (LR is calculated using parametric estimated pdf's)

3.3.2 One-Dimensional Processor for Multi-Channel EMI Sensor Data

3.3.2.1 One-Dimensional LRT

The received signal and its parameters for the multichannel EMI sensor are described in Sec. 2.2.1.2. The signal of EM61-3D, a multichannel sensor used by *DARPA* study is a time series signal at each location, which is a 20 by 1 vector. An example of the signals received from a target and from clutter is shown in Figure 3.17. Each component of the vector is simply a sample of an exponential damping. As mentioned before, it is assumed that the sensor is subject to additive Gaussian white noise $n(i)$ with zero mean and variance σ^2 . Hence, the received signal from EM61-3D sensor can be expressed as:

$$\text{Under } H_1: r_i = A_1 e^{-\alpha_1 t_i} + n(i)$$

$$\text{Under } H_0: r_i = A_0 e^{-\alpha_0 t_i} + n(i)$$

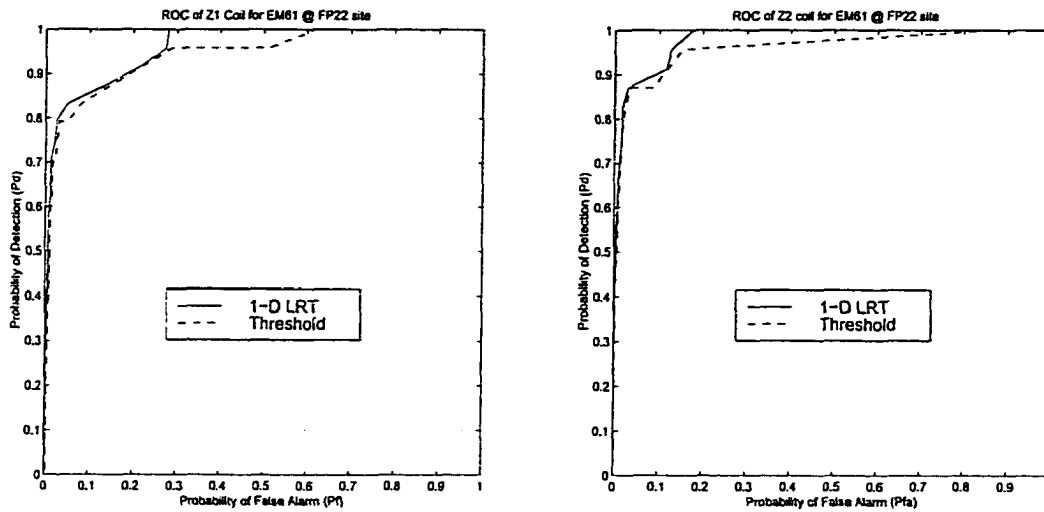


Figure 3.13: ROCs of 1-D Results for EM61 @ A.P. Hill FP22 site (LR is calculated using parametric estimated pdf's)

where r_i 's are elements of the vector \mathbf{r} , $i = 1, 2, \dots, 20$, α_1 and α_0 are the decay time and A_1 and A_0 are the initial magnitude of the response for H_1 and H_0 , respectively.

This is a composite signal with uncertain parameter problem, because the received data at each survey location is a 20 by 1 vector and with unknown parameters involved into the expression of the signal. As shown in Sec. 2.2, when the initial amplitude is normalized to 1, i.e. $A_1 = A_0 = 1$, the likelihood ratio can be formulated as:

$$\lambda(\mathbf{r}) = \frac{\int_{\text{all } \alpha_1} p(\mathbf{r}|\alpha_1, H_1)p(\alpha_1|H_1)d\alpha_1}{\int_{\text{all } \alpha_0} p(\mathbf{r}|\alpha_0, H_0)p(\alpha_0|H_0)d\alpha_0} \quad (3.53)$$

This is a very complicated integral to compute for most of the distribution function forms. By using Monte Carlo integration to evaluate the above integral, the likelihood ratio can be simplified to:

$$\lambda_{MC}(\mathbf{r}) = \frac{\sum_{k=1}^M e^{-\frac{\sum_i (r_i - e^{-\alpha_1 k t_i})^2}{2\sigma^2}}}{\sum_{k=1}^M e^{-\frac{\sum_i (r_i - e^{-\alpha_0 k t_i})^2}{2\sigma^2}}} \quad (3.54)$$

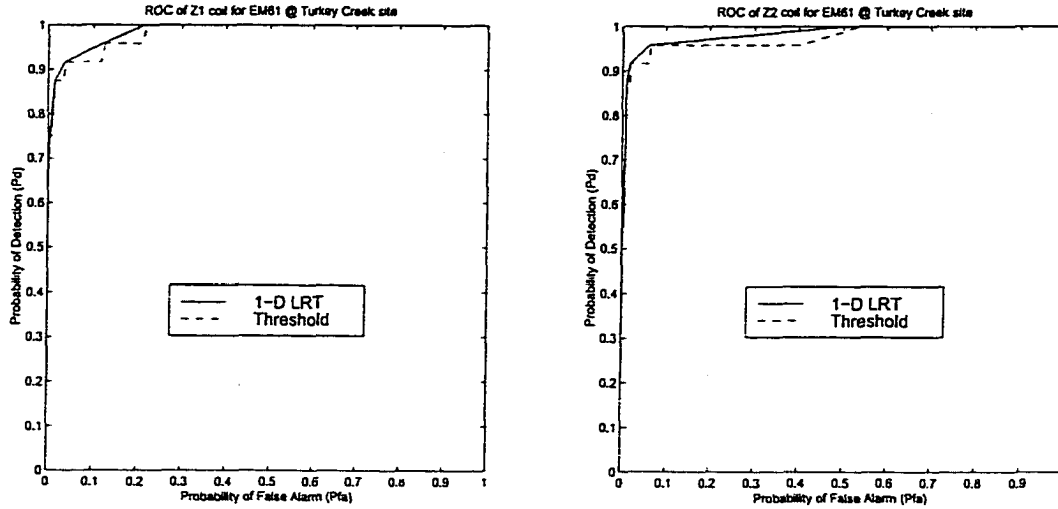


Figure 3.14: ROCs of 1-D Results for EM61 @ Fort Carson Turkey Creek site (LR is calculated using parametric estimated pdf's)

where α_{1k} and α_{0k} are random sample generated from $p(\alpha_1|H_1)$ and $p(\alpha_0|H_0)$. $p(\alpha_1|H_1)$ and $p(\alpha_0|H_0)$ are obtained by inspecting the histograms of α_1 and α_0 , which are calculated using the least squares method at each location. The choice of M depends on the SNR. High SNR requires a large number of samples, and low SNR requires a small number of samples to converge [58].

3.3.2.2 One-Dimensional GLRT

To avoid the computational complexity, the 1-D GLRT was also investigated. The clutter distributions of the outputs of multichannel time-domain EMI sensors were modeled with a multivariate Gaussian density function, thus the one dimensional generalized likelihood ratio test for a single location can be formulated as [26]:

$$\lambda(\mathbf{x}) = \frac{\prod_i \exp\left[-\frac{(x_i - s_{1i}(\hat{\alpha}_1))^2}{2\sigma^2}\right]}{\prod_i \exp\left[-\frac{(x_i - s_{0i}(\hat{\alpha}_0))^2}{2\sigma^2}\right]} \quad (3.55)$$

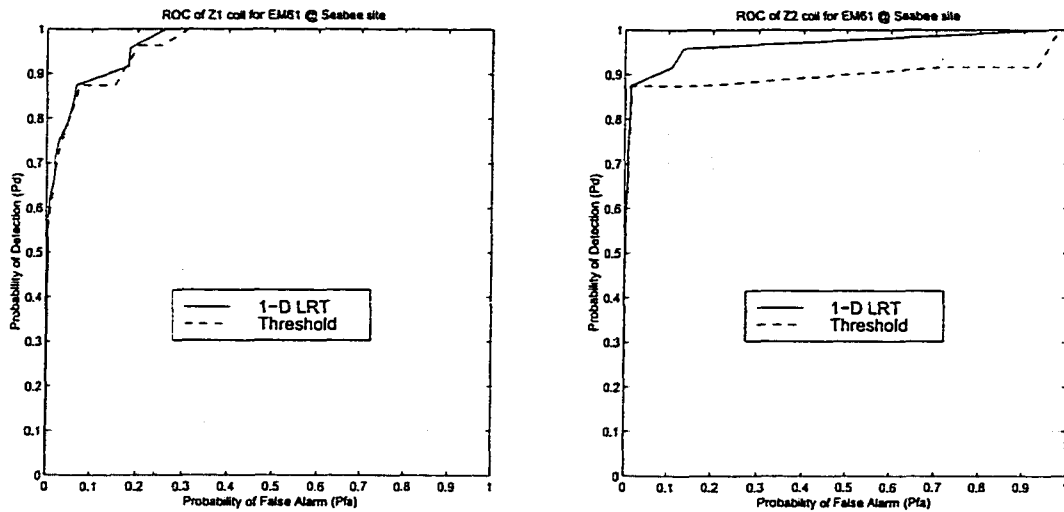


Figure 3.15: ROCs of 1-D Results for EM61 @ Seabee site (LR is calculated using parametric estimated pdf's)

where \mathbf{x} is the output of the sensors for time indices $i = 1, 2, \dots, 20$, and $\hat{\alpha}_1$ and $\hat{\alpha}_0$ are the maximum likelihood estimates (MLE) of α_1 and α_0 . The $s_{1i}(\alpha_1)$ and $s_{0i}(\alpha_0)$ correspond to theoretical values of the sensor output of target and clutter under the parameters of α_1 and α_0 , where α_1 and α_0 are the natural resonant frequencies (decay rate) of H_1 and H_0 . By taking the logarithm and incorporating all the constant terms into the threshold, it can be simplified as:

$$\log \lambda(\mathbf{x}) = \sum_{i=1}^{20} x_i [s_{1i}(\hat{\alpha}_1) - s_{0i}(\hat{\alpha}_0)], \quad (3.56)$$

which is essentially a matched filter. It should be noted that 1-D GLRT detectors provide a sub-optimal detector which in some instance achieves a performance close to that of the one dimensional likelihood ratio test.

3.3.2.3 Other Processors

For the multichannel EMI sensor data, the traditional detection scheme is to perform a threshold test at the energy presented at each surveyed location. Another *ad hoc*

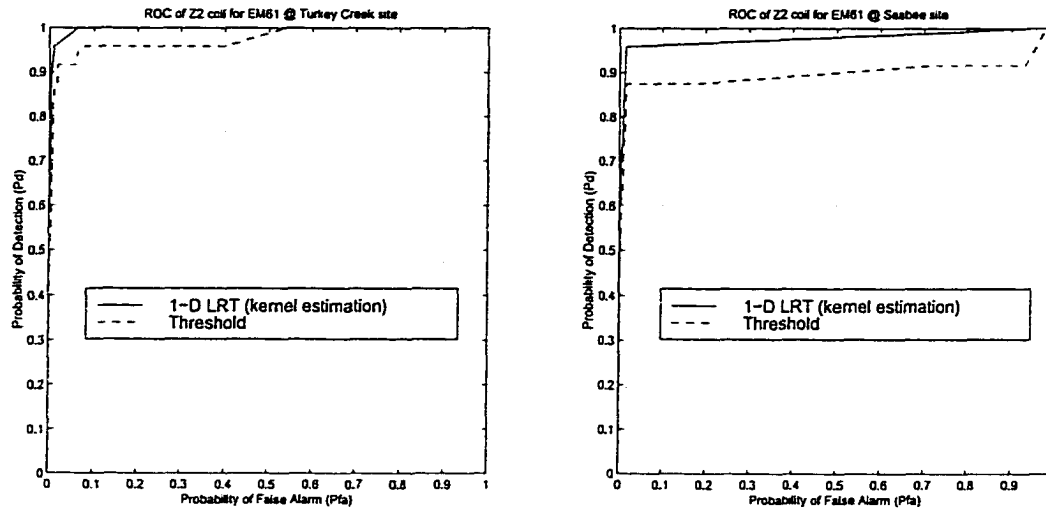


Figure 3.16: ROCs of 1-D Results for Turkey Creek and Seabee sites (LR is calculated using kernel estimation of pdf's)

method is to perform a processor which integrates or sums up the samples at each location and thresholds the output, which is called the integral detector. Other *ad hoc* processors that have been suggested in [62, 63] such as decay rate processor, in which the decay rate is estimated and then a threshold is applied, are also implemented.

3.3.2.4 Results

In this section, the performances of the 1-D LRT, the 1-D GLRT and various *ad hoc* techniques discussed in the preceding sections are presented. It is easy to distinguish the improvement by plotting all the ROCs in one figure. If good estimates of the parameters can be obtained, the 1-D GLRT processor is approximately equivalent to that of the 1-D LRT which varies from site to site. This variation is also discussed in [64]. Across all the four sites, the 1-D GLRT detector performs better than the standard threshold, energy, integral and decay rate test as shown in Figures 3.18 and 3.19.

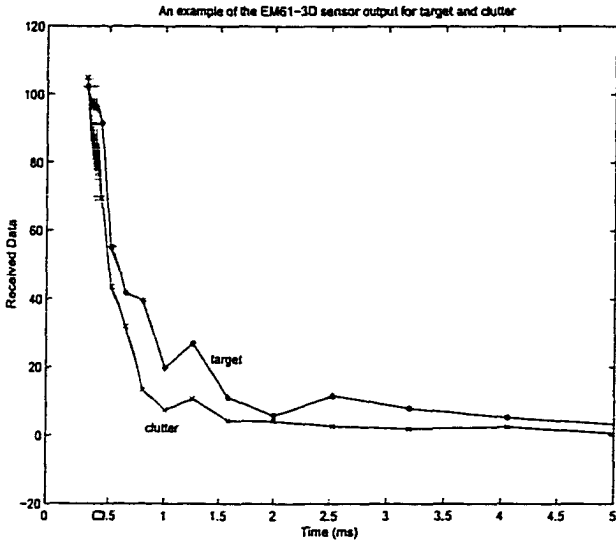


Figure 3.17: A typical plot of the EM61-3D sensor output for target and clutter

3.4 Two-Dimensional GLRT

In Sec. 3.3, we have applied signal detection theory to generate both the one-dimensional likelihood ratio test (LRT) and the GLRT for the Geonics EM61 and EM61-3D sensor data. The probability density functions describing the sensor response to target and clutter were used to formulate the likelihood ratio at each surveyed location. It is proven that for single channel EMI sensor data from a single location a threshold test on the raw data is the optimal processor, even when the decay rates for target and clutter are not deterministic parameters [26] in Sec. 3.2.3.1. It is also shown in Sec. 3.2.3.2 that the performance of the two detection approaches were the same experimentally and theoretically for multi-channel sensor data [65, 66]. In addition, the 1-D GLRT has been shown to improve performance dramatically over the performance achieved with the standard tests on multi-channel sensor data.

In this section, a statistical approach incorporating both the underlying physics of EMI sensors [14, 22, 21, 13, 19] and statistical signal processing theory [55], in

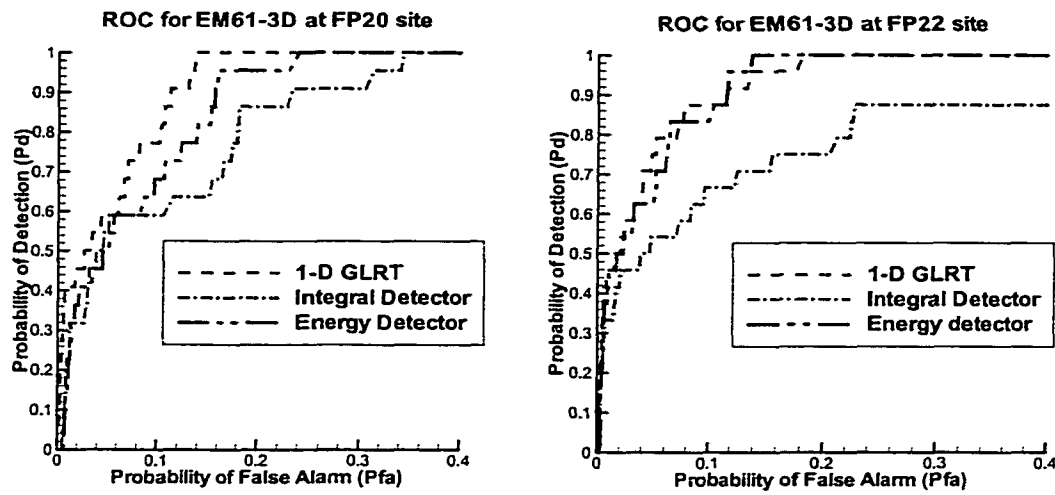


Figure 3.18: Comparison of the performance of 1-D GLRT and other processors for EM61-3D data @ Fort A.P. Hill FP20 and FP22 sites

which the statistics of local data surrounding the location under test are utilized, is presented. Since the minefields are sampled spatially, *i.e.* the sensor head is moved throughout the candidate area, it is hypothesized that the accuracy of the mine detectors would be improved when spatial information is incorporated into processor. The results demonstrate that this hypothesis is valid.

3.4.1 Detector Design - 2-Dimensional Likelihood Ratio Test

Generally, it can be assumed that data can be obtained at sample points which are laid out as a rectangular mesh as illustrated in Figure 3.20. The goal is to make a decision on whether there is a mine present at the center location, X . The data that is available consists of the outputs from the sensor both at the center location and the surrounding locations. Three possible situations can occur:

- (i) there is a mine buried under the center location; or
- (ii) there is nothing buried in this area; or

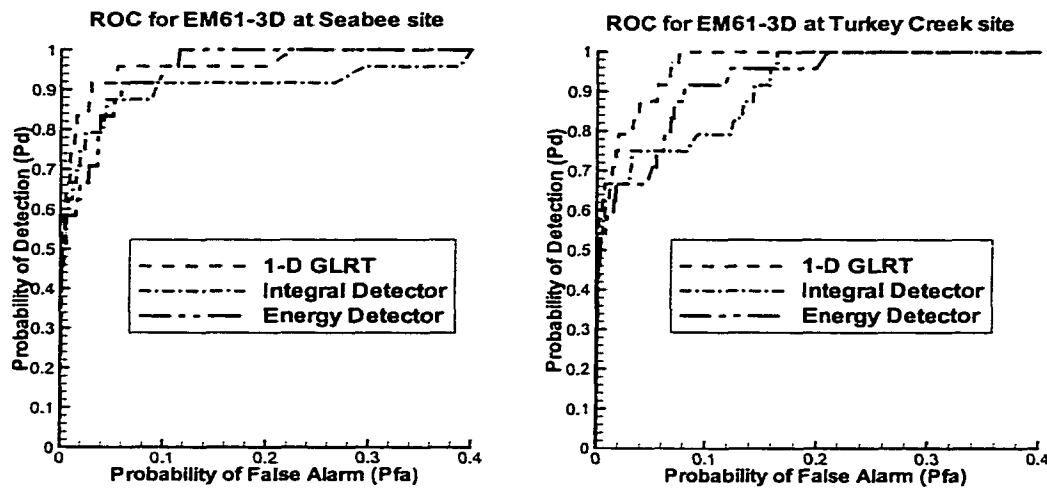


Figure 3.19: Comparison of the performance of 1-D GLRT and other processors for EM61-3D data @ Fort Carson Seabee and Turkey Creek sites

(iii) there is clutter located in this area.

N1	N2	N3
N8	X	N4
N7	N6	NS

Figure 3.20: Schematic of data placement and data available for a testing location

The fourth possibility is both a mine and clutter (potentially at different depths) are present at the location under test. This scenario is treated as situation (i) in this work. Since an EMI sensor is essentially a metal detector, when an object which contains metal is present the sensor will record an induced response due to the object, in addition to background noise. In situation (i), because of the presence of a mine, the sensor response at the surrounding locations may also include a response due to the mine, *i.e.* part of the response may induced by the mine. As the sensor head is

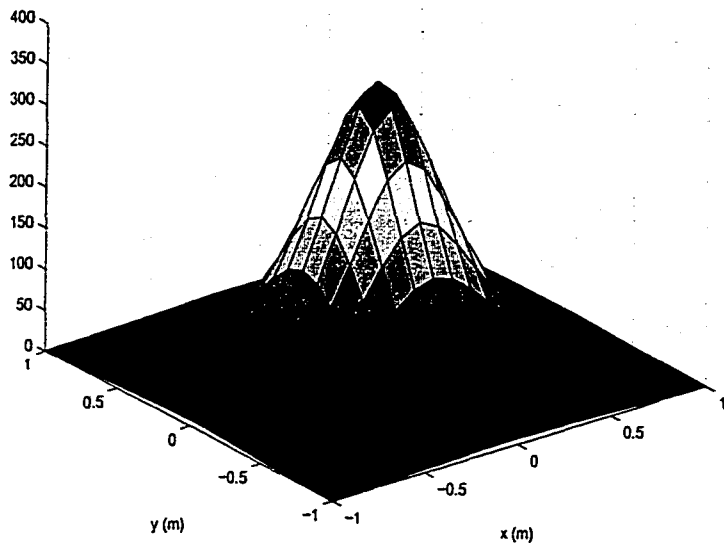


Figure 3.21: Theoretical prediction of EM61 response from a metal object with an aspect ratio of 0.5 at a depth of 0.5m

moved further and further away from the center point, the effect will vanish. Figure 3.21 is a plot of the theoretical prediction of the EM61 sensor response from a metal object with length to diameter aspect ratio of 0.5 at a depth of 0.5 m. The response is plotted over a 2 m by 2 m area. The prediction is obtained using a EMI model based on a dipole approximation of the object (in free space) with the dimension of the Geonics EM61 sensor and with the object parallel to the ground. The overall level of the response shown in Figure 3.21 varies depending on the strength of the sensor excitation. For situation (ii), the EMI sensor will only record background noise, and for situation (iii) the response from the position under test might be strong and the response at the surrounding locations might also be disturbed by the clutter response depending on the size and shape of the clutter.

To approach this detection problem statistically, two hypotheses are again made. H_1 is the hypothesis that a target (a mine or UXO) is present at the location under test; and H_0 is the hypothesis that a target is not present, *i.e.*, either clutter or background alone is present. The likelihood ratio test for a single sensor response, or location, is defined as Equation (3.52) [55].

In this section, it is hypothesized that for the land mine and small UXO detection problem the statistics of the sensor response obtained from the locations surrounding a test position may be a function of whether a target is present or not. This dependence will be a function of the target and sensor size, the data sampling grid, *etc.* Based on measured land mine, small UXO and clutter field data from EMI sensors, this hypothesis appears to be valid. Therefore, performance should improve when the information in the neighborhood of the test position is included in the decision process. Hence, a 2-D GLRT detector is developed, which incorporates not only the sensor response at the location under test, but also those obtained from the vicinity of the location under test. A GLRT, as opposed to a LRT, was used since parameters of the probability density functions describing the data are not known exactly and no reliable prior knowledge on these parameters are available. Thus, we chose to estimate the parameters based on training data in order to implement a GLRT.

In Sec. 3.2.3.1, it is shown that for a single channel EMI sensor (for instance, the Geonics EM61) the optimum decision statistic at the point by point level is the received signal from the sensor. This decision statistic is equivalent to the one-dimensional LRT, and it can also be shown [66] that for multi-channel EMI data the one-dimensional LRT is equivalent to the 1-D GLRT under some practical assumptions in Sec. 3.2.3.2. Hence, fusing data from the 1-D LRT/GLRT at various

locations as opposed to using the sensor output or energy level, should result in a further improvement in performance.

Based on the above argument, the input, x , of the 2-D GLRT was chosen to be the output from the one-dimensional LRT at each of the spatial positions. For the single channel time-domain EMI sensor, this is the raw data from the sensor since the single location optimal detector reduces to a threshold test on the raw data as shown in [26, 65]. Since we have assumed that the sensor is subject to Gaussian noise, x is a Gaussian rv. For the multi-channel EMI sensor, the data considered for the 2-D GLRT is the output of the 1-D GLRT. The 1-D GLRT is a simple version of the 1-D LRT which avoids extensive computation and provides the same performance to that of the 1-D LRT under a set of assumptions [66]. The 1-D GLRT is a matched filter-like processor. The output of the 1-D GLRT is the summation of N non-central Chi-square random variables [67] ($N = 20$), and thus, can be approximated as a Gaussian rv based on the Central Limit Theorem.

In the formulation of the 2-D GLRT, two physical properties of the input, x , are explored sequentially. The first property is the spatial change in x across a local area; the second property is the relative size of the center point compared to its neighbors. In fact, this cascade of two generalized likelihood ratio tests is first testing the mine *vs.* background hypothesis, and then testing the mine *vs.* clutter hypothesis.

Because of the small size of the target (between 10 cm and 20 cm) and the sensor dimensions of 1 m (EM61-3D) or 0.5 m (EM61), it was hypothesized that the target would only influence the response at nearby neighbors (within 1 m of the center of a target) [28]. Furthermore, since the input of the 2-D GLRT, x , is the likelihood

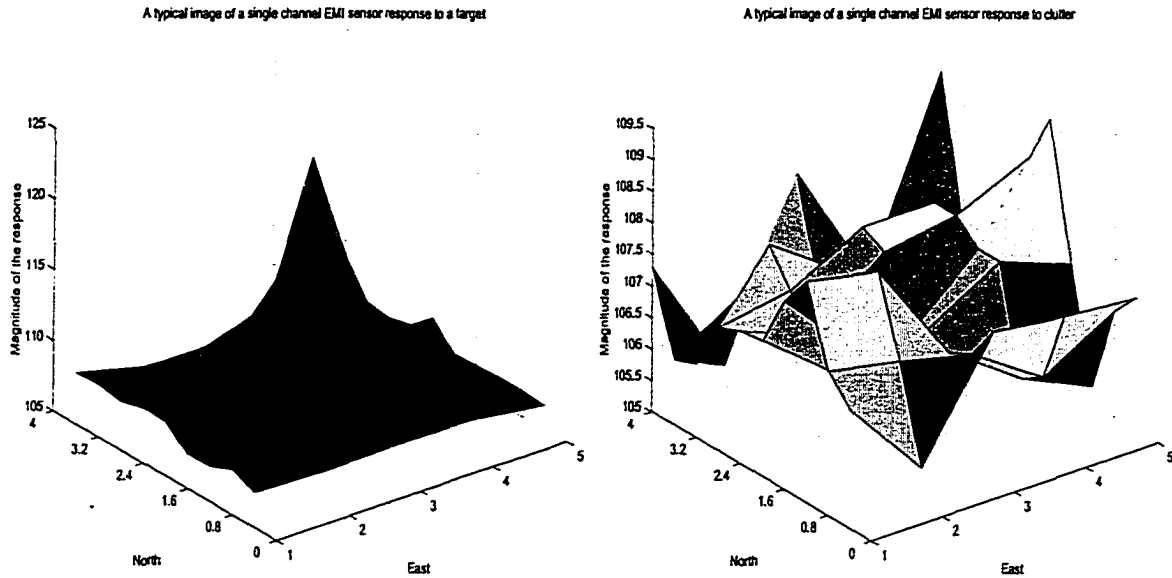


Figure 3.22: Typical spatial response patterns of both mine/UXO and clutter/noise from single channel EMI sensor data

ratio, its value at a “target present” location will theoretically be larger than those at the neighboring locations which are assumed not to contain targets. Hence, when the center location contains a target, which is often symmetric, the spatial pattern of x will resemble a “peaked” or hill shape, which has maximum value at the center location, and the value decreases from the center in all directions at an approximately equal rate (also see Figure 3.21). If there is no metal located at the test area (background only case), the spatial pattern of x will be a spatial Gaussian field (assuming the sensor is subject to white Gaussian noise). For clutter, this spatial pattern will have no predictable pattern; it will depend on the clutter type, shape, size, amount of metal, *etc.* It might appear as a symmetric hill pattern, but can follow other shapes as well (*e.g.* asymmetric). Examples of these patterns from experimental data for target and no-target are shown in Figures 3.22 and 3.23.

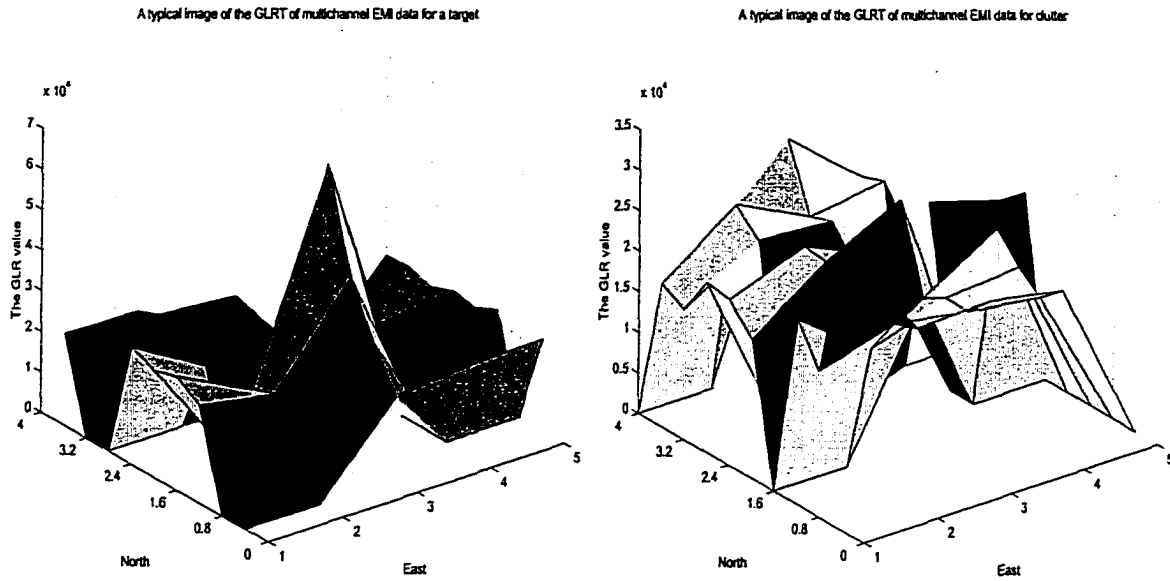


Figure 3.23: Typical spatial patterns of both mine/UXO and clutter/noise based on the 1-D GLR of multi-channel EMI sensor data

The second physical characteristic of a targets is that the absolute value of x for the target is substantially higher than those of its neighbors, and also that of the clutter across the whole area. For example, a 50 gallon drum will not be considered as a target by the 2-D GLRT detector because even though the spatial pattern somewhat follows a symmetric hill shape, the rate of fall-off of x is not as fast as that for land mines or small UXO across the 2 m by 2 m area.

Therefore, to incorporate the two phenomenologies described above, the 2-D GLRT is formulated as a cascade of two GLRTs, each of which exploits one the two previously described properties. The first GLRT primarily tests situation (i) that is a target buried at the center of the testing area *vs.* situation (ii) that is nothing buried in the testing area, which effectively rejects noise and some of the clutter classes (very small items). The second GLRT tests situation (i) *vs.* situation (iii), which is clutter present case, to eliminate additional clutter whose spatial pattern

appears to be a symmetric hill shape. Thus, the 2-D GLRT detector uses a cascade of two GLRTs formulated as follows.

3.4.1.1 Processing Stage 1

The first processing stage exploits the fact that the one-dimensional GLR data within a local area satisfies the symmetric hill pattern when a target is present. In order to achieve this goal, a new variable, \mathbf{d} , is formed as a vector of the differences between the input x at the center location and those values at the surrounding locations. Based on the sample speed and sensor size during experimental data acquisition, the grid size of data was chosen to be 1 m by 0.4 m, thus 10 surrounding locations are within 1 m (also the size of the bigger sensor, EM61-3D) of the center location, as illustrated in Figure 3.24. Hence, the vector of normalized differences from the center location, \mathbf{d} , is a 10 by 1 vector. Each element of \mathbf{d} is defined by:

$$d_i = \frac{x_c - x_i}{x_c} = 1 - \frac{x_i}{x_c} \quad (3.57)$$

where $i = 1, 2, \dots, 10$, x_c is the one-dimensional GLR value at the center location, x_i is the GLR value at i^{th} location as defined in Figure 3.24.

Based on the statistics derived above and the Central Limit Theorem, we have assumed that x is a Gaussian rv. In [68] and [69], the mathematical form of the distribution of the ratio of two Gaussian random variables is derived. If $x_1 \sim \mathcal{N}(\mu_1, \sigma_1^2)$ and $x_2 \sim \mathcal{N}(\mu_2, \sigma_2^2)$, the correlation coefficient between x_1 and x_2 is ρ , and $v = \frac{x_1}{x_2}$, then the pdf of v is

$$f(v) = \frac{1}{\pi} \frac{\sigma_1 \sigma_2 \sqrt{1 - \rho^2}}{\sigma_1^2 - 2\rho v \sigma_1 \sigma_2 + v^2 \sigma_2^2} \exp \left[-\frac{1}{2} \frac{1}{1 - \rho^2} \left(\frac{\mu_2^2}{\sigma_2^2} - 2\rho \frac{\mu_1 \mu_2}{\sigma_1 \sigma_2} + \frac{\mu_1^2}{\sigma_1^2} \right) \right]$$

	X7	
X1	X6	X8
X2	Center	X9
X3	X5	X10
	X4	

Figure 3.24: The neighborhood locations used when calculating generalized likelihood ratio 1 and 2

$$\begin{aligned}
 & + \frac{\sigma_1(\rho\mu_1\sigma_2 - \mu_2\sigma_1) + v\sigma_2(\rho\mu_2\sigma_1 - \mu_1\sigma_2)}{\pi(\sigma_1^2 - 2\rho v\sigma_1\sigma_2 + v^2\sigma_2^2)^{3/2}} \exp\left[-\frac{1}{2} \frac{(\mu_1 - v\mu_2)^2}{\sigma_1^2 - 2\rho v\sigma_1\sigma_2 + v^2\sigma_2^2}\right] \\
 & \times \int_0^{\frac{\sigma_1(\rho\mu_1\sigma_2 - \mu_2\sigma_1) + v\sigma_2(\rho\mu_2\sigma_1 - \mu_1\sigma_2)}{\sigma_1\sigma_2((1-\rho^2)(\sigma_1^2 - 2\rho v\sigma_1\sigma_2 + v^2\sigma_2^2))^{1/2}}} \exp\left[-\frac{1}{2}u^2\right] du
 \end{aligned} \tag{3.58}$$

In this problem, the two random variables (x_c and x_i) are assumed to be independent since noise is independent and identically distributed, thus, $\rho = 0$. Also, the variances of x_c and x_i are assumed to be equal, *i.e.* σ^2 . Therefore, the pdf simplifies to

$$\begin{aligned}
 f(v) &= \frac{1}{\pi(1+v^2)} \exp\left(-\frac{\mu_1^2 + \mu_2^2}{2\sigma^2}\right) + \frac{\mu_2 + \mu_1 v}{\pi\sigma(1+v^2)^{3/2}} \\
 &\times \exp\left[-\frac{(\mu_1 - \mu_2 v)^2}{2\sigma^2(1+v^2)}\right] \times \int_0^{\frac{\mu_2 + \mu_1 v}{\sigma(1+v^2)^{1/2}}} \exp\left[-\frac{1}{2}u^2\right] du
 \end{aligned} \tag{3.59}$$

In [69], the detailed analytical error analysis is provided. Here, we show examples of a comparison of the accurate pdf and Gaussian approximation using estimates of μ_1 , μ_2 and σ that were obtained from the calibration area data. Figures 3.25 and 3.26 provide such comparisons for H_1 and H_0 case, respectively. Clearly, for this problem, a Gaussian approximation to the pdf is acceptable. Thus, we assumed the

distribution of \mathbf{d} is a multivariate Gaussian. Under H_1 :

$$\mathbf{d}|H_1 \sim \mathcal{N}_{10}(\mu_{\mathbf{d}_1}, \Sigma_{\mathbf{d}_1}) \quad (3.60)$$

Under H_0 :

$$\mathbf{d}|H_0 \sim \mathcal{N}_{10}(\mu_{\mathbf{d}_0}, \Sigma_{\mathbf{d}_0}) \quad (3.61)$$

where \mathcal{N}_{10} represents 10-dimensional Gaussian distribution, $\mu_{\mathbf{d}_1}$ and $\mu_{\mathbf{d}_0}$ are the mean vectors, and $\Sigma_{\mathbf{d}_1}$ and $\Sigma_{\mathbf{d}_0}$ are the covariance matrices of \mathbf{d} under H_1 and H_0 , respectively. The sample means, $\hat{\mu}_{\mathbf{d}_1}$ and $\hat{\mu}_{\mathbf{d}_0}$, and the sample covariance matrices, $\hat{\Sigma}_{\mathbf{d}_1}$ and $\hat{\Sigma}_{\mathbf{d}_0}$, were calculated using the calibration area data (see Sec. 2.2.3), and then used as the estimated values of the true means and covariance matrices when calculating GLRs. The elements of the \mathbf{d} 's are not independent, especially under the H_1 hypothesis. The correlations between the elements are represented by the covariance matrix. This correlation provides an added incentive to utilize the Gaussian formulation for the GLRT as opposed to assuming independence of the elements of \mathbf{d} and using Equation (3.59).

Therefore, under these assumptions the decision statistic of the first processing stage has the form:

$$\begin{aligned} \Omega_1(\mathbf{d}) &= \frac{p(\mathbf{d}|H_1, \hat{\mu}_{\mathbf{d}_1}, \hat{\Sigma}_{\mathbf{d}_1})}{p(\mathbf{d}|H_0, \hat{\mu}_{\mathbf{d}_0}, \hat{\Sigma}_{\mathbf{d}_0})} \\ &= \frac{\frac{1}{(2\pi)^5 |\hat{\Sigma}_{\mathbf{d}_1}|^{1/2}} e^{-\frac{1}{2}(\mathbf{d}-\hat{\mu}_{\mathbf{d}_1})^T \hat{\Sigma}_{\mathbf{d}_1}^{-1} (\mathbf{d}-\hat{\mu}_{\mathbf{d}_1})}}{\frac{1}{(2\pi)^5 |\hat{\Sigma}_{\mathbf{d}_0}|^{1/2}} e^{-\frac{1}{2}(\mathbf{d}-\hat{\mu}_{\mathbf{d}_0})^T \hat{\Sigma}_{\mathbf{d}_0}^{-1} (\mathbf{d}-\hat{\mu}_{\mathbf{d}_0})}} \end{aligned} \quad (3.62)$$

By taking the logarithm of Equation (3.62) and incorporating the constant terms into the threshold [55], the log generalized likelihood ratio simplifies to:

$$\Omega_1(\mathbf{d}) = -(\mathbf{d} - \hat{\mu}_{\mathbf{d}_1})^T \hat{\Sigma}_{\mathbf{d}_1}^{-1} (\mathbf{d} - \hat{\mu}_{\mathbf{d}_1}) + (\mathbf{d} - \hat{\mu}_{\mathbf{d}_0})^T \hat{\Sigma}_{\mathbf{d}_0}^{-1} (\mathbf{d} - \hat{\mu}_{\mathbf{d}_0}) \quad (3.63)$$

Since a logarithm is a monotonic increasing function, transformation from the original values to logarithmic values does not change the order of the corresponding values, and the resulting performance remains unchanged.

Figure 3.27 illustrates the performance of the first processing stage evaluated on synthetic spatial data using the exact pdf of \mathbf{d} and the Gaussian approximation. Similar performance is achieved when evaluating Ω_1 using Equation (3.62) by substituting the corresponding parameters, or using Equation (3.63), which assumes Gaussian distributed rv's.

3.4.1.2 Processing Stage 2

The generalized likelihood ratio used in the second processing stage is formulated to exploit the second property of the physical nature of the data mentioned above. Another vector, \mathbf{y} , is formed as:

$$\mathbf{y} = [x_c \quad \frac{x_c - m(\mathbf{x}_n)}{x_c}]^T \quad (3.64)$$

where x_c is the value of the one-dimensional GLR at the center location as before, \mathbf{x}_n is a 10 by 1 vector which consists of the values of the one-dimensional GLR at the neighborhood locations around the center location as illustrated in Figure 3.24, and $m(\mathbf{x}_n)$ is the mean value of \mathbf{x}_n . The first element of \mathbf{y} is the original x value at the center location. The statistics of x_c partially represent the likelihood of target present at that location since the x 's are obtained from the one-dimensional LR, which is the best decision statistic at the single point by point level. The second element of \mathbf{y} models the relative size of the center location compared to the locations surrounding it. For targets, this value should be greater than for clutter.

Under the bivariate Gaussian distribution assumption, which was chosen for similar reasons as in the formulation of the generalized likelihood ratio at the first stage, the log generalized likelihood ratio was formulated as:

$$\Omega_2 = -(\mathbf{y} - \hat{\mu}_{\mathbf{y}_1})^T \hat{\Sigma}_{\mathbf{y}_1}^{-1} (\mathbf{y} - \hat{\mu}_{\mathbf{y}_1}) + (\mathbf{y} - \hat{\mu}_{\mathbf{y}_0})^T \hat{\Sigma}_{\mathbf{y}_0}^{-1} (\mathbf{y} - \hat{\mu}_{\mathbf{y}_0}) \quad (3.65)$$

where $\mu_{\mathbf{y}_1}$ and $\mu_{\mathbf{y}_0}$ are the means, and $\Sigma_{\mathbf{y}_1}$ and $\Sigma_{\mathbf{y}_0}$ are the covariance matrices of \mathbf{y} under H_1 and H_0 , respectively. Again, the estimated values, $\hat{\mu}_{\mathbf{y}_1}$, $\hat{\mu}_{\mathbf{y}_0}$, $\hat{\Sigma}_{\mathbf{y}_1}$ and $\hat{\Sigma}_{\mathbf{y}_0}$, were sample means and sample covariance matrices obtained from the data in the calibration area (see Sec. 2.2.3).

3.4.1.3 Cascade of the Two Generalized Likelihood Ratios to Make a Decision

The two generalized likelihood ratios described above exploit the two physical properties of the target and clutter respectively. The overall 2-D GLRT was implemented by cascading the two individual GLRTs by:

- First eliminating the locations at which generalized likelihood ratio 1 is less than its threshold, β_1 .
- Then calculating generalized likelihood ratio 2 for the remaining locations, the final decision is made by comparing generalized likelihood ratio 2 to its threshold, β_2 .

In the first stage, those locations which do not have a symmetric hill pattern indicative of targets are classified as clutter or noise. Then, the second GLRT is applied to further confirm the decision, and the locations which do not satisfy the second statistical model are discarded from H_1 hypothesis. The choice of β_1 and β_2 determines

the performance of the detector. If the threshold, β_1 , of GLR 1 is chosen to detect all the targets, *i.e.* set equal to the minimum value of mine data in calibration area, β_2 will dominate the probability of detection, on the other hand, if β_2 is chosen to detect all mines, P_d will depend on the value of β_1 . The probability of false alarm for the sequential application of both GLRTs is smaller than that of either one of these two GLRTs performed alone. In this analysis, we use the minimum value of GLR 1 corresponding to mine-present hypothesis of each site as the β_1 value, then vary β_2 from its minimum to maximum value to generate an ROC curve. The values of β_1 and β_2 required to achieve the same performance (same P_d and P_{fa}) are different from site to site because the signature for targets at different sites is not the same. This procedure is similar to sensor fusion, the only difference is that here we fuse GLR 1 with GLR 2 only for locations where GLR 1 gives H_1 .

3.4.2 Results

The data used to analyze the detection strategies were collected during the *DARPA Backgrounds Clutter Data Collection Experiment* [38] at four sites at two U.S. locations, Fort Carson, Colorado and Fort A. P. Hill, Virginia. The raw data were first divided into an appropriate raster based on the spatial separation of survey lines and the sampling rate of the sensors, and then all the responses collected in each grid were averaged.

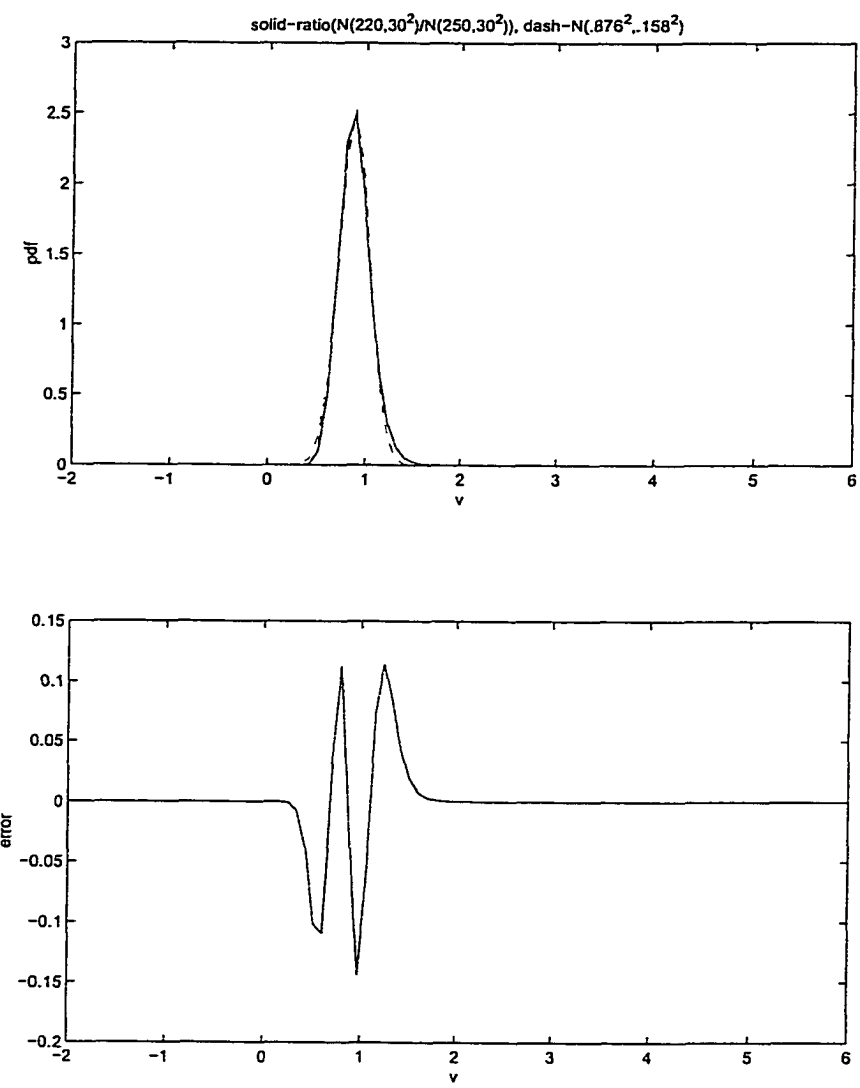


Figure 3.25: (Top) Probability density functions for the ratio of two Gaussian rv's. and a Gaussian approximation for a target present (H_1) case. (Bottom) Error between two pdf's shown in the top figure.

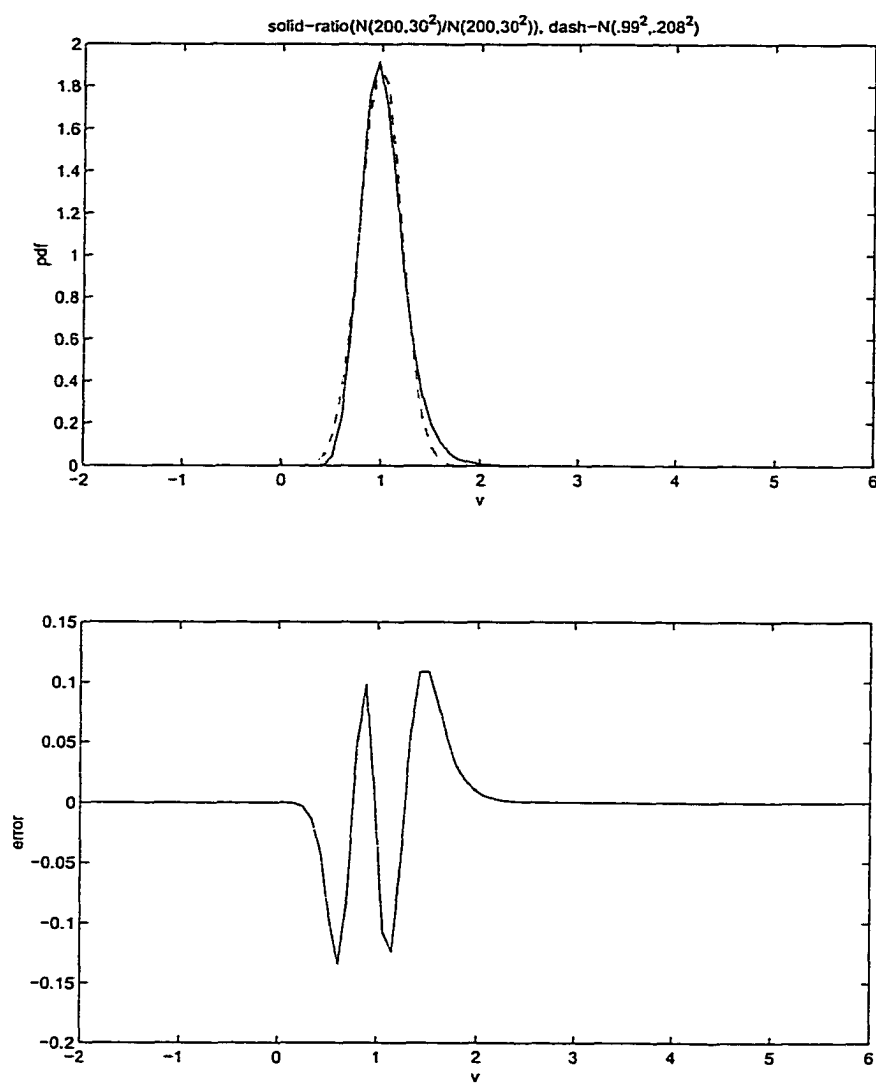


Figure 3.26: (Top) Probability density functions for the ratio of two Gaussian rv's. and a Gaussian approximation for a target not present (H_0) case. (Bottom) Error between two pdf's shown in the top figure.

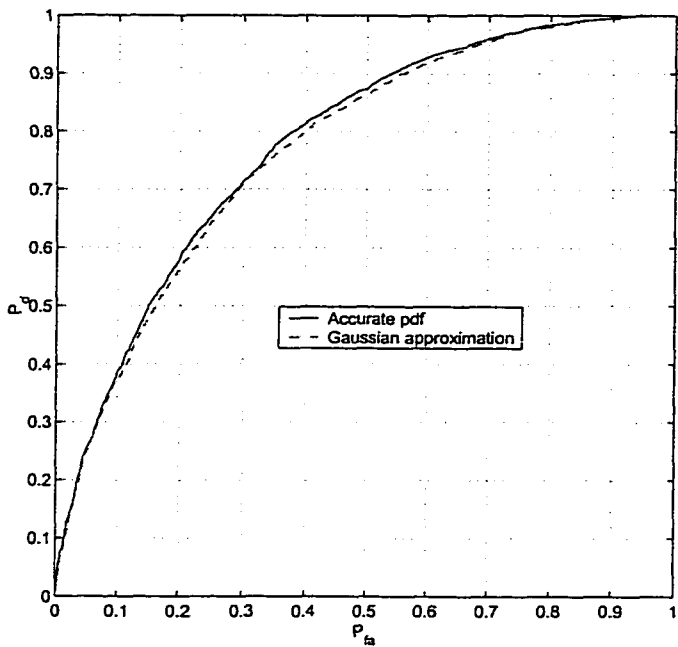


Figure 3.27: A comparison of performance of the first stage processing using synthetic data based on the exact pdf of d and the Gaussian approximation.

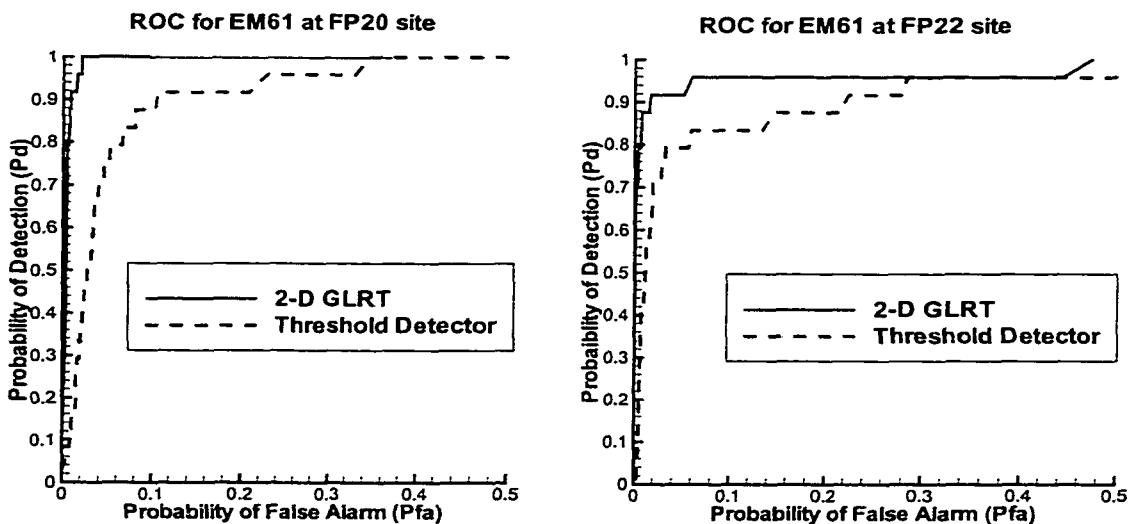


Figure 3.28: ROC of different detectors based on EM61 data at Fort A.P. Hill FP20 and FP22 sites. The left one is corresponding to Ft. A. P. Hill FP20 site, the right one is corresponding to FP22 site. Solid line = 2-D GLRT detector performance; dashed line = performance of standard threshold detector on the received data from EM61 sensor.

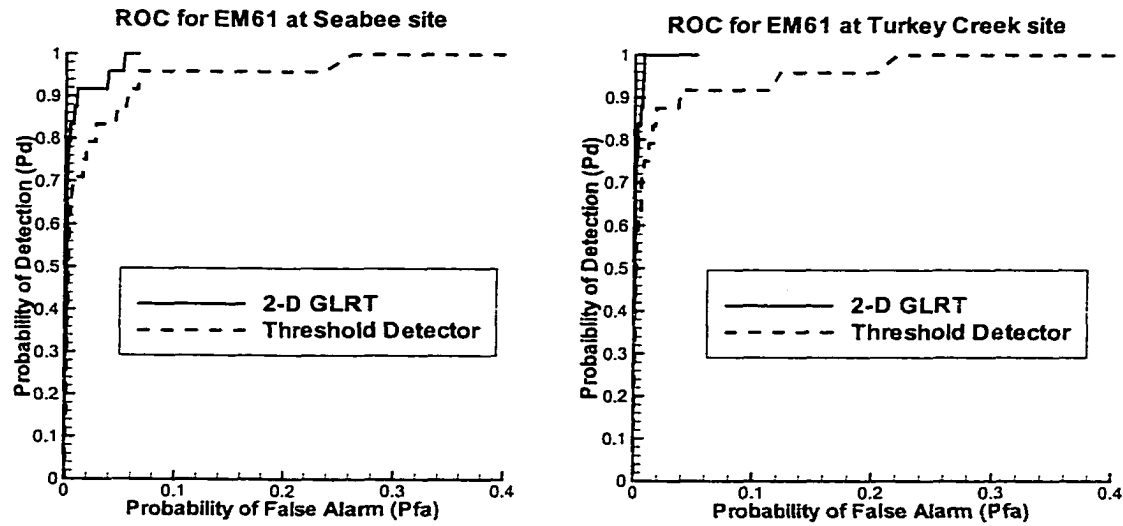


Figure 3.29: ROC of different detectors based on EM61 data at Fort Carson Seabee and Turkey Creek sites. The left one is corresponding to Ft. Carson Seabee site, the right one is corresponding to Turkey Creek site. Solid line = 2-D GLRT detector performance; dashed line = performance of standard threshold detector on the received data from EM61 sensor.

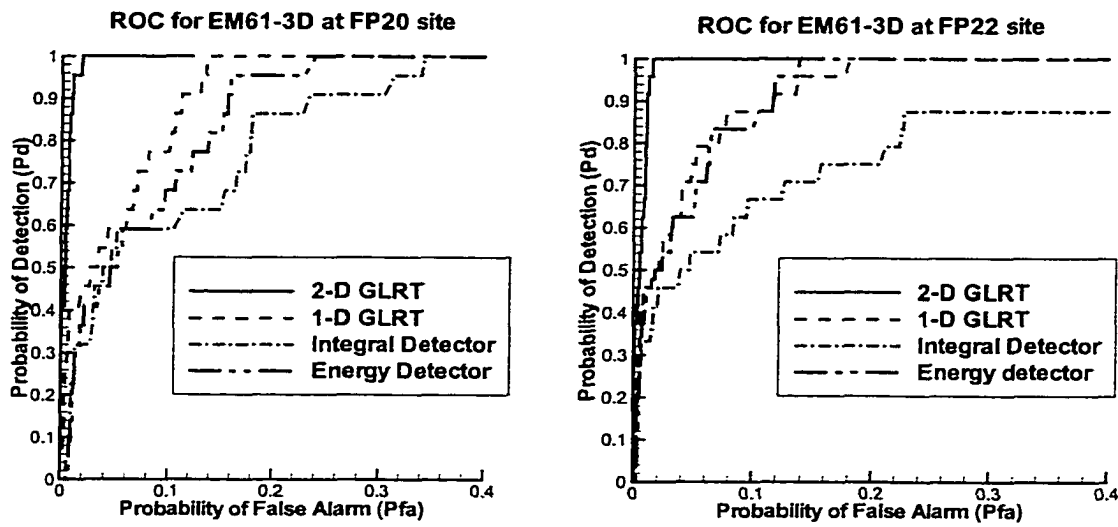


Figure 3.30: ROC of different detectors based on EM61-3D data at Fort A.P. Hill FP20 and FP22 sites. The left one is corresponding to Ft. A.P. Hill FP20 site, the right one is corresponding to FP22 site. Solid line = 2-D GLRT detector performance; dashed line = 1-D GLRT performance; dashed-dotted line = integral detector performance; dash-dot-dot line = energy detector performance.

The standard quantitative tool to evaluate performance of a detection algorithm is an ROC, which is a plot of probability of detection *vs.* probability of false alarm. The performance of each of the detection strategies is shown in terms of an ROC. Figures 3.28 and 3.29 illustrate that the 10-location 2-D GLRT detector operating on the Geonics EM61 sensor data provides a substantial improvement in performance, compared to the standard threshold test at all four sites. In [26, 65], it is shown that the threshold test is the single location optimal detector for the integrated time-domain EMI sensors, thus no separate single location LRT performance is shown.

The improvements of the 2-D GLRT on Geonics EM61-3D sensor data, compared to the standard energy detector, the integral detector, and the one-dimensional GLRT, are demonstrated in Figures 3.30 and 3.31.

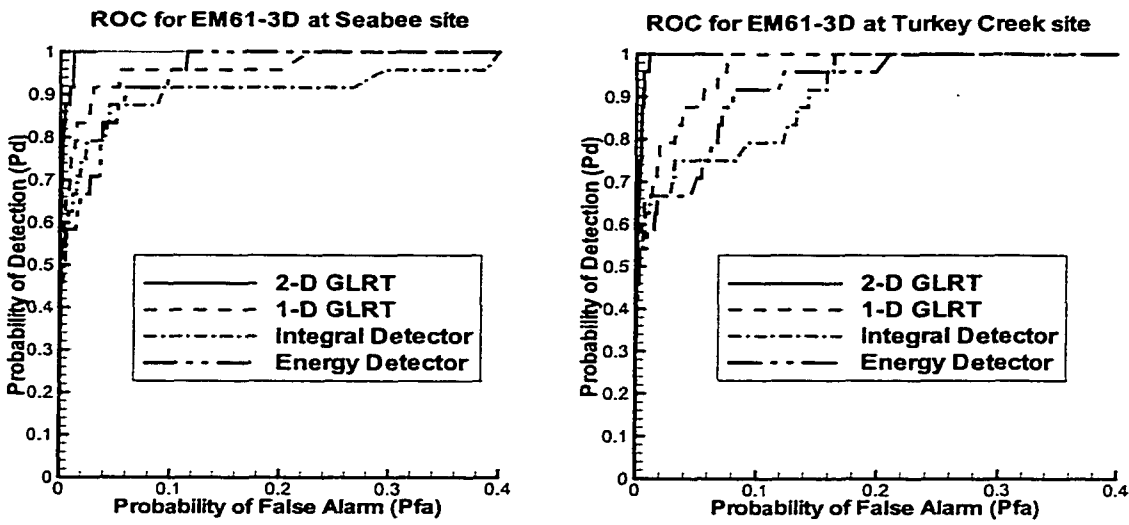


Figure 3.31: ROC of different detectors based on EM61-3D data at Fort Carson Turkey Creek and Seabee sites. The left one is corresponding to Ft. Carson Seabee site, the right one is corresponding to Turkey Creek site. Solid line = 2-D GLRT detector performance; dashed line = 1-D GLRT performance; dashed-dotted line = integral detector performance; dash-dot-dot line = energy detector performance.

Table 3.3 lists the actual threshold values used for β_1 for the first processing stage of the 2-D GLRT for all four test sites and two types of sensors. In Tables 3.4 and 3.5, the values of P_{fa} corresponding to P_d equal to 0.95 for various detection approaches are shown. Clearly, the improvement of 2-D GLRT is dramatic. The performance of the δ -technique is also shown in the tables. The decision rule was: if $m \geq 7$, H_1 is true; otherwise, H_0 is true, where m is the number of neighbors which have a smaller energy than that of the center location. The parameter m can be any integer from 1 to 8. Among these values, 8 can provide lowest P_{fa} ; however, the trade-off is that at this value P_d does not usually achieve 100% since there are always some mines which have 1 or 2 neighbors which have higher energy than the center location due to noise. Therefore, 7 was used to obtain the results shown in the tables. It is clear that δ -technique can provide better detection performance than the standard detection methods, but the 2-D GLRT outperforms these alternative detection tech-

niques. The 1-D GLRT performs better than a standard energy or integral test, and an energy detector is generally better than an integral detector. These results are consistent with the theoretical analysis of the performance of these detectors provided in [66].

Site	EM61	EM61-3D
FP20	-13.51	-2.23
FP22	-30.64	-3.00
Seabee	-1.08	-17.23
Turkey Creek	-1.70	-3.47

Table 3.3: Threshold values used for the first step process, β_1 , for all four test sites and two types of sensors, EM61 and EM61-3D sensor

Site	1-D LRT/GLRT	δ -technique ($m \geq 7$)	2-D GLRT
FP20	0.22	0.098	0.016
FP22	0.28	(cannot achieve $P_d=0.95$)	0.059
Seabee	0.066	0.038	0.038
Turkey Creek	0.12	0.048	0.0066

Table 3.4: P_{fa} value when $P_d = 0.95$ for EM61 sensor

Site	Integral x Detector	Energy Detector	1-D LRT/ 1-D GLRT	δ -technique ($m \geq 7$)	2-D GLRT
FP20	0.313	0.16	0.125	0.1	0.013
FP22	0.55	0.18	0.27	0.108	0.014
Seabee	0.287	0.099	0.057	0.047	0.016
Turkey Creek	0.158	0.12	0.086	0.059	0.008

Table 3.5: P_{fa} value when $P_d = 0.95$ for EM61-3D sensor

3.4.3 Summary

The above results indicate that the 2-D GLRT processor can significantly reduce false alarm rates in land mine and small UXO detection scenarios using EMI sensor data.

The performance improvement obtained for both multi-channel time-domain and single channel integrated time-domain EMI data were evaluated at four test sites, and were consistently high across all sites, even at the most highly cluttered Fort A.P. Hill FP20 site. This improvement occurs because the processor may correctly model some of the physical, statistical, and spatial properties of the output of EMI sensors.

Comparing the performance of different time-domain EMI sensors, single channel and multi-channel sensors, the multi-channel sensors provide slightly better performance. Even though the improvement is not significant at this point (because the multi-channel (EM61-3D) EMI is still a prototype sensor under development and the noise level at the receiving coil is high compared to the standard metal detector), it is believed that utilizing a time-domain waveform allows greater exploitation of the phenomenology embedded in the signatures.

For the multi-channel data, an energy detector provides better performance than an integral detector. This can be explained theoretically. At each time gate the noise that receiver is subject to is independent and identically distributed. Therefore, at lower signal levels, the SNR is less than that at higher signal levels. When applying the same weight to each channel and summing up all channels, (*i.e.* an integral detector), the influence of noise on the low-level signal is highlighted. The energy detector, however, assigns greater weight to the higher-level portions of the signal and less weight to the lower-level portions of the signal (squaring is not a linear, but a quadratic function). Thus, the noise present on the low-level signal will not interfere with the decision as much as it does for the integral detector.

Tables 3.4 and 3.5 list the performance of different detectors quantitatively. The

reduction of P_{fa} for a fixed $P_d = 0.95$ realized by using the 2-D GLRT is at least a factor of 2. For highly cluttered sites, or noisy data, this factor can be as high as 20 over the standard test; a dramatic improvement. This demonstrates that the 2-D GLRT is robust in a noisy environment. The performance of another spatially-based detection strategy, called δ -technique, was also evaluated. This approach is easy to implement and does improve performance over non-spatial algorithms, but the 2-D GLRT provides better performance.

The mean and covariance matrices of the vectors \mathbf{d} and \mathbf{y} defined in Sec. 3.4.1 and 3.4.2 vary across sites. Because close sites provide similar results for the estimated mean and variance, these variations might be caused by the geological differences between the test sites. The concentration of clutter also affects the variance of the data. To obtain such *a priori* knowledge before remediating an area at a particular site, one solution might be to take a sub-area close to the site as a calibration area to obtain the statistics of this site, then use these statistics to implement a 2-D GLRT. Another solution might be to find the parameters that affect those statistics and apply Bayesian analysis by assuming proper priors to obtain best estimates of those parameters or integrate over all the uncertain parameters.

Chapter 4

Analyses of Frequency-Domain EMI Data

In this chapter, the frequency-domain (FD) electromagnetic induction (EMI) work is summarized. In Sec. 4.1, detection performance of low-metal mines on a blind site at Fort A. P. Hill, VA. using FD EMI data is discussed; in Sec. 4.2, classification performance of metallic objects is provided using a Bayesian classification algorithm and the standard approach, evaluated by both simulated and experimental data.

4.1 Broadband FD EMI Signatures and Detection of Low-Metal Landmines

4.1.1 Introduction

Historically, electromagnetic induction (EMI) sensors have been used extensively to locate buried landmines and unexploded ordnance (UXO) by detecting the metal present in such targets. However, landmines vary in their construction from metal-cased varieties with a large mass of metal to plastic-cased varieties with minute amounts of metal. Unfortunately, there is often a significant amount of metallic debris (clutter) present in the environment. Consequently, EMI sensors that utilize traditional detection algorithms based solely on the metal content suffer from high false alarm rates. In order to reduce false alarms, we have developed successful techniques for time-domain (TD) EMI data for discriminating between mines and anthropic clutter using a statistical signal processing approach based on signal detec-

tion theory [26]. The improved performance provided by these algorithms has been validated using data obtained during the *DARPA background clutter data collection experiment* [38]. The metal content of the target set in the *DARPA* experiment was fairly high, however, and the number of targets was limited.

The Joint UXO Coordination Office (JUXOCO) located at Fort Belvoir, VA. is sponsoring a series of experiments designed to establish a performance baseline for a variety of sensors [70, 71]. The experimental design is focused primarily on low metal content mines. This baseline will be used to measure the potential improvements in performance offered by advanced signal processing algorithms. In conjunction with this effort, data from low-metal content mines and clutter has been gathered using a variety of sensors. As mentioned above, traditional EMI sensors, which operate in the time-domain, suffer from large false alarm rates. There have been some research efforts focusing on modifying EMI sensors in order to mitigate false alarms for landmine detection and other applications [14, 13, 20, 72, 24, 73, 74]. One promising approach is to operate the EMI sensor in frequency-domain utilizing wideband excitation. Thus, we chose to use a prototype broadband frequency-domain EMI sensor, the GEM-3 developed by Geophex Ltd. [17] during these experiments. A series of algorithms in order to evaluate performance for the GEM-3 sensor on real landmines are implemented.

In this section, results from a series of experiments are described. First, we investigate whether burying a low metal mine in soil changes the signature measured by the GEM-3 (Sec. 4.1.2). The statistical properties of the noise process associated with the GEM-3 were also investigated. In the second and third experiment, the GEM-3 was used to gather data at a prototype test site located at Fort A. P. Hill in

Virginia in the calibration area and main test grid, respectively. Ground truth data has been published for the calibration area, but not for the main test area. The data collection paradigm is discussed, as well as the mechanisms by which sensor drift (*i.e.* the instability of the sensor noise process) problems were mitigated. Finally, the detection algorithms that were developed are described and their performance (scored by JUXOCO) is presented and discussed in Sec. 4.1.4.2.

4.1.2 Experiment 1: Investigating the Statistical Properties and the Effects of Soil on Measured GEM-3 Signatures

4.1.2.1 Goals

The main goal for this preliminary experiment was to use the GEM-3 sensor to collect digital, multi-frequency signals from mines in free space and mines buried in soil. Extensive measurements of the background (without the presence of any clutter or mine object) were taken both in free space and in soil in order to characterize the sensor noise process. This data allows us to examine the stability of the sensor response. Geophex recently obtained data with the GEM-3 sensor that indicates that, in free space, it can both detect and discriminate various low-metal content mines. Our goals are not only to verify the free space data from Geophex with the same mine types but also to determine the effects associated with burying the mines in soil on the signatures of these low-metal mines. During this experiment, we also included two high-metallic content mines in the target set. These large metal mines were used to confirm a commonly held assumption: for “large” metal objects the effects of burial in soil are negligible on the EMI sensor response. Thus, by measuring the signatures of the high-metallic mines in “free space” and when buried in soil, we could determine whether the assumption that soil has no effect on the signature of

mines is valid. Prior to this work, the validity of this assumption had not been tested.

4.1.2.2 Mine Descriptions

To address the goals of this experiment, six inert land mines were provided by the Night Vision Electronic Sensors Directorate (NVESD) through the Joint UXO Co-ordination Office. These were actual mines that were “down-loaded” (all explosives removed). For the low-metal content mines, care was taken to insure that all the correct metal parts were present in the proper location and orientation. Table 4.1 lists the mines that were tested, along with their relevant characteristics [70, 71]. Both high-metal and low-metal content mines were evaluated in order to measure the effects of the soil and the statistics of the noise process as a function of metal content.

4.1.2.3 Sensor

The GEM-3 is a prototype wide-band frequency-domain EMI sensor developed by Geophex, Ltd. [17]. A detailed description of the GEM-3 sensor is provided in Sec. 2.2.2.1.

The GEM-3 can be programmed to sequentially record the induced current at a set of user defined frequencies. The process of recording the induced current (in-phase and quadrature components measured in ppm) at each of the specified frequencies is referred to as a measurement. Each of the individual data values is referred to as a sample. The GEM-3 can also be programmed to automatically take repetitive measurements multiple times. Multiple repetitions of measuring the frequencies pre-defined for a particular experimental setup is referred to as a scan. A scan can be

Mine Name	Type	Diameter (cm)	Description and Metal Content
Valmara	AP, M	10	Italian bounding fragmentation mine. Plastic case over large metal canister. Total metal: 2800 g.
VS50	AP, LM	9	Italian round plastic-cased blast mine. Mine case empty of any fill. Total metal: 18.21 g.
M14	AP, LM	5.6	US and Indian manufactured plastic bodied blast mine. Case empty of any fill. Total metal: 0.6 g.
M19	AP, LM	33	American rectangular plastic blast mine. Test mine case filled with room temperature vulcanized material (RTV). Total metal: 0.94g.
VS2.2	AP, LM	23	Italian plastic blast mine. Case empty of any fill. Total metal: 3.29 g.
TS50	AP, LM	9	Italian plastic-cased cylindrical blast mine. Case empty of any fill. Total metal: 4.41 g.

Table 4.1: Mines tested in the first experiment. AP = Anti-personnel mine, AT = Anti-tank mine. M = High metal content, LM = Low metal content

used to assess the repeatability of a measurement, and thus the statistics of the noise process. By evaluating the statistics of a particular sample across the set of measurements, we can characterize the noise process. This can further lead to an estimate of the distribution of the noise process.

In this experiment, we operated the GEM-3 remotely. A laptop PC was used to transmit data acquisition parameters to the GEM-3 and to record the measured responses through the serial port. Prior to data acquisition, the sensor was allowed to warm up for at least ten minutes. As the data is acquired, it is written to a log file on the hard disk of the computer. The log file consists of a header that lists the

acquisition parameters, followed by the recorded data.

4.1.2.4 Data Collection - General Protocol

In order to assess the detectability of the mines in free space and in soil and the effects of the soil on the "signature" of a mine, the response of the sensor to each mine as a function of frequency was determined both in free space and when buried in soil.

When a mine is present, the response of the sensor consists of a response due to both the mine and the background. To obtain the response due to the mine alone, it is necessary to determine the response of the sensor to the background alone and then subtract the background response from the response of mine plus background (this assumes that the system is linear). Therefore, in this experiment, we interspersed scans of the response of the sensor to the background (no-mine) with scans of the response of the sensor to the mine embedded in its background.

Data was collected under two conditions: a) with the sensor situated in "free-space" (*i.e.* suspended in the air) at a fixed distance from the targets, and b) with the sensor situated at a fixed distance above the ground in which the targets were buried to a depth of 1" in North Carolina clay soil. Under each condition, data was gathered alternatively with the target absent (background scan), then with the target present. The frequencies used, 24 total, were generated in a range from 300 Hz to 24 kHz using a logarithmic spacing. For each target and background scan, 25 measurements were taken.

In the first condition, which is in the free-space condition, the distance between the top of the mine and the bottom of the sensor head was approximately 10 cm for all of the mines except the Valmara. The exact distances are listed in Table 4.2. The sensor to mine distance for the Valmara had to be increased since, due to the higher metal content, the response exceeded the dynamic range of the sensor at 10 cm, and the sensor response was saturated. The GEM-3 sensor was mounted on a wooden rack with the sensor head approximately 6 feet from the wooden base of the platform. Both platform and rack were manufactured with no metal parts. The rack assembly allowed placement of targets on a wooden shelf at various distances beneath the sensor head. The sensor head was centered over the mine manually for each scan. The GEM-3 was linked via cable to the serial port of the laptop PC located approximately 30 feet from the test assembly.

Mine	Sensor/Mine Distance - Air (cm)	Sensor/Mine Distance - Soil (cm)
Valmara	28	27.5
M19	11	10.5
VS2.2	10	9.5
TS50	9.5	10
VS50	9.5	10
M14	10	9.5

Table 4.2: The distance from the top of the mine to the bottom of the sensor head in the first experiment when target is both in free space and buried conditions.

Next, data was gathered with the mines buried with the top of the mine 1 inch below the surface of the soil. Again, for all of the mines except the Valmara, the distance between the top of the mine and the bottom of the sensor head was approximately 10 cm (see Table 4.2). For the measurements taken in soil, the GEM-3 was mounted on a combination of a sawhorse and wooden stand. The radial location of the wooden stand was adjusted to raise and lower the sensor head to achieve the

desired distance from the ground. Care was taken to center the sensor head over the target manually for each scan.

Under these conditions, a complete scan (25 repeated measurements, each measurement taken at 24 frequencies) required approximately 6 minutes. The entire free space data collection was completed in approximately 2 hours, and the soil data collection required approximately 2.5 hours. The sensor was not turned off during the experiment.

An important observation that resulted from the analysis of this data set was that the mean or average value of the “background” scans varied as a function of time, for both conditions. Hereafter, this nonstationarity is referred to as “sensor drift”.

4.1.2.5 General Approach and Notation

This section describes the basic mathematical manipulations that were performed on the raw data measured by the GEM-3. Pre-processing transforms the raw current data into data proportional to the induced magnetic field strength. We then define notation that allows us to refer to specific measurements taken in a particular scan.

As discussed previously, the GEM-3 records in-phase and quadrature data as a function of frequency in ppm (a unit associated with the sensor, without physical meaning, defined in Equation (2.9)). These data are based on a current measurement, as opposed to a magnetic field measurement. Therefore, to convert these measurements to data that are proportional to magnetic field strength, an inverse dependence on the frequency and a 90-degree phase shift must be incorporated (see

Sec. 2.2.2.1 for details). Thus, the following calculations were performed on each of the measurements:

$$\begin{aligned} I(f) &= -\frac{Q_c(f)}{f} \\ Q(f) &= \frac{I_c(f)}{f}. \end{aligned} \quad (4.1)$$

Here, f is frequency, $I_c(f)$ and $Q_c(f)$ are the current-based in-phase and quadrature samples reported by the GEM-3, and $I(f)$ and $Q(f)$ are the calculated in-phase and quadrature samples that are proportional to the magnetic field. In a more recent version of the GEM-3 sensor, this calculation is performed by the sensor.

The in-phase and quadrature responses obtained on the i^{th} measurement of a particular scan as a function of frequency are denoted either $I_{scan_identifier}^i(f)$ or $Q_{scan_identifier}^i(f)$. Here, i ranges from 1 to 25 and $scan_identifier$ refers to the scan, as well as the file name that was used to store the data. For example, $I_{M14}^9(f)$ is the in-phase data measured at each frequency on the 9th (out of 25) measurements obtained during the M14 scan.

The mean in-phase and quadrature signatures for a particular scan, $\bar{I}_{scan_identifier}(f)$ and $\bar{Q}_{scan_identifier}(f)$, are calculated as the average of all of the 25 measurements. Thus, for instance, $\bar{I}_{M14}(f)$ is the mean of the in-phase measurements taken during the M14 scan as a function of frequency.

In order to extract the signatures of the mines from the measured data, we assume that the best estimate of the signal represented by the set of measurements comprising a scan is the average of those measurements. It is further assumed that when the average of the set of measurements comprising the background scans taken before and after a mine scan is subtracted from the average of the mine scan, the

result is an estimate of the signature of a mine. Below, we specifically define this relationship for this “background corrected” signature.

A “background corrected” average signature is derived for each mine by subtracting an estimate of the background signature from the mean of the scan for each mine. The background estimate is calculated as the average of the background measurements taken immediately prior to and after the mine scan. For example, the background estimate for the M14 mine in free space would consist of the mean of the 6th and 7th background scans. The background corrected signature is denoted by a ‘bc’ in the subscript, and is given by

$$\begin{aligned} I_{\text{scan_identifier}, \text{bc}}(f) &= \bar{I}_{\text{scan_identifier}}(f) - \frac{\bar{I}_{\text{previous_bg_identifier}}(f) + \bar{I}_{\text{next_bg_identifier}}(f)}{2} \\ \bar{Q}_{\text{scan_identifier}, \text{bc}}(f) &= \bar{Q}_{\text{scan_identifier}}(f) - \frac{\bar{Q}_{\text{previous_bg_identifier}}(f) + \bar{Q}_{\text{next_bg_identifier}}(f)}{2}. \end{aligned} \quad (4.2)$$

We also define the average background signature for each mine as the second term in Equation (4.2), or

$$\begin{aligned} \bar{I}_{\text{scan_identifier}}^{\text{BACKGROUND}}(f) &= \frac{\bar{I}_{\text{previous_bg_identifier}}(f) + \bar{I}_{\text{next_bg_identifier}}(f)}{2} \\ \bar{Q}_{\text{scan_identifier}}^{\text{BACKGROUND}}(f) &= \frac{\bar{Q}_{\text{previous_bg_identifier}}(f) + \bar{Q}_{\text{next_bg_identifier}}(f)}{2} \end{aligned} \quad (4.3)$$

The superscript ‘BACKGROUND’ indicates that this is an average background signature associated with the mine denoted by the *scan_identifier*.

To evaluate the statistics of the sensor noise process, the standard deviation of the set of measurements comprising a scan is calculated. This measure gives an estimate of the variability of the signature. For example, $\sigma_{M14}^I(f)$ is the standard deviation as a function of frequency of the in-phase measurements taken during the M14 scan.

These standard deviation metrics can be calculated for a mine scan, a background scan, and a background-corrected mine scan.

Finally, the set of data acquired during the course of a scan at a particular frequency is defined. This can be used to estimate the distribution of the noise process. The set of in-phase or quadrature samples taken during a particular scan at a given frequency, f_0 , is denoted as $I_{\text{scan_identifier}}^{\{i\}}(f_0)$ and $Q_{\text{scan_identifier}}^{\{i\}}(f_0)$, respectively.

4.1.2.6 Characterization of the Noise Process

The goal of this analysis is to characterize the statistics of the noise. These statistics are used to formulate the detection algorithm prescribed by signal detection theory. The pdf that describes the noise process (*e.g.*, Gaussian) was evaluated by forming histograms of the data taken during a scan at each frequency (see Sec. 4.1.2.5, *i.e.* using $I_{\text{scan_dentidier}}^{\{i\}}$ and $Q_{\text{scan_dentidier}}^{\{i\}}$). We generated these histograms in both soil and free-space. In order to determine whether or not the statistics of the noise process are stable, we examined the mean and variance of the statistical distributions as a function of the following parameters:

- the absolute amplitude level of the received signal
- the amount of time the sensor has been operating, corresponding to something akin to “drift” in the mean response of the sensor, and
- the frequency at which a measurement is made.

In the experimental design, 25 measurements were made in each scan. This data was to be used to 1) analyze the statistics of the noise process, and 2) to determine the detectability of low metal mines in both free space and when buried in soil. Although the original goal was to characterize the pdf’s of the noise process by analyzing all

of the background data together (a total of 350 measurements in both the free space and soil conditions), the sensor drift issue made this infeasible. Figure 4.1 illustrates the sensor drift problem using histograms of quadrature data measured in each of the free space background scans at the frequency of 2,370 Hz (*i.e.* $Q^{\{i\}}(2370)$). The histogram for each scan, labeled as “backg1” through “backg7” (corresponding to the background measurements at the same position before and after each of the six mine data collections), follows the grayscale scheme listed in the legend. In general, the mean of each scan is increasing with time (scan number), however the mean of backg5 is less than the means of backg3 and backg4. This indicates that the mean, as well as the standard deviation, of the sensor response is not stationary in time. Clearly, combining data across all scans cannot generate a valid estimate of the pdf of the noise process.

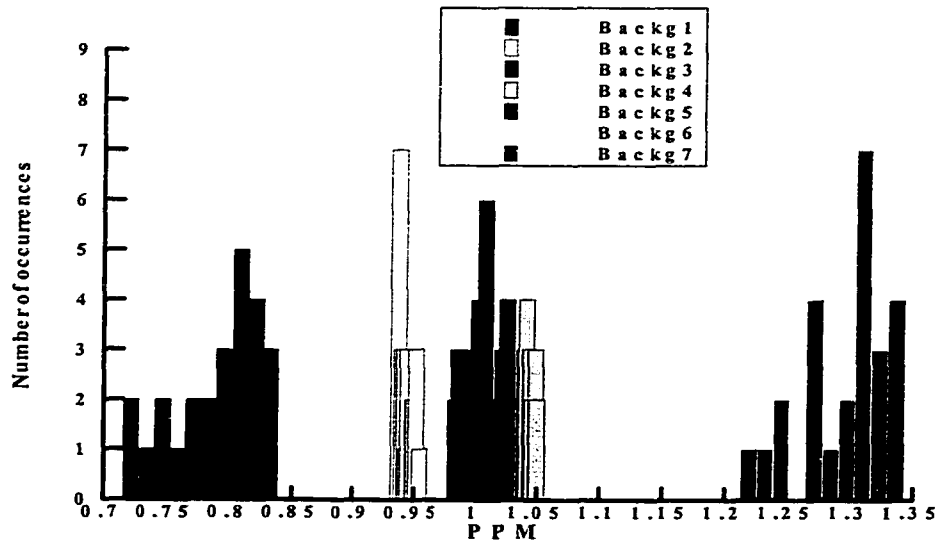


Figure 4.1: Grayscale-coded histograms of the in-phase data obtained at 2,370 Hz during the free space background measurements. The change in both the mean and standard deviation of each data set indicates that the sensor response “drifts”, or is not stable over time.

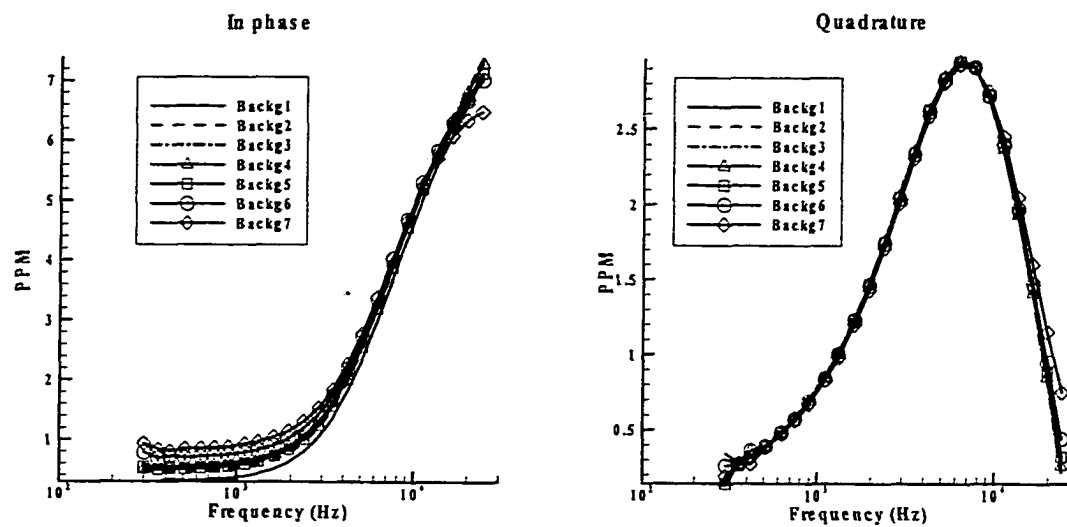


Figure 4.2: Variation of mean of in-phase and quadrature background scan for the seven measured samples in free-space. Line type order (beginning with backg1 and ending with backg7) = solid, dash, dash-dot, triangle, square, circle, diamond.

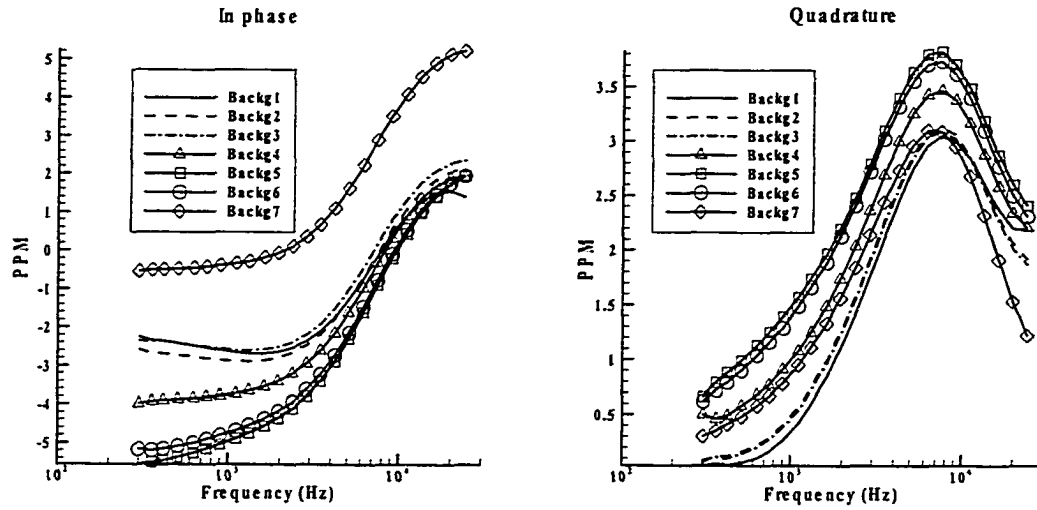


Figure 4.3: Variation of mean of in-phase and quadrature background scan for the seven measured samples in soil. Line type order (beginning with backg1 and ending with backg7) = solid, dash, dash-dot, triangle, square, circle, diamond.

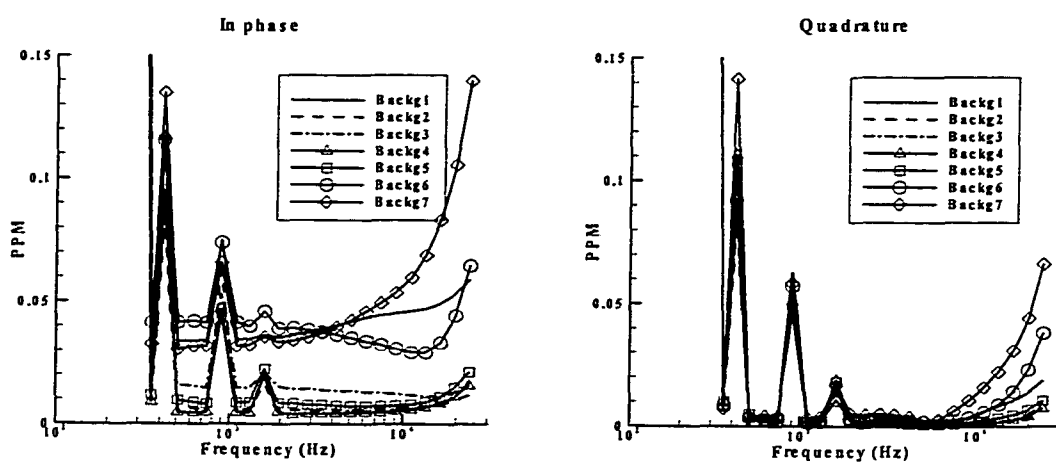


Figure 4.4: Standard deviation of the seven scans as a function of frequency in free-space (in-phase and quadrature). Line type order (beginning with backg1 and ending with backg7) = solid, dash, dash-dot, triangle, square, circle, diamond.

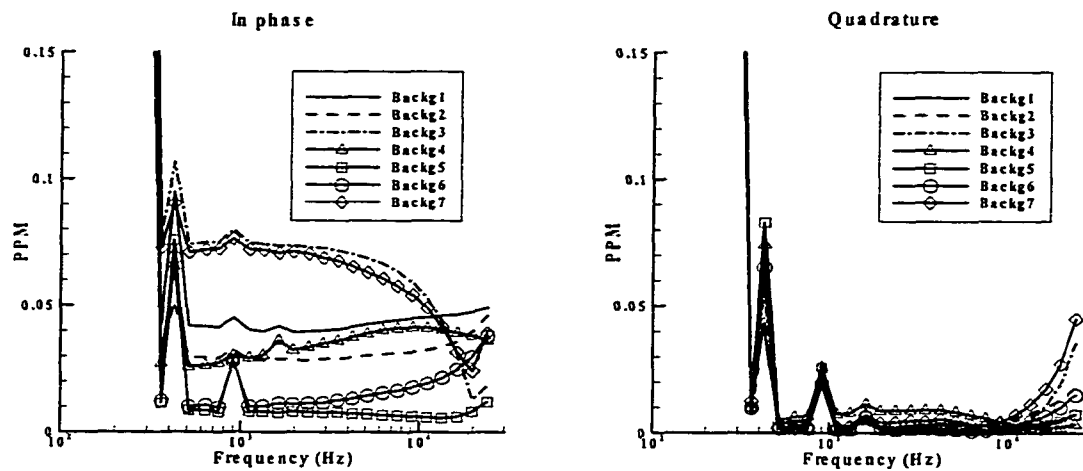


Figure 4.5: Standard deviation of the seven scans as a function of frequency in soil (in-phase and quadrature). Line type order (beginning with backg1 and ending with backg7) = solid, dash, dash-dot, triangle, square, circle, diamond.

In order to further investigate the sensor drift issue, Figures 4.2 and 4.3 plot the average response as a function of frequency for each of the background measurements (backg1 - backg7) for free-space and in-soil condition, respectively. These are based on the experimental data in which 25 measurements were taken. Figures 4.4 and 4.5 plot the standard deviation of the 25 measurements as a function of frequency for each of the background measurements taken in free-space and soil, respectively. Both Figure 4.2 and 4.3 indicate that the mean response of the sensor changes as a function of time, and thus indicate that the mean is not stationary. Additionally, comparing Figure 4.3 with Figure 4.2 indicates that variability in the density or moisture level of the soil (associated with digging) may also change the “background” signature

recorded by the sensor. However, it is also difficult to separate out the differences that result from changes in the soil density from differences that result from slight changes in the sensor to soil distance. This effect is considered later for advanced algorithm development. Figures 4.4 and 4.5 indicate that the level of the variability (standard deviation) is a function of frequency, and also appears to be a function of time. No dependence on the amplitude of the signal was observed when the standard deviation functions were compared for the different mine types. In general, more variability is observed at high and low frequencies than in the middle of the frequency range. Clearly, this should also be considered for algorithm development.

In general, 25 samples of a noise process are barely adequate to obtain valid estimates of its mean and variance and it is not a large enough sample to accurately estimate the functional form of a pdf, or histogram. Therefore, in a separate experiment, 1000 measurements of a "clean" background were obtained in order to obtain a better estimate of the functional form of the pdf, as well as to address the sensor drift issue in more detail (see Sec. 4.1.3.2).

4.1.2.7 Calculation of the Average Background Corrected Mine Signatures

To calculate the response of the sensor to the mines without including the background response, the background response must be subtracted from the response obtained with mine plus background. In free space, this was performed by subtracting an average of the background signature measured before and after each mine measurement (see Sec. 4.1.2.5) from response due to both background and a mine. In soil, the same approach was taken, with the exception of the Valmara. When the Valmara scan was performed in soil, the distance between the sensor and the ground was larger than the

distance used for the other mines. Consequently, the background signature measured following the Valmara scan (backg7) was taken with the sensor at the same (greater than other background measurements) distance from the ground. Therefore, for the Valmara scan in soil, the background-corrected signature was calculated by

$$\begin{aligned} I_{valm,bc}(f) &= I_{valm}(f) - I_{backg7}(f), \\ Q_{valm,bc}(f) &= Q_{valm}(f) - Q_{backg7}(f) \end{aligned} \quad (4.4)$$

As discussed above, the background changed substantially after the mines were emplaced for soil data. Therefore, in addition to calculating the background corrected signals as described in Sec. 4.1.2.5, mine signatures were also calculated by subtracting the initial average background measurement, backg1. This scan was taken prior to disturbing the soil. The drawback to this approach is that it does not incorporate any effects of sensor drift.

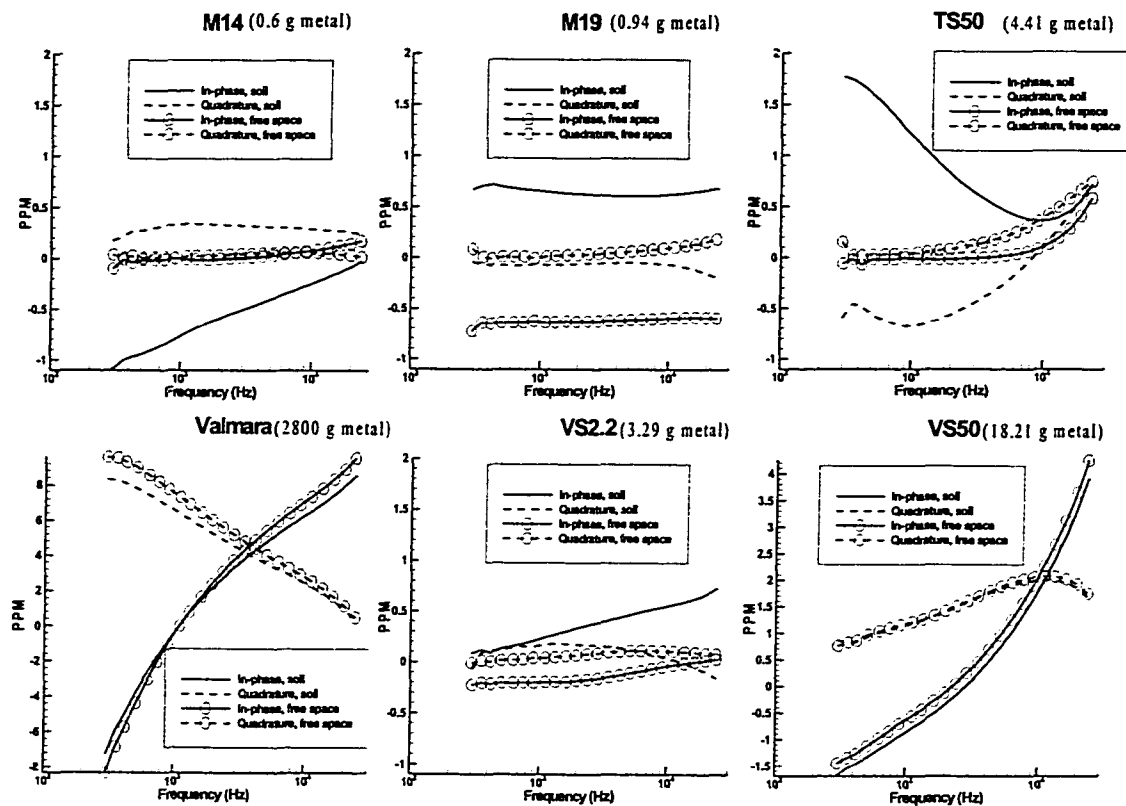


Figure 4.6: Comparison of background corrected signatures in air and soil. Solid = in-phase component, dashed = quadrature component, lines without symbols measured in soil, lines with circles measured in free-space.

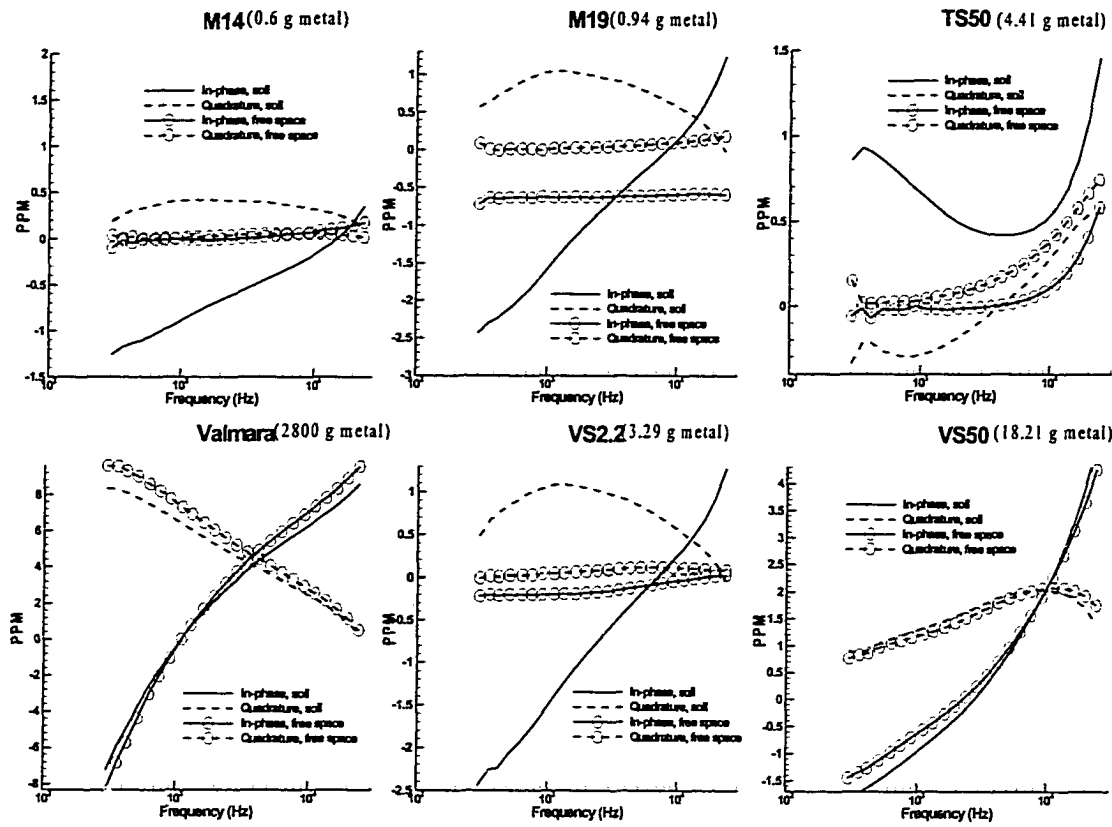


Figure 4.7: Comparison of background corrected signatures in air and soil. Soil signatures are corrected by initial background measurements. Solid = in-phase component, dashed = quadrature component, lines without symbols measured in soil, lines with circles measured in free-space.

Figure 4.6 shows the average background corrected signatures for the six mines in free-space. Each of the mines appears to have a different characteristic signature as a function of frequency. Note that no clutter signatures were measured for comparison. Figure 4.6 also illustrates the need for accurate background correction for the GEM-3. As discussed in Sec. 4.1.2.6, the mean sensor response that is measured when no objects are present “drifts” over time. The level of this drift can be as high as 1 ppm over the course of a 2-3 hour period (see Figures 4.1, 4.2 and 4.3). The ppm levels of

the background corrected signatures for some of the low metallic-content mines are smaller than this level of drift. Therefore, correcting a measured signal with an inaccurate background could substantially change the form of the background-corrected signal. Clearly, this statistical variability must be incorporated into detection algorithms for the GEM-3.

Figure 4.6 also shows the background-corrected signatures for the six mines buried 1" deep in soil. Again, each of the mines appears to have a different characteristic signature as a function of frequency. However, for the low-metal mines, the signatures are not the same, as those measured in free-space, although the signatures for the Valmara and the VS50 (high metal mines) match quite well.

Clearly, when comparing the signatures of low-metal mines in free space and in soil, the signatures measured in the ground are different from those measured in the air. In addition, the signatures measured in the ground have a higher magnitude than those measured in free-space. This may be a result of the GEM-3 measuring the dielectric discontinuity between the mine and the ground [44]. Figure 4.7 plots results similar to those of Figure 4.6, except that the soil signatures are corrected by the background measured initially - *i.e.* to undisturbed soil.

4.1.2.8 Detectability Analysis

As mentioned before, one of the goals of these analyses was to determine whether the sensor responses obtained from the mines were different from the sensor responses obtained from the background (either soil or free-space). Detection performance was measured using ROC analysis. In order to employ ROC analysis, the following are required. First, a set of data is needed in which repeated measurements were taken

under both conditions: mine present and mine absent. This data is available in the mine scans and background scans, respectively. For example, the detectability of the M14 in free space could be analyzed using the data collected in the M14 scan and data collected in the backg6 scan (background taken immediately prior to the M14 scan) and backg7 scan (background taken after the M14 scan). Second, an algorithm for processing the data must be specified. In this analysis, two different algorithms, an energy detector and a matched filter, each of which we consider to be a "baseline" algorithm, were implemented for each set of mine and its background data. These algorithms are categorized as "baseline" because they are fairly routine approaches to processing such data.

In order to perform the ROC analysis, it is assumed that the algorithm makes a decision on a set of measured in-phase and quadrature data, and the detector, or algorithm, does not have *a priori* knowledge on whether or not a mine was present when the data was measured. It is further assumed that the decision is made after background correction is performed on the measured data. This would result in a target hypothesis, H_1 , in which the background-corrected signal consists of the mine signature plus noise and the null hypothesis, H_0 , in which the background-corrected signal consists of noise alone. Therefore, to perform this analysis on the data collected in each set of mine/background scans, a "background" must be subtracted from each measurement taken in the scan. The average background signature associated with each mine scan, as defined in Sec. 4.1.2.5, was subtracted.

For the target hypothesis (H_1), the data available to the detection algorithms consists of the 25 measurements taken in a particular mine scan corrected by the appropriate average background. Thus, the detection algorithms have twenty-five

signals available that were obtained when H_1 is true. For the null hypothesis (H_0), the data available to the detector consists of the 25 background measurements taken prior to the mine scan along with the 25 measurements taken immediately after the mine scan, each corrected by the appropriate average background. A total of 50 signals that were obtained when H_0 is true is available for processing.

The performance of two standard algorithms was analyzed. The first algorithm implemented was an energy-based detection algorithm. The data for the target hypothesis (H_1) was the energy contained in the 25 background-corrected signatures defined above. The data for the null hypothesis (H_0) was the energy contained in the 50 background-corrected background signatures that were measured immediately prior to and following collection of the target data. Then, a thresholding operation is performed on the data in order to make decision (H_1 or H_0), and the threshold is varied to generate the ROC.

The second detection algorithm that was implemented was a matched filter. This approach is normally implemented by calculating a matched filter signature either from theoretical considerations or from a training set of measurements, and then implementing the filter on a second set of measurements. However, time constraints did not allow such a design to be implemented in this preliminary experiment. Therefore, for both soil and free space scans, the mean of the odd-numbered measurements within a mine scan were used to calculate the matched filter. Performance was evaluated on the even-numbered mine measurements and all of the associated background measurements. In addition, the matched filter derived from a free space mine scan was applied to data obtained in soil.

The matched filter formulation assumes that the in-phase and quadrature components of the received signal are independent and identically distributed. If the sensor noise is 1) additive, 2) Gaussian, 3) identically distributed across frequency and 4) uncorrelated across time, then the assumption of independence is reasonable. Clearly, at a minimum, the third assumption was invalid. This analysis was performed on both soil data and free-space data.

If the GEM-3 sensor responds solely to the metal contained in the mine, *i.e.*, the presence or absence of the soil does not affect the measurement, then identical (or very similar) signatures should be measured in both the free space and soil conditions. In this case, a matched filter derived from the free space measurement could be used to detect the presence of a particular mine in soil. Therefore, in addition to the matched filter analyses described above, the matched filters that were calculated for the free space condition were also applied to the buried targets. This analysis allowed us to determine whether the signatures measured in free space were useful for detecting the same targets in soil.

In free space, the energy detector achieves perfect performance on four of the six mines. It is slightly less than perfect for the VS2.2 (see Figure 4.8), and its performance falls below the chance diagonal for the M14. This anomaly results happen because the energy in the background-corrected signature is lower for the M14 than for the background. The ROC curve shown in Figure 4.8 for the energy detector applied to the M14 is obtained from flipping the decision rules to make the curve above the chance diagonal. The matched filter detector achieves perfect performance on five of the six mines, and substantially outperforms the energy detector on the M14. Thus, even though the assumptions for the validity of the matched filter are

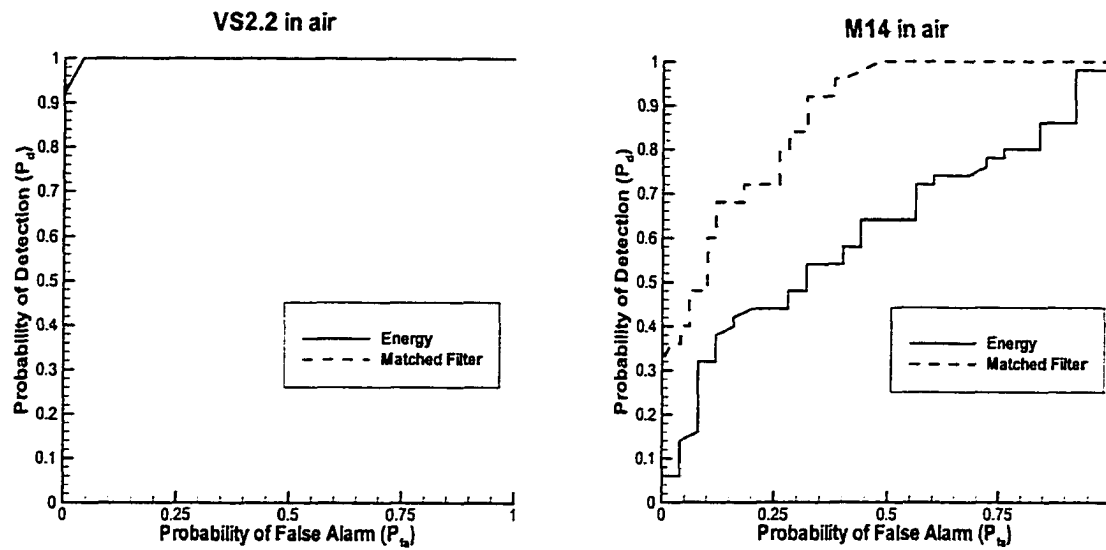


Figure 4.8: The ROC curves of the matched filter and energy detector for VS2.2 and M14 in free space.

at least partially invalid in this case, performance can not be improved upon for 5 of the 6 mines.

In soil, the matched filter detector performance is perfect on all mines. The energy detector performance is perfect on all but the VS2.2, where it always chooses the wrong hypothesis since again, the energy in the background corrected signature is lower when the VS2.2 is present. This, along with the above somewhat anomalous result, may be an artifact of a poor background correction, which results from drift in the background. When the mean background corrected signatures from free space were used as a matched filter in the soil, detection performance was still perfect.

4.1.2.9 Discriminability Analysis

In this section, the matched filters described above were used to perform classification for the six mines. The solution to this problem was a bank of matched filters, illustrated in Figure 4.9. The classification task was performed by assuming that the most likely target corresponds to the object associated with the filter with the maximum output. Classification was performed in free-space using the matched filters obtained in free space. For mines buried in soil, filters were defined based on both free space and soil measurements. The matched filter solution assumes that the target signals are known exactly; any uncertainty in the placement of the targets in the environment would substantially degrade classification performance using this approach. References [27] and [75] discuss this problem and suggest an alternate approach that incorporates such uncertainty into the classification algorithm.

Condition	Valmara	VS50	TS50	M14	M19	VS2.2
Air-Air	100%	100%	92%	100%	100%	100%
Soil-Soil	100%	100%	100%	100%	100%	100%
Air-Soil	100%	100%	92%	0%	0%	0%

Table 4.3: Discrimination performance of matched filter classifier for signatures estimated in free-space and applied in free-space (Air-Air), signatures estimated in soil and applied in soil (Soil-Soil), and signatures estimated in free-space and applied in soil (Air-Soil).

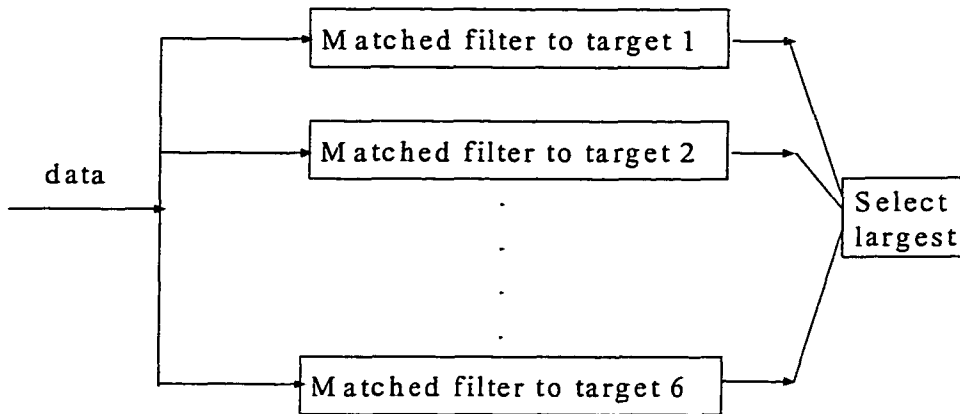


Figure 4.9: Schematic illustration of the implementation of the matched filter bank.

Table 4.3 lists the discriminability of the various mines. These measures were calculated using a matched filter bank. Half of the target signatures were used to generate the matched filter, the other half were used for testing. Clearly, it is possible to discriminate each type of mine from the others in free-space or in the ground when the signatures are known exactly. It is not possible to use the free-space signatures as discriminators for the in-soil measurements. In this case, the classifier can discriminate the Valmara, VS50, and TS50, but the M14, M19 and VS2.2 are always mis-classified as the TS50. It is also important to note that these data were obtained with little to no change in the environmental or geometric variables and thus are not necessarily indicative of real-world performance.

4.1.2.10 Summary of Results

The results of this experiment indicate that:

- The presence of soil does affect the signature recorded by the GEM-3 for low-metallic content mines.
- It is possible to detect low-metal land mines using the GEM-3, since the broadband EMI responses from low-metal mines are different from that of background.
- The measurements obtained are stochastic in nature, not deterministic. Detectors, or algorithms, which effectively incorporate the stochastic character of the signals should be able to out-perform traditional detection algorithms. Sensor noise appears to be a function of frequency, but not of the amplitude of the measured signal.
- The sensor experiences some drift in its response. Drift must be considered both in gathering data and in the analysis. At a minimum, background measurements must be made during data collection for accurate background correction.

4.1.3 Experiment 2: JUXOCO Calibration Lanes

Based on the results of the preliminary experiment described above, it appeared that data from a broadband EMI sensor could be used to detect landmines more effectively than traditional energy based detectors. However, this preliminary experiment did not include any source of false alarms other than a simple ground response. Thus, to investigate the utility of broadband EMI response in the low-metal content mines, it was necessary to obtain a more realistic data set from a large variety of mines and clutter. In Sections 4.1.3 and 4.1.4 we discuss experiments performed at Fort A. P. Hill, VA. that were sponsored by JUXOCO. Data was collected in a calibration area, where ground truth for both target and clutter has been released to the public, and in a main test site, where the ground truth is sequestered (known only to the

sponsor). Sec. 4.1.3 describes the experiment performed in the calibration lanes and the corresponding analyses on data from calibration lanes; and Sec. 4.1.4 describes the results of analyses performed on the main site data.

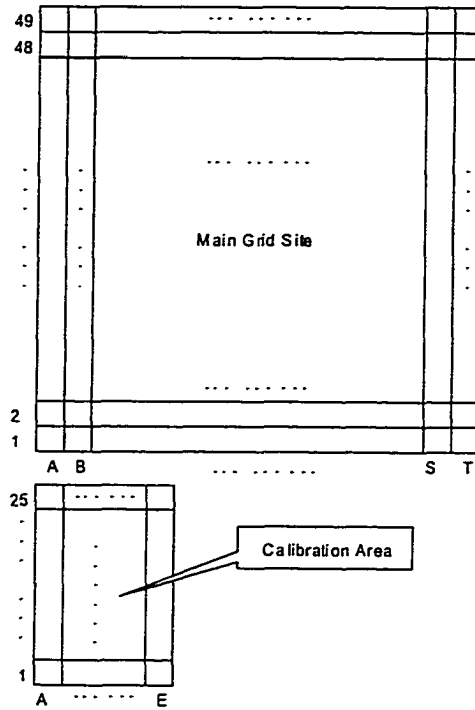


Figure 4.10: Layout of the test site at 71A, Ft. A. P. Hill, VA.

4.1.3.1 Data Collection

Details of the data collection plan can be found in [70], however for completeness the most salient points are summarized here. A 50 meter by 20 meter plot at Fort A. P. Hill, VA. was selected for construction of the test grid, and a calibration area was created in an adjacent 5 meter by 25 meter plot, as shown in Figure 4.10. Initially, all indigenous clutter was removed from the site. The ground truth associated with the calibration area is available; however, the ground truth associated with the main, or blind, test grid is sequestered. A mine or clutter object, when present in a particular

grid square, is buried at the center of the 1 m by 1 m grid square.

Mine targets emplaced in the main test grids were predominately "low metal" mines since these are the most challenging to detect. At least one mine of each type, as well as representative samples of clutter, were emplaced in the calibration area. "Tactical" burial depths were used for the mine targets [76]. Approximately 100 mine targets were buried in the blind main test grid.

The indigenous clutter initially removed from the A. P. Hill site included rusted shrapnel, exploded 50 mm rounds, 20 mm rounds, rusted nails, pieces of wire, small copper pieces and other unidentifiable metal. Samples of the indigenous clutter were re-emplaced in the center of selected grids to provide discrete opportunities for false alarms. Figure 4.11 shows some examples of the responses of clutter items measured in the calibration area. In many cases, clutter signatures are different from those of low-metal mines (Figure 4.6).

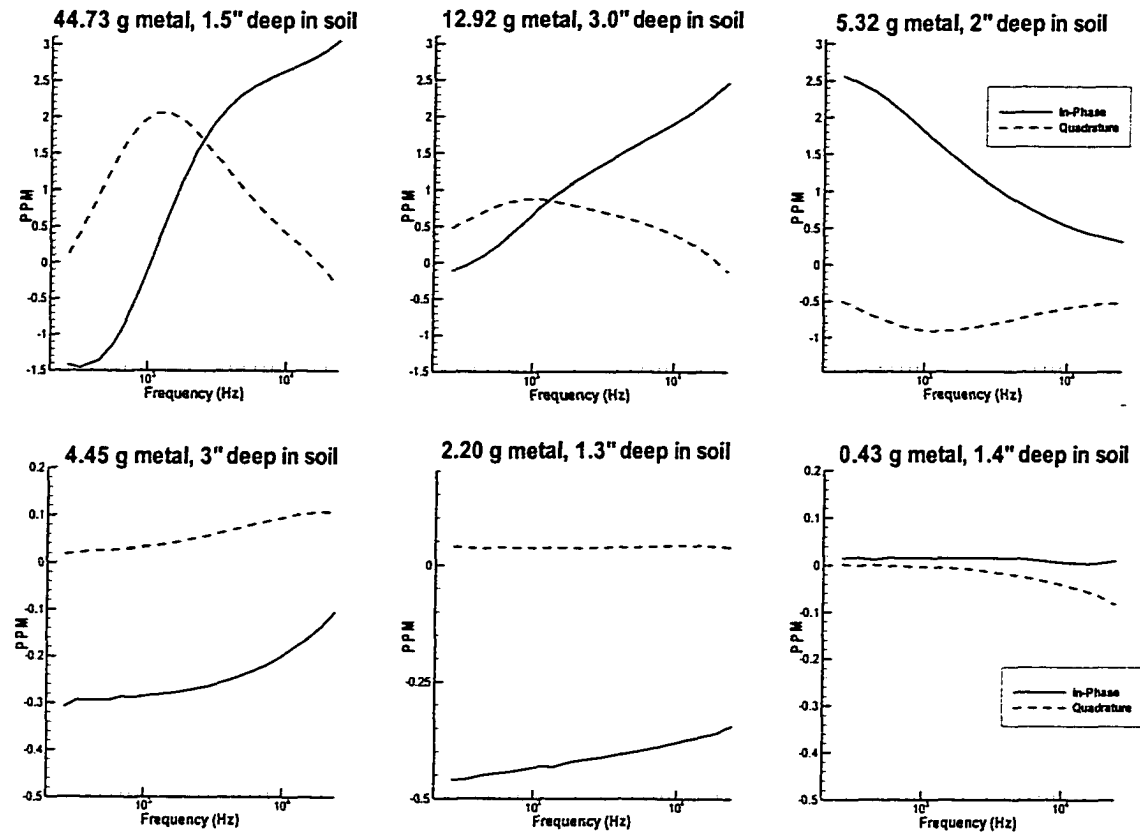


Figure 4.11: Examples of clutter frequency domain EMI responses, data measured on 7/7/99 in the calibration area

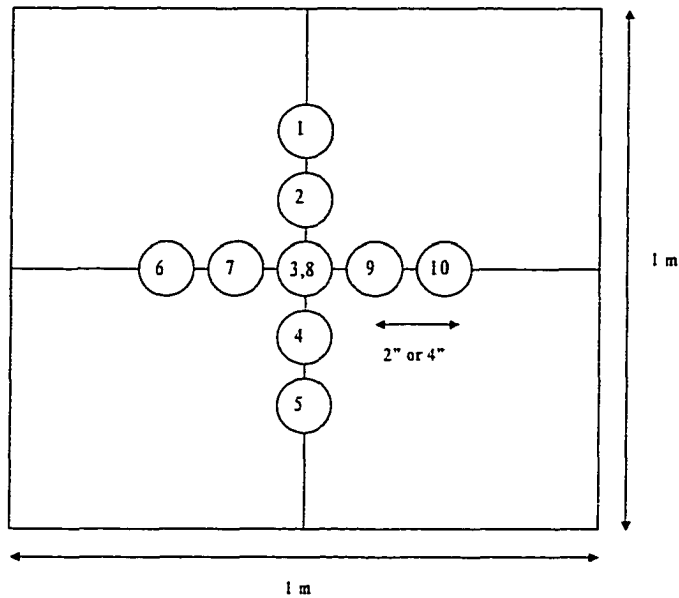


Figure 4.12: Example of spatial data collection and the associated numbering scheme

The GEM-3 sensor was programmed to measure responses at 20 frequencies spaced logarithmically between 270 and 23,790 Hz. One meter square data collection templates (illustrated in Figure 4.12) were constructed for placement at each grid location in both the calibration area and the main test grid to facilitate accurate sensor placement. The templates had a series of marks for use of locating the sensor head at the appropriate positions. Ten spatial positions were measured in each grid point. For grid points in which the GEM-3 response did not saturate, these points were located at -4", -2", 0", 2", and 4" from the center in both a vertical and a horizontal orientation [77]. Collection points were labeled 1 ~ 5 from top to bottom and 6 ~ 10 from left to right. When the sensor response saturated due to higher metal content of the underground object, the sensor head was raised 24" above the ground and the spatial samples were taken every 4" apart as opposed to every 2". Each signature was measured twice.

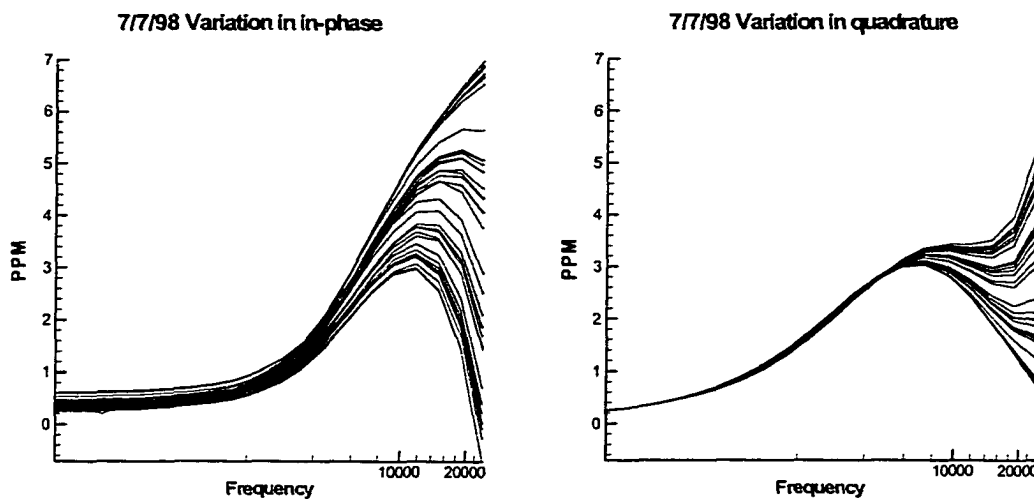


Figure 4.13: Variation in in-phase and quadrature signals measured on 7/7/98 in the calibration area.

Data was collected in the calibration area four times: on June 9-11, July 6-7, July 27, and September 30, 1998, respectively. Data was measured at each grid point where either a target or clutter had been emplaced. Following the collection of signatures at each of the 10 spatially distributed points corresponding to one grid square, a background measurement was taken at a blank grid point. These “background” measurements were used to track the sensor drift described in Section 4.1.2. They also provided examples of grid squares where nothing was buried. An example of the drift observed over a 4-hour period on July 7, 1998 is shown in Figure 4.13. Each curve represents one measurement. The drift observed at the higher frequencies was much greater than that observed in the previous experiment. This increase in the

amount of drift may be due to the relatively hotter temperatures experienced during this data acquisition. The sensor drift is being addressed in a newer version of the GEM-3 sensor. Based on histograms of the data obtained at each frequency, the data appeared to follow a Gaussian distribution, the statistics obtained from this data set were used in subsequent detection algorithms.

Following data collection, the data were manually corrected for any data drop-outs that occurred as a result of failure of the serial connection between the GEM-3 and the PC controller. On the average, data collection across all ten spatial points associated with a grid square and the subsequent background measurements required 10 minutes. The signatures measured in the calibration lane for the 6 mines which had been studied in the previous experiments were similar to those obtained in the previous experiment when the objects were buried.

4.1.3.2 Background Correction

Four approaches for background correction were analyzed for the measured data in this experiment. In the first, the background measured immediately prior to the measurement of a grid point was subtracted from each spatial signature. In the second, the background measured immediately after the measurement of a grid point was subtracted from each spatial signature. The third approach used the average of the background signatures measured immediately before and after measuring the signatures in the grid. The final approach utilized a linear prediction of the background obtained from the background measured before and the background measured after the data collection for a particular grid square for every one of the 25 measurements.

The performance of the background correction algorithms was analyzed by per-

forming one measurement in which a background was taken between every spatial measurement, *i.e.* the order of measurements was Background 1 - Spatial position 1 - Background 2 - Spatial position 2 - . . . - Background 10 - Spatial position 10 - Background 11. Using this approach the true background for a particular spatial position could be very accurately estimated from the bordering background measurements. The “actual” background-corrected signatures could then be compared to those obtained using the four methods, corresponding to using Background 1, Background 11, the average of Background 1 and 11, and linear prediction using Backgrounds 1 and 11.

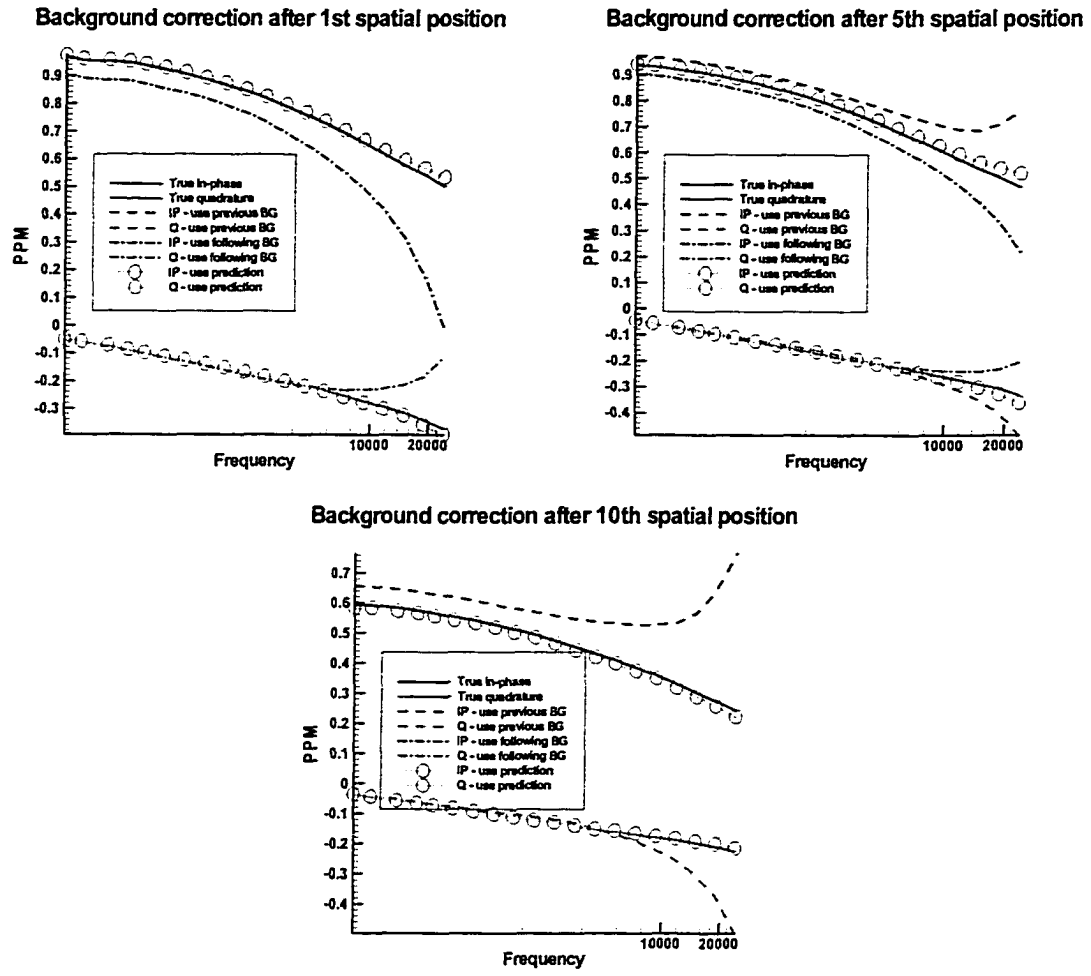


Figure 4.14: Background correction example at the first, fifth, and tenth spatial position. “Previous” background approach is coincident with true solution for the first spatial position, “Following” background approach is coincident with true solution for the final spatial position.

As expected, using only Background 1 produced substantial errors in the spatial positions measured later ($7 \sim 10$). Similarly, using only Background 11 produced substantial errors in the spatial positions measured earlier ($1 \sim 3$). Utilization of the average background produced fair estimates in the middle spatial positions ($4 \sim 6$), but poorer estimates in the earlier and later spatial positions. The linear predic-

tion method provided the best approach to background correction. Examples of the background corrected estimates for the signatures are shown for one grid point at the first, fifth, and tenth spatial position respectively in Figure 4.14. The true signature is shown with the solid line, the dashed line illustrates the prediction using the previous background, the dashed-dotted line illustrates the prediction using the following background. The gray line with the circle symbols shows the signature obtained using the linear prediction. Both in-phase (top curves) and quadrature (bottom curves) data are shown. Clearly, the linear prediction method provides the best estimate, especially at the higher frequencies.

In the main grid, grid points can consist of targets, clutter, or “blanks”, *i.e.*, empty spots. In the calibration lane, only grid points consisting of targets and clutter were measured, so the background measurements were used for the blank data.

4.1.3.3 Analysis of the Effects of Spatial and Environmental Parameters on Mine Signatures

The induced response measured by the GEM-3 to a low-metal mine changes dramatically between free space and soil, as illustrated in Figure 4.6. The response also changes as a function of soil moisture. Figure 4.15 illustrates the changes in the signature for a VS50 mine as a function of soil moisture. Conditions at A. P. Hill were wet on 7/7/98 and dry and hot on 7/27/98, and a change in the response (including crossover frequency) is evident. Clearly, it is important to develop signal processing algorithms that are robust to such environmental effects.

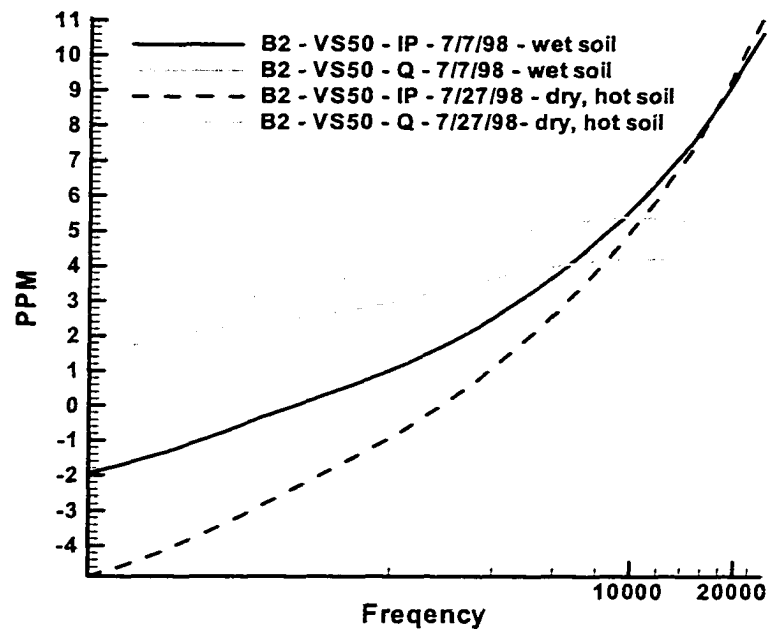


Figure 4.15: Change in the signature for a VS50 mine as a function of soil moisture.

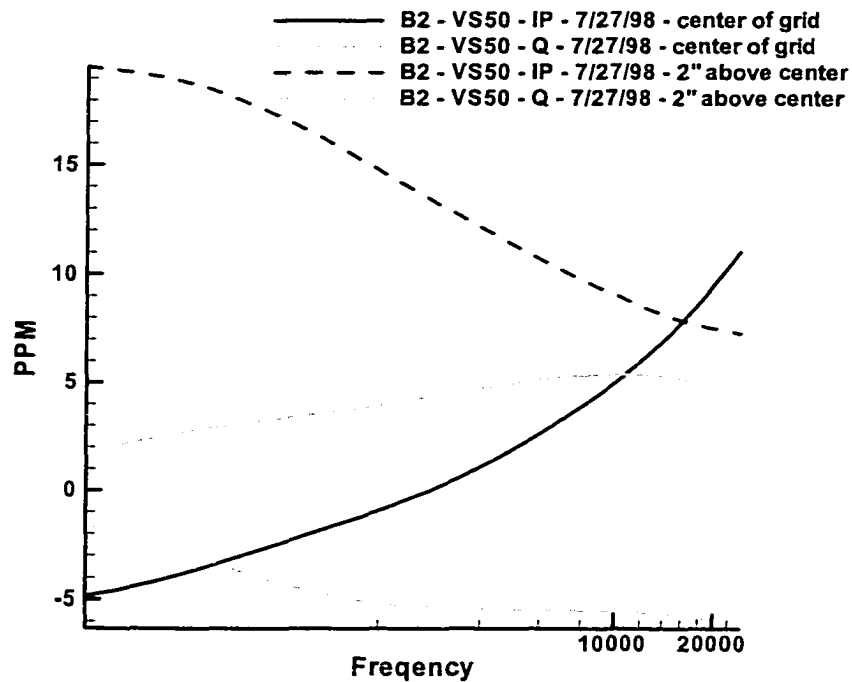


Figure 4.16: Change in the signature for a VS50 mine as a function of spatial position

Finally, based on the GEM-3 measurements taken at Ft. A. P. Hill, it is also observed that the response of the GEM-3 to low-metal objects placed off-axis is not simply a “scaled” version of the on-axis response (see Figure 4.16). The response does tend to approximately scale with burial depth. Unlike the case of large metallic mines or UXO items where small changes in target-sensor orientation do not dramatically affect the excited modes [78], in the case of low metal mines, small changes in orientation can result in dramatic changes in the response.

4.1.3.4 Discussion of Results

The main goal for the data collection in the calibration lanes was to use the GEM-3 sensor to collect data from a sample of mines and clutter in order to develop statistics for further algorithm development. The data was also used to (1) characterize the variability of the signatures, and (2) to develop a data-collection/data-processing technique to compensate for sensor drift. The results of analyzing data from calibration lanes can be summarized as:

- The sensor experiences some drift in its response and the drift is more substantial on hot days. Therefore, it is necessary to gather a “background” signature after every grid point measurement for the main test grid.
- A linear prediction using the background signature measured prior to data acquisition and immediately after data acquisition at a grid square provided the best “drift correction”.
- Measured signatures changed across days. This may be due to differences in soil moisture or temperature.
- The spatial variability in signatures was greater in low-metal targets than high-metal targets, and could not be described by a simple scaling.

4.1.4 Experiment 3: Main Test Grid at JUXOCO

4.1.4.1 Experiment Description

Hand-held mine detector experiments were conducted in the main grid between July and October 1998 at Range 71A of Fort A. P. Hill. The preparation of the main test site is described in detail in [70], and the data collection mechanisms are described in section 4.1.3.1. The main test grid was established consisting of approximately 100

targets, and an unknown number of clutter objects and blank squares. The main grid consisted of 20 lanes, labeled A ~ T, each of which is 49 meters long and 1 meter wide. The format of the data is described briefly below. At each grid point, the data and time of the collection were recorded. Data was collected on 7/27-31/98, 8/10-14/98, 9/21-25/98, 9/28-30/98, and 10/27-29/98. Background measurements were taken at one of four grid squares: E11, E39, O11 and O39. These squares were set aside as known “blanks” by JUXOCO. The closest blank was used as the background for each grid square.

4.1.4.2 Algorithm Development and Performance Evaluation

We consider two general classes of algorithms; those of which consider only the measured energy and those of which process the entire signature. We further divide these two classes into algorithms that operate only on the data measured at the center of the grid, and those measured at the various spatial points. In this way, we can quantify the performance of a “baseline”, which we consider to be center-point energy-based algorithms, and also quantify performance gains associated with using the entire frequency-domain signature, as well as incorporation of spatial information. We provide the output of their algorithms for each grid square or “decision opportunity” to JUXOCO for scoring to generate ROC curves. The data from the calibration lanes could be used to develop the parameters required for a generalized likelihood ratio test (GLRT) [55]. The GLRT is defined as:

$$\Omega(\mathbf{x}) = \frac{f(\mathbf{x}|\Theta, H_1)}{f(\mathbf{x}|\bar{\Gamma}, H_0)}$$

$$\bar{\Theta}, \bar{\Gamma} = \text{MLE of } \Theta \text{ and } \Gamma \quad (4.5)$$

where \mathbf{x} is the measured data, Θ and Γ are the unknown parameters associated with H_1 and H_0 , respectively, ‘MLE’ is the maximum likelihood estimate. H_1 is the hypothesis that a target is present, and H_0 is the hypothesis no target present, *i.e.* clutter or noise only. We assume, based on field measurements, that the pdf’s, $f(\mathbf{x}|\Theta, H_1)$ and $f(\mathbf{x}|\Gamma, H_0)$, follow a normal distribution whose mean and variance are a function of frequency and that the unknown parameters can be associated with a particular mine type in the case of H_1 , or a clutter class (large clutter versus small clutter object) in the case of H_0 . Thus, the decision statistic becomes

$$\Omega(x_1, x_2, \dots, x_N) = \frac{\frac{1}{M} \sum_{j=1}^M f(x_1, x_2, \dots, x_N | t_j, H_1)}{\sum_{j=1}^K f(x_1, x_2, \dots, x_N | c_j, H_0) \Pr(c_j)} \quad (4.6)$$

where t corresponds to the various target types and c to the various clutter classes, $\Pr(c_j)$ is the a priori probability that the j^{th} type of clutter class is present. We assume that each of the M mines is equally likely. We further assume three equally likely “clutter” classes corresponding to large and small clutter and “blanks”.

GEM3 Results. H1: Mines H0: Clutter and Blanks

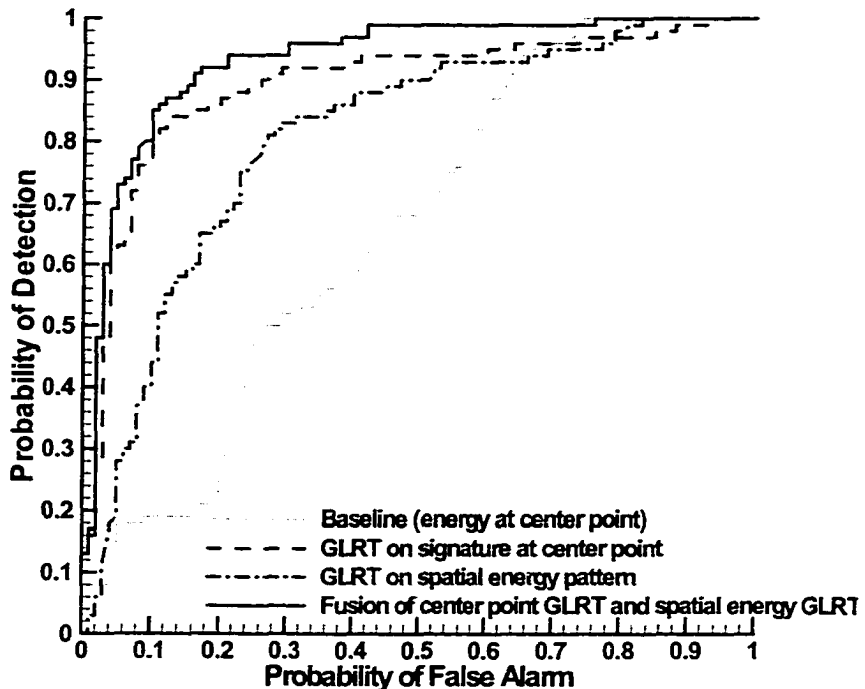


Figure 4.17: Performance of the baseline algorithm and three GLRT-based algorithms.

Figure 4.17 shows the performance of four detectors. The ground truth for the main grid has not been released by JUXOCO; thus the performance curves were produced at JUXOCO. One of the detectors presented is a GLRT operating on the frequency-domain EMI data measured at the center of each grid point, one is a GLRT operating on the energy data measured at the ten spatial positions, and one is an energy detector using the energy data from the center of each grid point. The final algorithm is a GLRT that operated on the output of the two GLRTs mentioned above (frequency domain signature at center point and spatial energy data). Thus, this algorithm performs “fusion” on the spatial and frequency domain EMI data.

However, it is not the optimal approach. An improved algorithm that utilizes all of the frequency domain data as a function of space and is more robust to environmental variables is the subject of future work.

The improvement in false alarm rates between the various GLRT-based algorithms and the baseline algorithms can be computed by fixing the probability of detection and calculating the ratio between the false alarm probabilities of the various algorithms to that associated with the baseline algorithm. These false alarm rate improvements are summarized in Table 4.4. Clearly, substantial improvements in false alarm probabilities can be obtained at each of the detection probabilities considered.

Probability of Detection	Fusion of Signature-Based GLRT and Energy-Based Spatial GLRT	Signature-Based GLRT at Center Point	Energy-Based Spatial GLRT
0.7	10.4	7.4	2.4
0.8	6.3	5.7	2.1
0.9	3.9	2.4	1.3

Table 4.4: Ratio between the false alarm probability of the various algorithms and the false alarm probability of the baseline algorithm at the particular probabilities of detection.

4.1.5 Discussions

In this section, we presented data from a series of experiments designed for the following purposes.

First, a commonly held assumption that for large metal objects the soil effects on the EMI response can be neglected was validated. The GEM-3 sensor was used

to measure the response from the Valmara (2800 grams of metal) and the VS50 (18 grams of metal), two high metal landmines, in air and when buried in soil. The signatures in free space and in soil were similar, which verified the assumption.

Second, the effects that burial in soil had on the induced response from low-metal mines were investigated. The data taken from four low metal mines in free space and in soil indicate that the EMI signatures of low metal mines in soil are substantially changed from those observed in free space. Therefore, modeling of EMII responses for this type of landmine must take the effects of the soil into consideration, and the signatures in free space can not be utilized directly to detect underground low-metal mines.

Third, the capability of the GEM-3 sensor to detect low metal mines in free space and in soil was investigated. The data show that the sensor can differentiate these targets from the background response. Finally, the experiments performed at Fort A. P. Hill, VA. provided a data set from low-metal mines and clutter in the calibration area and main test grid. This data set allowed us to develop algorithms, which provide improved performance over the traditional energy-based algorithm.

Preliminary work on algorithm development with this data set is promising. Substantial reductions in the false alarm rate have been obtained by applying a GLRT to the frequency-domain signature obtained at the center point in the grid square. Such algorithms require no modifications to the existing sensor hardware. Additional improvements in performance have been obtained by fusing information contained in the pattern of energy across space with the output of the signature-based GLRT. A frequency-domain EMI approach coupled with statistical signal processing algorithms

shows significant promise for the problem of detecting low-metal mines.

4.2 Classification of Landmine-Like Metal Targets Using Wideband Frequency-Domain EMI

4.2.1 Introduction

As has been noted earlier, a persistent problem with traditional narrowband EMI sensors involves not just detection of metal objects, but discrimination of targets from clutter. In most fielded sensors, the energy in the output of such sensors is calculated, and a decision regarding the presence or absence of a target is made using this statistic [26]. This approach leads to excessively large false alarm rates. In order to facilitate the discrimination of targets of interest from other pieces of metal, several modifications to traditional EMI sensors have been considered [14, 13, 20, 26, 72, 73, 24, 74]. For instance, the late time EMI fields are characterized by an exponential decay in the time-domain [14, 13, 20, 74]. The decay rate has been used for target identification, because it strongly depends on the target conductivity, permeability, shape, and orientation, as described in Chapter 3. Alternatively, a promising approach is to operate the sensor in the frequency-domain by utilizing wideband excitation. The frequency dependence of the induced fields excited by buried conducting targets can then be exploited by a detector.

A second problem that besets statistical algorithms is the need for adequate training data. A wide range of targets and clutter signatures must be obtained at all possible object/sensor orientations. Classically, this problem has been addressed by using data measured in the field [26, 17, 79]. However, a lack of sufficient training data can severely degrade performance [26, 80]. In general, it is difficult if not impos-

sible to obtain such data for all possible object/sensor orientations. An alternative is to train the algorithms with data produced by computational models, which have only recently become general enough to consider such problems [20].

In this section, we consider the problem in which we assume an object has been detected, and a decision as to “target” or “clutter” is required. In this approach, we use the complex frequency-dependent EMI response as a signature. A full-wave model developed by Drs. Geng and Carin and described in Sec. 2.2.2.2 for the wideband EMI response of targets is utilized, thus obviating the need for training on field collected data. Subsequently, a Bayesian classification algorithm is developed which incorporates the wave model and the target/sensor position uncertainty. Substantial improvements are achieved via this approach over a processor which ignores the orientation uncertainties.

Theoretical calculations and experimental data have shown that the frequency-domain EMI signatures differ significantly across targets [19], which provides the underlying physical mechanisms important for discriminating, identifying, or classifying targets.

4.2.2 Forward Model-Based Bayesian Classifier Formulation

In a real-world classification scenario, the uncertainty inherent in the sensor output is not only due to additive noise, but also to the fact that the relative position between the sensor and the target is unknown at the point when the measurements are obtained. In this work, we investigate the classification performance of a Bayesian classifier that incorporates modeled wideband EMI signatures as well as position

uncertainties, and compare its performance to an approach which ignores these uncertainties and assumes the target is at a fixed position corresponding to the mean assumed position.

In this section, we consider the task of classifying data from one of four known metal objects. It is always true that one of the objects is present and our goal is to decide which object is present. In the real world, such as landmine detection, it is often the case that a metal object can be located, the task is then to determine whether it is a target or clutter. In this case, a library of targets of interest can be established and typical clutter can also be modeled. Alternatively, a statistical model could be imposed for clutter based on localized measurements and the target models can be used as is described here. Thus, this approach can also be applied to an extended set of objects in practice.

In this work, four metal objects are considered (a more detailed description can be found in Sec. 4.2.3). Signals used to measure classification performance are either the modeled wideband frequency-domain EMI responses or measured EMI responses from the GEM-3. Since any sensor is subject to noise, which is usually assumed to follow a Gaussian distribution, the distribution of the sensor outputs (obtained data set of discrete frequencies) while the target/sensor is at a known height and horizontal position is a Gaussian random vector. The mean of this response is the theoretical response and the variance is equal to that of the additive noise. Let H_i represent the hypothesis that the i^{th} target is present, where $i = 1, 2, 3, 4$. The received data from the i^{th} target at a known position can be modeled as:

$$r_{ij} = A_{ij} + n_j \quad (4.7)$$

where j corresponds to the discrete frequencies of interest, $j = 1, 2, , N$, r_{ij} is the re-

ceived data from the sensor, A_{ij} is the predicted response obtained from the model (as described in detail in Sec. 2.2.2.2, the model can calculate the theoretical frequency-domain EMI responses for a well specified BOR object at a known position) for the i^{th} target at the j^{th} frequency at a known depth and horizontal position relative to the center of the sensor, and n_j is Gaussian noise with zero mean and variance of σ_n^2 . We assume that n_j 's are independent, however, their variance is a function of frequency. Let q_i represent the *a priori* probability that hypothesis H_i is true. We further assume that the cost of a correct decision is zero, and the cost of any wrong decision equals 1. Bayes' solution for this classification problem [55, 81] is to decide that H_i is true if

$$\frac{p(H_i|r)}{p(H_k|r)} = \frac{q_i p(r|H_i)}{q_k p(r|H_k)} > 1 \quad (4.8)$$

is satisfied for any $k \neq i$. Here $p(H_i|r)$ is the *a posteriori* distribution or discriminant function [82], $p(r|H_i)$ is the probability density or likelihood function of data r given H_i , and r is the received data from the sensor. Assuming the magnitude and the phase of the frequency response are independent, r is a vector containing both the magnitude and phase information. Therefore, when the sampled data r is received, we decide in favor of hypothesis H_i where

$$q_i p(r|H_i) = \max_k \{q_k p(r|H_k)\} \quad k = 1, 2, 3, 4 \quad (4.9)$$

Thus, we decide in favor of a hypothesis that has the largest *a posteriori* probability or largest discriminant function at r among all four possible pdf's. Since we usually have no *a priori* knowledge of q_i , in other words, do not know the probability that a particular target is going to be present, an equal probability assumption for each target is made, *i.e.* $q_i = 1/4$. Based on the uniform prior on q_i , Equation (4.9) can be further understood as seeking a hypothesis that provides the maximum likelihood among the four possible values, thus, it can also be referred to as a maximum likeli-

hood (ML) classifier. Since any monotonically increasing function of $p(H_i|r)$ is also a valid discriminant function [82], an alternative discriminant function based on the above assumptions is:

$$p(\mathbf{r}|H_i) = (2\pi)^{-N} |\Sigma|^{-1/2} \exp[-\frac{1}{2}(\mathbf{r} - \mathbf{A}_i)^T \Sigma^{-1}(\mathbf{r} - \mathbf{A}_i)] \quad (4.10)$$

where N is the total number of frequencies used, \mathbf{r} and \mathbf{A}_i are $2N$ by 1 vectors, and Σ is the covariance matrix of \mathbf{r} . Given the assumptions on the noise process, Σ is a diagonal matrix with on the j^{th} diagonal, where j corresponds to frequency. Since the coefficient of the exponential term of Equation (4.10) is the same for all the hypotheses, it can be neglected. After taking the logarithm, the alternative discriminant function simplifies to:

$$\log p'(\mathbf{r}|H_i) = -(\mathbf{r} - \mathbf{A}_i)^T \Sigma^{-1}(\mathbf{r} - \mathbf{A}_i) \quad (4.11)$$

where $(\mathbf{r} - \mathbf{A}_i)^T \Sigma^{-1}(\mathbf{r} - \mathbf{A}_i)$ is often referred as the Mahalanobis distance from \mathbf{r} to \mathbf{A}_i [82]. If Σ is a diagonal matrix with each diagonal element $\sigma_{n_j}^2$, Equation (4.11) can be expressed as:

$$\log p''(\mathbf{r}|H_i) = -\sum_{j=1}^{2N} (r_j - A_{ij})^2 / \sigma_{n_j}^2 \quad (4.12)$$

The discriminant function obtained above, Equation (4.12), is valid if the height and horizontal position of the object are both known and the noise is assumed to be independent at each frequency. This solution is optimal only under the assumptions that all the parameters are known, and the sensor is subject only to Gaussian noise. This formulation differs from a bank of matched filters since (1) the noise is not identically distributed and the variance of the noise is a function of frequency, and (2) the signals are not of equal energy. These two facts result in a formulation, which is similar to, but not identical to, the traditional matched filter $r^T A_i$, which is the

result of i.i.d. additive white Gaussian noise [55, 83].

The performance of the classifier given by Equation (4.12) is a function of the noise variance and the modeled response. Table 4.5 lists the theoretical performance of the classifier as the noise variance is increased from σ_n^2 to $2^9\sigma_n^2$, where σ_n^2 is a vector which contains the noise variance of the magnitude and phase as a function of frequency obtained from experimental data (see Sec. 4.2.3.3). As expected, an increase in the noise variance results in a decrease in the classification performance. This analysis provides insight into how the classification performance is affected by the sensor noise. Once the sensor is manufactured and well calibrated, the sensor noise cannot be changed artificially, thus, only simulated data was used to illustrate this effect.

Noise Variance	Probability of Correct Classification			
	Target 1	Target 2	Target 3	Target 4
σ_n^2	1.0000	1.0000	1.0000	1.0000
$2\sigma_n^2$	1.0000	1.0000	1.0000	1.0000
$2^2\sigma_n^2$	0.9993	1.0000	0.9990	1.0000
$2^3\sigma_n^2$	0.9862	1.0000	0.9887	1.0000
$2^4\sigma_n^2$	0.9365	1.0000	0.9394	1.0000
$2^5\sigma_n^2$	0.8604	1.0000	0.8640	1.0000
$2^6\sigma_n^2$	0.7809	0.9977	0.7747	1.0000
$2^7\sigma_n^2$	0.7134	0.9791	0.6854	1.0000
$2^8\sigma_n^2$	0.6545	0.9254	0.5756	0.9981
$2^9\sigma_n^2$	0.6101	0.8552	0.4554	0.9827

Table 4.5: The probability of correct classification of the optimal classifier when targets are at a fixed known position as the noise variance is increased from σ_n^2 to $2^9\sigma_n^2$.

A more realistic assumption for the classification problem is that the height and horizontal position are uncertain, since the exact sensor position where measurements

are obtained relative to the underground objects is unknown in practice. In this case, the previously derived processor (fixed position processor as in Equation (4.12)), which assumed a “fixed” target/sensor orientation, is not the optimal solution. Hence, in order to obtain the optimal discriminant function for the received data the effect of these random factors must be integrated out, *i.e.*

$$p(\mathbf{r}|H_i) = \int \int \int p(\mathbf{r}|H_i, h, x, y,)p(h)p(x, y)dh dx dy \quad (4.13)$$

where h represents the height of the sensor from the target; x, y represent the horizontal position of the sensor relative to the center of the target; $p(h)$ and $p(x, y)$ are the *a priori* distributions of the position factors; and $p(\mathbf{r}|H_i, h, x, y) = \frac{1}{(2\pi)^N |\Sigma|^{1/2}} \exp[-\frac{1}{2}(\mathbf{r} - \mathbf{A}_i(h, x, y))^T \Sigma^{-1} (\mathbf{r} - \mathbf{A}_i(h, x, y))]$, $\mathbf{A}_i(h, x, y)$ is the model prediction (described in detail in Sec. 2.2.2.2) of the i^{th} target response when it is located at the position (h, x, y) relative the sensor. The model predicts the theoretical frequency-domain EMI response as a function of constitutive parameters, exact dimensions of the object and the horizontal and vertical distance from the center of sensor to that of the object. Monte Carlo integration was implemented in order to calculate the integral in Equation (4.13).

4.2.3 Simulated and Experimental Data and Results of FPP and OP

The performance of both the fixed-position processor, FPP, (Equation (4.12)) and the optimal processor, OP, (Equation (4.13)) is investigated by using both simulations and measurements for the GEM-3 sensor. In this section, the method used to generate simulated data, the experimental design, and the methods used to take the measurements are described. Then, the corresponding results are followed by the

data descriptions.

Four metal targets are considered for both the simulations and experimental measurements: an aluminum bar-bell, an aluminum disk, a thick brass disk, and a thin brass disk. The dimensions of these targets are as follows. The diameter of each of the targets is 5.08 cm. The heights of the targets are 2.897 cm, 2.667 cm, 2.34 cm, and 0.3175 cm for the aluminum bar-bell, the aluminum disk, the thick and the thin brass disk, respectively. The response from a target depends on the constitutive parameters, geometry of the target, as well as the horizontal and vertical distance from the center of the sensor to that of the target. In the calculations, twenty-one linearly spaced frequencies were chosen, ranging from 3,990 Hz to 23,970 Hz. These frequencies are within the range that the GEM-3 operates.

4.2.3.1 Simulated Data

In order to test whether the classification performance is improved by incorporating the model into the classification formulation, several cases were considered. These cases are:

1. fixed position,
2. random height but fixed horizontal position,
3. random horizontal position but fixed height, and
4. both height and horizontal position random.

It is assumed that the distribution of the height, h , follows a Gaussian distribution with mean of 20 cm and variance of 1.53^2 cm^2 and the horizontal position is uniformly distributed in a 20 cm by 20 cm square. To generate the simulated data we

specify the constitutive parameters and the dimensions of the target, then generate 10,000 random sets of height (h) and horizontal position (x, y), which follow the distribution described above. Based on these parameters, the wideband EMI response is calculated by the model for each set of h, x , and y . After obtaining the theoretical responses of each target at all the specified positions (which are used in the formulation of the detector), Gaussian noise is added to the theoretical responses to create the simulated data set. Both the processor which assuming a fixed target/sensor orientation (in Equation (4.12)) and the optimal classifier (in Equation (4.13)) are then applied to these data. Results of these classifiers are discussed later.

4.2.3.2 Simulation Results

Fixed Height and Horizontal Position First, the case where all the position parameters are known exactly is considered. The model of each target at the same position and all desired frequencies is calculated. Then, by adding Gaussian random noise with zero mean and variance obtained based on the experimental data (see Table 4.6), 10,000 realizations of simulated data for each target are generated. The decision of which target is present is made based on Equation (4.9) by using the processor expressed in Equation (4.12), which is optimal for this case. Because of the fact that the wideband EMI signature of these targets is significantly different [17] and the experimentally derived σ_n^2 's are low, the performance is perfect.

Height Uncertain, Fixed Horizontal Position Next, the case where only the height of the sensor from the target is unknown and the target is located under the center of the sensor is considered. This situation occurs in a real detection scenario when the sensor operator can accurately center the sensor, but the burial depth of

the mine is unknown. The height of the sensor was modeled as a Gaussian distributed random variable with mean of 20 cm and variance of 1.53^2 cm². Figure 4.18 shows the performance of processor which assumed a fixed target/sensor orientation along with that of the optimal classifier. For the former, it is assumed the target is at the mean height of 20 cm. Clearly, substantial improvements in classification performance are achieved by the optimal classifier over a processor which assumes a fixed target/sensor orientation. This performance is achieved for a relatively small level of uncertainty in the height. The average performance improvement is over 70%.

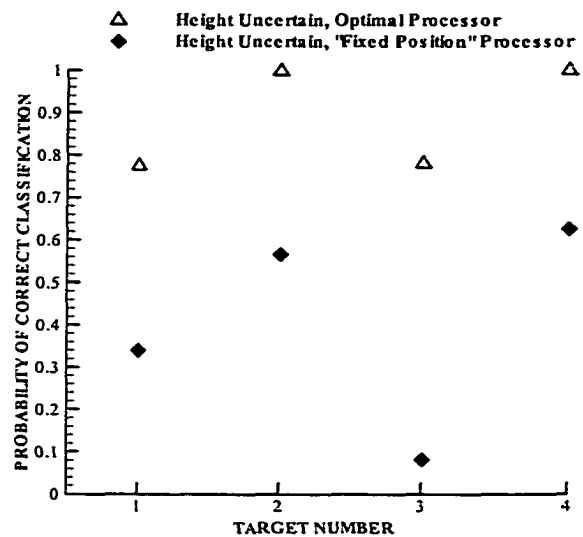


Figure 4.18: Comparison of the processor which ignores target/sensor orientation uncertainty (“fixed position” processor) and the optimal processor under uncertain height, fixed horizontal position conditions.

Horizontal Position Uncertain, Fixed Height Thirdly, we simulate the case where horizontal position is uncertain. It is assumed that the sensor is located at a

known, fixed height. Because the exact positions of mines are unknown to the sensor operator during detection, we assumed a uniform distribution in the horizontal plane. Figure 4.19 shows the simulation results of the processor that assumes a fixed target/sensor orientation and the optimal classifier when the horizontal positions of targets are uniformly distributed. For the former, it was assumed that the target was at the mean horizontal position and was directly under the sensor. Again, the performance of the optimal classifier is substantially better than that of the processor which ignores the target/sensor orientation uncertainty, it improves on average by 60%.

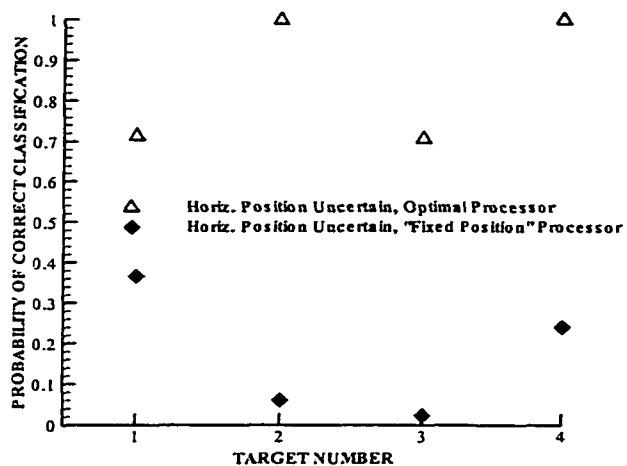


Figure 4.19: Comparison of the “fixed position” processor and optimal processor performance under the uncertain horizontal position, but fixed height condition.

Both Height and Horizontal Position Uncertain In the final simulation, both height and horizontal position are uncertain. The height is assumed to follow a Gaussian distribution with mean of 20 cm and variance of 1.53^2 . The horizontal position follows a uniform distribution (within a 20 cm by 20 cm square). Figure

4.20 illustrates the performance of the two processors. The “fixed position” processor assumes that the target is located at the mean height and horizontal position. Performance improves under these conditions by an average of 70% over that of the “fixed position” processor. The results in Figures 4.18, 4.19, and 4.20 indicate that for the “fixed position” processor the performance becomes progressively worse as the position uncertainty increases. Clearly, incorporating the uncertainty of these environmental parameters into the processor affords a significant performance gain over a processor, which ignores this uncertainty.

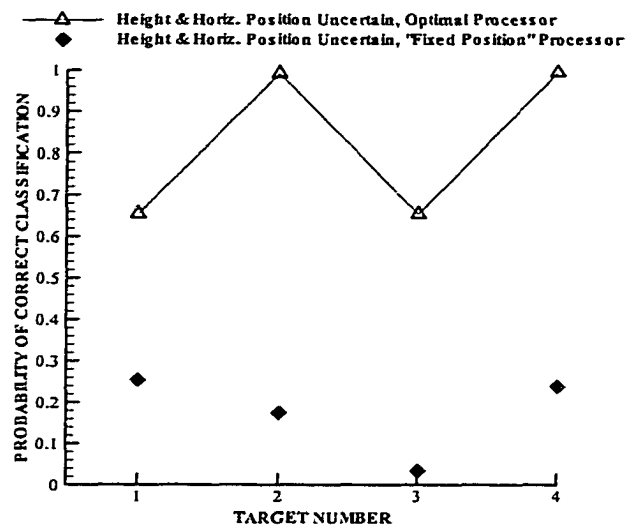


Figure 4.20: Comparison of the “fixed position” processor and optimal processor performance when both height and horizontal position are uncertain.

4.2.3.3 Measured Data

Using synthetic data to evaluate the performance of the classifier provides useful insight regarding performance bounds, but limiting the analysis to simulated data is not sufficient. Therefore, measurements of the wideband frequency-domain EMI response from the four metal targets were taken using the GEM-3 in order to evaluate the im-

provement of the classification algorithm in a more realistic scenario. In Sec. 4.1.2, we consider whether data taken from objects in air is comparable to data obtained when the objects are buried in soil. Figures 4.21 and 4.22 provide the wideband frequency-domain EMI responses measured using the GEM-3 from two metal landmines, a Valmara (an anti-personnel metal landmine) and a VS50 (an anti-personnel metal mine), in air and in North Carolina clay soil (buried 1 inch below the surface). As discussed in Sec. 4.1.2.7, the soil effects can be neglected at least for large metal objects. Therefore, the measured data used to evaluate the performance of various classification techniques was taken in free space.

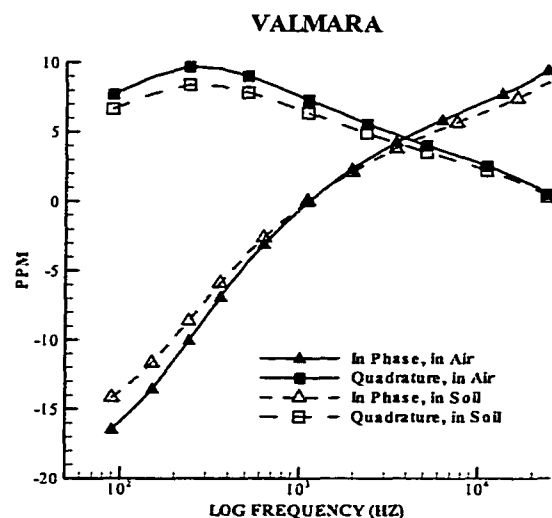


Figure 4.21: Wideband frequency-domain response of a Valmara in free space and buried 1 inch below the surface of the ground in North Carolina clay soil. The units “ppm” reflect the sensor output multiplied by 10^6 .

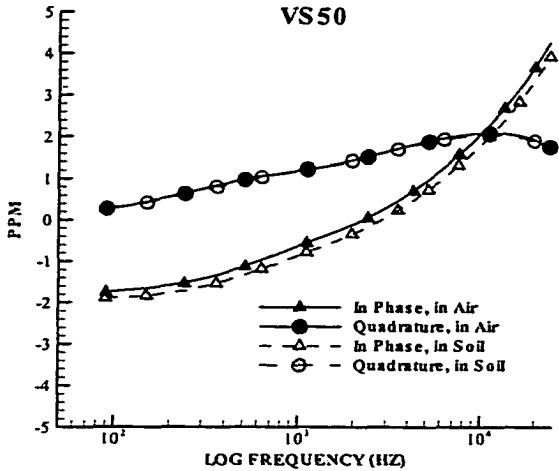


Figure 4.22: Wideband frequency-domain response of a VS50 in free space and buried 1 inch below the surface of the ground in North Carolina clay soil. The units “ppm” reflect the sensor output multiplied by 10^6 .

The experimental set up is the same as the JUXOCO Experiment 1 for the free space case, stated in Sec. 4.1.2.4. First, in order to obtain an estimate of the noise variance associate with the sensor for this particular experiment, 100 measurements were taken with the sensor at a fixed position and no target present. We refer to an individual measurement taken without a target present as a background response, as in Sec. 4.1.2.6. This response is subtracted from the responses measured with the target present to estimate the response due to the target alone. The background response is not the same at all frequencies and the noise variance is also a function of frequency. Table 4.6 lists the variance of the noise for the magnitude and phase of the complex response and the ratio between the mean value of the response and the standard deviation of the noise as a function of frequency, respectively. These estimates were used in the classifier given by Equation (4.12) and Equation (4.13).

Frequency (Hz)	$\sigma_{\text{magnitude}}^2$	$\frac{\text{mean}(\text{magnitude})}{\sigma_{\text{magnitude}}}$	σ_{phase}^2	$\frac{\text{mean}(\text{phase})}{\sigma_{\text{phase}}}$
3,990	8.25E-05	3.62E+02	8.86E-02	1.74E+02
5,010	8.99E-05	4.12E+02	5.55E-02	2.00E+02
5,970	9.41E-05	4.52E+02	3.91E-02	2.16E+02
6,990	9.47E-05	4.95E+02	2.83E-02	2.27E+02
8,010	8.96E-05	5.46E+02	2.19E-02	2.31E+02
8,970	8.35E-05	5.96E+02	1.77E-02	2.31E+02
9,990	7.47E-05	6.58E+02	1.44E-02	2.28E+02
11,010	6.57E-05	7.27E+02	1.21E-02	2.22E+02
11,970	5.73E-05	8.00E+02	1.05E-02	2.14E+02
12,990	5.44E-05	8.42E+02	8.99E-03	2.05E+02
14,010	5.70E-05	8.40E+02	8.05E-03	1.92E+02
14,970	6.23E-05	8.18E+02	7.20E-03	1.80E+02
15,990	9.25E-05	6.82E+02	6.23E-03	1.70E+02
16,950	1.11E-04	6.31E+02	5.14E-03	1.64E+02
17,970	1.55E-04	5.42E+02	4.87E-03	1.46E+02
18,990	1.49E-04	5.62E+02	9.35E-03	9.00E+01
19,950	1.63E-04	5.40E+02	1.39E-02	6.25E+01
20,970	7.26E-04	2.60E+02	3.64E-03	1.01E+02
21,950	3.90E-04	3.58E+02	9.92E-03	4.99E+01
22,950	7.81E-04	2.58E+02	9.23E-03	3.99E+01
23,970	1.21E-03	2.10E+02	8.32E-03	3.10E+01

Table 4.6: The variance of the background noise and the ratio of the mean of the response and its standard derivation as a function of frequency for the magnitude and phase components, respectively.

As described in Sec. 2.2.2.2, to calibrate the sensor measurements for the four targets were taken so the calibration coefficients could be calculated. Each target was placed beneath the center of the sensor head at distances of 17 cm, 19 cm, 20 cm, 21 cm, and 23 cm. Using these 20 measurements, calibration coefficients were calculated by the least-squares method.

To obtain the data used to evaluate algorithm performance, measurements were taken from each target at 7 heights from 17cm to 23cm in 1 cm increments. The

distribution of height is assumed to be Gaussian with mean of 20 cm and variance of 1.53^2 as for the simulations. At each height, between 11 and 36 measurements were taken. The exact count was calculated based on the assumed distribution. At each height the position of each measurement is uniformly distributed within a 20 cm by 20 cm square. For each target, there were a total of 328 measurements taken. These data were not used to train the algorithm, only to evaluate performance.

4.2.3.4 Experimental Results

The performance of these classifiers was also evaluated using experimental measurements.

The same two signal processing algorithms that were applied to simulated data: a “fixed position” processor which assumes each target at the mean position and the optimal classifier that incorporates the position uncertainty into the processor, were applied to the experimental data. Figure 4.23 illustrates the performance achieved by each of these two algorithms. Clearly, better performance is achieved by the optimal processor; performance improves on the average by 60%. This improvement, obtained on the measured data, is consistent with that observed in the simulated data set.

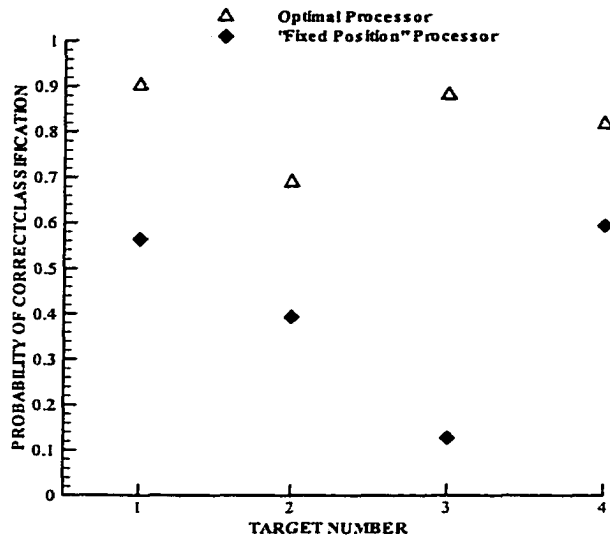


Figure 4.23: Comparison of the “fixed position” processor and optimal processor performance under the condition of both height and horizontal position unknown for measured data.

4.2.3.5 Summary

In this section, we utilize a Bayesian decision-theoretic approach to classify metal targets using wideband EMI data. Four man-made metal targets were used. Results from both simulation and measured data, shown in Sec. 4.2.3, indicate that incorporating the uncertainty associated with the target/sensor relative position into the processor affords a significant performance gain over a processor that matches to the predicted response at the mean expected target position. It is also noted that, as expected, under conditions of uncertainty the performance of both the “fixed position” processor and the optimal processors drops compared to that of the signal known exactly case. Though the optimal classifier can improve performance under uncertain conditions over processors which ignore the uncertainties, it will never achieve the performance obtained when no uncertainty is present.

As expected, simulations have shown that the SNRs of the signal affect the performance of a classifier. Since frequency-domain systems can achieve high SNRs compared to time-domain EMI systems, essentially it will improve the classification performance. Our work indicates that we can effectively discriminate different metal targets using wideband EMI signals by incorporating an accurate physical model and models of the uncertainty regarding environmental parameters into the classifier. Performance can be dramatically improved over the standard approach that ignores environmental uncertainty. In addition, extensive libraries of target signatures do not have to be measured experimentally in order to train the classifier.

This technique can be extended to apply to other applications, such as landmine detection, unexploded ordnance (UXO) detection, since in these applications targets of interests need to be discriminated from metallic clutter in order to reduce false alarm rates. The standard algorithms for these applications, such as matched filters, do not take the uncertainties associated with the target/sensor orientation into account and only partially explore the underlying physical nature of the outputs from the sensor. The work shown in this section provides a promising technique, which integrates both the uncertainties associated with target/sensor orientation and a forward model exploiting the physical signature of wideband frequency-domain EMI response. By developing a model for other signals and sensor modalities, this algorithm can be further applied to other applications which require classification of different targets.

4.2.4 Sub-Optimal Processor

4.2.4.1 Processor Design

The theoretical model predictions of the wideband EMI responses for the same target at different heights and horizontal positions show a somewhat ‘parallel’ structure as a function of frequency [78], as illustrated in Figure 4.24. The overall level varies substantially as the target/sensor orientation changes, but the basic structure of the response as a function of frequency changes only slightly. This is because the transfer function of a nonferrous target can be expressed as $H(\omega) = \sum_n \frac{a_n \omega}{\omega - j\omega_n}$, where ω is radian frequency, ω_n is the n^{th} resonant frequency, and a_n is the coefficient corresponding to each resonant frequency. When the target aspect ratios (length *vs.* diameter) are approximately equal, and only the first mode dominates, the frequency response scales directly with variable orientations [78]. Based on this phenomenon, we hypothesized that if the wideband EMI signatures were normalized, performance could be evaluated using a processor that avoids calculating the integration over position uncertainty (as in Equation (4.13)). Then, the processor can be implemented as previously described for the fixed-position processor after normalization. Therefore, the outputs of the sensor are normalized so that the energy in the response is equal to unity. This operation essentially decreases the uncertainties of the data collected in an uncertain environment. The sub-optimal processor takes the form of Equation (4.11), which uses the mean signature after normalization over all uncertainties as A_i for the i^{th} target.

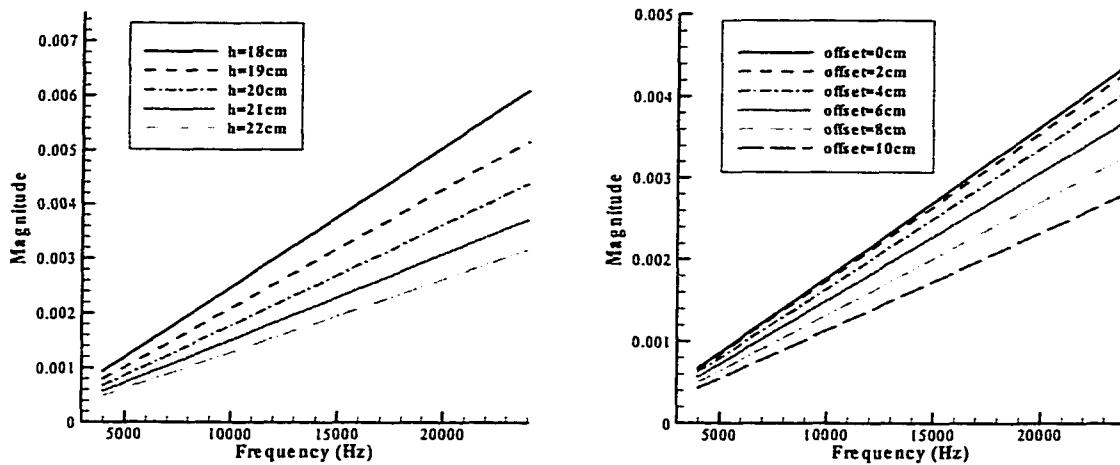


Figure 4.24: The wideband EMI signature of the thick brass disk while the height of the sensor (left) and the distance from the sensor to the target in a horizontal plane (right) change.

The performance of a fixed-position processor cannot exceed the performance of an optimal classifier operating on the same data set. However, by using the sub-optimal processor, computational savings are proportional to that required to evaluate the integral shown in Equation (4.13), thus can be implemented in real time.

4.2.4.2 Results

Table 4.7 illustrates the performance of the various processors operating on simulated data before and after normalization for the five metal objects. For the fixed position case, the FPP is optimal. The results indicate that when there is no uncertainty in

the target/sensor orientation (fixed position), performing the normalization degrades the performance of the processor. However, when the target positions are uncertain, better performance can be achieved if the output is normalized. Also, the matched filter performance is quite close to the optimal classifier performance for the normalized data. This indicates that applying the sub-optimal processor to normalized data only slightly sacrifices performance, but computational time is reduced significantly. Interestingly, the optimal classifier operating on the normalized data outperforms the optimal classifier operating on the unnormalized data. This occurs because the normalization uncorrelates the signals to a small extent, which improves classification performance [84]. For instance, the average correlation coefficient decrease before and after normalization between the target 2 and 4 is 0.711×10^{-4} .

Table 4.8 illustrates the performance of various processors using measured data. Data was gathered from four out of five targets used in simulations. The sub-optimal processor using normalized data also performs better in general than the processor using raw sensor output, and the optimal processor after normalization achieves better performance than the processor without normalization. This performance improvement validates the hypothesis that by normalizing the sensor data, the uncertainties associated with the sensor/target position can be decreased. Also, the performance of a fixed-position processor operating on normalized data is very close to that of the optimal processor operating on normalized data. However, the computational load is reduced significantly.

4.2.4.3 Discussion

Using wideband frequency-domain EMI data, metal objects of different dimensions and materials can be discriminated via classification algorithms carefully designed

			Probability of Correct Classification			
			Target 1	Target 2	Target 3	Target 4
Fixed Position	No Norm.	FPP/OP	1	1	1	1
	Norm.	FPP/OP	0.976	1	0.976	1
Height Uncertain	No Norm.	FPP	0.351	0.518	0.081	0.620
		OP	0.857	0.997	0.830	1
Horizontal Position Uncertain	Norm.	FPP	0.973	1	0.972	1
		OP	0.977	1	0.978	1
Both Height & Horiz. Position Uncertain	No Norm.	FPP	0.411	0.573	0.085	0.655
		OP	0.828	1	0.810	0.999
	Norm.	FPP	0.849	1	0.754	1
		OP	0.866	1	0.810	1
	Norm.	FPP	0.340	0.506	0.073	0.492
		OP	0.701	0.990	0.700	0.996

Table 4.7: The performance of the various processors before and after normalization using simulated data when (1) target position is known and fixed, (2) $h \sim \mathcal{N}(20\text{cm}, 1.53^2\text{cm}^2)$ and x, y is fixed, (3) horizontal position is uniformly distributed in a 20 cm by 20 cm square and height is fixed, and (4) both height and horizontal position are random, following the distributions mentioned above. ‘No Norm.’ means processing occurred without normalization, ‘Norm.’ means processing followed normalization. ‘OP’ means optimal classifier, and ‘FPP’ indicates fixed position processor.

using signal detection theory. Since the uncertainty inherent in the sensor output is not only due to the additive noise but also the unknown target/sensor orientation, both facts should be considered during the development of the processor. The optimal classifier, which integrates over the uncertainty in the sensor/target orientation, can provide dramatic performance improvement over a fixed-position processor; however, it suffers from a computational burden and is not always practical. For the class of targets considered (target aspect ratio close to one), normalizing the wideband EMI responses, which exploits the physical nature of the signals, mitigates the uncertainties of the response due to the unknown target position. By performing the normalization, a sub-optimal processor can provide significant performance

	Target 1	Target 2	Target 3	Target 4
OP, No Norm.	0.91	0.77	0.69	0.81
OP, Norm.	0	0.98	1	0.99
FPP, No Norm.	0.23	0.24	0.03	0.14
FPP, Norm.	1	0.99	0.89	0.83

Table 4.8: The performance of the sub-optimal and optimal processors before and after normalization evaluated on measured data. ‘FPP’ represents the fixed-position or sub-optimal processor, ‘No Norm.’ means processing occurred without normalization, ‘OP’ represents the optimal processor, and ‘Norm.’ means processing followed normalization

improvement over sub-optimal processors that operate on raw sensor output, and computational time can be dramatically decreased. Since for general targets the frequency-domain EMI response does not simply scale while the target/sensor orientation changes, we will investigate the relationship of the longitudinal and azimuthal modes of the response and integrate this information into the classifier design.

Chapter 5

A Comparison of the Classification Performance of Metallic Objects Using TD and FD EMI Data

In this chapter, a comparison of TD and FD classification performance is described. Theoretical derivations, along with simulated and experimental results are provided.

5.1 Introduction

In the humanitarian and military demining application the metallic clutter present in the environment results in prohibitively high false alarm rates. Recent theoretical and experimental [14, 13, 22, 21, 24, 20, 35, 36] work has indicated that the low frequency scattering from permeable and highly conducting objects is characterized by natural frequencies that are negative and real, and that these resonant frequencies can be used to effect discrimination. Modern computational models have allowed the calculation of these resonant frequencies with knowledge of an object's constitutive parameters, dimensions, and weight. Based on this theory, the time-domain response of a metallic object to a low frequency electromagnetic excitation can be modeled as a sum of weighted exponentials. A frequency-domain response can be modeled via a simple application of the Fourier transform.

A time-domain EMI sensor is usually a pulsed system that contains both a trans-

mitting coil and a receiving coil. After transmitting an excitation pulse, which generates the primary field, the receiving coil records the secondary field after the response due to the excitation pulse has died down, *i.e.* it records the response in the “late time”. TD EMI sensors that are limited to measuring the late time response (an example of one which is not is described in [13]) may be inherently limited in their discrimination performance capabilities because of the information that is lost. Alternatively, EMI sensors can be operated in the frequency-domain, in which case the excitation consists of periodic signals and the sensor measures the static response.

As mentioned above, several researchers have considered the classification of objects as either objects of interest (landmines, UXO) or clutter using data collected by either time-domain (TD) or frequency-domain (FD) devices. Sower *et al.* have considered discrimination of landmines from clutter using a pattern recognition approach which is based on extraction of decay rates from a time-domain signal [13]. Smith *et al.* have considered a complementary approach in which decay rates are extracted from time-domain sensor data and then used to determine whether the object present is a mine or a clutter object [36]. Riggs *et al.* have compared a variety of methods for decay rate extraction, and have successfully used a generalized likelihood ratio test to discriminate between metal objects, again using time-domain data [35]. Collins *et al.* have investigated performance bounds for time-domain data processing [85] as well as the utilization of spatial information [25, 26] to improve the false alarm rate. The difference in this approach is that the entire signal is utilized as opposed to utilizing the extracted decay rates to make a decision. Steedly and Moses have investigated the Cramer-Rao bound for pole and amplitude coefficient estimates of damped exponential signals in noise [86]. Tantum and Collins [37] have evaluated performance bounds for decay rate extraction for landmine-like and UXO targets, and have evalu-

ated the relative performance of detectors which utilize either extracted decay rates or the entire signal. Finally, Gao *et al.* have considered optimal and sub-optimal processors for discrimination of metal objects from frequency-domain EMI data [75], and Keiswetter *et al.* have also described an approach for discriminating UXO from clutter using frequency-domain data [79, 87].

The goal of the work presented in this chapter was to quantify the performance of each type of EMI sensor in terms of system parameters and investigate the trade-offs associated with the sensor design and operational parameters. Parameters to be investigated include the initial sample time, the final sample time, the number of sampled frequencies, the signal-to-noise ratio (SNR), and the sampling method (linear versus logarithmic sampling). Recently, Carin *et al.* performed a preliminary investigation in which a comparison between the classification performance for two objects was made for TD and FD data as a function of the initial sample time [78]. In addition, Tantum and Collins have derived the Cramer-Rao Lower Bound (CRLB) for decay rate estimates from TD data for arbitrary sampling [85]. However, a thorough theoretical and simulation study for classification of multiple objects for both TD and FD data in terms of the various system parameters has not been considered. In this chapter, we present theoretical and simulated classification performance for two and four metal objects using TD and FD EMI data. Classification performance is explored in terms of a variety of system parameters. In addition to the theoretical and simulation studies, experimental data were taken with the PSS-12, a standard army issued metal detector [39], and the GEM-3, a prototype frequency-domain EMI sensor [40, 17] from four objects at a variety of object/sensor orientations. Although the optimal classifier improves performance for both the TD and the FD data, FD classification rates are higher than those for TD systems.

In this chapter, the tradeoffs associated with data taken in the time and frequency domain from a signal processing point of view are considered. In Sec. 5.2 the theoretical analysis of the two-object classification problem using TD or FD data is presented. In the two-object classification case, an analytical expression can be obtained for the probability of correct classification, in all other cases the probability of correct classification must be evaluated numerically. The effects of a variety of parameters on performance are investigated. The theoretical predictions of the performance are compared with simulation results in Sec. 5.3. Next, we discuss classification of four objects using both simulated and experimental data in Sec. 5.4. We consider the scenario where the geometry of the sensor/object position is completely known, as well as the scenario in which the object is located at an unknown position relative to the sensor. A standard approach, which utilizes the signature at the mean position, and a Bayesian optimal approach for discriminating targets, which incorporates the uncertainty associated with underground objects, are discussed. Experimental data were taken with the PSS-12, a standard army issued metal detector, and the GEM-3, a prototype frequency-domain EMI sensor. Finally major findings based on these results are summarized in Sec. 5.5.

5.2 Theory - Classification of Two Objects in the TD and the FD

In this section, the classification performance for two metal objects using TD and FD EMI data is derived. As shown in [14, 13] and mentioned above, the TD EMI response from metal objects can be modeled as a sum of weighted exponential functions. The simplest model, which is often used for landmine and UXO detection problems, con-

sists of a single exponential $y(t) = Ae^{-\alpha t}$. Correspondingly, the simplest model for the FD EMI response is $Y(\omega) = \frac{A}{\alpha+j\omega}$.

5.2.1 Time-Domain Derivations

The task is to decide which of the two objects is present using a TD signal consisting of a single weighted exponential. The derivation follows that provided in [66], and is included here with the parameters of the specific problem that we are considering. A standard assumption is that the sensor is subject to independent and identical distributed (i.i.d.) noise, n . Thus, the outputs of the TD EMI sensor from each of the two objects, O1 and O2, can be modeled as

$$\begin{aligned} O_1 : y_1(t) &= A_1 e^{-\alpha_1 t} + n(t) \\ O_2 : y_2(t) &= A_2 e^{-\alpha_2 t} + n(t) \end{aligned} \quad (5.1)$$

where t is the sample time vector, y_1 and y_2 are the TD responses corresponding to Object 1 and Object 2, respectively. The amplitudes of the responses, A_1 and A_2 , depend on the distance from the sensor to the object, the strength of excitation, etc. The decay rates of the response, α_1 and α_2 , are functions of the conductivity, permeability of the material, etc [14, 13, 20]. The TD response is sampled from T_s to T_2 , and the total number of samples is M . We assume that the noise follows a Gaussian distribution, i.e. $n(t_n) \sim \mathcal{N}(0, \sigma_{n_t}^2)$, where t_n is an arbitrary element of the sample time vector t . Thus, the probability density function (pdf) of the data y given the presence of a particular object is

$$\begin{aligned} p(y|O_1) &= \prod_{i=1}^M p(y_i|O_1) = (2\pi\sigma_{n_t}^2)^{-M/2} \exp\left(-\frac{\sum_{i=1}^M (y_i - A_1 e^{-\alpha_1 t_i})^2}{2\sigma_{n_t}^2}\right) \\ p(y|O_2) &= \prod_{i=1}^M p(y_i|O_2) = (2\pi\sigma_{n_t}^2)^{-M/2} \exp\left(-\frac{\sum_{i=1}^M (y_i - A_2 e^{-\alpha_2 t_i})^2}{2\sigma_{n_t}^2}\right) \end{aligned} \quad (5.2)$$

Letting λ_t denote the ratio of likelihood functions of the data, \mathbf{y} , given whichever

object is present, then $\lambda_t = \frac{p(\mathbf{y}|O_1)}{p(\mathbf{y}|O_2)} = \exp\left(-\frac{\sum_{i=1}^M (y_i - A_1 e^{-\alpha_1 t_i})^2}{2\sigma_{n_t}^2} + \frac{\sum_{i=1}^M (y_i - A_2 e^{-\alpha_2 t_i})^2}{2\sigma_{n_t}^2}\right)$. Thus,

if the *priori* probability that one of the two objects is present is equal (1/2), then when $\lambda_t \geq 1$, a decision of “Object 1 present” is made, otherwise when $\lambda_t < 1$, object 2 is determined to be present by the classifier. After simplification, λ_t can be written as

$$\lambda_t = \exp\left\{-\frac{\sum_{i=1}^M (A_1^2 e^{-2\alpha_1 t_i} - A_2^2 e^{-2\alpha_2 t_i}) - 2 \sum_{i=1}^M y_i (A_1 e^{-\alpha_1 t_i} - A_2 e^{-\alpha_2 t_i})}{2\sigma_{n_t}^2}\right\} \quad (5.3)$$

By taking logarithm and re-arranging constant terms, Equation (5.3) can be further simplified to

$$\sum_{i=1}^M y_i (A_1 e^{-\alpha_1 t_i} - A_2 e^{-\alpha_2 t_i}) = \sigma_{n_t}^2 \log_e \lambda_t + \frac{1}{2} \sum_{i=1}^M (A_1^2 e^{-2\alpha_1 t_i} - A_2^2 e^{-2\alpha_2 t_i}) \quad (5.4)$$

Letting $\lambda'_t = \sum_{i=1}^M y_i (A_1 e^{-\alpha_1 t_i} - A_2 e^{-\alpha_2 t_i})$ and $K = \frac{1}{2} \sum_{i=1}^M (A_1^2 e^{-2\alpha_1 t_i} - A_2^2 e^{-2\alpha_2 t_i})$. When $\lambda_t = 1$, $\lambda'_t = K$. Thus, the decision rule becomes when $\lambda'_t \geq K$, Object 1 is present, otherwise, Object 2 is present.

To simplify notation, let $\mathbf{S}_1 = A_1 e^{-\alpha_1 \mathbf{t}}$ and $\mathbf{S}_2 = A_2 e^{-\alpha_2 \mathbf{t}}$. Then

$$\begin{aligned} \lambda'_t | O_1 &\sim \mathcal{N}(\mathbf{S}_1^T (\mathbf{S}_1 - \mathbf{S}_2), (\mathbf{S}_1 - \mathbf{S}_2)^T (\mathbf{S}_1 - \mathbf{S}_2) \sigma_{n_t}^2) \\ \lambda'_t | O_2 &\sim \mathcal{N}(\mathbf{S}_2^T (\mathbf{S}_1 - \mathbf{S}_2), (\mathbf{S}_1 - \mathbf{S}_2)^T (\mathbf{S}_1 - \mathbf{S}_2) \sigma_{n_t}^2) \end{aligned} \quad (5.5)$$

Letting $\mu_{1t} = \mathbf{S}_1^T (\mathbf{S}_1 - \mathbf{S}_2)$, $\mu_{2t} = \mathbf{S}_2^T (\mathbf{S}_1 - \mathbf{S}_2)$, $\sigma_t^2 = (\mathbf{S}_1 - \mathbf{S}_2)^T (\mathbf{S}_1 - \mathbf{S}_2) \sigma_{n_t}^2$. Then

$$\begin{aligned} \lambda'_t | O_1 &\sim \mathcal{N}(\mu_{1t}, \sigma_t^2) \\ \lambda'_t | O_2 &\sim \mathcal{N}(\mu_{2t}, \sigma_t^2) \end{aligned} \quad (5.6)$$

Since the correct classification probability of Objects 1 and 2 is defined as [55]

$$\begin{aligned} P_{c_1} &= \int_{K}^{\infty} p_{\lambda'_t | O_1}(\lambda'_t | O_1) d\lambda'_t, \\ P_{c_2} &= \int_{-\infty}^{K} p_{\lambda'_t | O_2}(\lambda'_t | O_2) d\lambda'_t. \end{aligned} \quad (5.7)$$

Letting $z = \frac{\lambda'_t - \mu_{1t}}{\sigma_t}$, then

$$P_{c_1} = \int_K^{\infty} \frac{1}{\sqrt{2\pi\sigma^2}} e^{-\frac{(\lambda'_t - \mu_{1t})^2}{2\sigma^2}} d\lambda'_t = \int_{\frac{K - \mu_{1t}}{\sigma_t}}^{\infty} \frac{1}{\sqrt{2\pi}} e^{-\frac{z^2}{2}} dz = cerf\left(\frac{K - \mu_{1t}}{\sigma_t}\right) \quad (5.8)$$

Similarly,

$$P_{c_2} = 1 - cerf\left(\frac{K - \mu_{2t}}{\sigma_t}\right) \quad (5.9)$$

where $cerf(\cdot)$ is the complementary error function defined as $cerf(x) = \int_x^{\infty} \frac{1}{\sqrt{2\pi}} e^{-t^2} dt$.

Also, the probability of deciding that Object 2 is present given that Object 1 is present is $1 - P_{c_1}$, and the probability of deciding that Object 1 is present given that Object 2 is present is $1 - P_{c_2}$.

From the analytical expressions of Equations (5.8) and (5.9), it is possible to determine how the classification performance is affected by a variety of parameters. The effect of system design parameters, such as the initial sample time, the final sample time, and sampling rate, as well as system operation parameters, such as the sampling strategy, can be evaluated. In Sec. 5.3, the theoretical prediction of the classification performance is compared with that obtained via simulation using synthesized TD EMI data. Although we compare performance for a particular case of two objects, the approach could be used for any set of objects, as is described in Sec. 5.4.

5.2.2 Frequency-Domain Derivations

For FD classification we consider two types of noise: 1) i.i.d. FD noise, which corresponds to a FD sensor which sweeps over a frequency range using sinusoidal excitation at one frequency sequentially (the sensor outputs are the FD EMI response plus additive noise); 2) FD noise that is equivalent to the TD i.i.d. noise, *i.e.* the i.i.d. noise present in the TD is transformed to the FD. Considering the second type of noise allows us to evaluate the effect of various parameters without the confounding factor of signal-to-noise ratio or differences in the actual generation of the noise process. The derivation of the distribution of this “equivalent” noise is provided in Sec. 5.2.2.2. The FD signal for the two objects is modeled as:

$$\begin{aligned} O_1 : Y_1(\mathbf{w}) &= \frac{A_1}{\alpha_1 + j\mathbf{w}} + N(\mathbf{w}) \\ O_2 : Y_1(\mathbf{w}) &= \frac{A_2}{\alpha_2 + j\mathbf{w}} + N(\mathbf{w}) \end{aligned} \quad (5.10)$$

where \mathbf{w} is a L by 1 vector of sample frequencies, $\mathbf{w} = [\omega_1, \omega_2, \dots, \omega_L]'$. The real part of the FD response due to Object 1 is denoted by \mathbf{R}_1 , and the imaginary part is denoted by \mathbf{I}_1 . Similarly, \mathbf{R}_2 and \mathbf{I}_2 denote the real and imaginary parts of the FD responses due to Object 2. $\mathbf{R}_1 = \frac{A_1 \alpha_1}{\alpha_1^2 + \mathbf{w}^2}$, $\mathbf{I}_1 = -\frac{A_1 \mathbf{w}}{\alpha_1^2 + \mathbf{w}^2}$, $\mathbf{R}_2 = \frac{A_2 \alpha_2}{\alpha_2^2 + \mathbf{w}^2}$, and $\mathbf{I}_2 = -\frac{A_2 \mathbf{w}}{\alpha_2^2 + \mathbf{w}^2}$.

5.2.2.1 i.i.d. FD noise

It is assumed that the FD noise is white Gaussian, *i.e.* $N(\mathbf{w}) \sim \mathcal{N}(0, \sigma_{n_f}^2 \mathbf{I})$, where \mathbf{I} is an identity matrix. The noise in the real part and the imaginary part are independent, since sine and cosine are orthogonal functions. We further assume that the variances are equal, *i.e.* $N_R(\mathbf{w}) \sim \mathcal{N}(0, \frac{1}{2} \sigma_{n_f}^2 \mathbf{I})$, and $N_I(\mathbf{w}) \sim \mathcal{N}(0, \frac{1}{2} \sigma_{n_f}^2 \mathbf{I})$, where N_R and N_I are

the real part and imaginary part of the complex noise. Thus, $\mathbf{Y}_{1R} \sim \mathcal{N}(\mathbf{R}_1, \frac{1}{2}\sigma_{n_f}^2 \mathbf{I})$, $\mathbf{Y}_{1I} \sim \mathcal{N}(\mathbf{I}_1, \frac{1}{2}\sigma_{n_f}^2 \mathbf{I})$, $\mathbf{Y}_{2R} \sim \mathcal{N}(\mathbf{R}_2, \frac{1}{2}\sigma_{n_f}^2 \mathbf{I})$, and $\mathbf{Y}_{2I} \sim \mathcal{N}(\mathbf{I}_2, \frac{1}{2}\sigma_{n_f}^2 \mathbf{I})$. Therefore, the likelihood of \mathbf{Y} when Object 1 is present is

$$p(\mathbf{Y}|O_1) = p(\mathbf{Y}_R|O_1)p(\mathbf{Y}_I|O_1) = \frac{1}{(\pi\sigma_{n_f}^2)^L} \exp\left\{-\frac{\sum_{i=1}^L (Y_{Ri} - R_{1i})^2}{\sigma_{n_f}^2} - \frac{\sum_{i=1}^L (Y_{Ii} - I_{1i})^2}{\sigma_{n_f}^2}\right\} \quad (5.11)$$

where \mathbf{Y} is the complex FD data, \mathbf{Y}_R is the real part of \mathbf{Y} and \mathbf{Y}_I is the imaginary part of \mathbf{Y} . Similarly, for Object 2,

$$p(\mathbf{Y}|O_2) = \frac{1}{(\pi\sigma_{n_f}^2)^L} \exp\left\{-\frac{\sum_{i=1}^L (Y_{Ri} - R_{2i})^2}{\sigma_{n_f}^2} - \frac{\sum_{i=1}^L (Y_{Ii} - I_{2i})^2}{\sigma_{n_f}^2}\right\} \quad (5.12)$$

Denoting the ratio of the above two likelihood functions by $\lambda_f = \frac{p(\mathbf{Y}|O_1)}{p(\mathbf{Y}|O_2)}$, then,

$$\lambda_f = \exp\left\{-\frac{1}{\sigma_{n_f}^2} [\sum_{i=1}^L (Y_{Ri} - R_{1i})^2 + \sum_{i=1}^L (Y_{Ii} - I_{1i})^2 - \sum_{i=1}^L (Y_{Ri} - R_{2i})^2 - \sum_{i=1}^L (Y_{Ii} - I_{2i})^2]\right\} \quad (5.13)$$

Based on detection theory, for equal *priori* probability that Object 1 or Object 2 is present, when λ_f is greater than 1, we say Object 1 is present, otherwise, Object 2 is present. By taking the natural logarithm of Equation (5.13) and rearranging the constant terms, the expression above can be simplified to

$$\sum_{i=1}^L [Y_{Ri}(R_{1i} - R_{2i}) + Y_{Ii}(I_{1i} - I_{2i})] = \frac{1}{2}\sigma_{n_f}^2 \log_e \lambda_f + K_f \quad (5.14)$$

where $K_f = \frac{1}{2} \sum_{i=1}^L (R_{1i}^2 - R_{2i}^2 + I_{1i}^2 - I_{2i}^2)$. Letting $\lambda'_f = \sum_{i=1}^L [Y_{Ri}(R_{1i} - R_{2i}) + Y_{Ii}(I_{1i} - I_{2i})]$.

The decision rule becomes if $\lambda'_f \geq K_f$, then Object 1 is present, otherwise, Object 2 is present.

Based on the statistics derived above,

$$\lambda'_f | O_1 \sim \mathcal{N}\left(\sum_{i=1}^L R_{1i}(R_{1i} - R_{2i}) + I_{1i}(I_{1i} - I_{2i}), \sum_{i=1}^L [(R_{1i} - R_{2i})^2 + (I_{1i} - I_{2i})^2] \frac{1}{2} \sigma_{n_f}^2\right) \quad (5.15)$$

To simplify notation, letting $\mu_{1f} = \sum_{i=1}^L [R_{1i}(R_{1i} - R_{2i}) + I_{1i}(I_{1i} - I_{2i})]$ and $\sigma_f^2 = \frac{1}{2} \sigma_{n_f}^2 \sum_{i=1}^L [(R_{1i} - R_{2i})^2 + (I_{1i} - I_{2i})^2]$. Similarly,

$$\lambda'_f | O_2 \sim \mathcal{N}(\mu_{2f}, \sigma_f^2) \quad (5.16)$$

where $\mu_{2f} = \sum_{i=1}^L [R_{2i}(R_{1i} - R_{2i}) + I_{2i}(I_{1i} - I_{2i})]$.

The correct classification probability for Object 1 and Object 2 is defined as

$$\begin{aligned} P_{c_1} &= \int_{K_f}^{\infty} p_{\lambda'_f | O_1}(\lambda'_f | O_1) d\lambda'_f, \\ P_{c_2} &= \int_{-\infty}^{K_f} p_{\lambda'_f | O_2}(\lambda'_f | O_2) d\lambda'_f. \end{aligned} \quad (5.17)$$

Using the same variable exchange as in Sec. 5.2.1,

$$\begin{aligned} P_{c_1} &= cerf\left(\frac{K_f - \mu_{1f}}{\sigma_f}\right) \\ P_{c_2} &= 1 - cerf\left(\frac{K_f - \mu_{2f}}{\sigma_f}\right) \end{aligned} \quad (5.18)$$

Using the expression of Equation (5.18), the effects of sample frequency spacing, frequency range, sampling strategy, and noise variance can be evaluated. In Sec. 5.3, the performance as a function of these parameters is presented.

5.2.2.2 FD Noise Equivalent to i.i.d. TD noise

First, the distribution of FD noise that is equivalent to i.i.d. TD Gaussian noise is derived. Since negative time has no physical meaning, only noise at the positive time indices is considered. We let $n(t)$ denotes the TD i.i.d. noise with a mean of μ and variance of σ^2 . In order to obtain the distribution of the equivalent noise in the FD, we take Fourier transform. $N(\omega) = \int_{-\infty}^{\infty} n(t)u(t)e^{-j\omega t}dt = \int_0^{\infty} n(t)e^{-j\omega t}dt$, where $u(t)$ is the step function. Since the Fourier Transform is a linear transformation, the resulting distribution for $N(\omega)$ is still Gaussian. Thus, to fully quantify the distribution, we only need to derive the mean vector and the covariance matrix. The expectation of $N(\omega)$ is calculated via

$$\begin{aligned} E[N] &= E\left[\int_0^{\infty} n(t)e^{-j\omega t}dt\right] = \int_{-\infty}^{\infty} \int_0^{\infty} n(t)e^{-j\omega t}dt f_n dn \\ &= \int_0^{\infty} e^{-j\omega t} \int_{-\infty}^{\infty} n(t)f_n dn dt = \mu \int_0^{\infty} e^{-j\omega t} dt \\ &= \mu \text{FT}[u(t)] = \mu[\pi\delta(\omega) + \frac{1}{j\omega}] \end{aligned} \quad (5.19)$$

where $\delta(\omega) = \begin{cases} 1 & \omega = 0 \\ 0 & \omega \neq 0 \end{cases}$, $j^2 = -1$, and

$$\begin{aligned} E[N(\omega_i)N(\omega_j)^*] &= \int_{-\infty}^{\infty} f_n \int_0^{\infty} n(t_1)e^{-j\omega_i t_1} dt_1 \int_0^{\infty} n(t_2)e^{j\omega_j t_2} dt_2 dn \\ &= \int_0^{\infty} \int_0^{\infty} \left[\int_{-\infty}^{\infty} f_n \cdot n(t_1)n(t_2) dn \right] e^{-j\omega_i t_1} e^{j\omega_j t_2} dt_1 dt_2 \\ &= \int_0^{\infty} \int_0^{\infty} (\sigma^2 + \mu^2)\delta(t_1 - t_2)e^{-j\omega_i t_1} e^{j\omega_j t_2} dt_1 dt_2 \\ &= \int_0^{\infty} (\sigma^2 + \mu^2)e^{-j(\omega_i - \omega_j)t} dt \\ &= \pi (\sigma^2 + \mu^2)\delta(\omega_i - \omega_j) + \frac{(\sigma^2 + \mu^2)}{j(\omega_i - \omega_j)} \end{aligned} \quad (5.20)$$

where $f_n = \frac{1}{\sqrt{2\pi}\sigma^2} \int_{-\infty}^{\infty} e^{-n^2/(2\sigma^2)} dn$.

For the problem we consider here and that observed in most cases, the mean of the TD noise is zero. Also most FD sensors do not measure the response at zero frequency, such as the GEM-3, thus, the mean of the FD noise is zero and the variance is $\pi\sigma^2$ for every sample frequency. The elements of the covariance matrix are given by

$$C_{ij} = \sigma^2[\pi\delta(\omega_i - \omega_j) + \frac{1}{j(\omega_i - \omega_j)}] \quad (5.21)$$

$$i.e. \mathbf{C} = \begin{bmatrix} \pi\sigma^2 & \frac{\sigma^2}{j(\omega_1 - \omega_2)} & \frac{\sigma^2}{j(\omega_1 - \omega_3)} & \cdots & \frac{\sigma^2}{j(\omega_1 - \omega_L)} \\ \frac{\sigma^2}{j(\omega_2 - \omega_1)} & \pi\sigma^2 & & \ddots & \frac{\sigma^2}{j(\omega_2 - \omega_L)} \\ \vdots & & \ddots & & \vdots \\ \frac{\sigma^2}{j(\omega_{L-1} - \omega_1)} & & & \pi\sigma^2 & \frac{\sigma^2}{j(\omega_{L-1} - \omega_L)} \\ \frac{\sigma^2}{j(\omega_L - \omega_1)} & \frac{\sigma^2}{j(\omega_L - \omega_2)} & \cdots & \frac{\sigma^2}{j(\omega_L - \omega_{L-1})} & \pi\sigma^2 \end{bmatrix}$$

In practice, the difference between adjacent sample frequencies, $(\omega_{i+1} - \omega_i)$, is large, on the order of hundreds or even thousands of Hz, thus, $1/(\omega_j - \omega_i)$ for $i \neq j$ is very small. Therefore, the terms on the upper and lower triangular of the covariance matrix can be considered as zero compared to the variance (diagonal terms), which means that the FD noise which is equivalent to TD i.i.d. noise is approximately $\mathcal{N}(0, \pi\sigma^2\mathbf{I})$, where \mathbf{I} is an identity matrix. Clearly, this case can be simplified to the i.i.d. noise considered in Section 5.2.2.1, thus, it is not necessary to consider this case separately in the following analyses.

5.3 Simulation Results for Classification Performance of Two Objects

In Sec. 5.2.1 and 5.2.2, the theoretical classification performance for discriminating two objects for both TD and FD data was derived. In this section, synthetic data are used to simulate the effects on performance due to manipulation of the various parameters, and the results are compared to the theoretical predictions. The mechanism by which we determine the appropriate bandwidth of the FD signal and the final sample time for the TD signal are described in the Appendix.

5.3.1 Comparison of TD simulations and their theoretical predictions

In this section we consider the effects of linear versus logarithmic sampling strategy, the initial and final sample time, and SNR on classification performance for TD data. The TD responses for the two objects are $y_1(t) = e^{-500t}$, $y_2(t) = 0.8e^{-1000t}$.

First, we simulate linearly and logarithmically spaced time samples of the exponential curves and vary the initial sample time (T_s). The sampling period remained fixed. The noise variance at each sample time is 0.8^2 , resulting in an average signal to noise ratio of -19.2 dB for Object 1 and -34.8 dB for Object 2. Figure 5.1 illustrates the classification performance by plotting the percent correct classification for each object as a function of the initial sample time along with the theoretical prediction. The left hand panel shows results for linear sampling, the right hand panel shows results for logarithmic sampling. For this particular problem, the theoretical probability of correct classification for Object 1 and Object 2 is identical, thus only one symbol is used for the theoretical value. A good match between the

theoretical predictions and the simulation results is observed. As shown in Figure 5.1, for the linearly sampled data the performance decreases monotonically as the initial sample time increases, while for the logarithmically sampled data, an increase in the performance occurs followed by a decrease in performance. The location where the maximum occurs depends on the location of the samples, the final sample time, and the noise variance. This effect results from the difference between the SNR of the signals due to the two objects. The performance depends on the difference between the signals, so placing samples where this difference is maximized improves performance. Selecting sampling times optimally has been considered previously by Cambanis and Masry [88].

Next, we investigate the effect of the final sample time. Figure 5.2 shows the classification performance of both the theoretical prediction and simulations for both objects as a function of the final sample time. Again, the theoretical and simulation results agree well. It is apparent that increasing the final sample time initially results in an increase in performance, however performance eventually saturates. Since the exponential decays to zero, as the final sample time increases the SNR will not continue to increase, and performance plateaus.

Finally, we verify the effect of increasing the noise variance, or decreasing the SNR on classification performance. Figure 5.3 illustrates the effect of the noise variance on classification performance for both linear and logarithmic sampling schemes. A monotonic relationship is observed as the noise variance increases from 0.1^2 to 2^2 . Overall, logarithmic sampling provides better performance than linear sampling, as this sampling strategy places more samples during the early time when the SNR is largest.

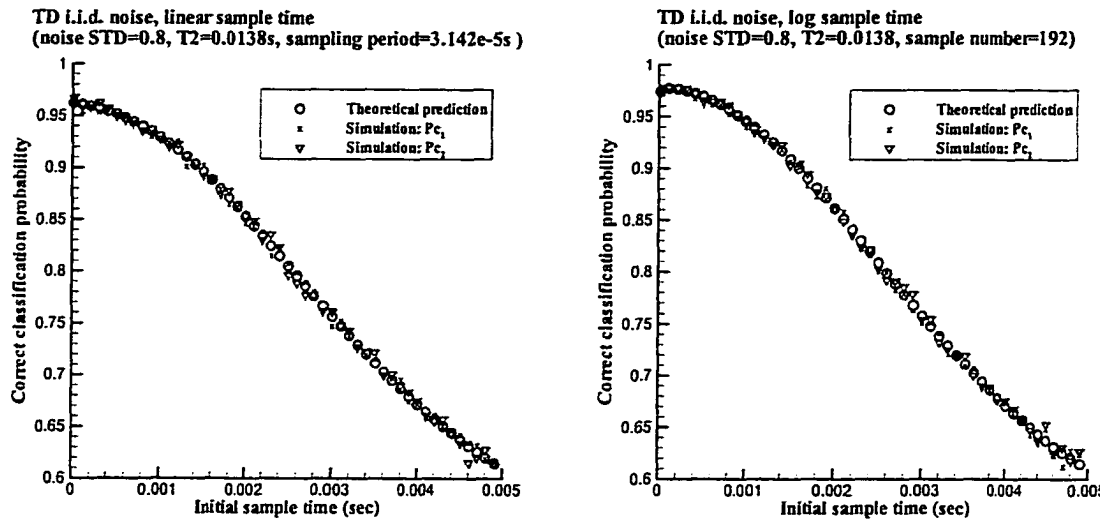


Figure 5.1: Comparison of the theoretical prediction (o) and simulation (x and *) of classification performance as a function of initial sample time using linear (left) and logarithmic (right) sample schemes for TD data. The final sample time T_2 is 0.0138s, the noise standard deviation (STD) is 0.8, and the sampling period is 3.142e-4s

5.3.2 Comparison of FD simulations and their theoretical predictions

In this section, the effects of the number of sample frequencies and the SNR on performance for the two types of noise proposed above are investigated. The FD responses for the two objects used for theoretical prediction and simulation are

$$Y_1(w) = \frac{1}{500 + jw}, Y_2(w) = \frac{0.8}{1000 + jw}.$$

The number of sample frequencies used was varied from 5 to 300, and the noise variance was fixed at 4e-4. Figure 5.4 illustrates the classification performance of both the theoretical prediction and the simulation results for linear and logarithmic sample spacing. The results of Figure 5.4 indicate that for these two objects, logarithmic frequency spacing provides better classification performance than linear frequency

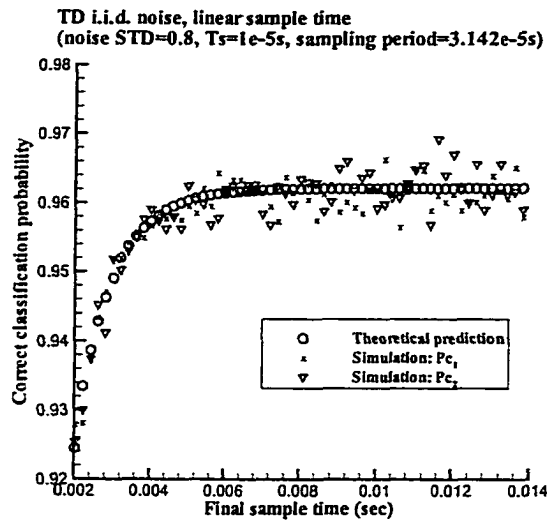


Figure 5.2: Comparison of theoretical prediction (o) and simulation (x and *) classification performance as a function of final sample time using linear sample scheme for TD data. The initial sample time T_s is 1e-5s, the noise standard deviation (STD) is 0.8.

spacing for a given number of frequency samples. Again, the optimal frequency spacing could be derived using the approach described by Cambanis and Masry [88].

Next, the noise variance is increased from 1e-4 to 1.5e-3 using linear and logarithmic frequency sampling for the i.i.d. FD noise and classification performance curves are shown in Figure 5.5. As expected, when the noise variance increases, the performance drops as a result of the decreasing SNR. Performance drops faster for linear frequency spacing than for logarithmic frequency spacing for these two objects. Note that at a variance of $(1.5e - 4)^2$ for the FD data, which is, on average, equivalent to the 0.8^2 variance in the TD data, the $T_s = 0$ data in Figure 5.1 is equivalent to the FD performance in Figure 5.5. This indicates that, as expected, when all of the time-domain information is available, the performance is identical to that obtained with adequately sampled frequency domain data.

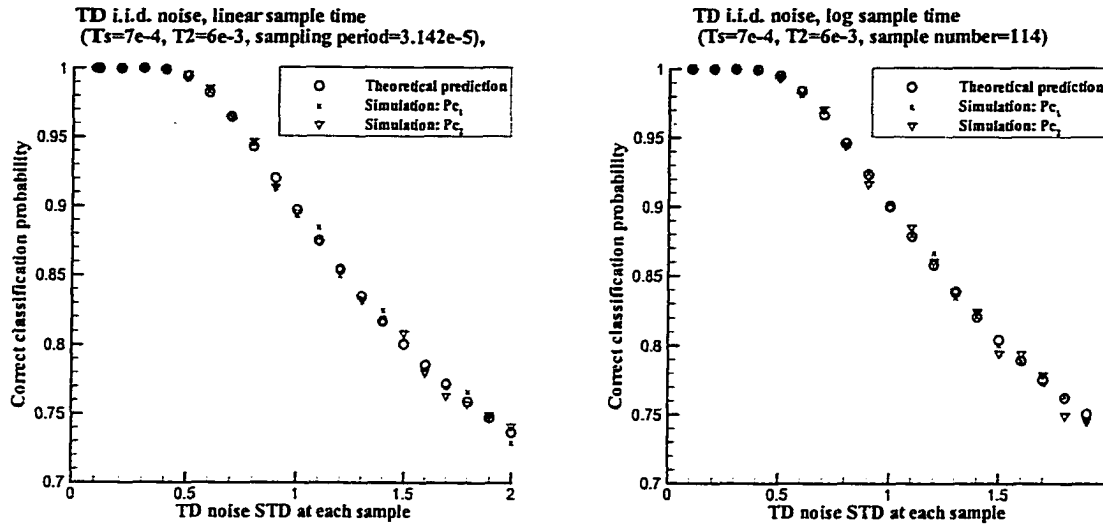


Figure 5.3: Comparison of theoretical prediction (o) and simulation (x and *) of classification performance as a function of noise variance using linear (left) and logarithmic (right) sample schemes for TD data. The initial sample time T_s is 7e-4s and the final sample time T_2 is 6e-3s.

5.4 Classification of Four Objects

The previous section compared theoretical and simulated results for the problem of classifying two objects using time-domain and frequency-domain data. Performance was considered as a function of several design and operational parameters. For the landmine and UXO detection problem, one is interested in discriminating multiple targets from multiple clutter objects in order to reduce the high false alarm rate associated with current systems. Therefore, in this section we evaluate the classification performance for four objects using synthesized TD and FD data. There is no closed form theoretical solution to this problem, however performance can be analyzed via simulation. This extends the analysis described in Sec. 5.2 by considering more than two objects and adopts a more accurate signal model. In addition, data from an experimental study using both TD and FD sensors for the classification of four metal objects is considered.

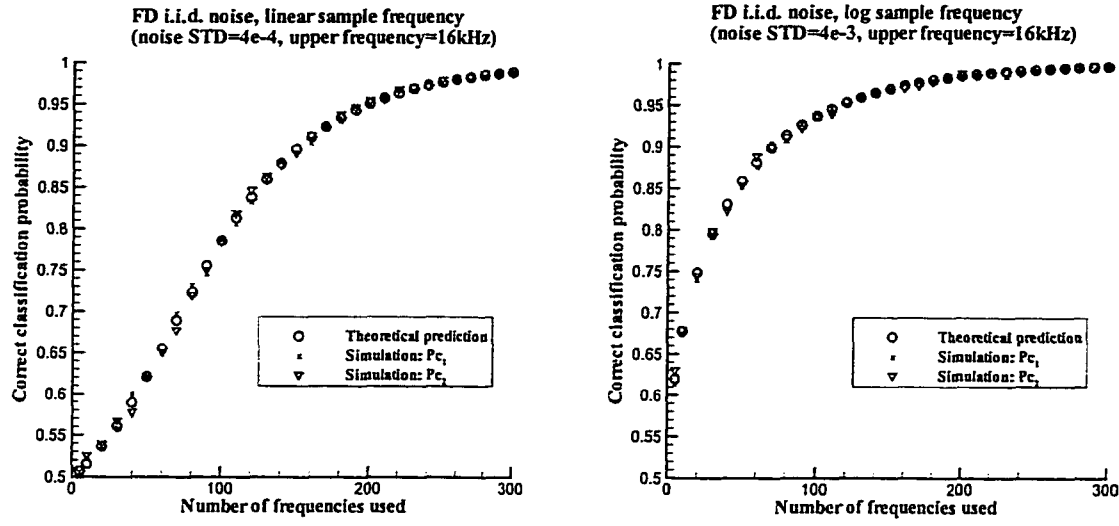


Figure 5.4: Comparison of theoretical prediction of classification performance (o) and simulation (x and *) as a function of number of sample frequencies using linear (left) and logarithmic (right) sample schemes for FD data. The noise standard deviation is 4e-4 for linear sampling case and 4e-3 for logarithmic sampling and the upper sample frequency is 16 kHz.

5.4.1 Simulation study

The signal model adopted for the simulation study is more consistent with the data measured in real-world scenarios involving landmine and UXO detection. A weighted sum of two exponential signals is used, where we do not always assume that we know the relative weights of the amplitudes. For the TD systems, the received data from the sensor is modeled as

$$y_j(t) = A_{j1}e^{-\alpha_{j1}t} + A_{j2}e^{-\alpha_{j2}t} + n(t) \quad (5.22)$$

where $j = 1, 2, 3, 4$, corresponding to the j^{th} object, t is the sample time vector, and $S_j(t) = A_{j1}e^{-\alpha_{j1}t} + A_{j2}e^{-\alpha_{j2}t}$. For the FD systems, the signal model is

$$Y_j(w) = \frac{A_{j1}}{\alpha_{j1} + jw} + \frac{A_{j2}}{\alpha_{j2} + jw} + N(w) = R_j(w) + N_R(w) + j(I_j(w) + N_I(w)) \quad (5.23)$$

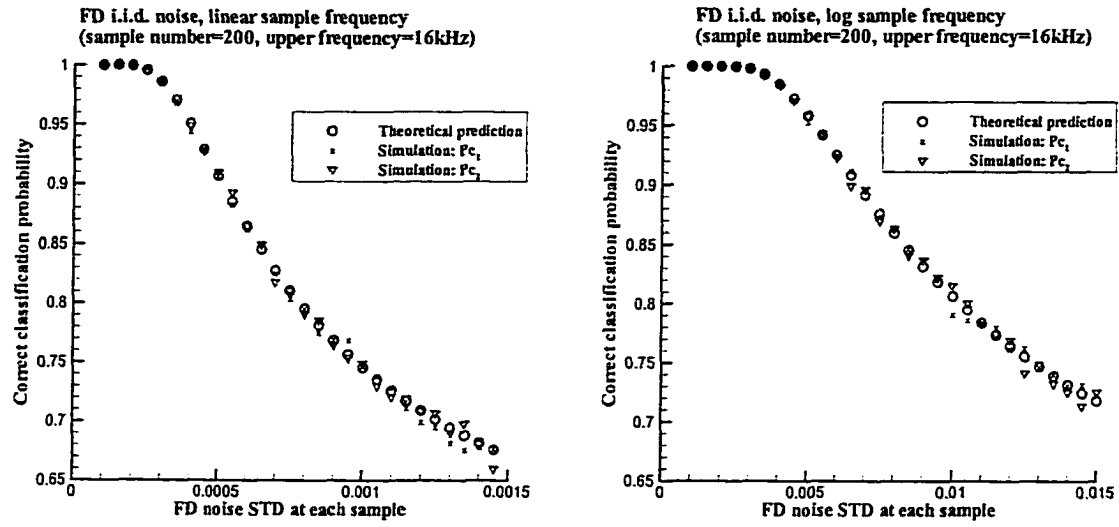


Figure 5.5: Comparison of theoretical prediction of classification performance (o) and simulation (x and *) as a function of noise variance using linear (left) and logarithmic (right) sample schemes for FD i.i.d. noise. The number of sample frequency is 200.

where R_j and I_j are the real and imaginary parts of the FD response due to the j^{th} object, N_R and N_I are the real and imaginary parts of the noise, and \mathbf{w} is the sample frequency vector.

5.4.1.1 Fixed Amplitude

For the TD signal, let y denote the output from the sensor. If the object is at a fixed known position, then the amplitudes and decay rates that define the response are also fixed. The signals used for the simulation are plotted in Figure 5.6. In [27], it is shown that the optimal classifier for the fixed position case has the form

$$\max_j \left\{ \sum_{k=1}^M (y_k - S_{jk})^2 \right\} \quad (5.24)$$

where y_k is the received data at the k^{th} sample time, S_{jk} is the TD signature of the j^{th} object at the k^{th} sample time, and M is the length of the signal.

For the FD signal, the real and imaginary parts of the response for the objects used for simulation are plotted in Figure 5.7. The optimal classifier for the FD signal with i.i.d. FD noise is of similar form to Equation (5.24) when the real and imaginary parts are independent, as is the case.

$$\max_j \left\{ \sum_{k=1}^M (Y_{Rk} - R_{jk})^2 + (Y_{Ik} - I_{jk})^2 \right\} \quad (5.25)$$

where Y_{Rk} and Y_{Ik} are the real and imaginary parts of the received FD data at the k^{th} sample frequency, R_{jk} and I_{jk} are the real and imaginary parts of the FD signature of the j^{th} object at the k^{th} sample frequency, and M is the length of the signal.

For the FD noise, which is equivalent to TD i.i.d. noise, the optimal classifier for this type of noise has the form

$$\max_j \{ [Y - (R_j + jI_j)]^* C^{-1} [Y - (R_j + jI_j)] \} \quad (5.26)$$

When the sample frequency spacing is in the order of hundred Hz or higher, Equation (5.26) can be approximately simplified to Equation (5.25).

Results for the TD Data As in Sec. 5.2, the effects of the initial sample time, the final sample time, the noise variance and sampling strategies (linear and logarithmic sampling) are investigated. Figure 5.8 illustrates the effect of the initial sample time on the performance for four-object classification problem. An interesting pattern for the classification performance of Object 3 and Object 4 is observed. By inspecting Figure 5.6, it can be seen that the responses of Objects 3 and 4 have an intersection point since the early time response of Object 3 is larger than that of Object 4; however, the response of Object 3 decreases faster than the response of Object 4. Thus,

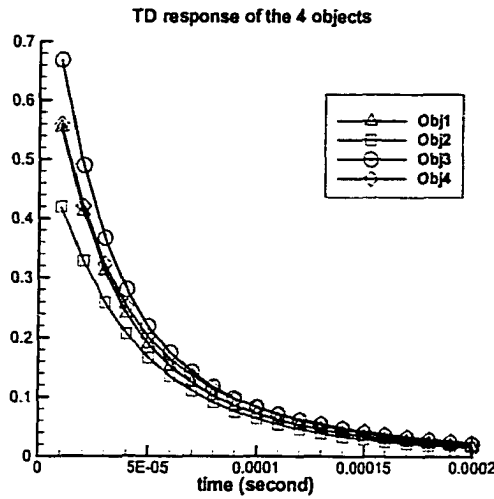


Figure 5.6: The TD responses of the 4 objects used in this study

when the initial sample time is prior to the intersection point, the signal energy for Object 3 is larger than that of Object 4, and when the initial sample time increases beyond the intersection point, the energy of Object 4 is larger. Therefore, the classification performance for Object 4 decreases, then increases as a function of the initial sample time. For Objects 1 and 2, a monotonic decrease in classification performance is observed. For the same noise variance and initial sample time, the performance using logarithmic sampling is better than that obtained using linear sampling. This results occur since the logarithmic approach has more samples in the early time and less in late time, resulting in a higher SNR if the noise level is identical across the sampling interval.

Figure 5.9 summarizes the effect that the final sample time has on classification performance. As the final sample time increases the performance increases then saturates, as was the case with the two-object classification problem. A similar trend is observed with the logarithmically sampled data. Figure 5.10 illustrates the per-

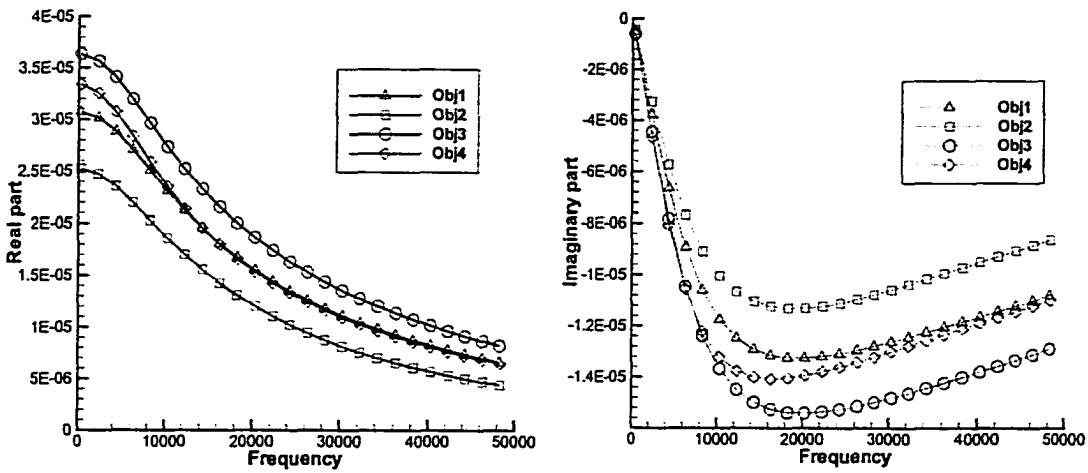


Figure 5.7: The FD responses of the 4 objects used in this study (left - real part and right - imaginary part).

formance as a function of the noise variance. Note that the performance decreases faster for linear sampling than for logarithmic sampling as a function of noise variance.

Results for the FD Data The performance of the classifier described by Equations (5.25) and (5.26) as a function of the number of sample frequencies and the noise variance for two types of noises in the FD were investigated.

First, i.i.d. noise at each sample frequency is considered. As illustrated in Figure 5.11, performance increases as the number of frequency samples increases in a similar fashion for both linear and logarithmic frequency sampling. Classification performance drops as the noise variance increases, as shown in Figure 5.12, and the decrease in performance is more rapid for linear sampling than for logarithmic sampling.

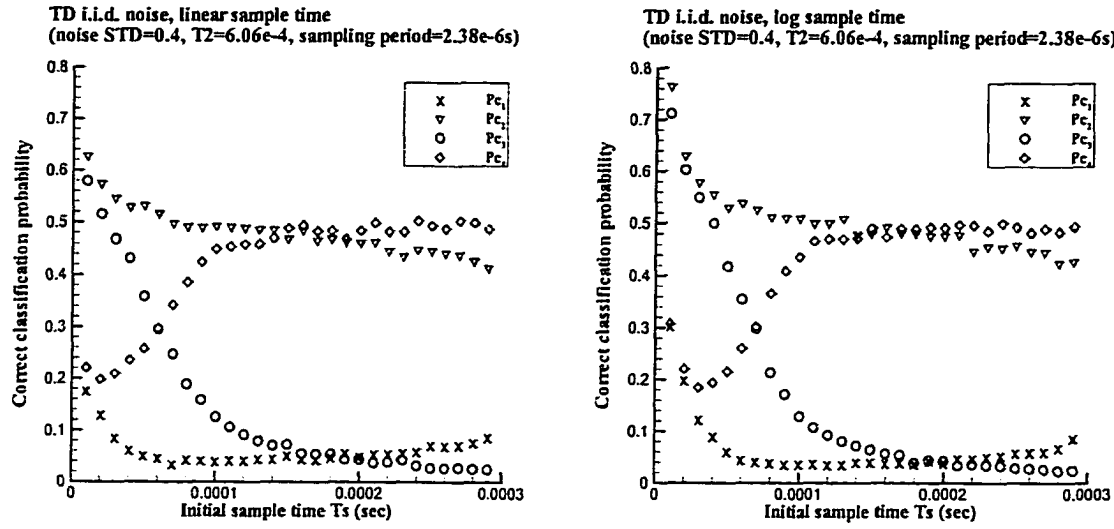


Figure 5.8: Classification performance of the 4 objects as a function of the initial sample time using TD linear (left) and logarithmic (right) samples for TD data. The noise standard deviation is 0.4, the final sample time is 6.06e-4s, and the sample period is 2.38e-6s.

5.4.1.2 Uncertain Amplitude

When the distance from the sensor to the underground object is unknown, the resulting responses are of uncertain magnitude (*i.e.*, A_1 and A_2 in the model). Based on experimental data (described in Sec. 5.4.2), A_1 and A_2 in Equation (5.22) can be modeled as correlated Gaussian random variables. Their mean vectors and covariance matrices, which are obtained from the experimental data, are listed in Table 5.1. For the uncertain amplitude case, the classifiers defined in Equations (5.24), (5.25), and (5.26) using the mean amplitude (referred as fixed position processor, or FPP) no longer corresponds to the optimal solution. In order to achieve better performance, the optimal processor (OP), which requires integration over the uncertain parameters [27], is used. In the following, the amplitudes, A_1 and A_2 , were simulated using a linear transformation of the Cholesky square root of desired covariance matrix times independent Normal random vector ($\mathcal{N}(0, 1)$) [89].

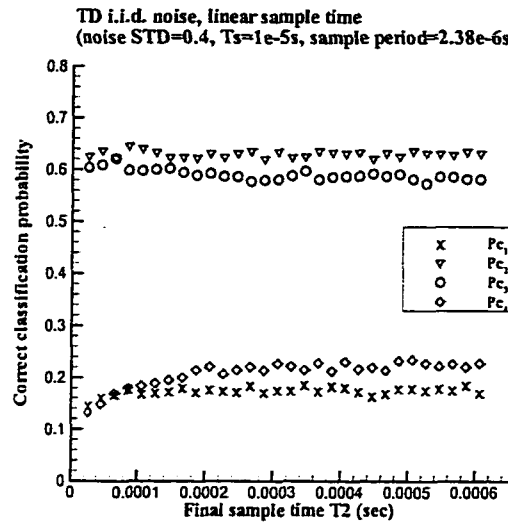


Figure 5.9: Classification performance of the 4 objects as a function of the final sample time using TD linear samples. The initial sample T_s is $1e-5$ s and the noise standard deviation is 0.4.

Results for the TD Data First, we compare the performance of the FPP operating on both the fixed amplitude and uncertain amplitude data as a function of the initial sample time, the final sample time, and the noise variance. The classification performance of the FPP classifier as a function of the initial sample time is shown in Figure 5.13. The results can be compared to those shown in Figure 5.8, in which no uncertainty was present. Clearly, when the amplitudes are uncertain, performance degrades. Figure 5.14 shows classification performance as a function of the final sample time, and the trends in performance are the same as for the fixed amplitude case, but with lower classification performance (see Figure 5.9). The effect of the TD noise variance for the uncertain amplitude case using linear and logarithmic sampling is shown in Figure 5.15, and again, the performance is similar in form but lower in absolute performance level than for the fixed amplitude case.

Next, we consider the performance of the OP. For the sake of brevity, only linearly sampled data is presented. In order to compare performance of the FPP and

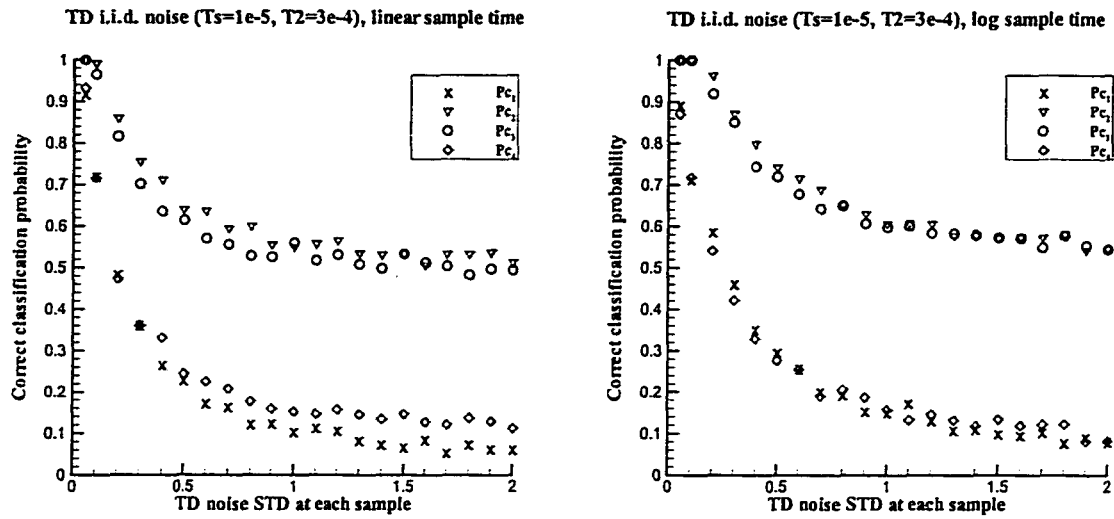


Figure 5.10: Classification performance of the 4 objects as a function of the noise variance $\sigma_{n_t}^2$ using TD linear (left) and logarithmic (right) samples. The initial sample time T_s is 1e-5s and the final sample time T_2 is 3e-4s.

the OP, Figures 5.16, 5.17 and 5.18 plot the performance of both the FPP (left) and the OP (right). Averaged across all objects, the OP performance is better than that of the FPP for the uncertain amplitude case. The trends in the OP performance as a function of the final sample time and the noise variance differ from those of the FPP. The FPP is solely based on the mean response. The mean response of Object 3 is the largest among the four objects and that of Object 2 is the smallest, and the mean response of Objects 1 and 4 are similar for the initial and final sample times considered. Therefore, the correct classification percentages of Objects 2 and 3 are highest, and those of Objects 1 and 4 are smaller. The OP incorporates the parameter uncertainty, which makes the classification performance of each object more accurate.

Results for FD i.i.d. noise First, we consider the performance of the FPP as the number of frequency samples increases for both linear and logarithmic sampling. Figure 5.19 in the left hand panel illustrates a similar pattern of results as those

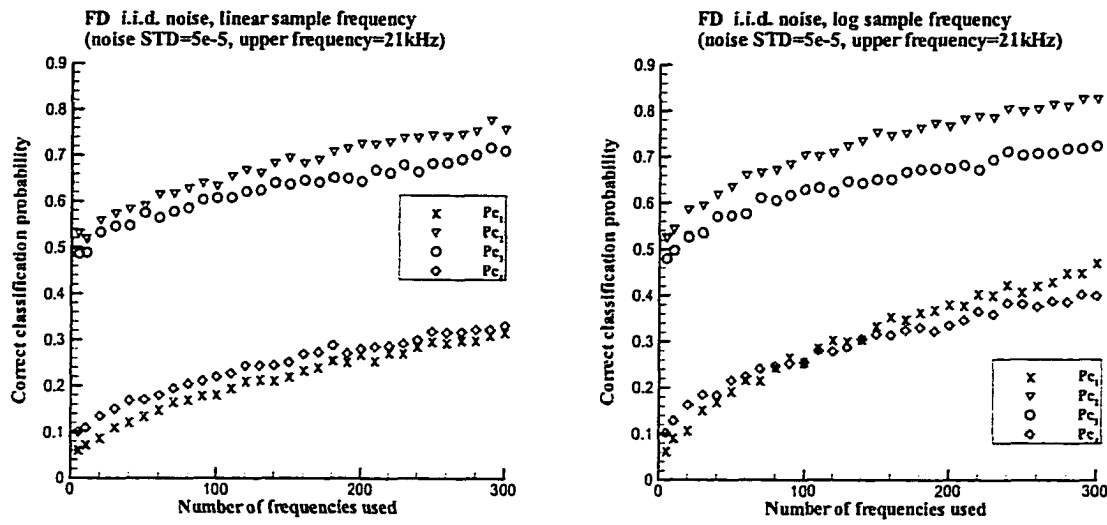


Figure 5.11: Classification performance as a function of number of frequencies used for linear (left) and logarithmic (right) samples with i.i.d. FD noise. The noise standard deviation is 5e-5 and the upper frequency is 21 kHz.

in Figure 5.11, however, the performance improves more slowly as the number of sample frequencies increases. Figure 5.20 in the left hand panel demonstrates the performance of the FPP as a function of the noise variance, which is similar in form but lower in absolute value than the results in Figure 5.12.

The performance of the OP when the noise variance is fixed and the number of sample frequencies increases is illustrated in Figure 5.19 (right hand panel), as well as when number of samples is fixed and noise variance increases in Figure 5.20. Comparing the results shown in Figures 5.19 and 5.20, it is clear that the OP outperforms the FPP in average percent correct classification.

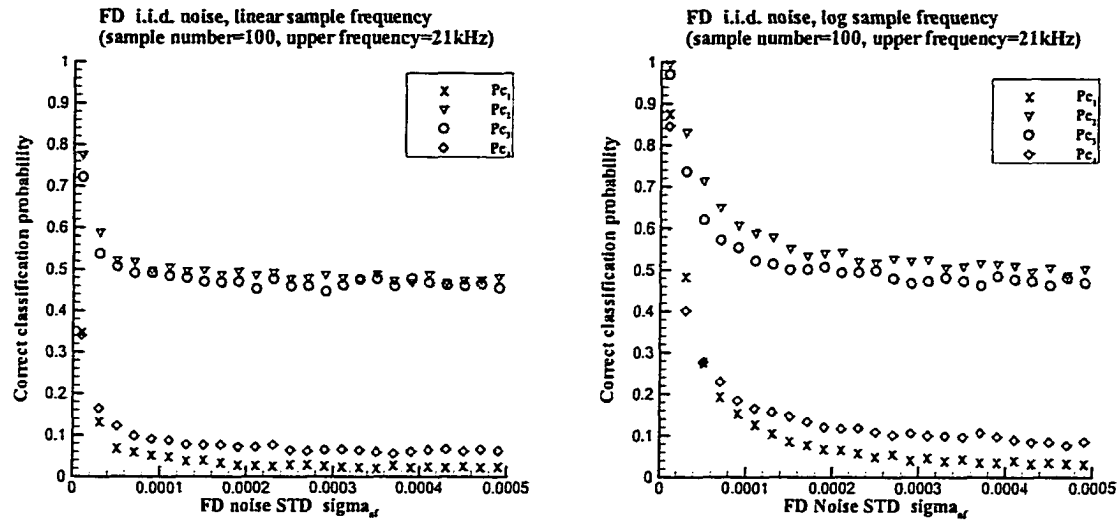


Figure 5.12: Classification performance as a function of noise variance σ_n^2 , for linear (left) and logarithmic (right) samples with i.i.d. FD noise. The number of sample frequency is 100 and the upper frequency is 21 kHz.

5.4.2 Experimental Study

In order to further verify the simulation results, experiments were performed to obtain real data. The experimental data has been taken using the PSS-12 (a TD EMI sensor) and the GEM-3 (a FD EMI sensor) sensors. All measurements were taken in air. The PSS-12 is the U.S. Army's hand held metal detector. It is a pulsed induction sensor. The current pulse in the transmitting coil establishes a field in nearby conducting objects. Then, eddy currents are established throughout the object in accordance to Faraday's Law of induction. A receiving coil detects the decaying magnetic field radiated by the eddy currents. In practice, the PSS-12 can only sense the late time response and integrate to a single scalar. A modification of the PSS-12 has been made to allow acquisition of the decay curves [39, 90]. The GEM-3 is a prototype wideband frequency-domain EMI sensor [17, 40], developed by Geophex Ltd. Its design of the transmitting coils allows the GEM-3 to sense a weak, secondary field returned from the earth and any buried objects. The sensor records the real

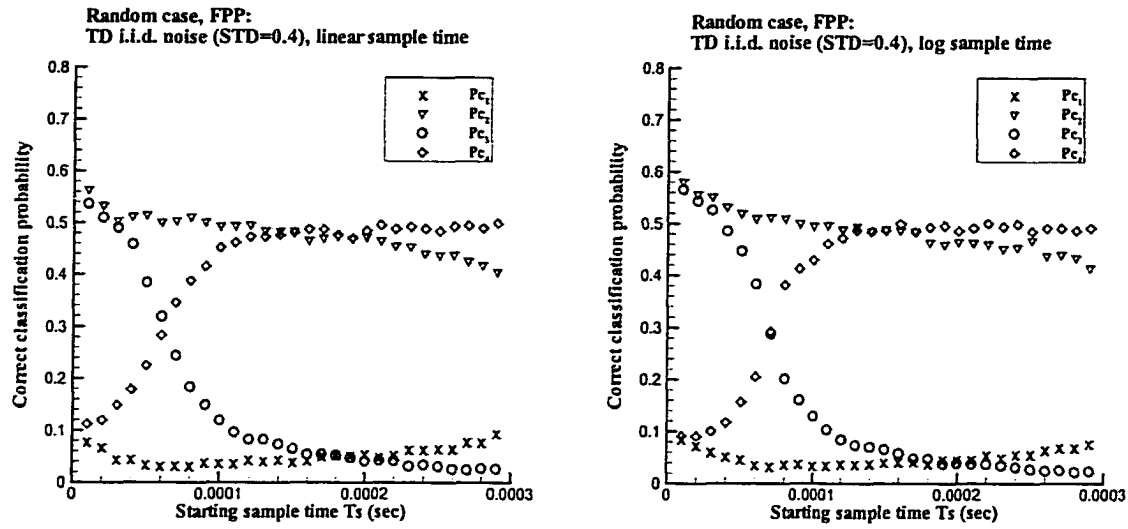


Figure 5.13: Classification performance of FPP as a function of the initial sample time for the TD data with uncertain amplitude. Left – linearly sampled data; right – logarithmically sampled data.

and imaginary parts (in-phase and quadrature) of the induced complex voltage at the receiving coil, relative to that on the transmitting coils.

Four metal targets, same as in Sec. 4.2.3.3, are considered for experimental measurements: an aluminum bar-bell, an aluminum disk, a thick brass disk, and a thin brass disk. The dimensions of these targets are as follows. The diameter of each of the targets is 5.08 cm. The heights of the targets are 2.897 cm, 2.667 cm, 2.34 cm, and 0.3175 cm for the aluminum bar-bell, the aluminum disk, the thick and the thin brass disk, respectively. The response from a target depends on the constitutive parameters, geometry of the target, as well as the horizontal and vertical distance from the center of the sensor to that of the target.

The experimental set up is as follows. The GEM-3 or the PSS-12 was mounted on a wooden rack with the sensor head approximately 1.8 m above the wooden base of

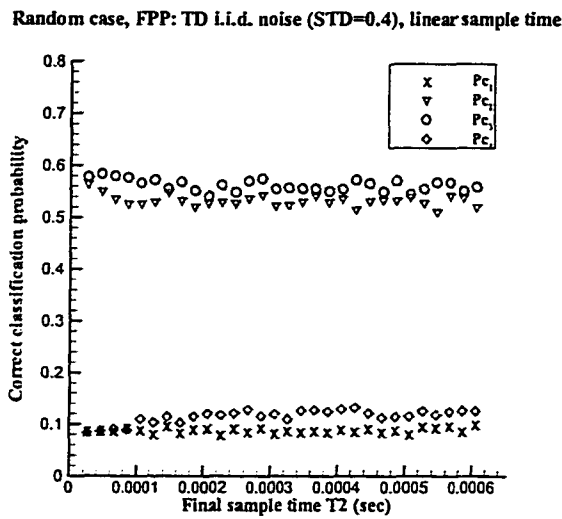


Figure 5.14: Classification performance of FPP as a function of ending sample time for the TD data with uncertain amplitude.

the platform. Both rack and platform contained no metal parts. The rack assembly allows placement of a target on a wooden shelf at various distances beneath the sensor head. For the GEM-3, twenty-one linearly spaced frequencies were chosen from 3,990 Hz to 23,970 Hz. For the PSS-12, the decay curves were sampled at 20MHz, and 10,000 samples were taken at each position.

Measurements were taken at 7 heights from 17 cm to 23 cm in 1 cm increments for the GEM-3 and from 2 cm to 8 cm for the PSS-12. The difference in heights was an attempt to adjust the SNR of the two sensors. The measured SNR was 29 dB for the PSS-12 and 24 dB for the GEM-3. The distribution of the height is assumed to be Gaussian with mean of 20 cm for the GEM-3 (5 cm for the PSS-12) and variance of 1.53^2 . At each height, between 11 and 36 measurements were taken. The exact count was calculated based on the assumed distribution. At each height the position of each measurement is uniformly distributed within a 20 cm by 20 cm square. For each object, there were a total of 328 measurements taken.

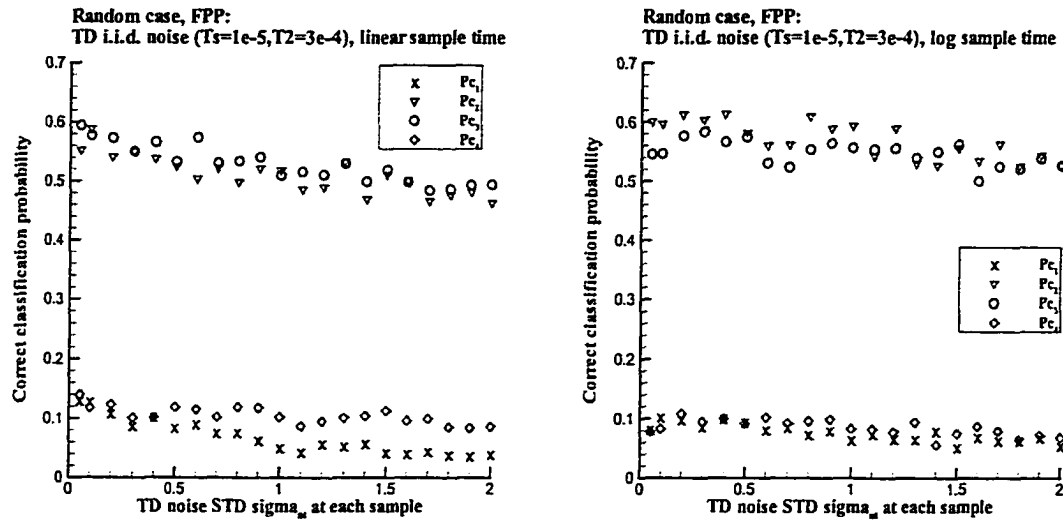


Figure 5.15: Classification performance of FPP as a function of noise variance for the TD data with uncertain amplitude. Left – linearly sampled data; right – logarithmically sampled data.

The classification performance of the FPP and the OP using the experimental data is listed in Table 5.2. Clearly, the OP achieves better performance than the FPP and the GEM-3 (FD sensor) data provides better performance when using the OP. This fact agrees with the results from simulations, although the SNR issues cannot be factored out.

5.5 Summary

In this chapter, we present a theoretical analysis as well as simulation results for a two-object classification problem using TD and FD EMI data. The effects of the initial and final sample time, and the noise variance are investigated for TD operation; the effects of the number of sample frequencies and the noise variance in the FD data are evaluated. Furthermore, a four-object classification problem is investigated using

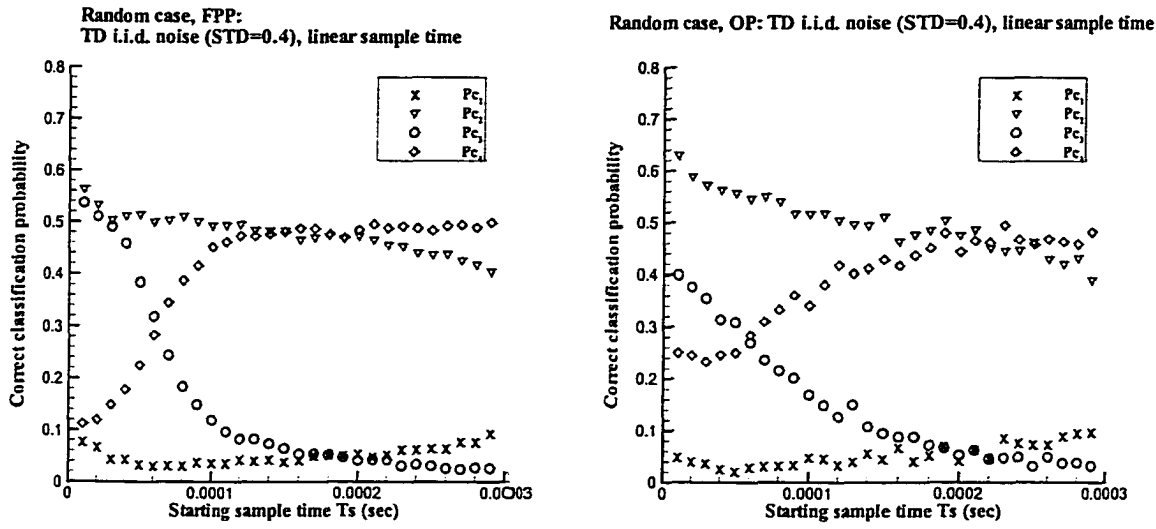


Figure 5.16: Classification performance of the FPP (left) and the OP (right) as a function of the initial sample time for TD data with uncertain amplitude case. The covariance matrices of the amplitude A_1 and A_2 are listed in Table 5.1. The final sample time is $6.06e-4$ s, and the noise standard deviation is 0.4.

TD and FD signals through simulations and experiments.

First, theoretical analysis suggests sampling more in the low frequencies for FD operation and more in the early time for TD operation in order to achieve better performance. Thus, as expected, since logarithmic sampling places more samples in the early time or the low frequencies which results in higher SNR for i.i.d. noise in either the TD or the FD, logarithmic sampling schemes can provide better performance than linear sampling schemes. This suggests that when designing or programming sensor parameters, logarithmic sampling is favored because of the higher SNRs.

It is observed that the TD classification performance is strongly affected by the initial sample time and objects with less metal are more affected by delaying the initial sample time.

Object	Mean Vector		Covariance Matrix	
1	0.24 0.52		0.018 0.029	0.029 0.100
2	0.16 0.38		0.010 0.012	0.049
3	0.26 0.67		0.017 0.034	0.114
4	0.23 0.53		0.016 0.018	0.068

Table 5.1: The mean vectors and covariance matrices of the Gaussian amplitude (A_1 and A_2) obtained from experimental data.

Sensor	Processor	Target 1	Target 2	Target 3	Target 4
PSS-12	FPP	.11	.20	.12	.26
	OP	.19	.51	.39	.39
GEM-3	FPP	.23	.24	.03	.14
	OP	.91	.77	.69	.81

Table 5.2: Correct classification probability of the FPP and the OP using the PSS-12 and the GEM-3 measured data.

The case when the weights on the exponential model (A_1 and A_2) are uncertain since, in practice, the underground objects are of unknown depth has also been considered. The OP provides better performance than that of the FPP on both simulated and experimental data. As expected, when A_1 and A_2 are uncertain, the performance is worse than that obtained from the fixed amplitude case. Both simulation results and classifier implementation using real, measured data verify this fact.

Additionally, although theoretical results can only be calculated for the two-object classification case in closed form, simulation and experimental results indicate that these conclusions hold for classification of N objects, not simply the two-object task, thus can be extended to applications such as landmine or UXO detection which re-

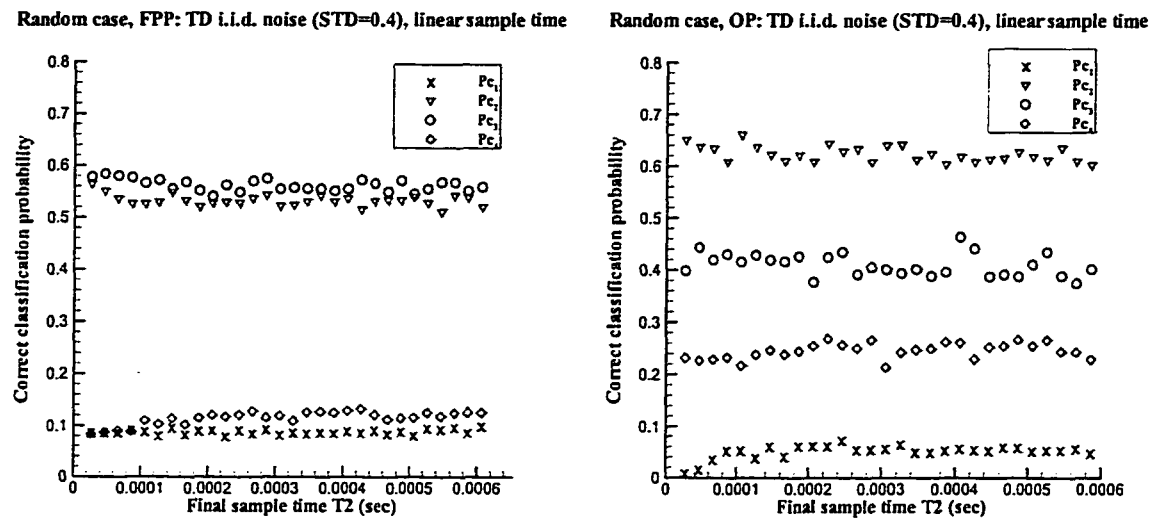


Figure 5.17: Classification performance of the FPP (left) and the OP (right) as a function of the final sample time for linear samples for uncertain amplitude case. The initial sample time is 1e-5s, the noise standard deviation is 0.4, and the sample period is 2.38e-6s.

quires classification/identification between targets and clutter.

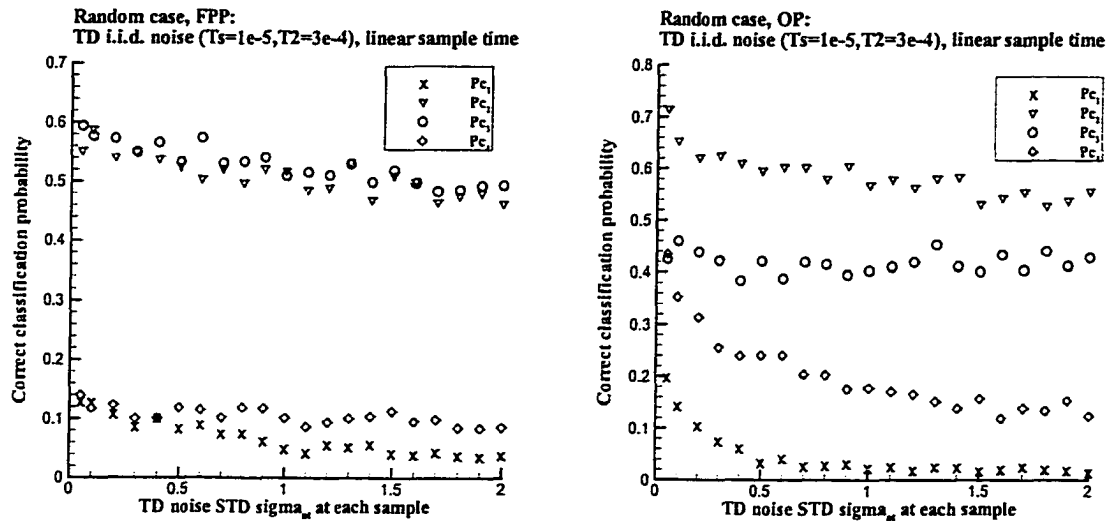


Figure 5.18: Classification performance of the FPP (left) and the OP (right) as a function of the noise variance $\sigma_{n_t}^2$ for TD linear samples for the uncertain amplitude case. The initial sample time is $1e-5$ s, the final sample time is $3e-4$ s, and the sample period is $1.0e-6$ s.

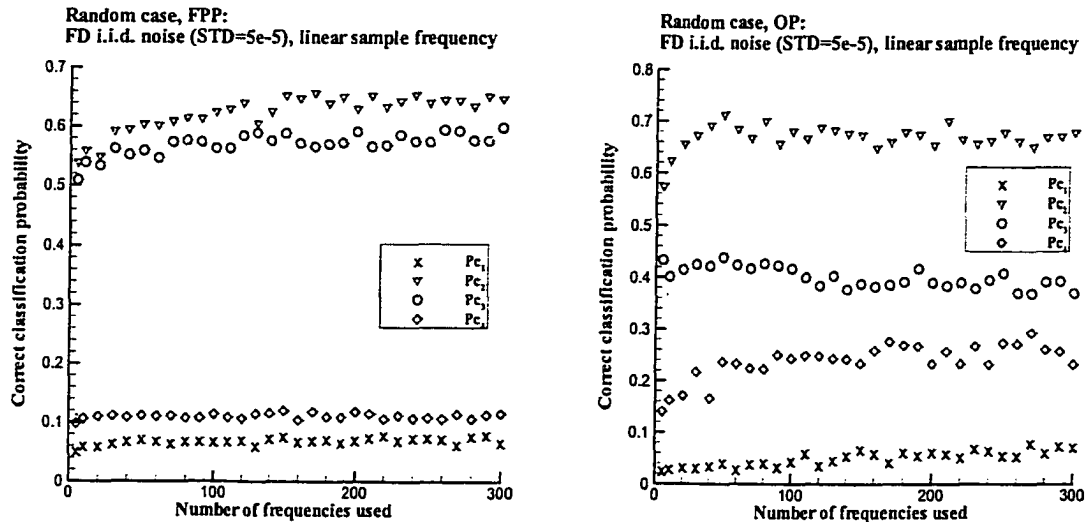


Figure 5.19: Classification performance of the FPP (left) and the OP (right) as a function of the number of frequencies used for linear samples for FD i.i.d. noise, the uncertain amplitude case. The noise standard deviation σ_{n_f} is $5e-5$ and the bandwidth is 21 kHz.

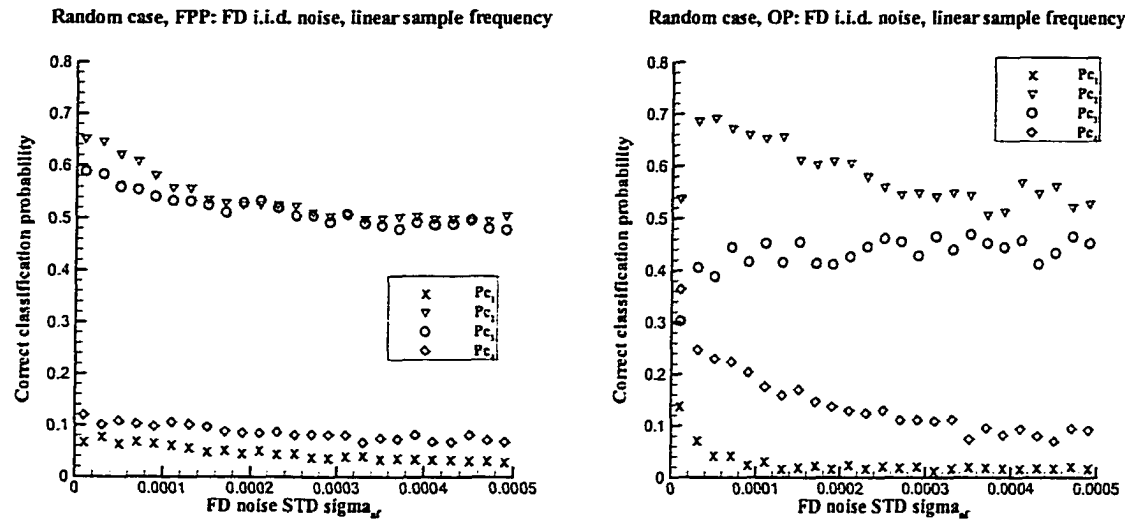


Figure 5.20: Classification performance of FPP (left) and OP (right) as a function of the noise standard deviation (STD) σ_{nf} for linear samples for FD i.i.d. noise, the uncertain amplitude case. The number of sample frequency is 100 and the bandwidth is 21 kHz.

Chapter 6

Conclusion

The goal of any detection systems is to achieve a high detection rate while minimizing the number of false alarms. While many traditional mine detectors achieve the first of these goals, it is often at the cost of a prohibitively large false alarm rate. The work presented here was motivated by the requirements of high P_d and low P_{fa} . Both the time-domain and frequency-domain electromagnetic induction data are used within the framework of Bayesian signal detection theoretic analysis. The performance of various algorithms is measured by a functional relationship between P_d and P_{fa} , termed the receiver operating characteristic (ROC).

In Chapter 3, the results of statistical, Bayesian approaches applied to synthetic and field data obtained in conjunction with the *DARPA Backgrounds Clutter Data Collection Experiment* [38] indicate that a rigorous Bayesian signal detection theoretic analysis can be used to improve detectability of a set of targets including landmines and some small UXO objects using EMI sensors over standard thresholding techniques. A suite of EMI sensors was evaluated, including those that integrate time-domain information to provide a single data point (standard metal detector, single channel EMI sensor) and those that provide a sampled portion of the time-domain waveform (multi-channel EMI sensor). Comparing the performance of those sensors, the multi-channel sensors outperform the single channel sensors. Since the multi-channel sensor used in the experiment is a prototype and still under develop-

ment, the improvement is not substantial. However, it is believed that providing a more complete time-domain waveform instead of integrating to a scalar value allows greater exploitation of the phenomenology embedded in the target signatures. This is also validated by theoretical analysis. The optimal detector operating on a single time sample of time-domain EMI data is the threshold test, and its performance is the worst among all the detectors considered.

It is shown theoretically that for a single channel (integrated) time-domain EMI sensor, the LRT reduces to the GLRT that is simply a threshold detector, and that for a multi-channel time-domain EMI sensor, the GLRT is optimal under certain assumptions on the distributions of the decay rates. These results are also verified using data obtained from the *DARPA* experiment. This demonstrates that the assumptions used to derive the LRT and GLRT equivalency are valid, at least for the data in question. Additionally, it is demonstrated in Chapter 3 that when spatial information is incorporated into the detector design in the framework of a Bayesian detection approach the performance can be improved substantially using single channel and multi-channel EMI data obtained from the *DARPA* experiment.

In order to develop the likelihood ratio, the probability density function of the data and the parameters upon which the signals depend are required. In general, these density functions were derived from the data that were acquired by each sensor in a calibration area, in which the location of the targets was known and the background, or clutter, was typical to that obtained in the remainder of the test site. Since the statistics of the data vary substantially across sites, it is necessary to estimate those density functions separately for each site. Using an estimate of the density function based on one of the sites at a different site usually degrades performance.

In Chapter 4, the signal processing approaches are applied to frequency-domain EMI data for classification/identification purposes. The problem focused on detecting and identifying low-metal mines using FD data. First, the detecting/identifying low-metal mines in background noise using FD data was considered. The soil effects on the signature are investigated via experiments. A commonly held assumption that for large metal objects the soil effects on the EMI response can be neglected was validated using the GEM-3 sensor. It is also shown that for low-metallic content mines the signatures can change significantly because of the presence of soil. Also, it is demonstrated that low-metal mines can be discriminated from the background using wideband EMI responses.

Further experiments were performed at Fort A. P. Hill, VA. in order to obtain low-metal mines and clutter data to allow us to develop algorithms. The results demonstrate that a frequency-domain EMI approach coupled with statistical signal processing algorithms shows significant promise for the problem of detecting low-metal mines. Also, incorporating spatial information into the detector design provides substantial performance improvement over performance obtained from data collected at a single location.

The task of classifying metal objects using wideband EMI simulated and measured data is also considered. A Bayesian decision-theoretic approach is implemented. Since an accurate forward FD EMI model and the uncertainty regarding environmental parameters are incorporated into the classifier design, performance can be dramatically improved over the standard approach that ignores environmental uncertainty. Even though only four objects were considered in this work, by building extensive libraries

of target signatures this approach can be applied to classify/identify these targets in real scenarios. By developing a model for other signals and sensor modalities, this algorithm can be further applied to other applications which require classification of different targets.

The approach that incorporated target position uncertainties suffers from a computational burden and is not always practical. Since it is observed that normalization mitigates the uncertainties of the response due to the unknown target position for the class of targets considered (target aspect ratio close to one) in this work, a sub-optimal approach using normalized the wideband EMI responses was also implemented. The sub-optimal processor (FPP) performed on normalized data can provide significant performance improvement over sub-optimal processors that operate on raw sensor output and computational time can be dramatically reduced.

In Chapter 5, a comparison of performance attained using TD and FD data for the classification problem is performed. The advantages and disadvantages of TD and FD EMI sensors are reviewed. Both theoretical studies and simulations are used to investigate the sensitivity of the performance of a Bayesian classifier to various parameters associated with TD and FD system operation, including sampling rate, the initial/final sample time, and the signal to noise ratio. Finally, experimental data is collected from both a TD and FD sensor in order to classify four metallic objects. Performance is compared both across sensors and across classification algorithms.

Theoretical analysis has shown that placing more samples in the early time or the lower frequencies results in a higher SNR for the i.i.d. noise either in the TD or in the FD. Therefore, logarithmic sampling can provide better performance than linear

sampling scheme, as verified by theoretical analysis and simulations.

Introducing uncertainties in the signal model, which is a result of unknown depth of underground objects, degrades the classification performance as expected. The OP provides better performance than the FPP when the uncertainties are present, though the performance of the OP can never exceed that of the FPP under the completely certain case. Experimental data also verified this fact.

In conclusion, the work presented here has demonstrated Bayesian detection theoretic approach can be applied to landmine detection problem and achieves better performance than the standard approaches. To do so, an understanding of the underlying physics and characteristics of the targets to be detected or classified, as well as the environmental factors is a necessity.

Appendix A

Deciding the upper frequency of the signal

For both the theoretical investigation reasons as well as to impact sensor implementation, it is of interest to determine the upper frequency of the FD sensor, as well as the sampling rate in the TD, which is of course dependent on the upper frequency of the sensor.

Based on the signal model defined in Section 5.2 (single exponential model), and assuming we choose the upper frequency at the frequency where the FD response is reduced to q percent of the amplitude at zero frequency,

$$\omega_u = \frac{\alpha\sqrt{10^4 - q^2}}{q} \quad (\text{A.1})$$

Usually, q is a small number, thus

$$\omega_u \approx \frac{100\alpha}{q} \quad (\text{A.2})$$

Based on the Nyquist sampling theorem, the sample frequency for a TD system should be at least twice the maximum frequency content of the signal. Thus we used $f_s = 2(\omega_u/2\pi)$, the sampling time spacing is $t_s = \pi/\omega_u$. From Equation (A.2), the upper frequency to be used is dependent on the decay rate of the object to be classified. Thus, based on the set of objects the sensor is designed to detect, the maximum upper frequency can be chosen

Appendix B

Defining the final sample time for the TD signal

For the TD EMI systems, the initial and final sample time are two important parameters that determine the sensor performance and the complexity of the physical implementation. Since exponential signals decay to zero, taking too many samples does not improve performance, but wastes system resources. There are two ways to determine the final sample time; one is based on the time at which the signal is reduced to a significantly small amount of the initial value, and the other is to run a simulation as a function of the final time to decide at which time the performance converges. The second of these is investigated in the text. Here, we consider the case where the final sample time occurs when the signal is reduced to r percent of the initial value. T_2 denotes the final sample time. For the single exponential signal model,

$$T_2 = -\frac{\log_e(r) + \log_e(10^{-2})}{\alpha} \quad (\text{B.1})$$

For the sum of two or more exponentials, there is no analytical solution for this problem.

Bibliography

- [1] G Strada. The horror of land mines. *Scientific American*, 1996.
- [2] <http://www.un.org/Depts/dha/mct/facts.htm>.
- [3] A. M. Rouhi. Land mines: Horrors begging for solutions. *Chemical & Engineering News*, 1997.
- [4] C.H. Yang and W. C. Hu. Center-surround filters for the detection of small targets in clutter multispectral imagery: Background and filter design. In *Proceedings of the SPIE*, volume 2496, Orlando, FL., April 1995.
- [5] Q. A. Holmes, C. R. Schwartz, and J. H. Seldin. Adaptive multispectral cfar detection of landmines. In *Proceedings of the SPIE*, volume 2496, Orlando, FL., April 1995.
- [6] C. D. L. Smith. Detection technologies for mines and minelike targets. In *Proceedings of the SPIE*, volume 2496, Orlando, FL., April 1995.
- [7] C. R. Schwartz, A. C. Kenton, W. F. Pont, and B. J. Thelen. Statisctical parametric signature/sensor/detection model for multispectral mine target detection. In *Proceedings of the SPIE*, volume 2496, Orlando, FL., April 1995.
- [8] M. A. LeCompte, F. J. Iannarilli, D.B. Nichols, and R.R. Keever. Multispectral signature polarimetry for detection of mines and unexploded ordnance (uxo). In *Proceedings of the SPIE*, volume 2496, pages 180–192, Orlando, FL., April 1995.
- [9] S. L. Earp, E. S. Hughes, T. J. Elkins, and R. Vickers. Ultra-wideband ground penetrating radar for the detectin of buried metallic mines. *IEEE Aerospace and Electronics Systems Magazine*, 11(9):30–34, 1996.
- [10] H. Brunzell. Impluse radar for detection and classification of buried landmines. In *Antenna 97*, pages 299–305, May 1997.
- [11] P.D. Gader, J. M Keller, and H. Liu. Landmine detectionusing fuzzy clustering in darpa backgrounds data collected with the geo-centers ground penetrating radar. In *Proceedings of the SPIE*, volume 3392, pages 1139–1149, Orlanda, FL., April 1998.

- [12] A. L. Warrick, S. G. Azevedo, and J. E. Mast. Prediction of buried mine-like target radar signatures using wideband electromagnetic modeling. In *Proceedings of the SPIE*, volume 3392, Orlando, FL., April 1998.
- [13] G. D. Sower and S. P. Cave. Detection and identification of mines from natural magnetic and electromagnetic resonances. In *Proceedings of the SPIE*, volume 2496, Orlando, FL., April 1995.
- [14] C. E. Baum. Low-frequency near field magnetic scattering from highly, but not perfectly, conducting bodies. Interaction Note 499, Phillips Laboratory, Cambridge, MA, 1993.
- [15] H. H. Nelson and J. R. McDonald. Target shape classification using the mtads. In *UXO Forum*, Atlanta, GA, May 1999.
- [16] N. Khadr, B. J. Barrow, T. H. Bell, and H. H. Nelson. Target shpae classification using electromagnetic induction sensor data. In *UXO Forum*, Atlanta, GA., May 1998.
- [17] I. J. Won, D. A. Keiswetter, and D. R. Hansen. Gem-3: A monostatic broadband electromagnetic induction sensor. *Journal of Environmental and Engineering Geophysics*, 2:53–64, 1997.
- [18] I.J. Won, D. Keiswetter, and E. Novikova. Elstromagnetic induction spectroscopy. *Journal of Environmental and Engineering Geophysics*, 3(2):27–40, 1998.
- [19] N. Geng, P. Garber, L. Collins, L. Carin, D. Hansen, D. Keiswetter, and I. J. Won. Wideband electromagnetic induction for metal-target identification: Theory, measurement and signal processing. Technical report, Duke University, Durham, NC, 1997.
- [20] N. Geng, C. E. Baum, and L. Carin. On the low-frequency natural response of conducting and permeable targets. *IEEE Trans. Geoscience Science and Remote Sensing*, 37(1):347–359, 1999.
- [21] Y. Das and J. E. McFee. A simple analysis of the electromagnetic response of buried conducting objects. *IEEE Trans. Geoscience Science and Remote Sensing*, GE-28:278–288, 1990.
- [22] Y. Das, J. E. McFee, and R. H. Cherry. Time-domain response of a sphere in the field of a coil: Theory and experiment. *IEEE Trans. Geoscience Remote Sensing*, GE-22:360–367, 1984.

- [23] Y. Das and J. E. McFee. A simple analysis of the electromagnetic response of buried conductive objects. *IEEE Trans. Geoscience Remote Sensing*, GE-29(2):342–344, 1991.
- [24] S. Vitebskiy and L. Carin. Late-time resonant frequencies of buried bodies of revolution. *IEEE Trans. Antennas Propagation*, 44:1575–1583, 1996.
- [25] P. Gao and L. M. Collins. A 2-dimensional generalized likelihood ratio test for land mine detection. *Signal Processing*, 80:1669–1686, 2000.
- [26] L. M. Collins, P. Gao, and L. Carin. An improved bayesian decision theoretic approach for land mine detection. *IEEE Trans. Geoscience and Remote Sensing*, 37(2):811–819, 1999.
- [27] P. Gao, L. M. Collins, P. Garber, N. Geng, and L. Carin. Classification of landmine-like metal targets using wideband electromagnetic induction. *IEEE Trans. Geoscience and Remote Sensing*, 38(3):1352–1361, 2000.
- [28] T. E. Olson and C. E. Priebe. Detection and classification of mines via discriminant features and borrowed strength. In *Proceedings of the SPIE*, volume 3079, Orlando, FL., April 1997.
- [29] C. E. Priebe. Exploiting stochastic partitions for minefield detection. In *Proceedings of the SPIE*, volume 3079, Orlando, FL., April 1997.
- [30] I. V. Basawa. Unilateral markov random fields for minefield modeling and detection. In *Proceedings of the SPIE*, volume 3079, Orlando, FL., April 1997.
- [31] M. R. Leadbetter. Extremal methods in mine detection and classification. In *Proceedings of the SPIE*, volume 2496, Orlando, FL., April 1995.
- [32] M. R. Leadbetter. Extremal methods in mine detection and classification. In *Proceedings of the SPIE*, volume 2765, Orlando, FL., April 1996.
- [33] S. L. Earp and J. M. Dang. Maximum likelihood multispectral pixel-level fusion using a linear-quadratic detector. In *Proceedings of the SPIE*, volume 3079, Orlando, FL., April 1997.
- [34] R. Muise and J. A. Wright. Coastal mine detection using cobra multispectral sensor. In *Proceedings of the SPIE*, volume 2765, Orlando, FL., April 1996.

- [35] L. S. Riggs, J. E. Mooney, and D. E. Lawrence. Identification of metallic mines using low frequency magnetic fields. *IEEE Trans. Geoscience and Remote Sensing*, in press.
- [36] D. Smith, C. Nelson, K. Sherbondy, and J. Huynh. Algorithms for detecting and identifying landmines using the time-domain electromagnetic identification (temid) sensor system. In *EuroEM 2000*, Edinburgh, Scotland, June 2000.
- [37] S. L. Tantum and L. M. Collins. A comparison of algorithms for subsurface object detection and identification using time domain electromagnetic induction data. *IEEE Trans. Geoscience and Remote Sensing*, submitted.
- [38] V. George, T. Altshuler, A. Andrew, J. Nicoll, E. Cespedes, D. Butler, T. Broach, and R. Mehta. Background data collection plan. Technical report, DARPA/Defense Science Office, 1996.
- [39] L. Riggs. Overview of the fundamental operating characteristics of the an/pss-12. Technical report, JUXOCO, Ft. Belvoir, VA., 1999.
- [40] I.J. Won, D. Keiswetter, G.R.A. Fields, and L. C. Sutton. Gem-2: A new multifrequency electromagnetic sensor. *Journal of Environmental and Engineering Geophysics*, 2:129–137, 1996.
- [41] D. K. Butler. Landmines and uxo. *The Leading Edge*, 1997.
- [42] C. A. Balanis. *Advanced Engineering Electromagnetics*. John Wiley and Sons, Inc., New York, 1989.
- [43] P. Gao, L. M. Collins, J. Moulton, L. Makowsky, D. Reidy, and R. Weaver. How soil effects the broadband emi signatures and detection of low-metal landmine. *IEEE Trans. Geoscience and Remote Sensing*, submitted.
- [44] T.J. Yu and L. Carin. Analysis of the electromagnetic inductive response of a void in a conducting-soil background. *IEEE Trans. Geoscience Remote Sensing*, GE-38(3):1320–1327, 2000.
- [45] R. F. Harrington. *Field Computation by Moment Methods*. The Macmillan Company, New York, 1968.
- [46] J. R. Mautz and R. F. Harrington. Radiation and scattering from bodies of revolution. *Applied Scientific Research*, 20:405–435, 1969.

- [47] T. Wu and L. L. Tsai. Scattering from arbitrarily-shaped lossy dielectric bodies of revolution. *Radio Science*, 12:709–718, 1977.
- [48] J. R. Mautz and R. F. Harrington. Electromagnetic scattering from a homogeneous material body of revolution. *AE U*, 33:71–80, 1979.
- [49] A. W. Glisson and D. R. Wilton. Simple and efficient numerical methods for problems of electromagnetic radiation and scattering from surfaces. *IEEE Trans. Ant. and Prop.*, 28:593–603, 1980.
- [50] A. W. Glisson, D. Kajfez, and J. James. Evaluation of modes in dielectric resonators using a surface integral equation formulation. *IEEE Trans. Microwave Theory Tech.*, 31:1023–1029, 1983.
- [51] R. F. Harrington. *Integral Equation Techniques*, pages 259–325. Dielectric Resonators, ed. D. Kajfez and P. Guillon. Artech House, Dedham, MA., 1986.
- [52] K. Simonyi. *Theoretische Elektrotechnik, in German*. VEB Deutscher Verlag der Wissenschaften, Berlin, 1980.
- [53] I. Selin. *Detection Theory*. Princeton University Press, New Jersey, 1965.
- [54] M. H. DeGroot. *Probability and Statistics*. Addison-Wesley Publishing Inc., 1989.
- [55] Van Trees H. L. *Detection, Estimation, and Modulation Theory*. John Wiley and Sons, New York, 1968.
- [56] A. D. Whalen. *Detection of Signal in Noise*, page 352. Academic Press, Inc., New York, 1971.
- [57] P. L. DeVries. *A First Course in Computational Physics*. John Wiley and Sons, New York, 1994.
- [58] M. A. Tanner. *Tools for Statistical Inference: Methods for the Exploration of Posterior Distributions and Likelihood Functions*. Springer-Verlag Inc., 2nd edition, 1993.
- [59] G. B. Folland. *Real Analysis: Modern Techniques and Their Applications*. John Wiley and Sons, Inc., New York, 1984.
- [60] B. W. Silverman. *Density Estimation in Statistics and Data Analysis*. Chapman and Hall Ltd., 2nd edition, 1986.

- [61] D. W. Scott. *Multivariate Density Estimation: Theory, Practice, and Visualization*. John Wiley and Sons, Inc., 1992.
- [62] A. C. Dubey, I. Cindrich, J. M. Ralston, and K. Rigano (eds.). Detection technologies for mines and minelike targets. In *Proceedings of the SPIE*, volume 2496, Orlando, FL., April 1995.
- [63] A. C. Dubey and R. L. Barnard (eds.). Detection technologies for mines and minelike targets. In *Proceedings of the SPIE*, volume 3079, Orlando, FL., April 1997.
- [64] T. W. Altshuler, A. M. Andrews, and D. A. Sparrow. Mine and uxo detection: Measures of performance and their implication in real-world scenarios. In *Proceedings of the SPIE*, volume 3079, Orlando, FL., April 1997.
- [65] P. Gao. Improved approaches to land mine remediation using signal detection and estimation theory. Master's thesis, Duke University, Durham, NC., 1997.
- [66] P. Gao and L. M. Collins. A theoretical performance analysis and simulation of time-domain emi sensor data for land mine detection. *IEEE Trans. Geoscience and Remote Sensing*, 38(4):2042–2055, 2000.
- [67] N. L. Johnson, S. Kotz, and N. Balakrishnan. *Continuous Univariate Distributions*, page 433. vol. 2. John Wiley and Sons, Inc., New York, 2nd edition.
- [68] E. C. Fieller. The distribution of the index in a normal bivariate population. *Biometrika*, 24:428–440, 1932.
- [69] D. V. Hinkley. On the ratio of two correlated normal random variables. *Biometrika*, 56:635–639, 1969.
- [70] Hand held metallic mine detector performance baselining collection plan. Technical report, JUXOCO, Fort Belvior, VA., 1998.
- [71] L. Collins and P. Gao. Progress report i: Signatures of land mines in soil and in air: Are they different? what are the characteristics of the sensor noise? Technical report, JUXOCO, Ft. Belvoir, VA., 1998.
- [72] A. H. Trang, P. V. Czipott, and D. A. Waldron. Characterization of small metallic objects and non-metallic anti-personnel mines. In *Proceedings of the SPIE*, volume 3079, Orlando, FL., April 1997.

- [73] S. Vitebskiy and L. Carin. Short-pulse plane wave scattering from a buried perfectly conducting body of revolution. *IEEE Trans. Antennas Propagation*, 44:112–120, 1996.
- [74] C. E. Baum, N. Geng, and L. Carin. Integral equations and polarizability for magnetic singularity identification. Interaction Note 524, Phillips Laboratory, Cambridge, MA, 1997.
- [75] P. Gao and L. Collins. A comparison of optimal and sub-optimal processors for classification of buried metal objects. *IEEE Signal Processing Letters*, 6(8):216–218, 1999.
- [76] Fm 20-32, mine/countermine operations manual. Technical report, 1998.
- [77] L. Collins. Final report, statistical signal processing for demining: Experimental validation. Technical report, JUXOCO, Ft. Belvoir, VA., 1998.
- [78] L Carin. Wideband time- and frequency-domain emi: Phenomenology and signal processing. Technical report, Technical Report on U.S. Air Force Philip's Laboratory Project, 1998.
- [79] D. Keiswetter, I.J. Won, B. Barrow, and T. Bell. Object identification using multifrequency emi data. In *UXO Forum*, Altlanta, GA., May 1999.
- [80] P. Gader, H. Frigui, G. Vaillette, B. Nelson, and J. Keller. New results in fuzzy set based detection of landmines with gpr. In *Proceedings of the SPIE*, Orlando, FL., April 1999.
- [81] J. C. Hancock and P. A. Wintz. *Signal Detection Theory*, pages 80–84. McGraw Hill, New York, 1966.
- [82] R. J. Schalkoff. *Pattern Recognition: Statistical, Structural and Neural Approaches*, pages 34–43. John Wiley and Sons, New York, 1992.
- [83] K. Fukunaga. *Introduction to Statistical Pattern Recognition*, page 127. 2nd Ed. Academic Press, Inc., San Diego, 1990.
- [84] J. G. Rasimas. Signal detection and classification of targets using multiple aspect angles. Master's thesis, Duke University, 1998.
- [85] S. L. Tantum and L. M. Collins. On estimating decay rates from exponential signals. *IEEE Signal Processing Letters*., submitted.

- [86] W. M. Steedly and R. L. Moses. The cramer-rao bound for pole and amplitude coefficient estimates of damped exponential signals in noise. *IEEE Trans. Signal Processing*, 41(3):1305–1318, 1993.
- [87] D. Keiswetter, I.J. Won, J. Miller, T. Bell, E. Cespedes, and K. O'Neill. Electromagnetic induction spectroscopy for detecting and identifying buried objects. In *UXO Forum*, Altanta, GA., May 2000.
- [88] Cambanis and Masry. Sampling designs for the detection of signals in noise. *IEEE Trans. Information Theory*, 1983.
- [89] Y. L. Tong. *The multivariate normal distribution*. Springer-Verlag, New York, 1990.
- [90] L. Riggs. Performance evaluation of metal detects and metal detector enhancement leading to improved discrimination capability. Technical report, JUXOCO, Ft. Belvoir, VA., 2000.

Biography

Ping Gao was born in Jilin, P. R. China on June 29, 1970. Ping received her Bachelor of Science in Electrical Engineering (*honor*) and her Master of Science in Electrical Engineering from Beijing University of Post and Telecommunications (BUPT) in June 1993, and April 1996 respectively. In December 1997, she earned her Master of Science in Electrical Engineering from Duke University. Her publications include:

REFEREED JOURNAL ARTICLES

- [1] Ping Gao, Leslie M. Collins, "A Comparison of Object Classification Performance Using Time- and Frequency-Domain Electromagnetic Induction Data" *IEEE Trans. Geoscience and Remote Sensing* (under review).
- [2] Ping Gao, Leslie M. Collins, John Moulton, Larry Makowsky, Denise Reidy, and Richard Weaver, "How Soil Effects the Broadband EMI Signatures and Detection of Low-Metal Landmine," *IEEE Trans. Geoscience and Remote Sensing* (under review).
- [3] Ping Gao and Leslie M. Collins, "A Theoretical Performance Analysis and Simulation of Time-Domain EMI sensor Data for Land Mine Detection," *IEEE Trans. Geoscience and Remote Sensing* **38**(4):2042-2055 (July 2000).
- [4] Ping Gao, Leslie M. Collins, Phil Garber, Norbert Geng, and Lawrence Carin, "Classification of Landmine-Like Metal Targets Using Wideband Electromagnetic Induction," *IEEE Trans. Geoscience and Remote Sensing* **38**(3):1352-1361 (May 2000).
- [5] Ping Gao and Leslie M. Collins, "A 2-Dimensional Generalized Likelihood Ratio Test for Land Mine Detection," *Signal Processing* **80**: 1669-1686 (2000).
- [6] Ping Gao and Leslie M. Collins, "A Comparison of Optimal and Sub-Optimal Processors for Classification of Buried Metal Objects," *IEEE Signal Processing Letters* **6**(8):216-218 (August 1999).
- [7] Leslie M. Collins, Ping Gao, and Lawrence Carin, "An Improved Bayesian Decision Theoretic Approach for Land Mine Detection," *IEEE Trans. Geoscience and Remote Sensing* **37**(2):811-819 (March 1998).

INVITED PAPERS

- [1] Leslie Collins, Ping Gao, Larry Makowsky, John Moulton, Denis Reidy, and Dick Weaver, "Improving Detection of Low-Metallic Content Landmines Using EMI Data", *Proceedings of IGARSS*, International Geoscience and Remote Sensing Symposium, Hawaii, July 2000.
- [2] Leslie Collins, Ping Gao, "Hypothesis Testing for Landmine Detection with EMI Images", IEEE International Conference on Fuzzy Systems, Anchorage, Alaska, May 4-9 1998, p.237-240.
- [3] Ping Gao and Leslie M. Collins, "Improved Signal Processing Approach for Land Mine Detection", *Proceedings of SPIE*, vol. 3392, SPIE Conference on Detection and Remediation Technologies for Mines and Minelike Targets III, April 1998.

REFEREEED CONFERENCE PROCEEDINGS

- [1] Leslie Collins, Ping Gao, John Moulton, Larry Makowsky, Denis Reidy, and Dick Weaver, "A Comparison of Statistical Signal Processing Algorithms for Detection and Identification of Low Metal ", Proceedings of UXO Forum, Atlanta, GA, May 2000.
- [2] Ping Gao and Leslie Collins, "Time-Domain Metal Detector and GPR Data Processing and Fusion for Landmine Detection", *Proceedings of SPIE*, SPIE Conference on Detection and Remediation Technologies for Mines and Minelike Targets V, FL. April 2000,
- [3] Ping Gao, Leslie Collins, and Lawrence Carin, "Bayesian Optimal Classification of Metallic Objects: A Comparison of Time-Domain and Frequency-Domain EMI Performance" *Proceedings of SPIE*, SPIE Conference on Detection and Remediation Technologies for Mines and Minelike Targets V, FL. April 2000,
- [4] Leslie Collins, Stacy Tantum, Ping Gao, John Moulton, Larry Makowsky, Denis Reidy, and Dick Weaver, "Improving Detection of Low-Metallic Content Landmines Using EMI Data", *Proceedings of SPIE*, SPIE Conference on Detection and Remediation Technologies for Mines and Minelike Targets V, FL. April 2000,
- [5] Ping Gao and Leslie Collins, "Signal Processing for Low Metal Mine Detection and Identification: Results from a Blind Field Test", EuroEM, 2000.
- [6] Ping Gao and Leslie Collins, "Classification of Buried Metal Objects Using Wideband Frequency-Domain EMI Responses: A Comparison of Optimal and Sub-Optimal Processors", *Proceedings of IGARSS*, 1999 International Geoscience and Remote Sensing Symposium, Hamburg, Germany, June 1999.
- [7] Ping Gao and Leslie Collins, "Statistical Signal Processing Techniques for the Detection of Low-Metal Land Mines Using EMI and GPR Data", *Proceedings of IGARSS*, 1999 International Geoscience and Remote Sensing Symposium, Hamburg, Germany, June 1999.

- [8] Leslie M. Collins, Ping Gao, Norbert Geng, Lawrence Carin, Dean Keiswetter, I.J. Won, "Discrimination of UXO-Like Metal Targets Using Wideband electromagnetic Induction", *Proceedings of UXO Forum*, Atlanta, GA, May 1999.
- [9] Leslie M. Collins, Ping Gao, Lloyd Riggs, John Moulton, Larry Makowsky, Denis Reidy, and Richard Weaver, "Detection of Low-Metal Mines Using Time-Domain and Frequency-Domain EMI", *Proceedings of UXO Forum*, Atlanta, GA, May 1999.
- [10] Ping Gao, Stacy Tantum, and Leslie M. Collins, "Single Sensor Processing and Sensor Fusion of GPR and EMI Data for Landmine Detection", *Proceedings of SPIE*, SPIE Conference on Detection and Remediation Technologies for Mines and Minelike Targets IV, Orlando, FL, April 1999.
- [11] Ping Gao, Leslie M. Collins, John Moulton, Larry Makowsky, Richard Weaver, Dean Keiswetter and IJ Won, "Enhanced Detection of Landmines Using Broadband EMI Data", *Proceedings of SPIE*, SPIE Conference on Detection and Remediation Technologies for Mines and Minelike Targets IV, Orlando, FL, April 1999.
- [12] Sandy Throckmorton, Yingyi Tan, Ping Gao, Lisa Gresham, and Leslie Collins, "Enhanced auditory processing for landmine detection using EMI sensors", *Proceedings of SPIE*, Detection and Remediation Technologies for Mines and Minelike Targets III Conference, 1999 International Symposium on Aerospace/Defense Sensing and Controls, Orlando, FL, April 1999.
- [13] Ping Gao, Leslie M. Collins, Norbert Geng, Lawrence Carin, Dean Keiswetter, I.J. Won, "Classification of Landmine-Like Metal Targets Using Wideband Electromagnetic Induction", *Proceedings of ICASSP*, IEEE International Conference on Acoustics, Speech and Signal Processing, Phoenix, AZ, March 1999.